Molecular concepts for pandemic viruses: Membrane fusion assays and targeting of reservoir cells

Dissertation
zur Erlangung des Doktorgrades
der Naturwissenschaften

vorgelegt beim Fachbereich Biochemie, Chemie und Pharmazie
der Johann Wolfgang Goethe-Universität
in Frankfurt am Main

von
Samuel Arthur Theuerkauf
aus Frankfurt am Main

Frankfurt am Main, 2024
(D 30)

Vom Fachbereich Biochemie, Chemie und Pharmazie (14) der

Johann Wolfgang Goethe – Universität als Dissertation angenommen.

Dekan:	Prof. Dr. Clemens Glaubitz
Gutachter:	Prof. Dr. Rolf Marschalek
	Prof. Dr. Christian J. Buchholz
Datum der Disputation:	04.07.2024

‘In the fields of observation chance favors
only the prepared mind.’

- Louis Pasteur

Content

1 Summary

Recent pandemic viruses have led to substantial health impacts, highlighting the crucial need for ongoing development and adaptation of diagnostic assays and therapies. This thesis focuses on the two pandemic viruses severe acute respiratory syndrome coronavirus type 2 (SARS-CoV-2) and human immunodeficiency virus (HIV).

The SARS-CoV-2 spike protein (S) mediates cell entry by fusing the viral envelope membrane with the cell membrane and is therefore in focus for antiviral therapies. Initial studies have demonstrated a high fusion activity of the S protein. Therefore, new *in vitro* assays needed to be established to assess neutralizing binders that inhibit cell entry and fusion activity. This thesis demonstrates in its first part the establishment of quantitative and highly sensitive assays assessing cell-cell and particle-cell fusion mediated by S.

Despite extensive research, HIV remains incurable, with global transmission persisting. Effective therapeutics have vastly improved the life of HIV patients, but the establishment of HIV reservoir cells remains the major problem. Previous studies have reported that CD32a expression on CD4 T cells mark HIV reservoir cells harboring highly enriched and replication-competent proviruses. One strategy for achieving a cure is the selective inactivation of the HIV provirus in infected cells using Cas9 nuclease. However, its efficient delivery to HIV reservoir cells remains challenging. Adeno-associated vectors (AAV) might be used for the delivery but their broad tropism results in inefficient delivery into the target cells. Therefore, the second part of this thesis demonstrates the establishment of an AAV vector system targeted to the HIV reservoir markers CD4 and CD32a.

In this thesis, three assays to analyze the fusion activity of S were established covering cell- and particle-cell fusion activities, providing a comprehensive readout of S fusion activity. Moreover, S-particles were shown to initiate the fusion of neighboring cells in absence of a productive infection in a process known as fusion-from-without (FFWO). For particle-cell fusion assay, (LV) displaying the S protein were generated. The transduction efficiency of S-LV transferring *LacZ* was highest on cells overexpressing the SARS-CoV-2 receptor ACE2 and remarkably reached a signal 2000-fold over background. Through display of S on virus-like particles FFWO activity of S was observed and quantified. For the quantification, a reporter complementation assay was established by expressing the alpha and omega fragments of the beta-galactosidase separately in two cell populations which both expressed ACE2. The addition of S-particles caused the fusion of both cells enabling the complementation of alpha- and omega-fragments and the quantification of functional beta-galactosidase by substrate-specific luminescence reaction. Under optimal conditions this assay reached a signal-to-noise ratio of 2.7 orders of magnitude. Then the complementation assay was used in a cell-cell fusion assay in which effector cells expressed S and the alpha fragment, and target cells expressed

ACE2 and the omega fragment. Using extremely low levels of S on effector cells significant fusion was still detectable. Similar to the FFWO assay, the cell-cell fusion assay reached a signal-to-noise ratio of 2.9 orders of magnitude. Next, S-specific inhibitors were used in the fusion assays. In contrast to particle-cell fusions, the fusion activity of S presented on cells was only moderately inhibited by antibody and sera, suggesting that particle cell entry can be more efficiently prevented than spreading via cell-cell fusion.

To redirect AAV2 towards the HIV reservoir, CD4 and CD32a-specific designed ankyrin repeat proteins (DARPin) were incorporated into receptor-blinded AAV particles. Furthermore, to aim for a preference of cells expressing both markers, both DARPins were connected and displayed on AAVs. These bispecific AAVs showed no altered capsid structures compared to an unmodified capsid as demonstrated by cryo-electron tomography. When these particles were added to a cell mixture of CD4-, CD32a- and CD4/CD32a-expressing cells, bispecific AAVs preferably transduced double-positive cells. This preference was highest in cell cultures containing highly underrepresented CD4/CD32a-expressing cells and when a low number of 107 genome copies per cell was used reaching a preference of 66-fold above CD32a-expressing cells. Even when binding and transduction of isolated primary cells or within human whole blood was assessed, bispecific AAVs showed much higher preference for double-positive cells than monospecific AAV. This held true after systemic injection into a humanized mouse model, where bispecific AAVs were more active in transducing double-positive cells than a mix of AAVs monospecific for CD32a or CD4.

This thesis describes membrane fusion assays monitoring the activities of SARS-CoV-2 spike protein which are active at a high signal-to-noise ratio thus allowing the detection of subtle differences of S-directed inhibitors. Interestingly, syncytia formation can proceed at minimal levels of S and is less efficiently neutralized by antibodies than particle-cell fusion. This may be especially concerning regarding the disease progression of COVID-19 which associates syncytia formation in patients with multiorgan dysfunction characterized as pneumonia, thrombosis and leukopenia. Also, FFWO, which mediates cell fusion in absence of a productive infection, may contribute to the disease progression.

A surprising finding of this thesis was the preference of bispecific AAV for cells double-positive for CD4 and CD32a. Remarkably, DARPin insertions were well tolerated by the capsid assembly process and did not interfere with gene delivery. The AND-gated binding behavior might be explained by an increase in attachment points on the cell surface for the engaging AAV particles which increase binding strength through a gain of avidity. Towards HIV gene therapy, such bispecific AAV might be well suited to target the highly underrepresented HIV reservoir cells expressing CD32a on CD4 T cells in peripheral blood of patients. Nevertheless, recent studies indicate that reservoir cells can be characterized by other surface markers, which can be easily addressed by the flexible adaption of the vector system.

2 Zusammenfassung

In den letzten Jahren haben verschiedene pandemische Viren zu beträchtlichen Krankheits- und Todesfällen geführt. Aufgrund der zunehmenden Vernetzung der Menschen können sich Viren schneller und leichter verbreiten. Um dieser ständigen Bedrohung entgegenzuwirken ist es wichtig, diagnostische Testsysteme und Therapien anzupassen oder neu zu etablieren. Diese Arbeit konzentriert sich auf die pandemischen Viren „severe acute respiratory syndrome coronavirus type 2“ (SARS-CoV-2) and „human immunodeficiency virus“ (HIV).

Der Zelleintritt von SARS-CoV-2 wird durch das Spike-Protein (S) ausgelöst und ist deshalb im Fokus für die Entwicklung neuer antiviraler Medikamente. Der Zelleintritt von SARS-CoV-2 erfolgt nach der Fusion der Virushülle mit der zellulären Membran. Erste Studien haben eine hohe Fusionsaktivität des S-Proteins gezeigt. Aus diesem Grund sollten in dieser Arbeit neue Fusionstests etabliert werden, welche potenzielle Inhibitoren der Zellfusion evaluieren können. Zu diesem Zweck demonstriert diese Thesis im ersten Teil die Etablierung von sensitiven und quantitativen Tests zur Evaluierung der Zell-Zell und Partikel-Zell Fusionsaktivität, welche durch S bewirkt wird.

Trotz jahrelanger Forschung können HIV-Patienten nicht geheilt werden und Virusinfektionen treten weiterhin weltweit auf. Dennoch hat die Entwicklung von antiretroviralen Therapien die Lebensbedingungen von HIV-Patienten signifikant verbessert. Das größte Problem bei der Entwicklung eines Heilmittels ist die frühe Etablierung von Reservoirzellen während einer Infektion. Um diese Reservoirzellen zu identifizieren, wurde kurz vor dem Beginn dieser Arbeit der Oberflächenmarker CD32a vorgeschlagen. Dieser ist auf CD4+ T-Zellen hochreguliert, die angereicherte und replikationskompetente HIV DNA (Proviren) besitzen. Eine Möglichkeit, HIV zu inaktivieren, besteht in der Behandlung mit Cas9-Nukleasen, welche selektiv das Provirus schneiden und somit eine Replikation von HIV verhindern. Obwohl das System *in vitro* erfolgreich ist, bleibt die effiziente Einbringung in die Reservoirzellen eine Herausforderung. Für diesen *in vivo* Gentransfer können Adeno-assoziierte Vektoren (AAVs) verwendet werden, welche bereits in der Klinik aufgrund ihrer Sicherheit und geringen Immunogenität eingesetzt werden. Diese AAVs haben einen breiten Tropismus, wodurch der Gentransfer in die Reservoirzellen ineffizient ist. Eine Möglichkeit, dieses Problem zu beheben, besteht darin AAVs selektiv an Oberflächenmarker einer Zielzelle zu binden. Daher wird im zweiten Teil dieser Thesis die Etablierung und Charakterisierung von Rezeptor-gerichteten AAVs für die HIV-Gentherapie demonstriert, welche die Oberflächenmarker CD4 und CD32a für den Zelleintritt nutzen.

Zur Charakterisierung der Fusionsaktivität von SARS-CoV-2 wurden drei quantitative Fusionstests etabliert, welche Partikel- und Zell-Zell Fusionen berücksichtigen. Für den Partikel-Zell Fusionstest wurden lentivirale Vektoren (LV) verwendet, welche das S Protein auf ihrer Oberfläche präsentierten. Der Einbau von S in LVs wurde mithilfe von Western Blots

nachgewiesen und bestätigte, dass eine C-terminale Verkürzung zu einem besseren Einbau in das Kapsid führt. Die Transduktionseffizienz von S-LV erreichte auf Zellen, die den SARS-CoV-2 Rezeptor ACE2 exprimieren, ein Signal-zu-Hintergrund Verhältnis von über 2000.

Durch die Präsentierung von S auf leeren LV-Partikeln konnte die Fusion von benachbarten Zellen detektiert und quantifiziert werden („fusion-from-without“ (FFWO)). Für die Quantifizierung wurde ein Reporter-Komplementationstest etabliert, indem die Alpha- und Omega-Fragmente der β-Galaktosidase getrennt in zwei Zielzellpopulationen exprimiert wurden, die beide ACE2 exprimierten. Die Zugabe von S-Partikeln führte zur Fusion der Zielzellen und ermöglichte die Komplementation der Alpha- und Omega-Fragmente und die Quantifizierung der resultierenden β-Galaktosidase-Aktivität durch eine substratspezifische Lumineszenzreaktion. Unter optimalen Versuchsbedingungen erreichte dieser Assay ein Signal-zu-Hintergrund Verhältnis von 2,7 Größenordnungen. Das bereits hohe Signal-zu-Hintergrund-Verhältnis konnte durch eine extrazelluläre Aktivierung des S-Proteins mithilfe von Trypsin weiter erhöht werden.

Ausgehend von der hohen Fusionsaktivität von S-Partikel mit Zielzellen wurde die Fusionsaktivität zwischen Zellen untersucht. Nach Ko-Kultivierung von S-präsentierenden Zellen mit ACE2-Zielzellen konnte eine ausgeprägte Synzytienbildung beobachtet werden. Diese Zellen zeigten eine charakteristische Zunahme des Zellvolumens und enthielten mehrere Zellkerne, was auf die Fusion mehrerer Zellen schließen ließ. Um die geringste Menge an S zu bestimmen, welche ausreicht, um eine Zellfusion zwischen Zellen auszulösen, wurde ein quantitativer Zellfusionstest etabliert. Dazu wurde erneut der alpha-Komplementationstest der β-Galaktosidase verwendet. In diesem Test exprimierten Effektorzellen S und das Alpha-Fragment, Zielzellen ACE2 und das Omega-Fragment. Eine Zellfusion zwischen Effektor- und Zielzelle resultierte hierbei in der Bindung von Alpha an Omega, sodass das funktionale Enzym anhand einer Substratumsetzung quantifiziert werden konnte. Effektorzellen mit unterschiedlich hoher S-Expression wurden hergestellt, indem 293T-Zellen mit seriell verdünntem S-Plasmid transfiziert und anschließend mit Zielzellen kultiviert wurden. Effektorzellen, die mit der geringsten Plasmiddosis transfiziert worden waren, zeigten bereits nach einer Übernacht-Inkubation ein signifikantes Fusionssignal. Bemerkenswerterweise konnte die geringe Menge an S-Protein auf diesen Effektorzellen weder mittels Western Blot noch Durchflusszytometrie detektiert werden. Auch hier konnte unter optimalen Versuchsbedingungen ein hohes Signal-zu-Hintergrund Verhältnis von 2.9 Größenordnungen festgestellt werden. Nachdem drei sensitive Fusionstests etabliert wurden, wurden S-spezifische Seren und Antikörper zur Inhibition der Fusion eingesetzt. Während die Partikel-basierenden Fusionstests effizient neutralisiert wurden, konnten Zell-Zell-Fusionen nur mäßig inhibiert werden, obwohl die Menge an S-Protein auf Effektorzellen geringer war als die Menge an S-Protein, die auf Partikeln präsentiert wurde.

Im zweiten Teil der Thesis wurden AAVs, die spezifisch an CD4 und CD32a binden, erzeugt und charakterisiert. Um den Tropismus des parentalen AAV2-Serotyps zu den angesteuerten Rezeptoren zu ändern, wurde zunächst die Bindung an den natürlichen Rezeptor Heparansulfat-Proteoglykan (HSPG) durch das Einbringen zweier Punktmutationen (R585A und R588A) verhindert. Anschließend wurden in diese verblindeten Kapside DARPins, die spezifisch an CD4 oder CD32a binden, in die exponierte GH2/GH3-Region des viralen Kapsidproteins VP1 eingebaut. Um eine höhere Spezifität für Zellen zu erreichen, die beide Rezeptoren auf ihrer Oberfläche präsentieren, wurden beide DARPins genetisch miteinander verbunden und anschließend für die Vektorproduktion verwendet. Der Einbau der monospezifischen und bispezifischen DARPins in das AAV-Kapsid wurde anschließend mittels Western Blot bestätigt. Die Insertion des großen bispezifischen DARPins hatte im Vergleich zu unmodifizierten AAV2 keine Auswirkung auf die Struktur des AAV-Kapsids. Die Rezeptor-gesteuerten AAVs zeigten eine hohe Thermostabilität zwischen 68.5 und 69.5°C. Alle AAV-Vektoren konnten mit einem physischen Titer von ungefähr $1x10^{10}$ Genomkopien pro µl produziert werden. Nach der biochemischen Charakterisierung wurde der Gentransfer mono- und bispezifischer Vektoren untersucht. Dazu wurden SupT1 Zellen genutzt, die entweder CD4, CD32a oder beide Rezeptoren auf ihrer Oberfläche präsentierten. Alle AAV-Vektoren zeigten einen strikt Rezeptor-spezifischen Gentransfer. Interessanterweise wiesen bispezifische Vektoren die höchste Transfereffizienz auf SupT1 Zellen auf, welche beide Rezeptoren präsentieren. Bereits in diesem Experiment zeigte sich eine stärkere Präferenz der bispezifischen Vektoren für doppelt-positive Zellen im Vergleich zu monospezifischen Vektoren. In weiteren Experimenten wurden die unterschiedlichen SupT1 Zellen gemischt, sodass die doppelt-positiven Zellen stark unterrepräsentiert waren. Unter diesen Bedingungen zeigten bispezifische Vektoren eine starke Präferenz für CD4/CD32a-positive Zellen, wohingegen monospezifische Vektoren einzeln-positive Zellen präferierten. Diese Präferenz der bispezifischen Vektoren trat noch stärker hervor, wenn wenige AAV-Partikel mit dem Zellgemisch inkubiert wurden. Unter diesen Voraussetzungen erreichten bispezifische Vektoren eine bis zu 66-fach höhere Transduktionseffizienz auf CD4/CD32a-positive Zellen gegenüber CD32a-exprimierenden Zellen. Ursächlich für den präferentiellen Gentransfer war ein deutlich effizienterer Zelleintritt der bispezifischen Vektoren. Anschließend wurde der Tropismus der Vektoren auf primären Zellen überprüft. Dazu wurden in einem Bindungstest AAVs für kurze Zeit mit mononukleären Zellen des peripheren Blutes (PBMC) inkubiert und anschließend der gebundene Zelltyp mittels Durchflusszytometrie quantifiziert. In diesem Gemisch der primären Zellen zeigten CD4+ T-Zellen eine starke CD4-Expression und Monozyten exprimieren zusätzlich zu CD32a eine geringere Menge CD4. Wie erwartet zeigten auch hier die bispezifischen Vektoren die stärkste Bindung an die doppelt-positiven Monozyten im Gegensatz zu monospezifischen Vektoren. Alle CD4-gerichteten Vektoren zeigten

Anbindung an CD4+ T-Zellen und Monozyten, während der CD32a-gerichtete Vektor nur mit Monozyten assoziierte. Voraussetzend für die Verwendung der Vektoren für die HIV-Gentherapie ist ein effizienter Gentransfer in primäre T-Zellen. Im Gegensatz zum AAV2-Wildtyp, zeigten alle CD4-gerichteten Vektoren eine effiziente und ähnliche Transduktionseffizienz auf primären, aktivierten CD4+ T-Zellen. Mit einer Genomkopienanzahl von $2{,}5 \times 10^5$ pro Zelle konnten 20-30% der primären CD4+ T-Zellen transduziert werden. Aufbauend auf den zellselektiven Bindungs- und Transduktionstests mit primären Zellen wurde der Gentransfer im menschlichen Blut untersucht. Dazu wurden wenige SupT1-Zellen in menschliches Blut von gesunden Spendern gemischt, um das Vorhandensein von HIV-Reservoirzellen zu simulieren. Anschließend wurden AAV-Vektoren hinzugefügt. Nach sechs Stunden Inkubation wurden PBMC einschließlich der SupT1 Zellen isoliert und für drei Tage kultiviert. Bispezifische Vektoren zeigten auch hier die stärkste Transduktionseffizienz und erreichten bis zu 85% der SupT1-Zellen, wohingegen der CD32a-gerichtete Vektor kaum GFP-Expression in den SupT1-Zellen zeigte. Letztlich wurden die AAV-Vektoren systemisch in NSG-Mäuse injiziert, welche zuvor mit humanen SupT1-CD4-, SupT1-CD32a- und SupT1-CD4/CD32a-Zellen transplantiert worden waren. Die bispezifischen Vektoren zeigten die höchste Transduktion der CD4/CD32a-Zellen, während die Transduktionseffizienz monospezifischer Vektoren in einfach-positiven Zellen höher war. Erwähnenswert ist ebenfalls, dass die bispezifischen Vektoren eine 1.5-fach höhere Gentransfereffizienz in doppelt-positive Zellen zeigten als ein Mix aus beiden monospezifischen Vektoren. Schließlich wurde der Transfer der HIV-spezifischen Cas9-Nuklease mithilfe der gerichteten Vektoren untersucht. In einem ersten Versuch wurden aufgrund der Größenlimitierung von AAV-Genomen die kodierenden Sequenzen für spCas9 und einer Kombination aus drei verschiedenen gRNAs getrennt in zwei Kapside verpackt. Beide CD32a-gerichteten Kapside mussten dieselbe Zelle transduzieren, um spCas9 mit den gRNAs zu komplementieren. Transduzierte Zellen zeigten eine hoch signifikante Inhibierung der HIV-Replikation zwölf Tage nach HIV Infektion. Außerdem wurde in einem bispezifischen Kapsid eine gRNA zusammen mit spCas9 verpackt. Zellen, die mit diesem Vektor transduziert wurden, zeigten ebenfalls eine effiziente Inhibierung der HIV-Replikation.

In dieser Thesis werden neue molekulare Konzepte beschrieben, die zum Verständnis von Infektionen durch Pandemieviren und zur Therapie von Patienten beitragen. Die im ersten Teil durchgeführten Membranfusionstests zur Überwachung der Aktivitäten von S führten zu folgenden Schlussfolgerungen: Erstens, alle etablierten Fusionstests zeigten ein hohes Signal-zu-Hintergrund-Verhältnis, was eine wesentliche Voraussetzung für die Evaluierung von Antikörpern und Patientenseren ist. Das lentivirale Vektorsystem der zweiten Generation, welches für den Partikel-Zell-Fusionstest verwendet wurde, bietet mehrere Vorteile. Im

Gegensatz zu den pseudotypisierten Vektoren, welche vor dieser Thesis publiziert wurden, haben die verwendeten Vektoren in dieser Thesis eine geringere Anforderung an die biologische Sicherheit und diese Partikel können für Hochdurchsatz-Testsysteme verwendet werden. Zweitens demonstrieren die im Rahmen dieser Thesis erhobenen Daten zum ersten Mal FFWO für Coronaviren und hebt dadurch die hohe Fusionsaktivität von S hervor, welches Zellfusionen in Abwesenheit einer produktiven Infektion durchführen kann. Diese Zellfusionen können auch durch Partikel vermittelt werden, welche verkürzte oder defekte Genome inkorporiert haben. Dementsprechend kann dieser Fusionsmechanismus zur Synzytienbildung in COVID-19 Patienten beitragen. Der FFWO-Test untersucht zudem die neutralisierenden Eigenschaften eines Antikörpers im Hinblick auf den Zelleintritt von Partikeln und die Fusion von benachbarten Zellen. Dies qualifiziert den Test als Alternative für die präklinische Evaluierung. Drittens können Zellfusionen mit minimalen Mengen an S ablaufen und durch die in dieser Thesis verwendeten Seren und Antikörper wenig effizient neutralisiert werden. Dies könnte insbesondere im Hinblick auf den Krankheitsverlauf von COVID-19 Patienten bedeutend sein, bei denen die Synzytienbildung mit Multiorganfunktionsstörungen wie Pneumonie, Thrombose und Leukopenie einhergeht.

Bispezifische Vektorsysteme sind eine relevante Ergänzung zu den bisher etablierten monospezifischen Vektoren. Wie im zweiten Teil dieser Thesis gezeigt wurde, können sie zwei Rezeptoren gleichzeitig ansteuern und präferentiell Gene in die doppelt-positive Zellpopulation transferieren. Dies ist wichtig, da viele Zelltypen eher durch mehrere als durch einzelne Oberflächenmarker definiert sind. Der präferentielle Gentransfer in doppelt-positive Zellen wurde in dieser Studie mithilfe von AAVs ermöglicht, die zwei DARPins spezifische für CD4 und CD32a enthalten. Bemerkenswerterweise wurde die Insertion des bispezifischen DARPins toleriert und beeinträchtigte nicht die Verpackung des Reportergens. Die Präferenz der bispezifischen AAV-Vektoren deutet auf ein logisches UND-Bindeverhalten hin. Dies könnte auf eine Zunahme an Bindungsstellen auf der Zelle zurückgeführt werden, wodurch eine hohe Bindungsstärke zur Zielzelle vermittelt wird. Es ist zu erwarten, dass diese Strategie auf andere Oberflächenmarker-Kombinationen angewendet werden kann. In Bezug auf die HIV-Gentherapie könnten solche bispezifischen Vektorsysteme geeignet sein, die unterrepräsentierten HIV-Reservoirzellen anzusteuern. Neuere Studien deuten darauf hin, dass HIV-Reservoirzellen durch weitere Oberflächenmarker definiert sein können. Gentransfer in diese Reservoirzellen kann durch die flexible Anpassung des Vektorsystems leicht erreicht werden.

3 Introduction

3.1 Viral pandemics

Mankind has always been challenged by infectious diseases, which have had huge impacts on evolution and survival. While most of the encountered pathogens can be controlled and restricted by intrinsic human defense mechanisms, such as the immune system, some pathogens have managed to adapt more quickly and consequently gain fitness advantages leading to a wide-reaching spread. In the past, epidemic and pandemic viruses such as human immunodeficiency virus (HIV), influenza virus, Ebola virus and coronaviruses have caused substantial morbidities and mortalities (Baker et al. 2022). Although in modern times medical treatments have advanced and vaccines are developed in unprecedented speed (Polack et al. 2020), viral pandemics still require enormous efforts to restrict the viral spread and to keep health systems functioning. The transmission of viruses is one of the most concerning problems in the age of globalization. Historically, viral spread was associated with international trading routes leading to the expansion of viruses at places with appropriate conditions. Increased global connectivity by utilizing international travel systems, such as planes, ships and trains, leads to the rapid spread of viruses around the world. Additionally, economic, political and environmental driven migration further increases the risk of transferring infectious pathogens. Climate change can create new environmental conditions that allow viruses to emerge in new biological niches. In this regard, the extensive use of land for agricultures restricts the habitat of wild animals and forces a close contact of workers to animals increasing the possibility of an animal-to-human transmission of viruses (zoonosis) (Baker et al. 2022).

Therefore, it is highly likely that new viruses or virus variants will emerge or re-emerge in future. To meet these ongoing threats, diagnostic and therapeutic systems need to be consistently established and adapted, allowing for the fast containment of the virus or therapy of infected patients. This thesis focuses on two pandemic viruses, HIV and SARS-CoV-2.

3.1.1 HIV

Acquired immunodeficiency syndrome (AIDS) remains a major health threat having caused the deaths of 40.4 million people to date, with ongoing transmissions occurring worldwide. Estimated numbers indicate more than 39 million are currently infected with HIV, with the majority of cases occurring in African countries. This has established AIDS as the leading cause of death for young people in these countries (World Health Organization 2023).

The first AIDS patients were diagnosed 1981 in the United States showing symptoms of pneumonia and Kaposi sarcoma, which were typically seen in immunocompromised patients (MS et al. 1996). These opportunistic infections indicate a severe immune deficiency hinting towards an acquired immune deficiency syndrome. Shortly after, the virologists Luc

Montagnier and Francoise Barre-Sinoussi identified in 1983 the T-lymphotropic retrovirus HIV being the responsible pathogen (Barré-Sinoussi et al. 1983).

In the early years of HIV research, the modes of HIV transmission via blood, breast milk, semen and vaginal secretion were identified. Notably, sex workers, male homosexual and intravenous drug users who shared unsterile needles showed high infection rates (Ghosn et al. 2018).

The origin of HIV can be traced back to the closely related simian retroviruses (SIV), whose natural hosts are non-human primates. Currently, two types of HIV are known: HIV-1, which originated from zoonosis of SIV_{cpz} found in chimpanzees and HIV-2, which is derived from SIV_{sm} circulating in sooty mangabey populations (Hahn et al. 2000).

While a cure for HIV is currently unavailable, patients can be effectively treated with anti-retroviral therapy (ART) which suppresses viral replication and reduces the viral load to undetectable levels in blood. Certain milestones have been reached for the identification of suitable inhibitors. Although the first anti-HIV drug (azidothymidine in 1987) was released shortly after the identification of HIV, the lethality of patients was still high (Fauci 2003). First revolutionary therapies were achieved using the combination of drugs designed to target at least two viral proteins. Such highly active antiretroviral therapies (HAART) reduced AIDS-related death by 50% within three years. Further improvements in drug development and combination led to new classified treatments termed combination antiretroviral therapy (cART), which increased efficacy from 43% to 78% in 2010 as measured by the decrease in viremia (Lee et al. 2014). However, a complete eradication of the virus remains an elusive goal due to the proliferation and activation of latently infected cells (Menéndez-Arias and Delgado 2022).

New methods have been developed aiming to eradicate HIV reservoir cells, overcoming the need for livelong drug dependency of patients. Gene therapeutics are the most promising approach, as they can specifically eliminate infected cells, remove the stably integrated provirus or knock out one of the entry receptors of HIV. The latter approach was inspired by the rare cases in which the 'Berliner' (Hütter and Thiel 2011), 'Düsseldorfer' (Jensen et al. 2023) and 'London' (Gupta et al. 2020) patients were cured after receiving cell transplantations from CCR5-deficient donors. As a result there was a strong emphasis on designing nucleases which specifically disrupt the reading frame of *CCR5* with the hope of providing lifelong resistance against HIV infections (Haworth et al. 2017). Alternative approaches use clustered regular interspaced short palindromic repeats (CRISPR)-Cas9 nucleases targeted towards multiple positions of the HIV provirus. This results in a fragmented sequence which efficiently prevents viral protein expression and also effectively inhibits the emergence of escape mutants (Fan et al. 2022).

3.1.2 HIV reservoir

The major obstacle in the development of a cure for HIV is the persistence of the HIV provirus in latently infected cells. Once ART is discontinued, HIV quickly rebounds from infected cells spreading to new host cells and destroying CD4 T cells leading to a high susceptibility for opportunistic infections (McCune 2001). The establishment of a HIV reservoir occurs early during the acute infection phase. In as little as three days after infection, HIV provirus can already be detected in resting CD4 T cells (Whitney et al. 2014). Although it was shown that early treatment with cART is essential to significantly reduce the size of the reservoir, it does not prevent the establishment or eradication of the reservoir (Colby et al. 2018). Depending on the latently infected cell type, the half-life of a reservoir cell reaches on average 43 months which almost guarantees lifelong persistence of HIV (Siliciano et al. 2003).

The molecular basis for the persistence is the integration of the HIV DNA into the host chromosome. To achieve this, HIV first has to initiate attachment and fusion with a target cell expressing the required receptor combination. The HIV envelope glycoproteins GP41 and GP120 bind consecutively to the CD4 receptor followed by the attachment to one of the coreceptors CXCR4 or CCR5. Both envelope proteins undergo complex conformational changes leading to the exposure and insertion of the fusion peptide into the cell membrane resulting in the cell fusion of the viral and the host membranes (Wilen et al. 2012). Subsequently, the HIV capsid is released into the cytoplasm and the viral reverse transcriptase converts the single-stranded RNA to DNA facilitating the entry into the nucleus. The integrase inserts the provirus into the host DNA with a preference for gene segments associated with high transcription activity (Craigie and Bushman 2012). The provirus is then either actively transcribed leading to the expression of new viral proteins which assemble in the cytoplasm and are proteolytically cleaved, resulting in mature infectious particles. Alternatively, the infected cell may not produce viral particles and become latently infected. The majority of latently infected cells produce short, abortive viral transcripts distinguishing them from cells that are transcriptionally silenced and in a state of deep latency (Einkauf et al. 2022).

Ongoing research aims to understand the mechanism underlying the persistence of HIV in some infected cells. The major factors are thought to be associated with the functions of T cell subsets. The majority of HIV reservoir cells are memory CD4 T cells which have a long lifespan contributing to the sustained persistence of HIV (Finzi et al. 1997). Furthermore, homeostatic and antigen- induced proliferation of T cells lead to clonal expansion of HIV reservoir cells (Chomont et al. 2009; Mendoza et al. 2020). T cell differentiation and maturation results in the distribution of the HIV provirus to all CD4 subsets. Furthermore, the expression of checkpoint inhibitors, such as PD-1 and CTLA-4, marks T cell subsets showing enriched provirus sequences (Fromentin et al. 2019; McGary et al. 2017). This is associated with a selective advantage by inhibiting interacting immune cells. It is important to note that, despite ART treatment, viral replication might still go on in tissues inaccessible fur the drugs, such as the gut. As a result, HIV is replenished from these sources. Current opinions on the persistence of HIV envision a highly dynamic existence of reservoirs characterized by frequent expansions and reductions associated with the proliferative functions of T cells and the counter actions of immune cells (Fromentin and Chomont 2021; Pasternak and Berkhout 2023) (see Figure 1).

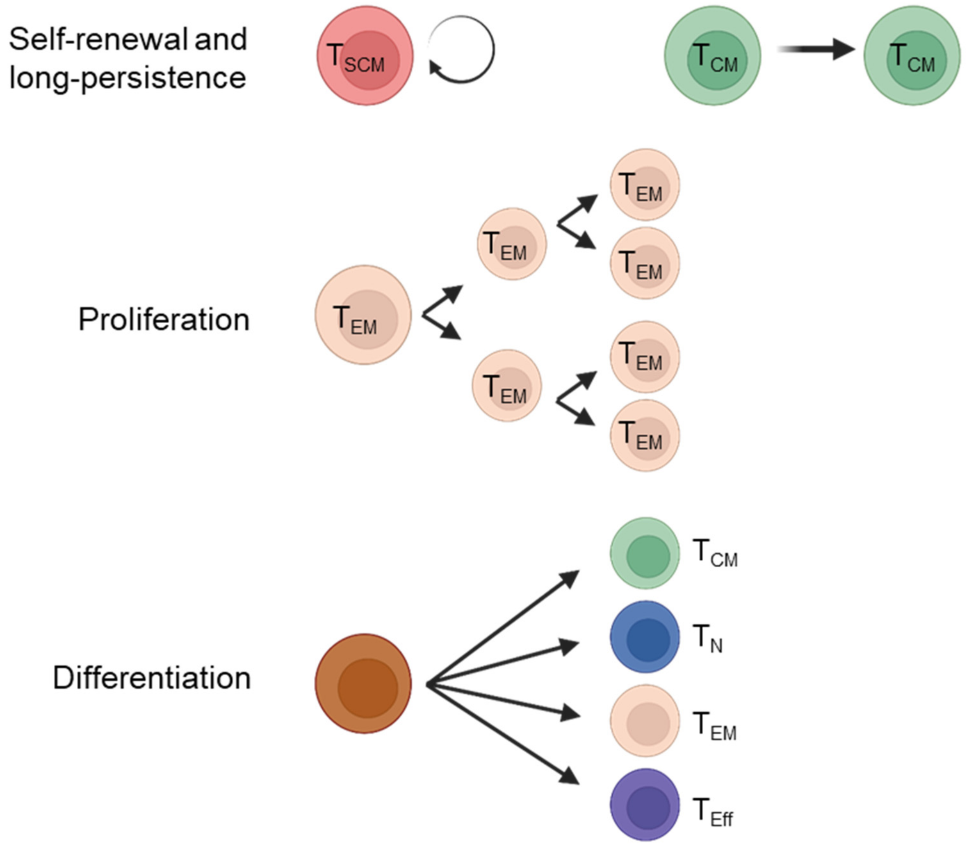

Figure 1: **Persistence of HIV in ART treated patients.**
The self-renewal, long-term persistence, proliferation and differentiation abilities of CD4 T cell subsets are thought to be major drivers of HIV persistence in patients with suppressed viral replication due to ART treatment. SCM: stem cell memory T cell, CM: central memory T cell, EM: effector memory T cell, N: naïve T cell, Eff: effector T cell. Adapted from (Fromentin and Chomont 2021).

Right before the start of this PhD project, first cell surface markers have been suggested to identify HIV reservoir cells including CXCR3, CCR6, CD2, PD-1, Lag-3, TIGIT and others (Adams et al. 2021; Darcis et al. 2019). However, CD32a has gathered prioritized attention. Descours et al. proposed that the low-affinity Fc-receptor FcγRIIa (CD32a) marks cells containing replication-competent proviruses with a 10^3-fold enrichment for total HIV DNA (Descours et al. 2017) (see Figure 2). In this study, the authors focused on differential gene expression in resting CD4 T cells being the major cell compartment harboring HIV reservoir cells. The experiment was designed to first remove the intrinsic HIV restriction factor SAMHD1 by exposing PBMC of healthy donors with virus-like particles presenting the Vpx accessory protein from SIV_{mac251}, inducing its degradation followed by the infection with HIV-1. RNA expression profiles of HIV-infected and non-infected cells were then compared revealing 103 genes exclusively expressed in infected cells. Sixteen of these genes were transmembrane proteins which were subsequently validated on protein level using flow cytometry. Of all the analyzed markers, CD32a was most potently induced and distinct from uninfected cells. The authors further stated that CD32a does not mark the entire CD4 T cell reservoir. However, viral induction assays demonstrate that a substantial number of CD32a-positive reservoir cells contain replication-competent proviruses.

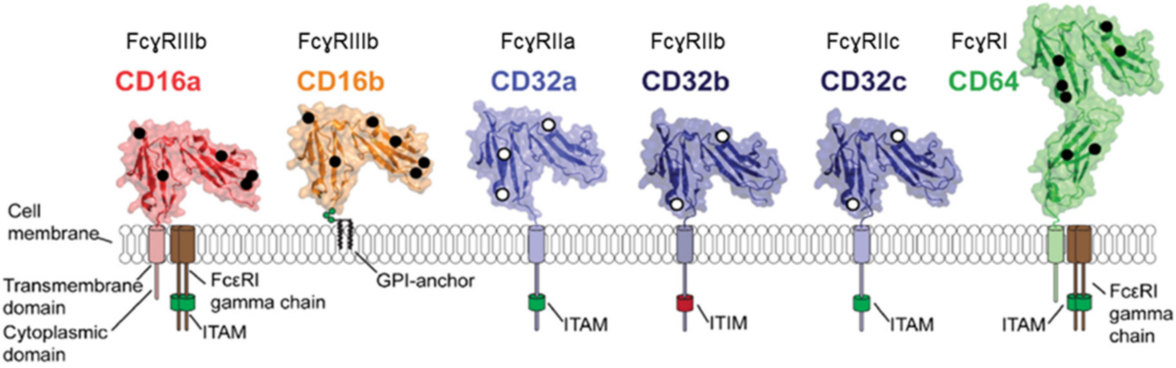

Figure 2: **Structure of human Fcγ-receptors.**
Fcγ-receptors activate the immune system through the binding to the fragment crystallizable (Fc) domain of Immunoglobolin G. All Fcγ-receptors are expressed on leukocytes of both myeloid and lymphoid lineage which can be further differentiate in their ability to transmit activating signals via the immunoreceptor tyrosin-based activating motif (ITAM) or inhibitory signals via immunoreceptor tyrosin-based inhibiting motif (ITIM). The ratio of activating and inhibitory signals influences the outcome of an immune response. Adapted from (Patel et al. 2019).

Although, the CD32a marker indicates promising enrichment for HIV DNA, detecting CD32a on primary CD4 T cells remained challenging. A major difficulty was the absence of a CD32a-specific antibody which reliably discriminates the a-isoform from other closely related FcγRII-receptors. Together with colleagues in the host laboratory for this thesis, a CD32a-specific binder based on designed ankyrin repeat proteins (DARPin) was identified (Riechert et al. 2023) (see Figure 3). Remarkably, this DARPin F11 did not show any off-target binding to the CD32b receptor, which only differs from CD32a in ten amino acid residues in the extracellular region of the protein. Additionally, F11 showed a high affinity of 6.1 nM towards CD32a. By using F11 it was possible to reliably stain CD32a on CD4 T cells without the necessity for multiple rounds of cell selection.

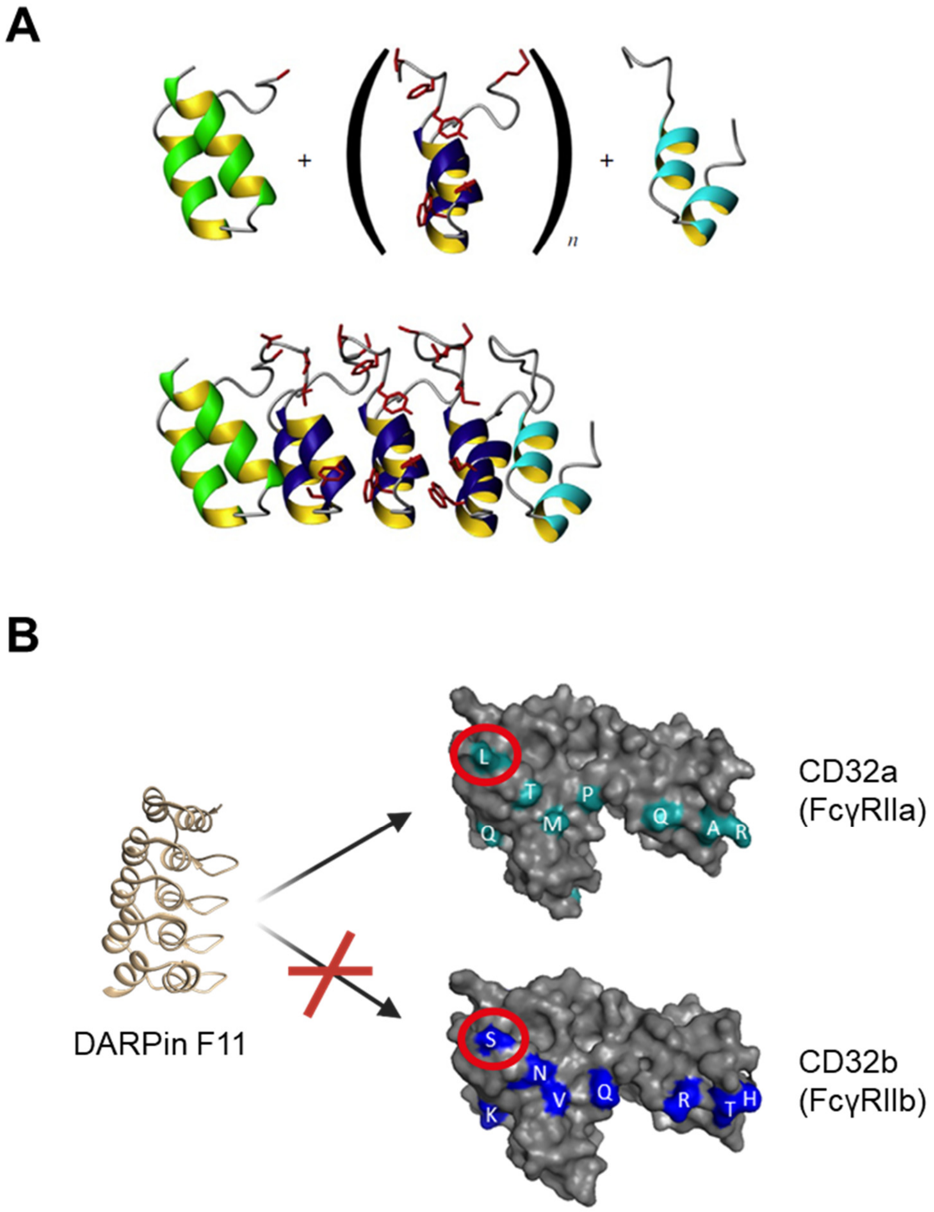

Figure 3: **DARPin structure and binding properties of F11.**
A) The DARPin structures comprises N- and C-terminal capping repeats which ensure a rigid and stable structure of the molecule. Between the cap modules a variable number of internal repeats is inserted, which contains six randomized amino acids per repeat. These amino acids confer the specificity towards a selected receptor. Figure is adapted from (Tamaskovic et al. 2012). **B)** F11 has been selected to specifically bind CD32a while not recognizing the closely related CD32b receptor. Amino acids that are different in each molecule are shown in white. L135 in CD32a was shown to be critical for the binding of the F11 which is replaced in CD32b by S135. Figure is adapted from (Riechert et al. 2023). DARPin F11 structure was predicted using Alphafold (Mirdita et al. 2022).

3.1.3 SARS-CoV-2

SARS-CoV-2 was first detected in December 2019 in Wuhan (China). It quickly spread to many countries and was shortly after declared as a pandemic virus in January 2020. Until now, there have been over 680 million reported cases with 6.8 million deaths associated with COVID-19 and an estimated lethality rate of 1% (Johns Hopkins University of Medicine 2023).

SARS-CoV-2 belongs to the family of Coronaviridae and the genus of Betacoronavirus, which members are known to cause typical respiratory infections. Three viruses of this family have now emerged during zoonotic events, causing epidemics in 2002 by SARS-CoV and 2012 by MERS-CoV (Marschalek 2023). While MERS was transmitted from camels, the natural reservoir of SARS and SARS-COV-2 seems to reside in horseshoe bats (Apaa et al. 2023). Nevertheless, it is expected that a yet unknown mammalian intermediate host finally facilitated the transmission to human (Pekar et al. 2022). Human coronaviruses are primarily transmitted through respiratory droplets (Baselga et al. 2022), making face masks an effective tool to counteract viral spread (Bar-On et al. 2020). In contrast to SARS- and MERS-CoV, SARS-CoV-2 was shown to be transmitted between humans before the onset of symptoms or even in asymptomatic cases which constitute a major concern for controlling virus spread (Baker et al. 2022).

COVID-19 is associated with flu-like symptoms such as fever, cough and dyspnea that can progress to life-threatening acute respiratory distress, pneumonia, renal dysfunctions and multi-organ dysfunctions. SARS-CoV-2 depends on the expression of angiotensin-converting enzyme 2 (ACE2) receptor which is primarily found in the type II alveolar cells and ciliated cells in bronchial and nasal epithelia. Thus, these cells are the initial targets in the respiratory tract enabling viral replication and spread to connected organs (Ahn et al. 2021). Additionally, ACE2 is highly expressed on endothelial cells resulting in the disruption of membrane barriers having significant impact on organ functions, blood pressure control and thrombosis risk (Badraoui et al. 2021; Marschalek 2023).

The COVID-19 pandemic has required drastic official regulation in many countries to contain the virus, protect risk-groups and to prevent healthcare systems from becoming overwhelmed. These measures have ranged from restricted social contacts to curfews, resulting in polarized political tensions and protests. Furthermore, governments allocated significant financial resources to industries and businesses threatened by insolvency due to lockdowns and reduced customer numbers. Additionally, scientific research was redirected towards the development of therapeutics against SARS-CoV-2. This focus, while necessary to deal with the crisis, held back research activity in other fields.

3.1.4 SARS-CoV-2 spike protein

SARS-CoV-2 is an enveloped, single-stranded RNA virus encoding four structural proteins present in the virion: nucleocapsid (N), membrane (M), envelope (E) and spike (S) proteins (Schoeman and Fielding 2019; Jackson et al. 2022). While the N protein stays associated with the viral RNA incorporated into the capsid, M, E and S are transmembrane proteins displayed on the surface of SARS-CoV-2. E and M contribute to the maturation of the virion and subsequent budding. Cell entry of SARS-CoV-2 is mediated by the S protein which enables interaction to the ACE2 receptor and subsequent cell internalization (Hoffmann et al. 2020a).

The S protein is a type I transmembrane protein and assembles as a homotrimer on the surface of the virion (Watanabe et al. 2020). The structure comprises the two subunits S1 and S2. The S1 subunit contains four sub-domains: N-terminal domain (NTD), receptor-binding domain (RBD) and two C-terminal domains (CTD1 and CTD2). In the prefusion state, S1 winds around the S2 subunit shielding it from the extracellular milieu (Walls et al. 2020; Jackson et al. 2022). The NTD is heavily glycosylated hindering the binding and supports the evasion from antibodies. Whether the NTD has a functional role in cell entry is unclear. The RBD can change between a down or up conformation determining whether receptor interaction is possible (Shang et al. 2020; Lan et al. 2020). In the up-configuration only one of the three RBS domains is exposed conferring an intermediate state which allows binding to ACE2. The adjacent CTD domains mediate important conformational changes which stabilize both conformations of the RBDs. The S1 subunit is followed by a multibasic furin-cleavage site which separates S1 and S2. After cleavage both domains remain non-covalently associated and S2 anchors S in the viral membrane (Belouzard et al. 2009; Jackson et al. 2022). S2 harbors the fusion peptide which is buried in the prefusion state. Two heptad repeat domains (HR1 and HR2) fulfill conformational changes upon engagement of the S1 subunit to the receptor resulting in the insertion of the fusion peptide into the cell membrane and subsequent membrane fusion (Fan et al. 2020; Jackson et al. 2022). Additionally, a second proteolytic cleavage site (S2’) located in the S2 needs to be cleaved to activate the fusion process (Jackson et al. 2022) (see Figure 4).

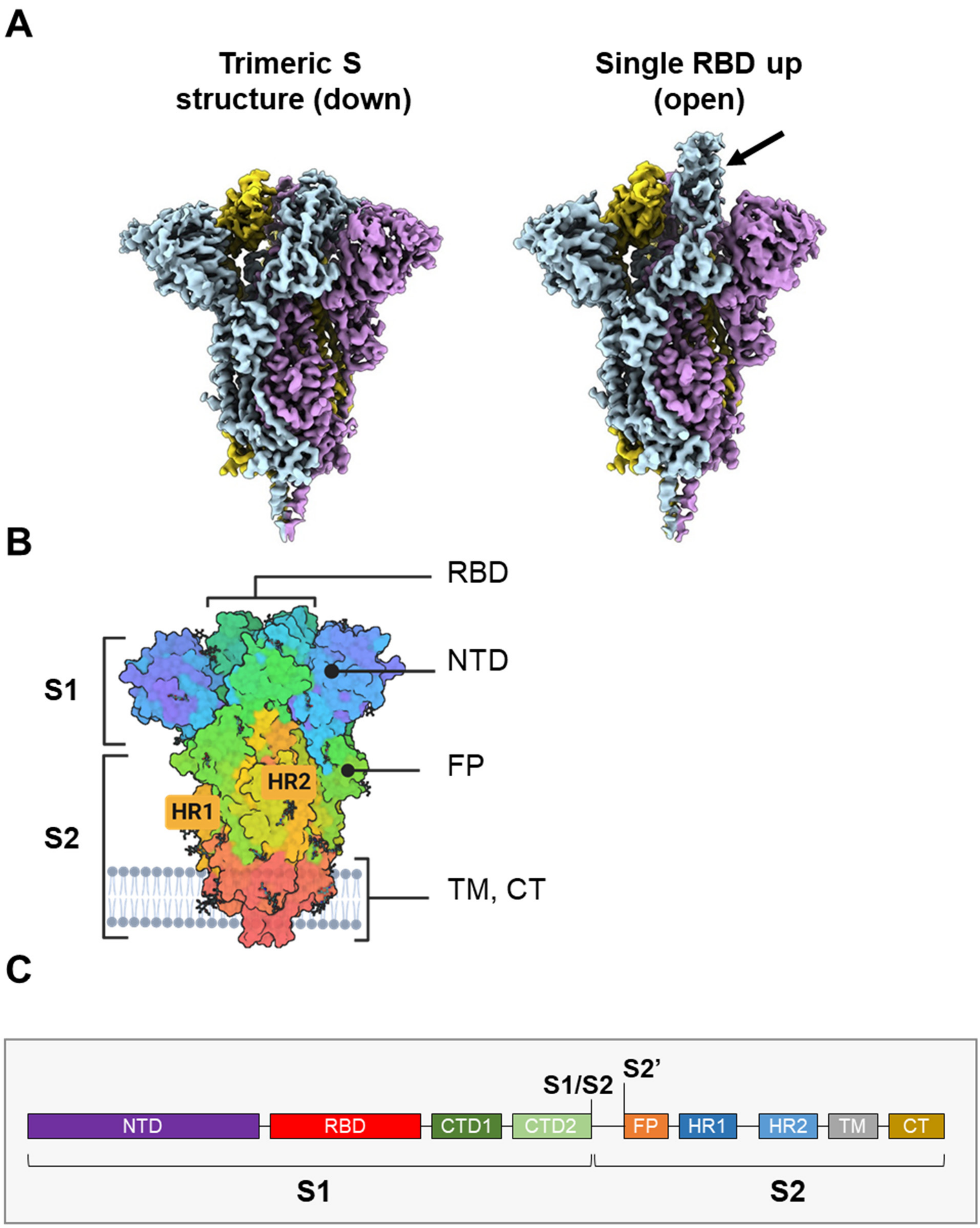

Figure 4: **Structure of the SARS-CoV-2 spike protein.**
A) Cryo-EM structure of the homotrimeric S. The down (left) and up (right) conformation of the RBDs are shown. **B)** Annotated subdomains of the S structure. A-B) Adapted from (Walls et al. 2020). **C)** Schematic representation of the S subdomains. Adapted from (Jackson et al. 2022). NTD: N-terminal domain, RBD: Receptor-binding domain, CTD: C-terminal domain, S1/S2: furin cleavage site, S2’: cleavage site recognized either by TMPRSS2 or cathepsin L, FP: fusion protein, HR: heptad repeat domain, TM: transmembrane domain, CT: cytoplasmic tail, S1: subunit 1, S2: subunit 2.

During viral biosynthesis, the S1-S2 boundary is cleaved by furin in the endoplasmic reticulum (ER) resulting in the non-covalently associated S1 and S2 subunits. Released particles can then engage with ACE2-expressing cells facilitating the interaction with the transmembrane serine protease 2 (TMPRSS2) located on the cell surface which cleaves the S2' site. Although the interaction with TMPRRS2 is preferred, in its absence, S can be cleaved by cathepsin L in the endosomes after receptor-mediated endocytosis. The interaction with TMPRSS2 results in the fusion with the plasma membrane followed by the uncoating of the RNA in the cytosol. In contrast, the activation of the fusion machinery by cathepsin L leads to endosomal escape (see Figure 5). In both cases the viral RNA is then replicated and translated in the ER resulting in the formation of new particles (Jackson et al. 2022). Particles then utilize the lysosomal egress pathway for cell release. The specialized orf3a protein prevents the acidification of lysosomes which are then used as vehicles for transportation to the cell surface and particle secretion following the fusion with the plasma membrane (Ghosh et al. 2020).

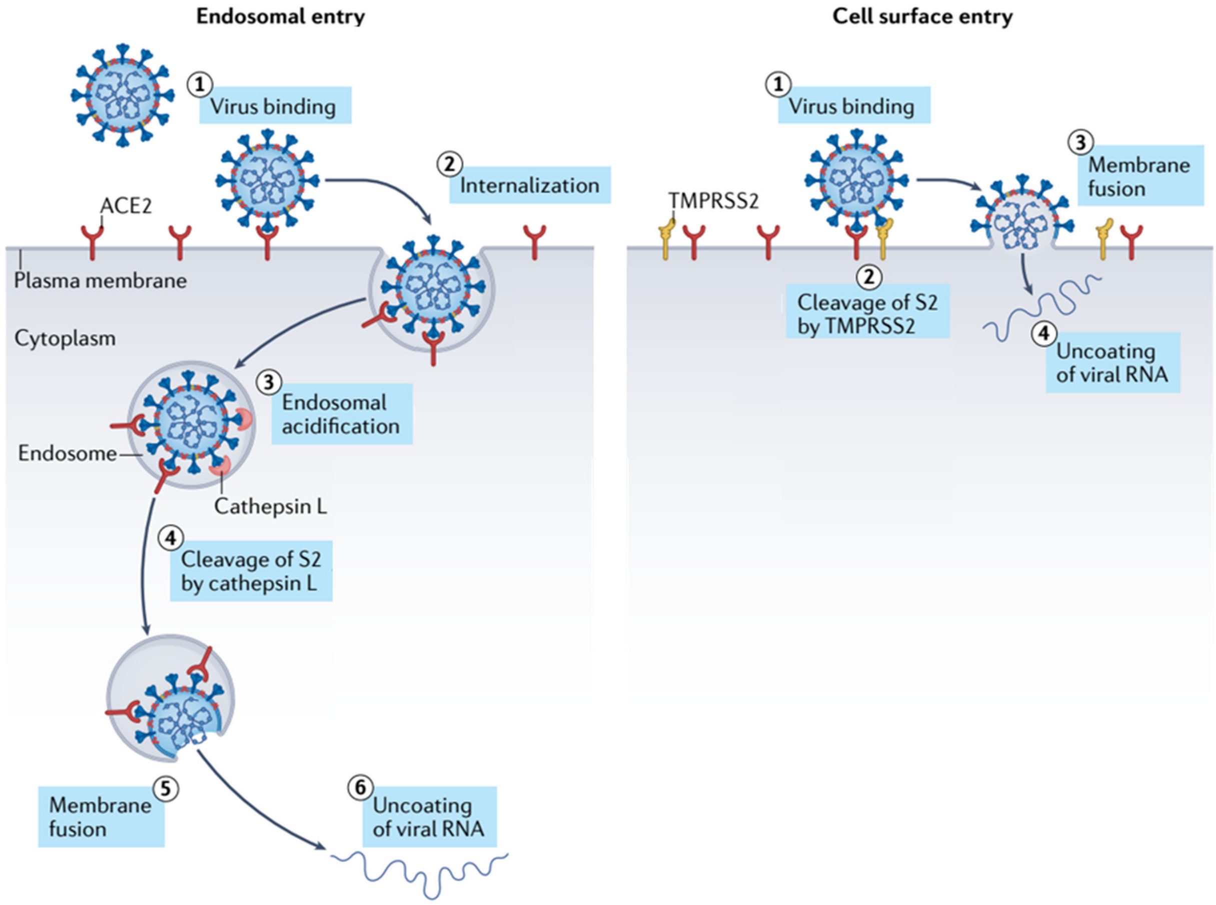

Figure 5: **Two cell entry pathways for SARS-CoV-2.**
The cell entry mechanism of SARS-CoV-2 requires first the interaction with the ACE2 receptor on the target cell. Conformational changes in the S1 subunit exposes the S2' cleavage site which needs to be cleaved to expose the fusion peptide. This can either be mediated by TMPRSS2, which is presented on the cell surface (right) or by cathepsin L, which is active in late endosomes (left). In the endosomal pathway, SARS-CoV-2 endocytosis is mediated by ACE2 and endosomal escape is triggered by cathepsin L, leading to uncoating of the RNA into the cytoplasm. Alternatively, SARS-CoV-2 will gain cell entry via fusion with the cell membrane, provided TMPRSS2 is expressed on the cell surface. Adapted from (Jackson et al. 2022).

As S is responsible for cell entry, it is the primary target for neutralizing antibodies. These antibodies can either be developed during an infection as a response of the immune system preventing or delaying the viral spread (Lamerton et al. 2022), or they can be produced recombinantly and used prophylactically in therapies or as functional reagents in experimental assays (Shitaoka et al. 2023).

Previous studies reported the ability of S to mediate cell-cell fusion (Buchrieser et al. 2020). Once a cell is infected with certain viruses, the responsible fusion protein can be presented on the cell surface. Similar to its function in the viral particles, the presentation on the cell membrane can lead to fusion with adjacent cells provided the target receptor is expressed (Leroy et al. 2020). Although this process can theoretically continue until all cells presenting either the envelope protein or the cognate receptor have fused, affected cells usually die within short time due to a massively dysregulated metabolism (Buchrieser et al. 2020). This is known as the formation of syncytia and can have serious pathological consequences (Rajah et al. 2022).

Apart from the fusion of particles with cells and cell-cell fusions,a third mechanism of cell fusion by viral particles is called fusion-from-without (FFWO) (Roller et al. 2008). FFWO was first described for HIV (Clavel and Charneau 1994) and herpes virus particles (Falke et al. 1985) postulating two possible scenarios: In the first scenario, the viral particle fuses with the cell, transferring the envelope protein to the cell membrane. This subsequently enables the cell to fuse with a receptor-positive, adjacent cell. Alternatively, the virus can bridge two cells by interactions with receptors on neighboring cells simultaneously (Clavel and Charneau 1994). Importantly, this mechanism does not require gene transfer and can in general also be performed by particles having no or defective genes incorporated.

3.1.5 Assays to measure membrane fusion

Various assays have been established to analyze membrane fusion events which are one of the most important properties of viruses. Microscopy can be used for a qualitative analysis of cell-cell fusions by identifying cells with an increased cell volume and the presence of multiple nuclei within a single cell body. To further verify the interacting cells that mediate the cell fusion, target and effector cells can be stained or can express different fluorescent reporters. After syncytia formation, colocalization of the fluorophores can be visualized by fluorescence microscopy to indicate the fusion partners (Wünschmann and Stapleton 2000). A quantitative approach can be achieved through reporter complementation assays. In these assays, the effector cells express a fragment of a reporter protein and the complementary protein fragment is expressed by the target cells. Both reporter fragments are initially inactive. Only after the fusion of target and effector cells both fragments bind each other and form the functional reporter. Such split-reporter assays have been developed for GFP (Buchrieser et al. 2020), allowing a fluorescent readout, or for reporter enzymes utilizing a substrate-specific reaction, which allows for a highly sensitive quantification (Abdul et al. 2022; Meyrath et al. 2022).

Apart from cell-cell fusions, the fusion of viral particles with a cell can be analyzed by a successful gene delivery into the target cell. The viral genome can then be analyzed by qPCR and signals are normalized to housekeeping genes, allowing the determination of the viral copy number per cell. Additionally, lentiviral vector systems have been developed to replace the original HIV envelope protein with heterologous viral glycoprotein. This modification renders their receptor-specificity and fusion mechanism towards the properties of the incorporated glycoproteins. Transduction efficiencies can then be calculated by the quantification of an expressed reporter gene. Such pseudotyped lentiviral vectors were used to specifically target T cells and tumor cells by incorporating blinded measles and Nipah viral glycoproteins conjugated to DARPins or single-chain Fv allowing for the specific binding to the targeted receptors (Funke et al. 2008; Bender et al. 2016). Additionally, the most commonly used pseudotyped lentiviral vector uses the G-protein of the vesicular-stomatitis virus (VSV), which specifically targets the LDL-receptor being expressed on a broad variety of activated cells (Finkelshtein et al. 2013). This vector is frequently used in clinical trials and in approved gene therapies to deliver a chimeric antigen receptor into autologous T cells. These cells are then reinfused into the patient, where they recognize and specifically kill tumor cells based on the expression of the targeted receptor (Vormittag et al. 2018). Importantly, while the VSV-G pseudotyped LV requires, like the VSV, receptor-mediated endocytosis for its cell entry (Cureton et al. 2009), measles and Nipah pseudotyped LVs mediate the cell fusion at the plasma membrane (Bender et al. 2016; Funke et al. 2008). Thus, pseudotyped LV are valuable tools to explore the cell entry of the incorporated viral envelope protein.

3.2 Receptor-targeted adeno-associated vectors

Adeno-associated vectors (AAVs) are commonly used as gene delivery vehicles to treat inherited and acquired genetic diseases. In recent years, there has been a steady increase in clinical trials and market authorizations for AAV gene therapy products demonstrating AAV vectors as a favored vector system for *in vivo* gene manipulation (Wang et al. 2019). The first product authorized by the U.S. Food and Drug Administration (FDA) was Glybera® in 2012, which was based on AAV1 and used for the treatment of inherited lipoprotein lipase deficiency. Although Glybera® was removed from the market shortly after release due to its high costs, it was the first gene therapy approved in the European Union (EU). Glybera® paved the way for several AAV-based gene therapies which have recieved market authorization in the EU (Bryant et al. 2013). These include Luxturna® (AAV2) for treating inherited retinal dystrophies, Zolgensma® (AAV9) for spinal muscular atrophy, Upstaza® (AAV2) for aromatic L-amino acid decarboxylase deficiency, Roctavian® (AAV5) for hemophilia A (Shen et al. 2022) and Hemgenix® (AAV5) for hemophilia B (EU gets first hemophilia B gene therapy 2023).

3.2.1 Adeno-associated virus

AAVs are derived from the non-pathogenic adeno-associated virus which was first discovered in 1965 as a contaminant of adenovirus productions (Hastie and Samulski 2015; Rose et al. 1966). The virus belongs to the family of *Parvoviridae*, the genus Dependoparvovirus and packages a 4.7 kb single-stranded DNA genome (Gao et al. 2004). Replication is dependent on the superinfection of a helper virus, such as adenovirus or herpes simplex virus (Geoffroy and Salvetti 2005). In absence of a helper virus, adeno-associated virus persists latently in infected cells. In rare cases, approximately 1% of the time, the viral genome integrates preferentially into the AAVS1 locus of the host chromosome (Surosky et al. 1997). Otherwise, the provirus persists episomally in the cell nucleus. The AAV capsid is composed of 60 VP proteins resulting in a 25 nm diameter icosahedral structure (Wörner et al. 2021).

The genome contains two open reading frames (ORF), rep and cap, which are flanked by inverted terminal repeats (ITRs). These ITR structures serve as packaging signals and promoter elements. The p5 promoter drives the expression of the Rep78 and Rep68 proteins, while Rep52 and Rep40 is under the control of the p19 promoter. Rep68 and Rep40 are produced through alternative splicing. The rep proteins are involved in the replication, packaging and insertion into the host chromosome of the provirus. The p40 promoter in the rep ORF drives the expression of the three capsid proteins VP1, VP2 and VP3 encoded in the cap ORF. All VP proteins are encoded from overlapping reading frames and share common C-termini. VP1 has the longest N-terminal elongation and encodes additionally for a phospholipase (PLA) which is important for endosomal escape after cell entry through receptor-mediated endocytosis. The relative expression levels of VP1, VP2 and VP3 are regulated in a ratio of 1:1:10, respectively, through a less efficient splice reaction for VP1 expression and a weak start codon for VP2, resulting in a preferential gene expression of the shorter VP3 (Samulski and Muzyczka 2014). Although stoichiometric ratios of the VP composition in the capsid are on average 1:1:10, the incorporation of VP proteins into the capsid is divergent and stochastic leading to highly heterogenous particles whereby the single most abundant population makes up only 1% of all capsids (Wörner et al. 2021). In a frameshifted cap reading frame the assembly-activating protein (AAP) and membrane associated accessory protein (MAAP) are encoded which aid in capsid assembly and secretion of viral particles, respectively (Elmore et al. 2021; Grosse et al. 2017) (see Figure 6).

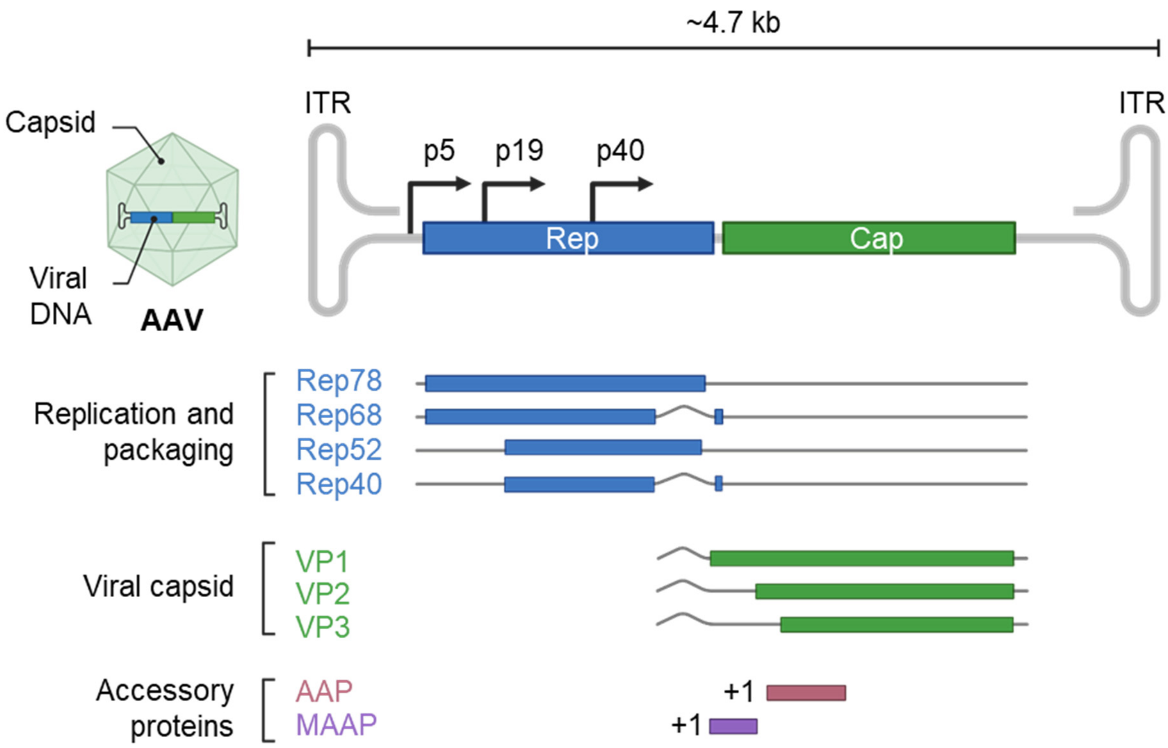

Figure 6: **AAV genome structure.**
The AAV genome is flanked by ITR regions and encodes for nine proteins, whose expression is driven by the three promotors p5, p19 and p40. The first ORF encodes for 4 rep proteins (Rep78, Rep68, Rep52, Rep40) involved in replication, packaging and integration. The second cap ORF contains the structural protein VP1-3 which assemble the viral capsid harboring the viral genome. For successful assembly of some AAV serotypes, the AAP is necessary, which is encoded in the +1 frame shifted cap ORF along with the MAAP playing a role in capsid secretion. The size of the AAV genome is approximately 4.7 kb.

3.2.2 Receptor-mediated endocytosis of AAV

Over a hundred AAV serotypes have been identified and isolated from different animals. Among them, only 13 are currently used for gene therapies. Although AAV capsids exhibit high structural similarities, certain serotypes have distinct tropism due to the recognition of either heparan sulfate proteoglycan (HSPG) (AAV2, AAV3, AAV6, and AAV13), sialic acid (AAV1, AAV4, AAV5 and AAV6) or galactose (AAV9). Initially, the AAV serotypes attach to the primary attachment sites, however functional transduction is dependent on the presence of co-receptors. Among several co-receptor suggested, AAVR and GPR108 are used by most serotypes (Pupo et al. 2022). Although these co-receptors are not essential for the binding of the capsid to the cells, they are suggested to bind after endocytosis and facilitate the intracellular trafficking (Dudek et al. 2020). AAVs can enter cells through three different pathways after initial attachment: clathrin-mediated endocytosis, micropinocytosis and clathrin-independent carriers and GPI-enriched endocytic compartment (GLIC/GEEC) pathway. Which endocytotic route is chosen, is dependent on the serotype and the interacting cell types. Recent studies revealed that only the GLIC/GEEC pathway leads to efficient transduction, although clathrin dependent and micropinocytosis are also used (Nonnenmacher and Weber 2011). After receptor-mediated endocytosis, the capsid is retrogradely transported to the trans-Golgi network. At this point, the endocytosed vesicle has transitioned to late endosomes resulting in the acidification of the vesicle lumen. This leads to conformational changes in the AAV capsid exposing the N-terminal domain of VP1 containing the PLA. Alternatively, the interaction with cellular proteases, such as cathepsin B and L, can also mediate the necessary conformational change of the AAV capsid, which triggers the exposure of the PLA. The PLA then promotes the endosomal escape followed by the trafficking to and entrance of the entire capsid into the nucleus. After viral uncoating, the AAV genome is released, followed by second-strand synthesis and expression of viral proteins. However, a significant number of AAV capsids do not escape the endosome, resulting in the fusion of the vesicle with the lysosome and subsequent proteasomal degradation (Riyad and Weber 2021).

3.2.3 Vector engineering

For gene therapeutic application of AAV vectors, reporter or therapeutic genes are packaged into the capsid. For this purpose, the rep and cap ORFs are replaced and only the flanking ITR regions are retained to enable packaging of the gene of interest under a suitable promoter (Grieger et al. 2006). Importantly, due to the small capsid volume, sequences longer than 4.7 kb result in reduced viral titer. Additionally, the second strand synthesis of single-stranded DNA conformation represents a rate-limiting step for the transduction of target cells. To overcome this limitation, self-complementary genomes were designed. Such genomes contain a deletion in the 5’ ITR and a mutation in the terminal resolution site resulting in the packaging of double-stranded genomes. However, this approach comes at the cost of only half the coding sequence length being available for the gene of interest (McCarty 2008). The Rep and Cap proteins are encoded on a separate plasmid along with the helper plasmid encoding the adenoviral V2A, E1 and VA proteins. AAV particles are then produced by triple transfection of HEK293T cells followed by purification from the cell lysate three days after transfection. Alternatively, AAV particles can be produced in SF9 cells using a baculovirus superinfection. Subsequently, AAV particles present in the cell lysates are purified by centrifugation using CsCl or iodixanol-gradient to separate them from empty particles lacking vector genomes (Grieger et al. 2006).

Especially the broad tropism of natural AAV serotypes and the interference of pre-existing immunity have led to a strong interest in engineering AAV particles, forcing the tropism to target receptor expressing cells and evade neutralizing antibodies.

3.2.4 Capsid modifications for cell-type selective gene transfer

Due to the broad tropism of natural serotypes, which often target the liver, high vector doses must be injected to target other cell types and organs, since only a minute fraction of particles transduce the therapy-relevant cells. These high vector doses can be associated with life-threatening side effects, such as hepatoxicity (Kishimoto and Samulski 2022). In a recent gene therapy trial for the treatment of children with X-linked myotubular myopathy (MTM), six patients were injected with $1.3\text{x}10^{14}$ genome copies/kg body weight, while thirteen patients received a three times higher dose. The patients were injected with an AAV8 vector encoding a functional copy of the *MTM1* gene. Although patients receiving the lower dose showed good responses, those treated with the highest vector dosages experienced severe hepatotoxicity and three died due to cholestatic liver failure (Shieh et al. 2023).

Various strategies have been used to prevent the expression of the vector genome in off-target cells. These include incorporating tissue-specific microRNA binding sites and cell type-specific promoters to prevent the expression in off-target cells while still allowing vector particles to enter these cells (Pupo et al. 2022).

A different approach involves the engineering of the AAV capsids to target only the cells relevant for the therapy. This can be achieved through library-based screening approaches coupled to selections via directed evolution or through rational capsid engineering strategies. During library-based screening, the AAV Cap ORF is randomly modified using error-prone PCR, insertion of DNA fragments/domains from other AAV serotypes or insertion of randomized peptides into distinctive capsid loops. The randomized capsids obtained are subsequently exposed to selective pressure, either within cell culture or in an appropriate animal model. Such selections can be repeated multiple times and the recovered variants are then identified through sequencing (Becker et al. 2022).

Rationally designed AAV particles are genetically modified to ablate the binding to the natural receptor and equipped with high-affinity binder for the receptor of choice. In context of AAV2, two point mutations are introduced which change the arginine residues 585 and 588 to alanine, effectively preventing the binding to HSPG (Kern et al. 2003). Next, nanobodies or designed ankyrin repeat proteins (DARPins) are genetically fused to one of the VP proteins to mediate the specific binding to targeted receptors. Initially, DARPins were fused to the N-terminus of VP2 in AAV2. However, since VP2 is non-essential for capsid formation, produced particles required purification by affinity chromatography to yield homogenous particles presenting the DARPin (Münch et al. 2015). Eichhoff et al. presented a major improvement in the presentation of binders by inserting nanobodies into the GH2/3 loop of AAV2's VP1 (Eichhoff et al. 2019). Michels et al. and Günther et al. adapted this targeting strategy to DARPin display and demonstrated that this insertion site leads to more potent particles in terms of production yield and transduction efficiency (Michels et al. 2021; Günther et al. 2023) (see Figure 7).

Importantly, these particles did not require additional chromatographic purification. Among these DART (designed ankyrin repeat protein targeted)-AAVs, specific vectors for the receptors hCD8, mCD8, hCD4, hCD30, hHer2, hEpCAM and mGluA4 have been generated (Hartmann et al. 2018; Hartmann et al. 2019; Münch et al. 2013). Although, these particles were successfully re-targeted to the receptor of choice, functional transduction is still dependent on the presence of the AAVR co-receptor (Hartmann et al. 2019).

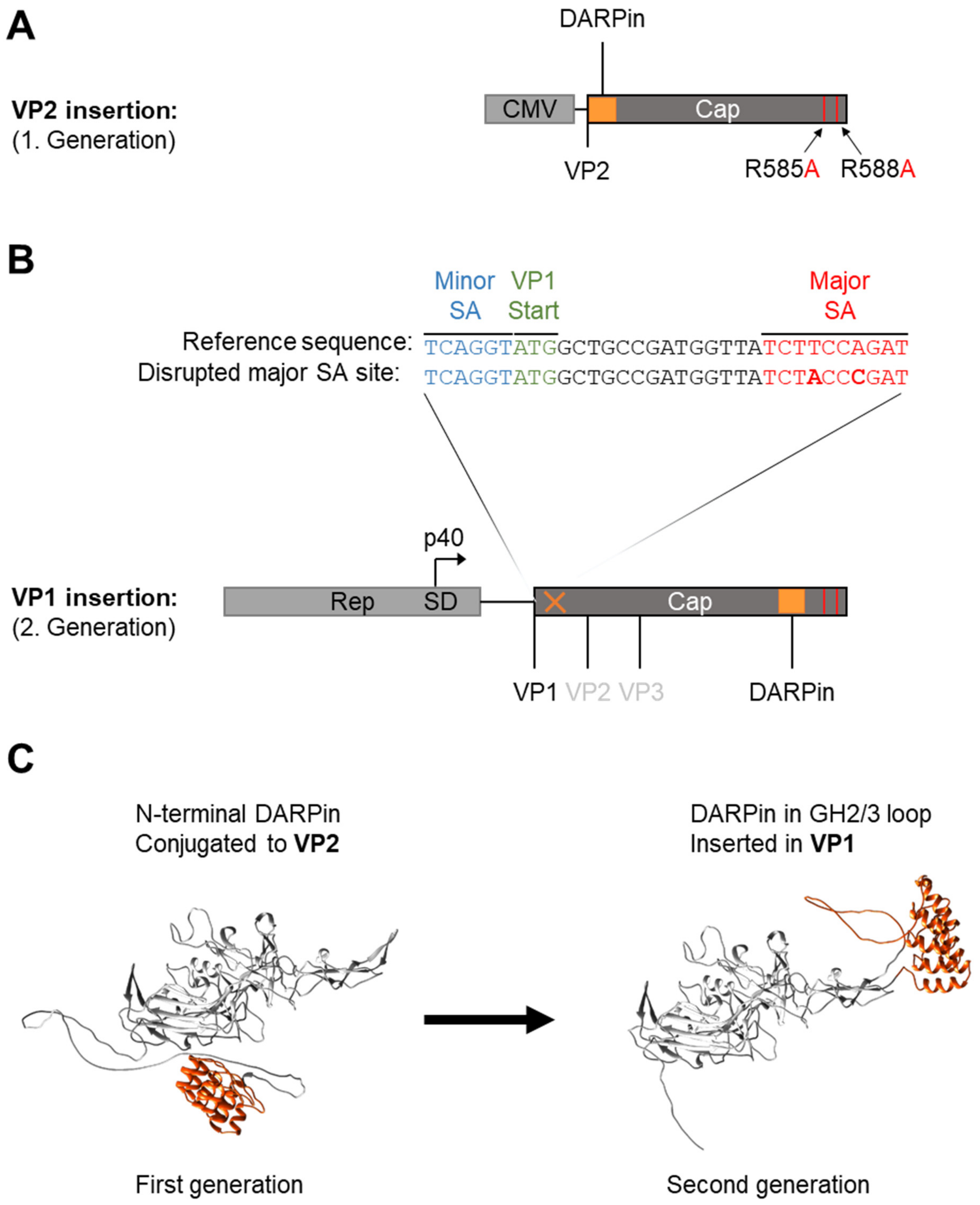

Figure 7: **DARPin insertions for first and second generation AAVs.**

A) In the first generation of DARPin-targeted AAV, the DARPin was conjugated N-terminally to the VP2 protein. The expression of the VP2-DARPin protein was driven by a CMV promoter. To prevent binding to the natural receptor of AAV2, HSPG, two arginine residues 585 and 588 were mutated to alanine. VP1 and VP3 were encoded on a separate plasmid (not shown). **B)** In the second generation of DARPin-targeted AAV2, the DARPin is inserted into the GH2/3 loop of VP1. To prevent the protein expression of VP2 and VP3, two point mutations were introduced into the major splice acceptor site (major SA), which is located downstream of the VP1 start codon (marked with orange “x”) and is shown in bold red letters in the inset above. These point mutations disrupt the splice site leading to the excision of the RNA fragment ranging from the splice donor site (SD) to the minor splice acceptor site (minor SA, see inset above). Thus, the translation is initialized at the VP1 start codon, resulting in the exclusive protein expression of VP1. To create the VP1-DARPin fusion protein, the DARPin was incorporated into the GH2/3 loop of VP1 (depicted as orange bars). For capsid assembly the non-modified VP2 and VP3 proteins were expressed from a separate plasmid (not shown). **C)** Alphafold prediction of the VP2 protein conjugated N-terminally to the CD4-specific DARPin (left) and inserted into the GH2/3 loop of VP3 (right). The DARPin structure is colored in orange-red. The shorter VP3 was used for this calculation to reduce computational time.

3.3 Objectives

The primary aims of this thesis were i) the development of quantitative assay systems to determine the membrane fusion activity of the SARS-CoV-2 virus and ii) the design and experimental evaluation of a targeting strategy for the HIV reservoir cells with AAV vectors.

Towards the first goal, the three different fusion mechanisms particle-cell fusion, cell-cell fusion and fusion-from-without should be investigated. The particle-cell fusion assay utilized lentiviral vector pseudotyped with the spike protein, enabling highly sensitive quantification of cell entry through the expression of a reporter protein. In the fusion-from-without assay, the spike protein had to be inserted into HIV-based VLPs which were then added to cell mixtures of target cells expressing one of the split-reporter proteins. Reporter complementation was then used to quantify the fusion activity after particle-mediated cell fusion of the target cells. Lastly, the cell-cell fusion assay had to be based on the complementation assay. In this case, effector cells expressed and presented the spike protein on their surface and these cells were then mixed with target cells expressing ACE2. This allowed for a direct linkage of syncytia formation and reporter complementation. To determine the fusogenicity of the spike protein, titration of the spike protein amounts should indicate the lowest level of spike which is still sufficient to mediate fusion. Once fusion assays had been established, the neutralizing activity of purified recombinant anti-spike antibodies and patient sera had to be analyzed.

The second goal aimed at the generation and characterization of receptor-targeted AAVs for HIV gene therapy, thus meeting the major challenge for HIV therapy, which is the delivery to reservoir cells. Recent studies have shown that CD32a expression on CD4 T cells is a marker for HIV reservoir cells harboring highly enriched replication-competent proviruses. Promising studies have reported the use of CRISPR-Cas9 to specifically destroy the HIV provirus by inducing multiple double-strand breaks. Therefore, to establish a delivery strategy for HIV reservoir cells, AAVs should be targeted to CD4 and CD32a for delivery of HIV-specific Cas9 nucleases. This vector system should deliver the nuclease to the target cell and secondly allow for the introduction of double-strand breaks into the HIV provirus, preventing HIV replication.

To target AAV2s to CD4 and CD32a, receptor-specific DARPins had to be incorporated into the VP1 capsid protein of AAV2. While the CD4 DARPin 55.2 had been used before for the re-targeting of AAV2 using the N-terminus of VP2 as an insertion site, CD32a had not been targeted by viral vector systems before. To reach this goal, the DARPin F11 had to be displayed on AAV2. To enable selective gene delivery to all cells positive for both CD4 and CD32a, both DARPins had to be connected by linker sequences on the genetic level and then presented on the AAV capsid. The receptor preference of such bispecific vectors should then be compared to that of monospecific vectors. For this purpose, mixtures of CD32a and CD4-expressing cells as well as of cells expressing both receptors should be transduced to determine the selectivity. Additionally, cell trafficking studies should investigate differences in transduction by bispecific and monospecific AAV. The cell tropism should then be verified on primary cells utilizing binding assays. Having shown the specificity and transduction efficiency *in vitro*, vector particles should be injected systemically into NSG mice transplanted with human target cells in order to analyze the biodistribution *in vivo*. Finally, reservoir-targeted AAVs should be equipped with the Cas9 nuclease directed against the HIV provirus.

4 Results

This thesis focuses on the fusion activity of the SARS-CoV-2 spike protein (S) assessed in particle- and cell-based assays in the first part, the second part describes the generation and characterization of targeted AAV vectors for HIV gene therapy.

Results of Part A: Fusion activity of the SARS-CoV-2 spike protein

4.1 Setting up quantitative fusion assays for SARS-CoV-2 spike protein

S protein mediated fusion activity can be followed in the context of viral particles that fuse with target cells or of cells expressing S on their surface. To investigate those two fusion events, S was incorporated into LV particles or displayed on 293T cells serving as effector cells.

For the first approach, two strategies were followed. First, the *LacZ* gene delivery into cells expressing different levels of ACE2 on their surfaces was quantified. Second, S displayed on the viral particle lacking the incorporated genome (virus-like particles, VLP) was used to trigger the fusion of neighboring cells (fusion-from-without). Finally, 293T cells transfected with the S plasmid were used to fuse with ACE2 expressing target cells (fusion-from-within) (see figure 8).

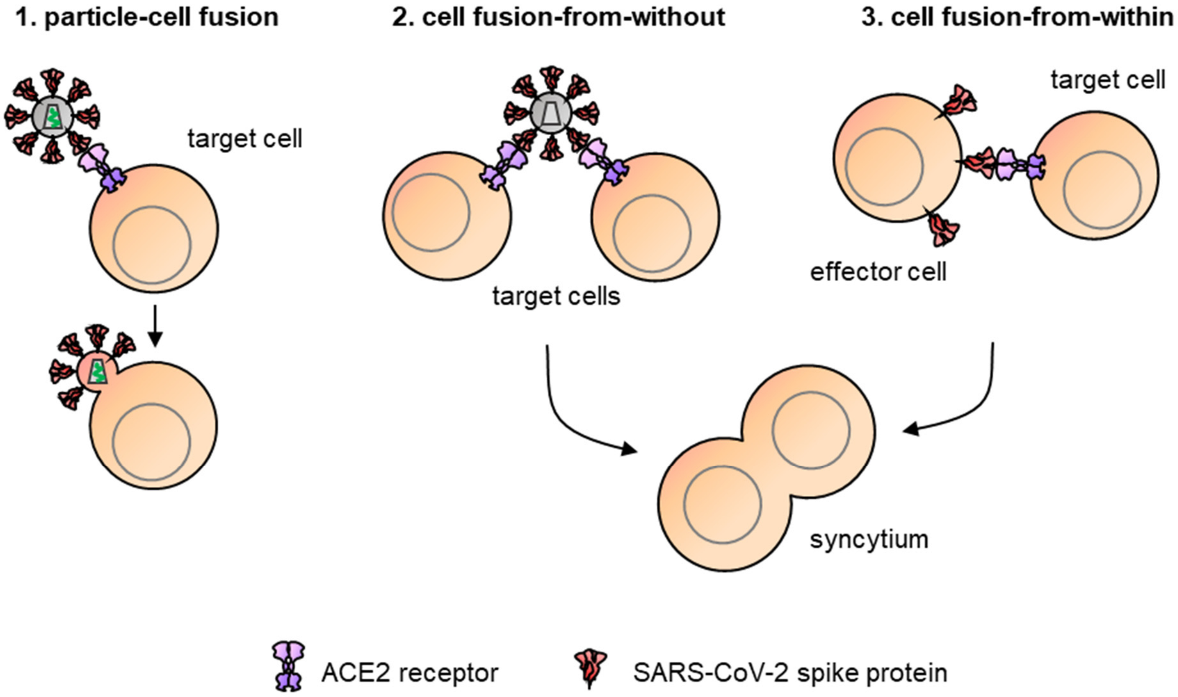

Figure 8: **Assays to analyze fusion activity of S.**
In the particle-cell fusion assay, Lentiviral vectors pseudotyped with S were used to transduce ACE2 expressing target cells (left). VLP displaying S were used to trigger the fusion of adjacent target cells expressing ACE2 in the fusion-from-without assay (middle). Effector cells expressing S fused with target cells expressing ACE2, resulting in cell-cell fusion and syncytia formation (right). Adapted figure which was originally created by Alexander Michels (Paul-Ehrlich-Institut).

Starting with the particle-based fusion assays, pseudotyped LVs were used, since they tolerate the incorporation of a variety of viral glycoproteins and allow for the quantification of the fusion activity by the delivery of a reporter gene. Key for the establishment of pseudotyped lentiviral vectors is a high abundance of the viral glycoprotein displayed on the particle which correlates with the expression level on the producer cells. Furthermore, the cytoplasmic tail of the viral glycoproteins are usually truncated to prevent steric hindrance in the capsid (Funke et al. 2008; Bender et al. 2016).

To achieve high incorporation levels of S, the coding sequence was codon optimized for high protein expression in human 293T cells and the optimized plasmid was kindly provided by Klaus Conzelmann (Munich) (Hennrich et al. 2021). Additionally, the C-terminus of the S sequence was truncated by 19 amino acids using PCR amplification and subsequently inserted into the PCG backbone (Lamp et al. 2013) by restriction cloning yielding plasmid pCG-SARS-CoV-2-SΔ19. To produce S-pseudotyped lentiviral vectors, the envelope plasmids encoding the full-length (pCG-SARS-CoV-2-S) or the truncated S (pCG-SARS-CoV-2-SΔ19) were mixed with the packaging plasmid pCMV-d8.9 encoding the structural proteins of HIV (Zufferey et al. 1997) and the transfer plasmid pCMV-LacZ containing the coding sequence of beta-galactosidase driven by the CMV promoter (Holland et al. 2004). For the production of S-VLPs, only the S plasmid and the packaging plasmid were combined. After co-transfection of 293T cells, S-LV and S-VLP particles were isolated and concentrated from the cell culture supernatant by filtration and centrifugation (see Figure 9).

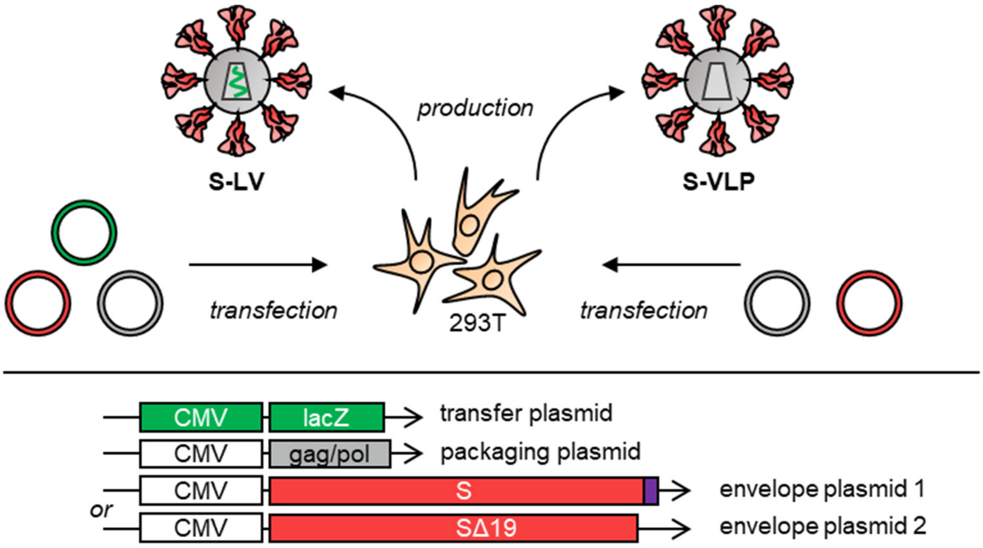

Figure 9: **Production of LVs and VLPs displaying S.**
For the production of lentiviral vector displaying S, the transfer plasmid pCMV-LacZ and the packaging plasmid pCMV-ΔR8.9 were mixed with either the envelope plasmid encoding full-length S (envelope plasmid 1) or the truncated S protein (SΔ19) (envelope plasmid 2). For VLP production, 293T cells were co-transfected with only the packaging plasmid and one of the envelope plasmids. Particles were purified and concentrated from the cell culture media of 293T cells three days after transfection. Figure is adapted from (Theuerkauf et al. 2021).

4.2 Particle-cell fusion assay

4.2.1 Spike protein incorporation into lentiviral vector

Having produced S-LV transferring the *LacZ* gene, the incorporation of S into particles was assessed next. For that, the producer cells and isolated particles were lyzed and analyzed for S protein by Western blot, respectively.

Several signals for the S protein were observed according to the molecular weights of the S0 and the S2 protein fragments. These signals were detectable in producer cells and with stronger intensities on vector particles but were absent in VSV-G pseudotyped lentiviral vector serving as a negative control. Furthermore, the intensity of vector particles incorporating the truncated S protein was much higher compared to the full-length S-LV although similar vector amounts were loaded on the gel, as seen by the staining for the HIV capsid protein P”$. Additionally, S and SΔ19 protein signals in the cell lysates were comparable. P24 signals were absent in cell lysates because most of the particles are secreted to the cell culture supernatant and only a low amount of P24 stays inside the cells. These results clearly show an increased incorporation rate of the truncated S protein compared to the full-length S and for the further experiments the SΔ19-LV particles were used (see Figure 10).

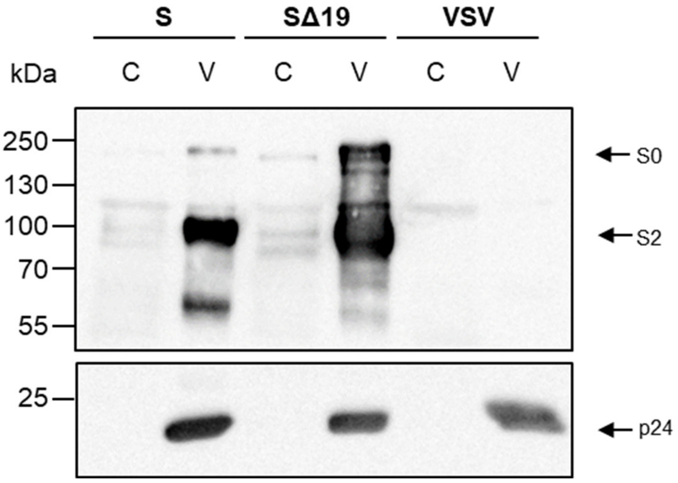

Figure 10: **S incorporation into LV particles.**
Viral particles (V) and the corresponding producer cell lysates (C) were separated on a 10% SDS-polyacrylamide gel followed by western blot analysis for the detection of S and p24. For comparison and to verify the specificity of S staining, VSV-G pseudotyped LV and the lysates of producer cells were loaded (VSV). Signals related to the S0 and S2 fragment of S and the p24 signal are marked by arrows. The blots for S and p24 detection were exposed for 30 and 5 s, respectively. Image contrast was optimized while retaining relative signal strength. Figure is adapted from (Theuerkauf et al. 2021).

4.2.2 Functional characterization of SΔ19-LV

Subsequently, the capability of pseudotyped LV to successfully deliver its genetic payload into ACE2-expressing target cells was evaluated. For that, SΔ19-LVs were titrated on the cell lines 293T, Calu-3, MRC-5, Vero and 293T-ACE2. Since the 293T-ACE2 cell line was engineered for high expression of ACE2 by transfection, a mock- (empty plasmid) transfected 293T cell line was included to evaluate impacts on transduction efficiencies related to the transfection procedure itself. VSV-LV served as positive control to show that the cell lines tolerate transduction by lentiviral vector and expression of the reporter protein is not prevented by potential restriction factors post cell entry.

Three days after transduction, SΔ19-LV had similar transduction efficiencies on wild-type all cell lines which were, as expected, lower than with VSV-LV. However and in contrast to VSV-LV, SΔ19-LV transduction efficiency increased a 100-fold on 293T cells overexpressing ACE2. When 0.2 µl of SΔ19-LV were used, transduction efficiencies of 3.4x10^6 relative light units (RLU) were observed, almost matching the efficiency of VSV-LV on 293T-ACE2 cells, where 1.2x10^7 RLU were reached. Notably, under this condition, SΔ19-LV achieved an impressive maximum signal-to-noise ratio of 2000 related to untransduced cells (see Figure 11). These results prove that S pseudotyped LV show receptor-dependent transduction of target cell lines. Additionally, due to the assay's high sensitivity, it is highly suitable for evaluating transduction inhibitors.

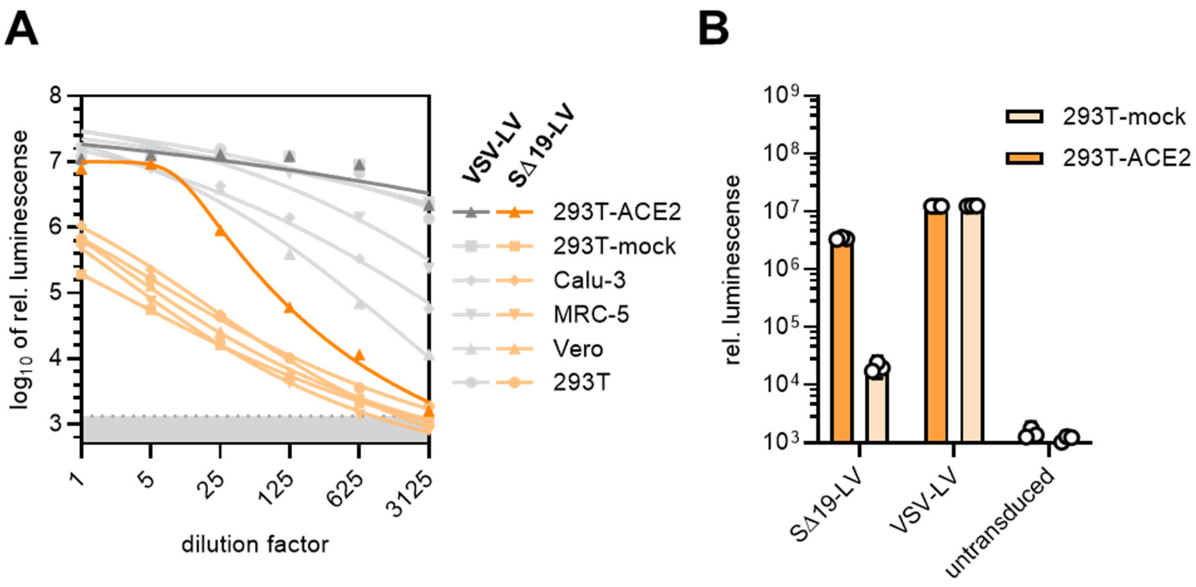

Figure 11: **Gene transfer of SΔ19-LV into cell lines.**
A) 5 µl of VSV-LV (grey) or SΔ19-LV (orange) transferring *LacZ* were serially diluted and added to the indicated cell lines. Reporter signals were determined after cell lysis three days post transduction. The grey area at the bottom indicates the background signal of untransduced cells. Data points represent means of technical triplicates. **B)** 0.2 µl of SΔ19-LV and VSV-LV were added to 293T cells mock transfected with an empty plasmid (light orange) or 293T cells transfected to overexpress ACE2 (dark orange). Background signals were determined by untransduced cells. Reporter signals were determined three days after vector addition. Bars indicate technical triplicates and the 95% confidence interval (CI) is reported. Figure is adapted from (Theuerkauf et al. 2021).

4.2.3 Inhibition of particle-cell fusion assay by antibodies and patient sera

Having setup the transduction assay, inhibition of the gene delivery was assessed using a commercially available anti-S antibody or sera from patients four month after infection with SARS-CoV-2. For the neutralization assay 0.2 µl of SΔ19-LV or VSV-LV were pre-incubated with 4 µg/ml antibody or 1:1 with sera for 60 min and added subsequently to 293T-ACE2 cells. Reporter signal was measured three days after transduction by luminescence reaction.

Compared to the antibody control, the anti-S antibody reduced the reporter signal by 2.3 orders of magnitude which corresponds to 99% neutralization. Similar, patient sera reduced the luminescent signal by 2 and 1.7 magnitudes of order resulting in 98.5% and 97.4% neutralization, respectively. Importantly, gene transfer with VSV-LV was not affected by sera or antibody treatment (see Figure 12). These results proved that particle-cell entry mediated by S can be efficiently neutralized by purified antibodies and patient sera.

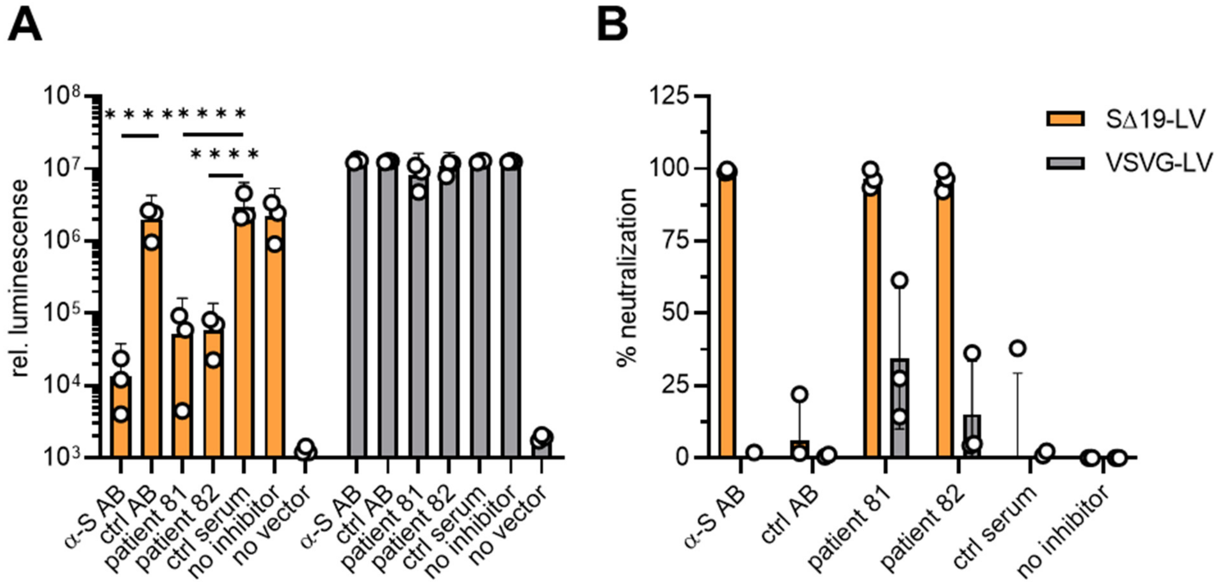

Figure 12: **Inhibition of SΔ19-LV cell entry by antibody and patient sera.**
0.2 µl of SΔ19-LV or VSV-LV transferring *LacZ* were pre-incubated with 4 µg/ml of anti-S antibody or control isotope antibody. Furthermore, vector particles were incubated 1:1 with sera of SARS-CoV-2 patients or of healthy donors. After 30 min of incubation, particles were added to 293T-ACE2 cells and luminescence signals were measured three days after vector addition. **A)** Reported are the relative luminescence signals of lyzed 293T-ACE2 cells after addition of SΔ19-LV (orange) or VSV-LV (grey) pre-incubated with sera or antibodies and **B)** the percentages of neutralization relative to the control without inhibitor. Bars represent means and error bars indicate 95% CI of three independent experiments. Significant differences were calculated by two-way analysis of variance (ANOVA), p-value **** < 0.0001. Figure is adapted from (Theuerkauf et al. 2021).

4.3 Fusion-from-without, cell-cell fusion mediated by virus-like particles presenting S

4.3.1 Quantification of SΔ19-VLP mediated cell-cell fusion

Next, the fusion activity of S was investigated regarding its ability to induce fusion of neighboring cells in the absence of newly expressed S protein. To investigate such a mechanism, cell fusion needs to be triggered by a fixed amount of S which can subsequently be quantified by a reporter system. For this assay, cell fusion was mediated by VLPs displaying S. As target cells, 293T cells were transfected to co-express ACE2 and either the alpha- or omega-fragment of the beta-galactosidase (see Figure 13). Upon addition of S-VLPs, fusion between adjacent target cells results in the complementation of both protein fragments and functional beta-galactosidase formation. Thus, syncytia formation is directly linked to reporter complementation. On the next day, the cell culture was lyzed and the amount of beta-galactosidase was quantified by substrate-specific luminescence reaction.

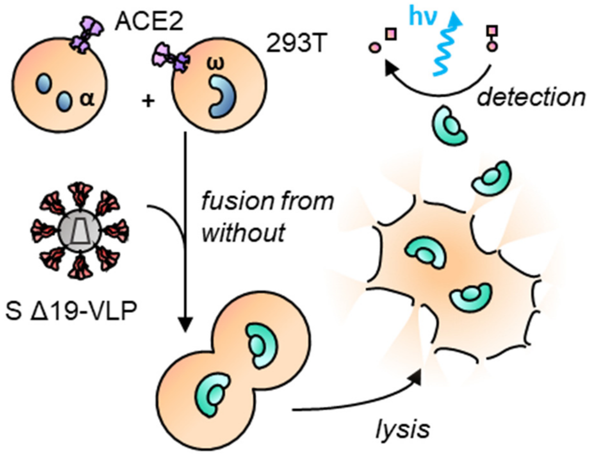

Figure 13: **Alpha-complementation assay to analyze fusion-from-without.**
For the fusion-from-without assay, 293T cells were transfected to co-express ACE2 and either the alpha- or omega fragment of the beta-galactosidase. Upon addition of SΔ19-VLPs, the target cells fuse leading to the complementation of the alpha- and omega protein fragments. Functional beta-galactosidase can then be quantified after cell lysis. Figure is adapted from (Theuerkauf et al. 2021).

To identify sufficient amounts of S-VLP that mediate reporter signal above background, 293T-ACE2 cells expressing alpha or omega were mixed in a 1:1 ratio and luminescence signal was measured one day after S-VLP addition.

In contrast to VLP particles lacking the S protein (bald VLP), 5x10^8 S-VLP per 1x10^5 target cells resulted in a fusion signal of 9.3x10^4 RLU, which is more than one order of magnitude above background. This signal further increased with increasing particle numbers and reached the signal plateau at 1.48x10^6 RLU using 5x10^9 particles. At this particle number, a signal-to-noise ratio of 2.7 orders of magnitude was reached (see Figure 14A). Furthermore, the fusion signal between alpha and omega cells was above background when ACE2 was overexpressed, 293T cells displaying natural levels of ACE2 did not show fusion signals even at highest particle dose of 1x10^{10} particles (see Figure 14B). In order to confirm that the fusion signal obtained is not an artefact of the truncated S protein, the fusion-from-without assay was conducted using VLPs presenting the full-length S protein. Although signals were slightly lower than with SΔ19-VLP, significant signals above background were obtained (Figure 14C). The observed differences in fusion activity might be related to different S incorporation ratios as already demonstrated for the S-LV versus SΔ19-LV (for comparison see Figure 10). Thus, the less efficient incorporation of full-length S might result in lower amounts of S proteins in the assay leading to reduced fusion signals. Overall, from these results it is conceivable that S on viral particles is highly fusogenic and can induce cell fusion in absence of productive infection.

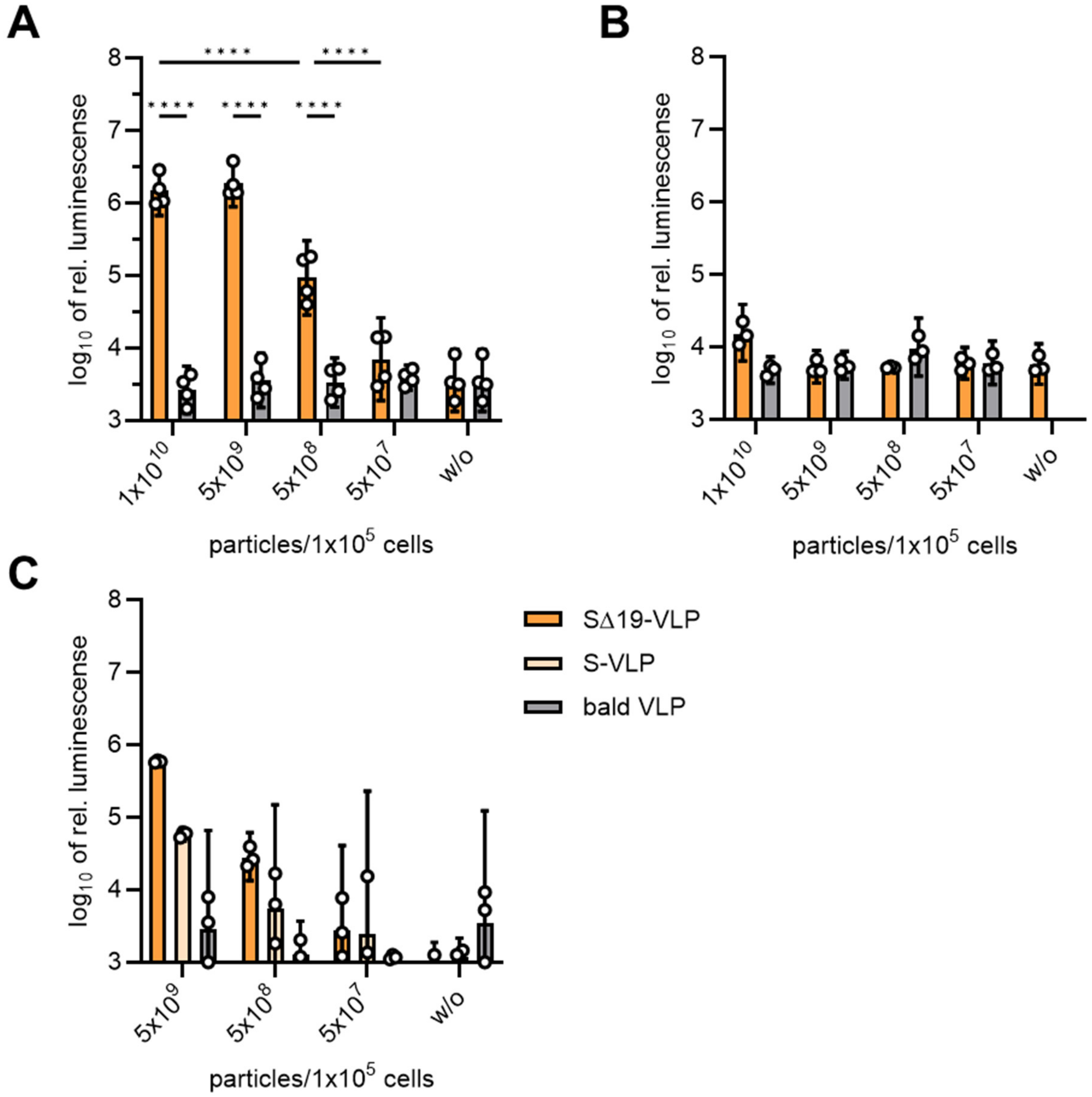

Figure 14: **S display on virus-like particles is sufficient to mediate cell-cell fusion.**
The indicated amounts of SΔ19-, S- or bald-VLP (no S display on VLP) were added to trigger the fusion of 5x10^4 omega- and 5x10^4 alpha-expressing cells. The amount of complemented beta-galactosidase was quantified from the cell lysate after overnight incubation. **A** and **C)** Relative luminescence signal of lyzed 293T-ACE2 cells after incubation with the indicated vectors. Bars represent means of biological triplicates and 95% CI is reported. **B)** Relative luminescence signal of lyzed 293T cells after incubation with the indicated vectors. **A-B)** Bars represent means of biological triplicates and 95% CI is reported. Statistical differences were calculated by two-way ANOVA, p-value **** < 0.0001. **C)** Bars represent means of technical triplicates and 95% CI is reported. Figure is adapted from (Theuerkauf et al. 2021).

4.3.2 Proteolytic activation of S enhances fusion-from-without

Having demonstrated fusion-from-without with SΔ19-VLPs, the next experiment investigated whether S' fusion activity is dependent on post-translational processing. To assess whether the fusion activity in the fusion-from-without assay can be enhanced, S was treated with trypsin known to cleave at the S1/S2 cleavage site (see Figure 4). For that, 5x10^8 SΔ19-VLPs were incubated with 2 mg/ml trypsin for 2, 10, 30 and 60 min (see Figure 15A). Subsequently, trypsin-treated VLP were added to 293T-ACE2 cells and reporter signals were measured on the next day.

With longer incubation times, the fusion signal increased from 2.7x10^5 RLU at 2 min and reached highest signal of 8.9x10^5 RLU at 30 min incubation time. At this incubation time a 5.7-fold higher fusion signal over background was measured. Compared to the fusion activity of untreated SΔ19-VLP, there was a 1000-fold increased signal-to-noise ratio. Surprisingly, the fusion signal declined after 60 min treatment back to the level of untreated S-VLP.

During the incubation time of SΔ19-VLP for up to 30 min, there was a concurrent decline of S0 signal and an increase in cleaved S2 protein fragment, as observed by western blot analysis in Figure 15B. Interestingly, extending the incubation time to 60 min led to pronounced decrease of the S2 signal, while p24 was not affected. This correlated with the reduction of reporter signal back to the level of untreated S-VLP, indicating that prolonged trypsin treatment leads to strong S modifications reducing the fusion activity. Overall, the fusion activity of S was increased after proteolytic activation with trypsin, but timing of the trypsin treatment was crucial, since excessive incubation led to reduced fusion signals.

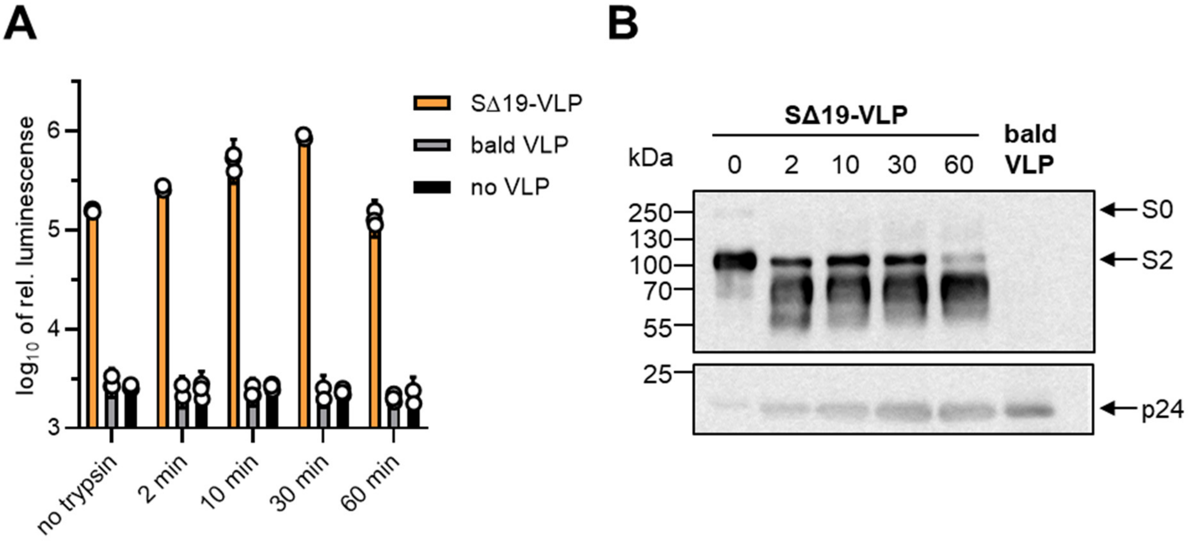

Figure 15: **Proteolytic activation of S on VLPs enhances fusion activity.**
A) SΔ19-VLP and bald-VLP were pre-treated with 2 mg/ml trypsin for the indicated incubation times and subsequently added to 1x10^5 target cells overexpressing ACE2. Relative luminescence signals were measured after overnight incubation and background signals were determined by untreated cells. **B)** SΔ19-VLPs were treated with trypsin for the indicated incubation times (2, 10 and 60 min) and analyzed by western blot targeting S and p24. Untreated SΔ19-VLPs (0 min) and bald-VLP served as controls. Arrows indicate the signal heights of S0 fragment, S2 fragment and p24. Image contrast was optimized while retaining relative signal strength. Figure is adapted from (Theuerkauf et al. 2021).

4.3.3 Inhibition by antibody and patient sera

Lastly, anti-S antibody and patient sera were used to assess their neutralization capacity in the fusion-from-without assay (see Figure 16A-B). For the neutralization assay, SΔ19-VLP or bald-VLP were pre-incubated with 4 µg/ml antibody or 1:1 with sera for 60 min and added subsequently to 293T-ACE2 cells. Reporter signal was measured three days after transduction by luminescence reaction.

Similar to the transduction assay before, the anti-S antibody reduced reporter signal by 1.7 orders of magnitude which correlates to 97.9% neutralization. Furthermore, determining the inhibitory efficiency of the antibody by titration yielded an IC50 of 0.37 µg/ml (see Figure 16C-D). Surprisingly, when using the pooled serum from healthy donors (control serum), there was a notable decrease in the reporter signal compared to the condition without any inhibitor. Additionally, patient serum 82 exhibited specific inhibitory effects against S, resulting in 94% neutralization, whereas patient serum 81 showed no significant differences compared to the control serum. Nevertheless, the inhibitory effect of serum 82 was only measureable at highest serum concentration and absent at dilution 1:20. Interestingly, both sera efficiently neutralized the particle-cell assay in a previous experiment (see chapter 4.3.2). Conclusively, patient sera and purified anti-S antibody significantly reduced the fusion activity on S. Nevertheless, the antibody showed a more potent inhibition compared to the patient sera.

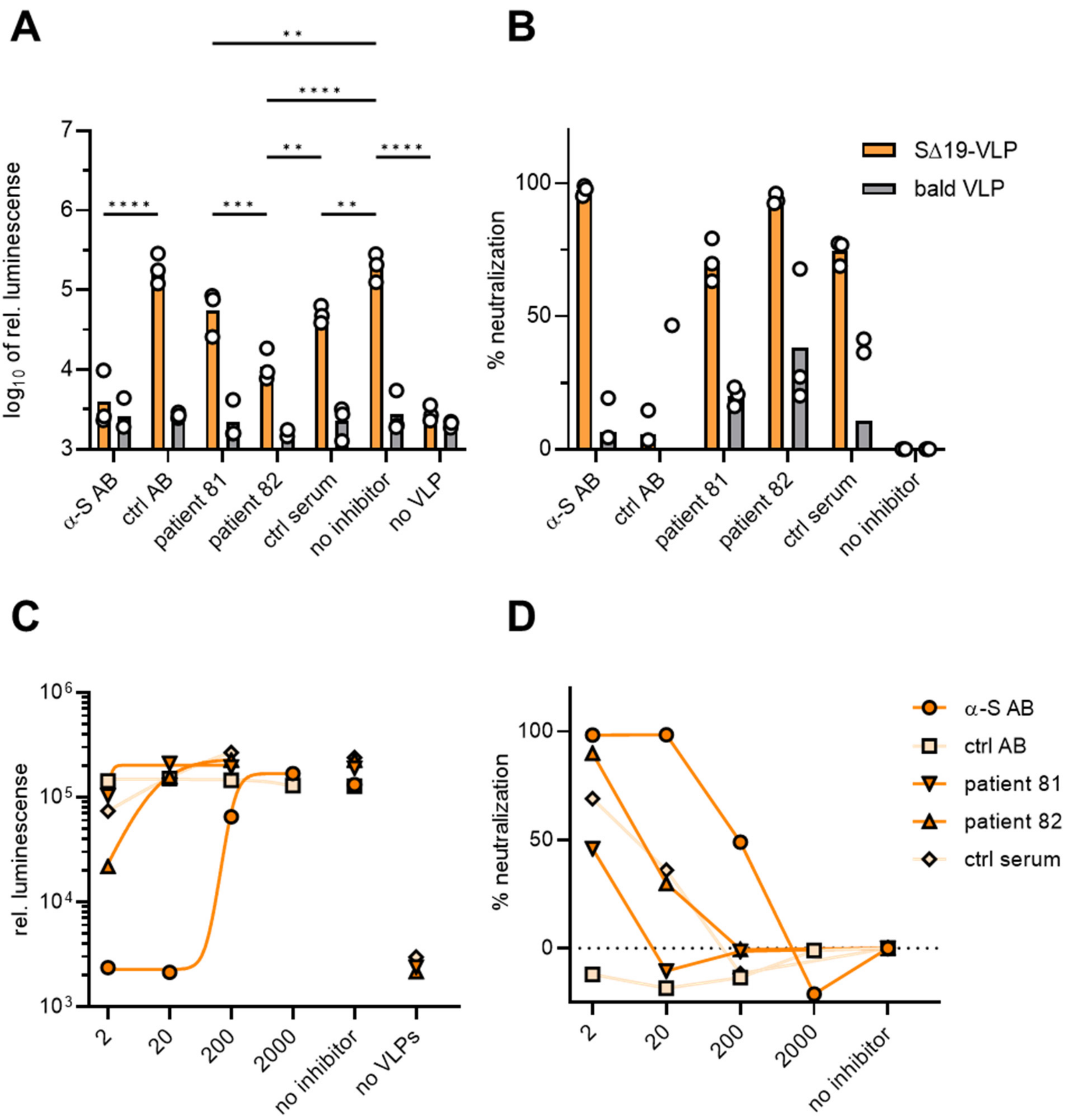

Figure 16: **Neutralization of fusion-from-without using S-specific inhibitors.**
A-B) SΔ19-VLPs and bald-VLPs were pre-treated with 4 µg/ml of anti-S antibody or control isotope antibody. Furthermore, VLPs were incubated 1:1 with patient sera or pooled sera from healthy donors. After 30 min incubation, particles were added to target cells and luminescence signal was measured on the next day. Bars represent means and error bars indicate 95% CI of three independent experiments. P-values are from two-way ANOVA, p-value **** < 0.0001, p-value *** = 0.0001-0.001, p-value ** = 0.001-0.01 **A)** Reported is the relative luminescence signals of lyzed 293T-ACE2 cells after addition of SΔ19-VLP (orange) or bald-LV (grey) pre-incubated with sera or antibodies and **B)** the percentages of neutralization relative to the control without inhibitor. **C-D)** SΔ19-VLPs were treated with serially diluted inhibitors starting with twofold down to 2000-fold dilution. Relative luminescence signals were measured after overnight incubation and data points represent means of three independent experiments. **C)** Relative luminescence is plotted against the dilution factor of the inhibitor. **D)** Percentage of neutralization is plotted against the dilution factor of the inhibitor. Figure is adapted from (Theuerkauf et al. 2021).

4.4 Fusion-from-within, the fusion activity of cells producing and presenting S on the cell surface

4.4.1 Syncytia formation of S presenting cells

Having seen a high fusogenic activity of S particles, we assessed whether S presented on cells fuse with ACE2-expressing cells, leading to the formation of syncytia. For an initial experiment, the producer cells of SΔ19-LV, which express S on their surface, were trypsinized and cocultivated with Vero cells (see Figure 17). Additionally, the rearranged cell morphology of fused cells was investigated by confocal laser scanning microscopy (see Figure 18). For that, 293T cells engineered to co-express RFP and either the S or SΔ19 variant were cocultured with Vero cells expressing GFP. After overnight incubation, cell nuclei were stained by Hoechst and the cytoskeleton by actin staining.

After the cocultivation of SΔ19-LV producer cells and Vero cells the cell culture dish was covered with large, multinucleated syncytial cells one day after coculture set up (see Figure 17). Since, for this production, 293T cells were transfected with a transfer plasmid encoding GFP, the fused cells could not only be identified in the microscopic brightfield images but also by the GFP expression. Many of the large syncytia contained more than 10 up to hundred nuclei, already indicating a high fusion activity of S on cells.

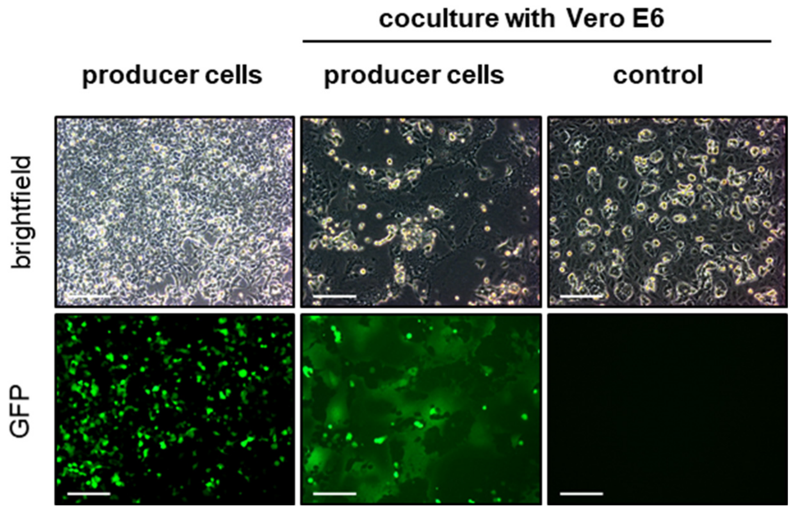

Figure 17: **Producer cells of SΔ19-LV form syncytia upon cocultivation with Vero cells.** Producer cells of SΔ19-LV were analyzed by brightfield (top) and fluorescence microscopy (bottom) three days after transfection (left). Cells were then detached by trypsin treatment and cocultured with Vero cells overnight (middle). As control, untransfected 293T cells were cocultured with Vero cells (right). The scale bar indicates 500 µm. Figure is adapted from (Theuerkauf et al. 2021).

Furthermore, syncytia formation was investigated in greater details by confocal microscopy (see Figure 18). While Vero and 293T cells showed expected cell morphologies and expression of the dedicated reporter signals, the cocultivated 293T cells expressing either the S or SΔ19 variant induced large syncytia formation. These were clearly visible by rearranged cytoskeletons and clustered multiple nuclei. Moreover, the coexpression of RFP and the GFP reporters clearly indicated the fusion of Vero-GFP and 293T-RFP cells. These experiments indicate a potent fusion activity of S-presenting cells.

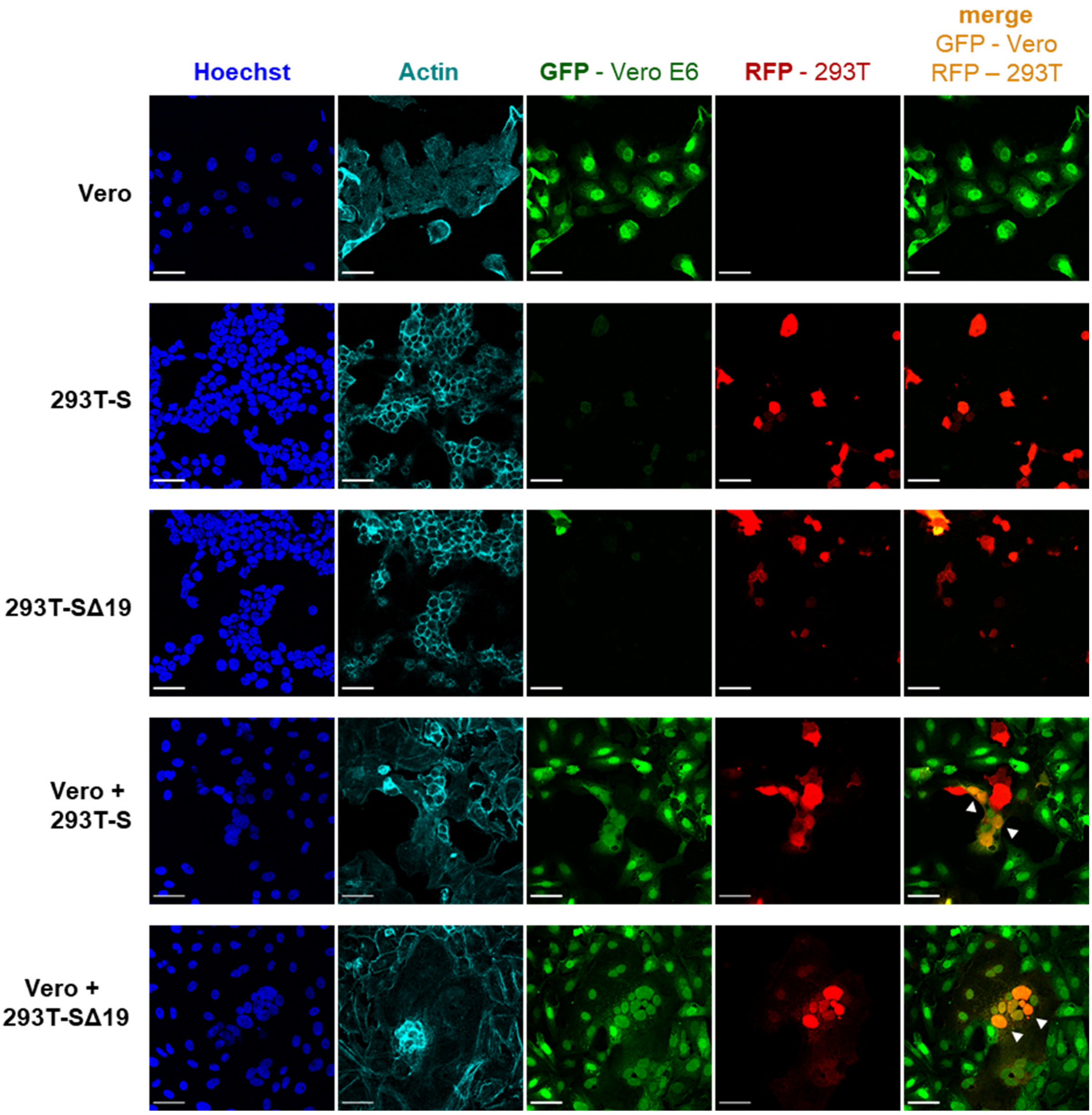

Figure 18: **S presentation on 293T cells mediates cell fusion when cocultured with Vero cells.** Vero cells stably expressing GFP (green) were cocultivated with transfected 293T cells co-expressing RFP (red) and either the full-length S or the truncated SΔ19 protein. After overnight incubation cells were fixed and stained with HOECHST3342 (blue) to visualize nuclei and phalloidin conjugated to Atto633 was used to stain actin (turquoise). Images were taken at a confocal laser scanning microscope. Scale bar indicates 50 µm. Arrows point to colocalization of RFP and GFP signals (yellow) indicating the fusion of S-presenting 293T and Vero cells. Figure is adapted from (Theuerkauf et al. 2021).

4.4.2 Setting up the assay to quantify fusion-from-within

Similar to the fusion-from-without assay, the efficiency of S mediated syncytia formation should be quantified utilizing the alpha-complementation of the beta-galactosidase. For this assay, 293T cells co-expressing the alpha fragment and S served as effector cells and 293T cells expressing the omega fragment as target cells (see Figure 19). Three days after transfection, effector and target cells were mixed in a 1:1 ratio and incubated for a given time. Then, cells were lyzed and the amount of complemented beta-galactosidase was quantified by luminescence reaction.

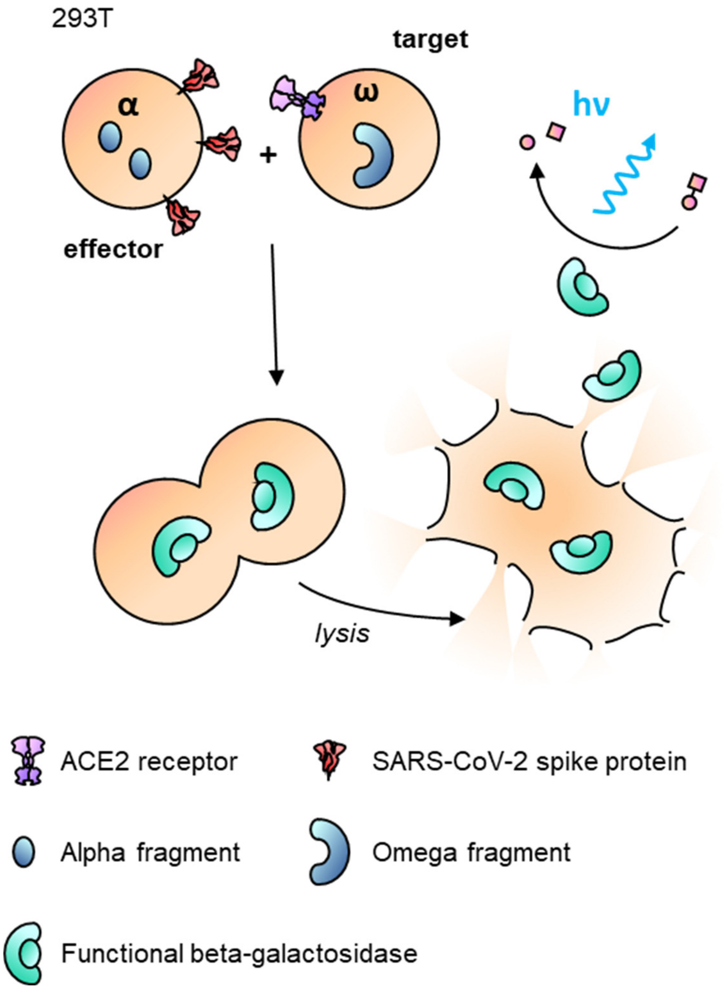

Figure 19: **Setup of cell-cell fusion assay.**
To generate effector cells, 293T cells were transfected to co-express alpha and S. 293T cells transfected with the omega plasmid served as target cells. Three days after transfection, effector and target cells were mixed 1:1 and co-incubated for a given time. Then, the culture was lyzed and reporter complementation was quantified by luminescence reaction. Figure is adapted from (Theuerkauf et al. 2021).

To identify the minimal amount of S required on effector cells to induce syncytia formation, cell lines presenting different levels of S on their surface had to be generated. For that, the plasmid encoding S was titrated for the transfection of 293T cells. Starting from 7500 ng of S plasmid, a tenfold dilution series was carried out, resulting in four different effector cell types with S plasmid amounts ranging from 7500 ng down to 7.5 ng per T75 flask. Three days after transfection, these effector cells were detached by trypsination and analyzed for the amount of S expression on their surface by flow cytometry using a primary anti-S antibody followed by secondary anti-IgG1-PE antibody (see Figure 20). After applying a gating strategy which verifies the analysis of single, viable cells, the percentage and the mean fluorescence intensity (MFI) of S expressing cells was reported. 293T cells expressing either omega or alpha without the S protein determined the background of the analysis.

With the highest plasmid dose, 45% of the cells were transfected and had an MFI of $4x10^3$. With decreasing amounts of S plasmid, the MFI on effector cells declined and reached background levels with the lowest plasmid dose (MFI of 392). Although the MFI was indistinguishable from the background signal, these effector cells still exhibited 1.3% of cells expressing S, demonstrating that in this transfection approach, a few cells expressed a low amount of spike on their surface. Overall, for the cell-cell fusion, four effector cell types differing in the expression level of S were available.

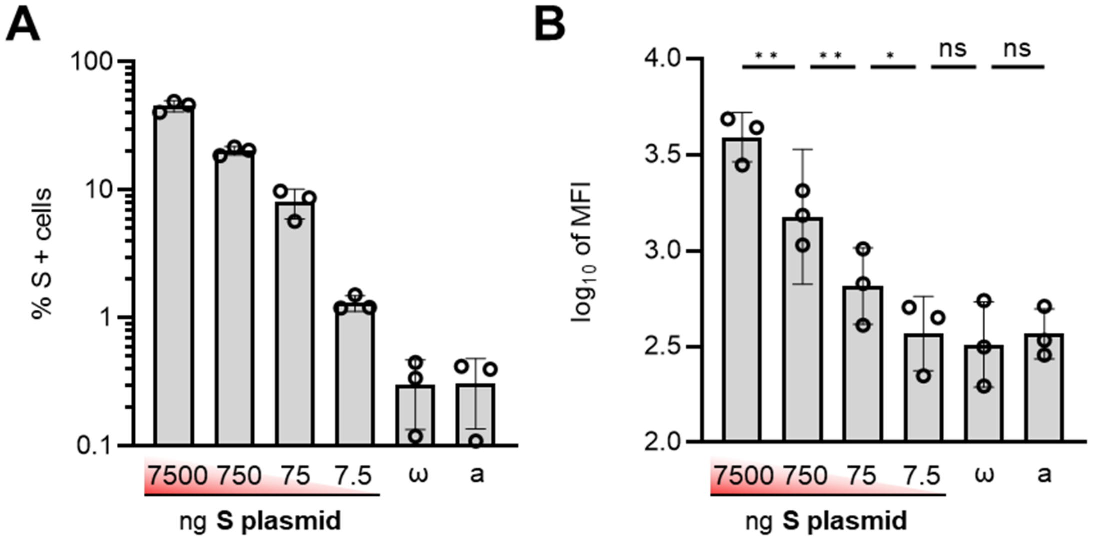

Figure 20: **S expression levels on effector cells.**
A-B) Four effector cell types were generated by transfection with 7500, 750, 75 and 7.5 ng S plasmid per T75 flask, respectively. Three days after transfection S expression level was determined by flow cytometry using anti-S antibody followed by a secondary anti-IgG-PE antibody. The background signal was determined by alpha and omega expressing 293T cells without S expression. **A)** Percentage of single, viable cells expressing S for all cell types is shown. **B)** Mean fluorescence identity of S specific signals. Bars represent means ± 95% CI of three independent experiments. Statistical differences were calculated by one-way ANOVA, p-value ** = 0.001-0.01, p-value * = 0.01-0.05. Figure is adapted from (Theuerkauf et al. 2021).

4.4.3 Minimal levels of S on effector cells are required to induce cell fusions

Having generated the effector cells, the cell-cell fusion assay was utilized to identify the minimal amounts of S expression on cells sufficient to cause a fusion signal above the assay's background signals. Three days after transfection, effector cells were mixed in a 1:1 ratio with target cells and incubated for 1 hour, 3 hours and overnight. At the cultivation endpoint, the cell cultures were lyzed and reporter signals were analyzed by substrate-specific luminescence reactions (see Figure 21). The background was determined by a coculture of alpha- and omega-expressing cells lacking S expression. As negative controls, background luminescence activity of single cell types was reported.

The highest fusion signal was determined for effector cells receiving the highest plasmid doses of 7500 ng and 750 ng S plasmid per T75 flask and when the assay proceeded overnight. Under this condition, the fusion signal reached up to $9.8x10^5$ RLU and was three orders of magnitude higher than the background signals ($3x10^3$ RLU). Shortening the assay time significantly reduced the fusion signal. While three hours incubation were still sufficient to cause a fusion signal after overnight incubation of $3x10^4$ RLU, one hour did not cause a reporter signal above background. Remarkably, effector cells generated with only 7.5 ng S plasmid per T75 flask exhibited a significant fusion signal of $4.3x10^4$ RLU after overnight incubation, although the MFI of S expression on these cells was indistinguishable from background (labeled by arrow). This clearly demonstrates that very low levels of S protein are sufficient to cause cell-cell fusion and highlights the high fusion activity of S.

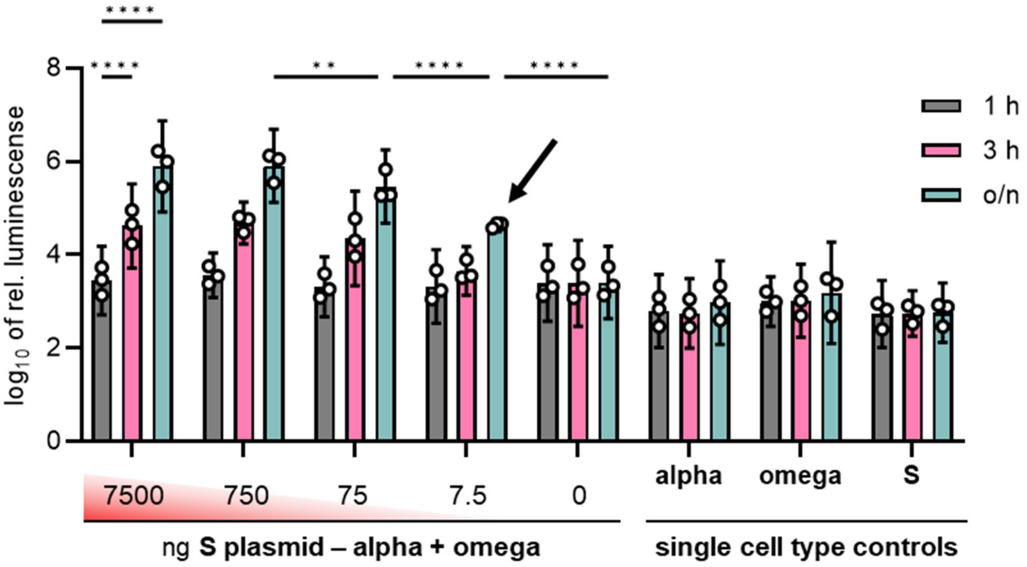

Figure 21: **Quantification of S dependent cell-cell fusion.**
Effector cells transfected with the alpha fragment and the indicated amount of S plasmid were detached three days after transfection by trypsin treatment and co-incubated with target cells expressing omega. Fusion signals were determined after cell lysis by luminescence reaction at the assay's endpoint (1 h, 3 h and overnight). Background signals were determined by the cocultivation of alpha and omega cells without S expression. Single cell types served as negative controls. Bars represent means ± 95% CI of three independent experiments. Statistical differences were calculated by two-way ANOVA, p-value **** < 0.0001, p-value ** = 0.001-0.01. Figure is adapted from (Theuerkauf et al. 2021).

4.4.4 Impact of ACE2 protein levels and proteolytic activation of S on fusion activity

In the aforementioned cell-cell fusion assay, effector cells were detached by trypsin treatment and mixed afterwards with target cells. Having demonstrated an enhanced fusion activity of S after trypsin treatment in the fusion-from-without assay, the impact of trypsinization on the cell-cell fusion assay was investigated. For that purpose, effector cells were detached using PBS supplemented with 5 mM EDTA without trypsin addition and subjected to the cell-cell fusion assay.

Fusion signals obtained after assay set up were at least tenfold lower compared to effector cells being detached by trypsin treatment (see Figure 22A). Significant reporter signal above background was measured from all effector cell variants only after overnight incubation indicating that trypsin-dependent proteolytic activation of S is important for cell-cell fusion events.

Next, we assessed the impact of the ACE2 expression level on the assay performance, since increased fusion activity was already seen in the particle fusion assays. Effector cells being detached by trypsination and cocultured with ACE2 overexpressing target cells revealed a tenfold higher signal compared to coculture setups missing ACE2 overexpression (see Figure 22B). Now, the fusion signal exceeded two orders of magnitude above background already one hour after assay start. Furthermore, the fusion activity of all effector cells was similarly high at each certain time point, indicating that ACE2 overexpression massively induced cell-cell fusion events. Similar to the particle-mediated fusion assays, the cell-cell fusion assays further verified the influence of ACE2 expression level and trypsin-dependent proteolytic activation.

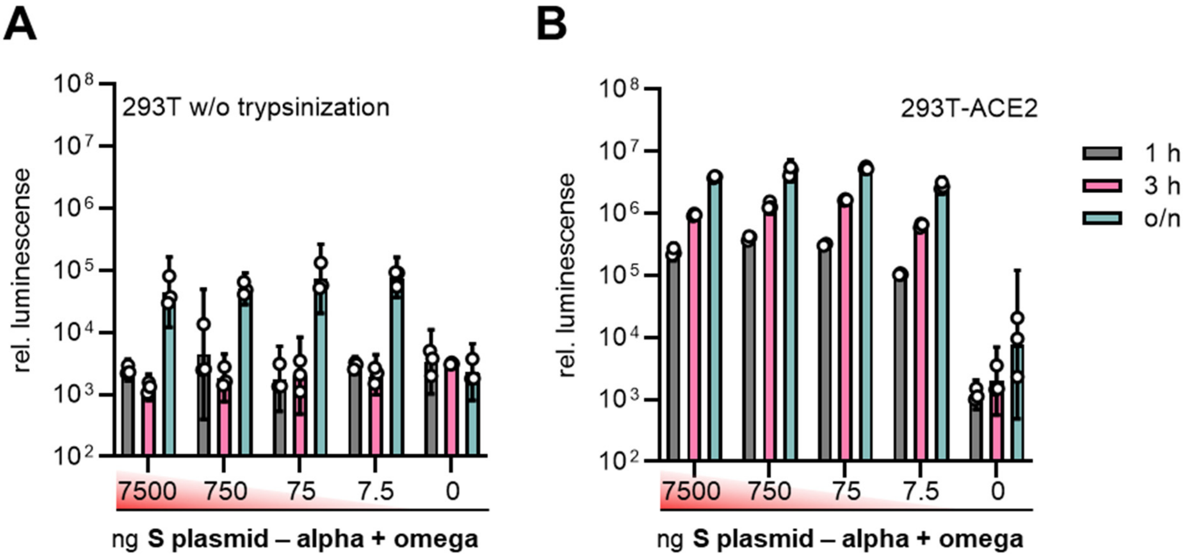

Figure 22: **Cell-cell fusion activity is dependent on the proteolytic activation of S displayed on effector cells and the expression level of ACE2 on target cells.**
A) Effector cells transfected with the indicated amounts of S plasmid were detached with PBS + 5 mM EDTA and cultivated with target cells expressing omega. **B)** Effector cells were detached by trypsin treatment and co-incubated with target cells overexpressing ACE2. **A-B)** Effector and target cells were mixed 1:1 and co-incubated for 1 h, 3 h and overnight. Fusion signals were determined by luminescence reaction after cell lysis and background signals were determined by cocultivation of alpha and omega cells without S expression. Bars represent means ± 95% CI of three technical replicates. Figure is adapted from (Theuerkauf et al. 2021).

4.4.5 Neutralization capacity of antibody and sera in the cell-cell fusion assay is lower compared to particle-cell fusion assays

Finally, S-specific inhibitors were used to neutralize the fusion activity. Effector cells were detached by trypsin treatment and mixed with either 4 µg/ml antibodies or 1:1 with human sera for 30 min. Afterwards, effector cells were cocultured with target cells overexpressing ACE2 and the assay was allowed to proceed overnight (see Figure 23). Fusion signals from cultures treated with spike-specific antibody (8.6×10^5 RLU) or with patient sera (6.4×10^5 and

4.6×10^5 RLU) were reduced compared to the isotope control (2.1×10^6 RLU) or sera of healthy persons (1.2×10^6 RLU), respectively. However, neutralization efficiency only yielded 60.8% for the antibody, 71% and 79.1% for the patient sera. Surprisingly, the neutralization capacity of all inhibitors was lower compared to the particle-based fusion assay, although identical amounts of inhibitors were used.

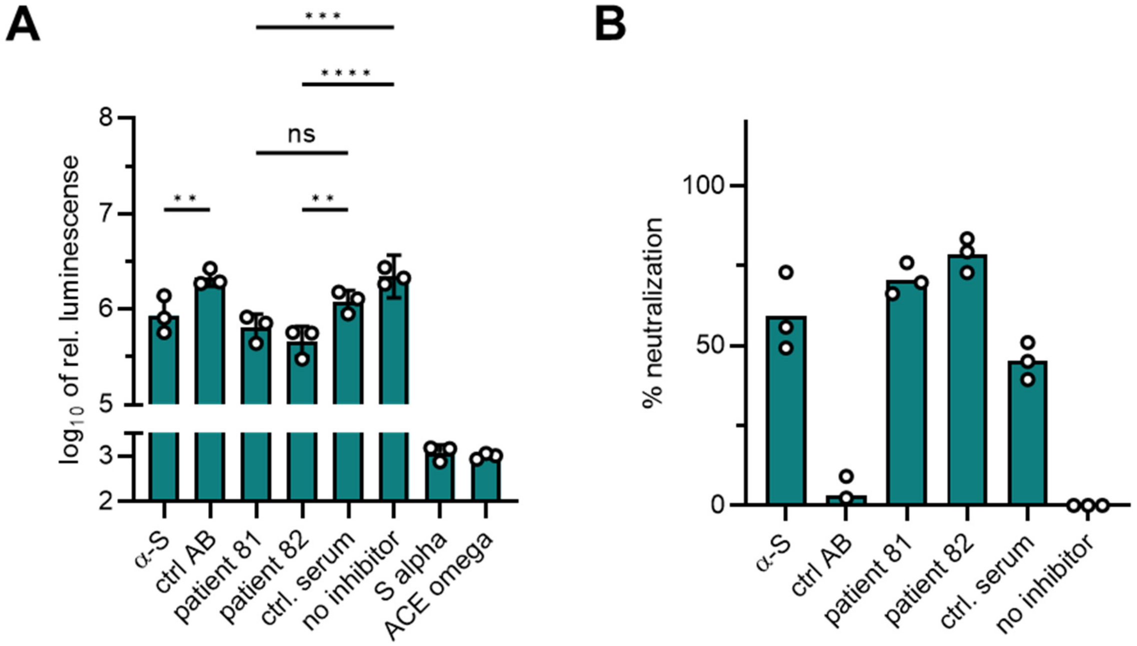

Figure 23: **Neutralization activity of S-antibody and patient sera on cell-cell fusion events.** Effector cells co-transfected with 7.5 ng S plasmid per T75 flask and the alpha fragment were pre-treated with 4 µg/ml of anti-S antibody or control isotope antibody. Furthermore, effector cells were treated 1:1 with patient sera or pooled sera from healthy donors. Sera and antibodies were incubated with effector cells for 30 min and subsequently added to 293T-ACE2 cells expressing omega. Fusion signals were determined after overnight incubation. Bars represent means of three independent experiments. **A)** Relative luminescent signal is plotted against the treatment of effector cells. Statistical differences were calculated by one-way ANOVA, p-value **** < 0.0001, p-value *** = 0.0001-0.001, p-value ** = 0.001-0.01. **B)** Percentage of neutralization relative to the control without inhibitor is plotted against the treatment of effector cells. Figure is adapted from (Theuerkauf et al. 2021).

4.4.6 S levels in fusion-from-within is lower than in particle-cell assays

Having demonstrated a lower neutralization capacity of antibodies and patient sera in the cell-cell fusion assays compared to their potency in the particle-based assays, it was investigated whether a higher amount of S-protein in the cell-cell fusion assay was the cause. Consequently, the amount of applied inhibitors would have been too low to completely neutralize S' fusion activity on cells. To compare the levels of S protein in all fusion assays, SΔ19-LV, SΔ19-VLP and effector cells were analyzed by western blot. SΔ19-LV and SΔ19-VLP used in the particle fusion assay were serial-diluted and probed for S and p24 proteins. S levels from the lysates of 2.5×10^5 effector cells produced with 750, 75 and 7.5 ng S plasmid were determined as well.

The western blot revealed the expected signals for S0 and S2 fragments in all particles with decreasing intensities for serial-diluted particles (see Figure 24). The signal decline was well in line with the reduction of the p24 signal and the absence of S signals in VSV-LV particles proved the specificity of the staining. The S-level in cells was detectable solely in effector cells that received the highest S plasmid dose of 750 ng. Consequently, the expression of S in the remaining effector cells was below the detection limit. Most importantly, the signal intensity of particles and cells used for the neutralization assays showed highest S amounts in SΔ19-VLP, followed by threefold less S in SΔ19-LV and was non-detectable for the effector cells. These clearly argues against that higher amounts of S in effector cells had been causative for the low neutralization in the cell-cell fusion assay.

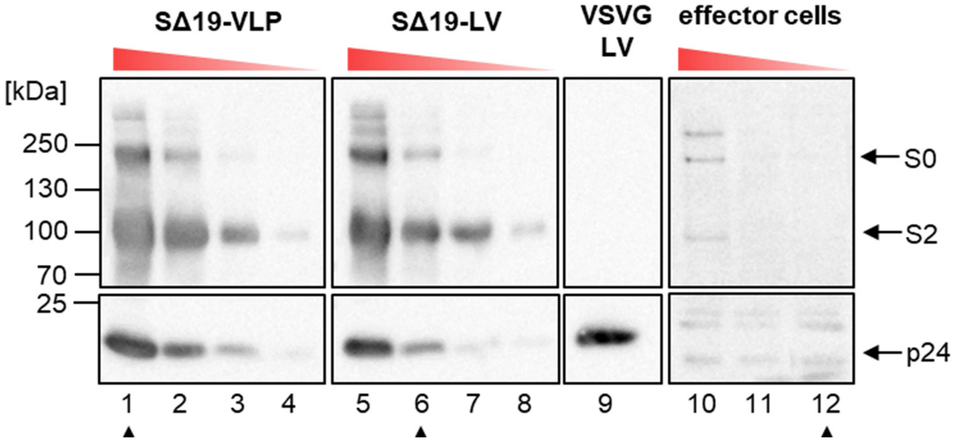

Figure 24: **Western blot to show S protein level in SΔ19-VLP, SΔ19-LV and effector cells used for fusion assays.**
Western blot analysis for the detection of S (upper part) and p24 (lower part) proteins: Serial dilutions of 2.5×10^9 SΔ19-VLP (lane 1-4) and serial dilutions of 3 µl SΔ19-LV (lane 5-8) were loaded. 3 µl of VSV-LV served as negative control (Lane 9). The cell lysate of 2.5×10^5 effector cells transfected with 750 ng (lane 10), 75 ng (lane 11) and 7.5 ng (lane 12) S plasmid per T75 flask, respectively, were loaded. Arrowheads below the blot indicate samples used for neutralization assays. Arrows on the right site indicate the signal heights of the S0, S2 fragments and p24 signals. Blots containing viral particles were exposed for 3 s, whereas blots showing effector cell signals were exposed for 800 s. Image contrast was optimized while retaining relative signal strength. Figure is adapted from (Theuerkauf et al. 2021).

4.4.7 S levels in effector cells is lower compared to cells infected by authentic SARS-CoV-2

Having excluded that incomplete inhibition of cell-cell fusion can be attributed to higher levels of S compared to the particles assays, the next step involved a comparison of S levels on effector cells with infected 293T and Vero cells using authentic SARS-CoV-2. For this experiment, Bevan Sawatsky (Paul-Ehrlich-Institut) infected 293T and Vero cells with two different isolates at a multiplicity of infection (MOI) of 1. After inactivation, the samples were received and prepared for Western Blot analysis. Spike levels were determined 24 or 48 hours after infection and compared to effector cells transfected with highest 7500 down to 7.5 ng S plasmid per T75 flask.

As seen from the staining against glycolytic glyceraldehyde-3-phosphate dehydrogenase (GAPDH), similar amounts of cell lysate were loaded in all lanes for the western blot analysis (see Figure 25). As expected, uninfected 293T and Vero cells did not show S signals. This time, the S2 signal was detectable in all effector cells. However, S0 signal was only detectable in effector cells receiving highest S plasmid amounts of 7500 and 750 ng. Infected Vero cells overall showed stronger S signals compared to infected 293T cells indicating that SARS-CoV-2 replication is more efficient in Vero cells leading to higher S expression. Compared to the infected Vero cells, the transfected effector cells used for neutralization assay (transfected with 7.5 ng S plasmid) showed much lower spike expression. In conclusion, effector cells used in our assays did not express unrealistic high amount of S. As a result, they serve as a suitable model for investigating the fusion activity of S.

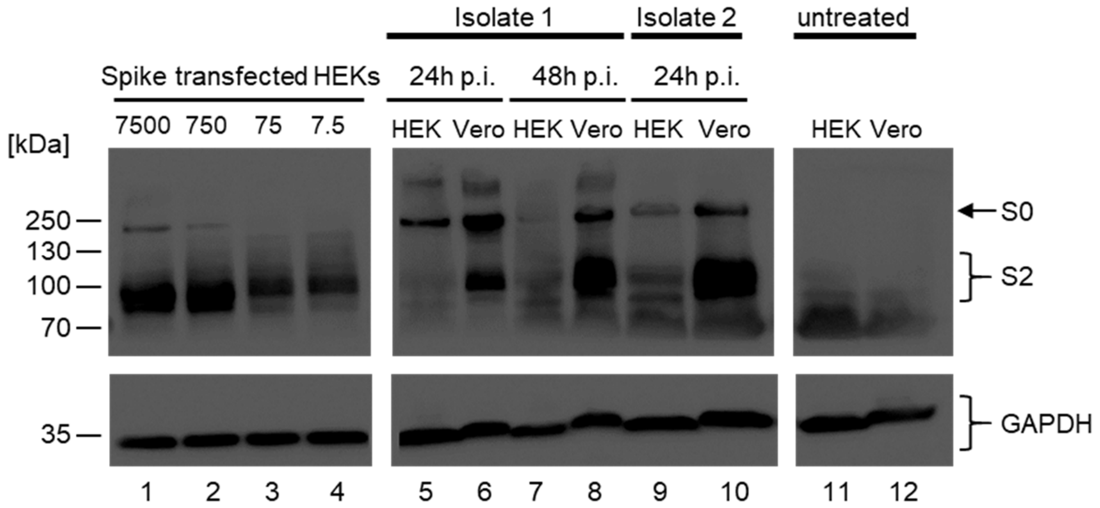

Figure 25: **Western blot to show S expression level on effector cells compared to cells infected with authentic SARS-CoV-2.**
Western blot analysis for the detection of S (upper part) and GAPDH (lower part) proteins. Lanes 1-4 show 293T cells transfected with 7500 ng (Lane1), 750 ng (lane 2), 75 ng (lane 3) and 7.5 ng (lane 4) S plasmid per T75 flask, respectively. Lanes 5-10 show cells infected with two SARS-CoV-2 isolates at a MOI of 1. Lysates of 293T and Vero cells 24 h after infection with the isolate 1 were loaded in lane 5 and 6, and 48 h after infection in lane 7 and 8, respectively. Lanes 9 and 10 show 293T and Vero cells 24 h *post* infection with isolate 2, respectively. To verify signal specificity, untreated 293T and Vero cells were loaded as controls in lane 11 and 12, respectively. Image contrast was optimized while retaining relative signal strength.

Results of Part B: Targeting strategies for adeno-associated vectors for HIV gene therapy

DARPins specific for the HIV reservoir marker CD32a (F11) and CD4 (55.2) were incorporated into receptor-blinded AAV2 and the resulting particles were biochemically characterized and evaluated for receptor-selective gene transfer. Furthermore, to achieve a selectivity for cells expressing CD4 and CD32a, both DARPins were connected in both orientations and then presented on the AAV capsid. After showing the specificity of the vector in mixed cell cultures, their ability to transduce target cells in human whole blood, followed by intravenously injection into NSG mice transplanted with human cells was shown. Finally, these particles were used to inhibit HIV replication *in vitro*.

4.5 Setting up the system

4.5.1 Generation of packaging plasmids

The packaging plasmid encoding the CD4-specific DARPins (55.2) in the GH2/3 loop of AAV2's VP1 was available and kindly provided by Luca Zinser (Paul-Ehrlich-Institut). This plasmid (pRC22-VP1-**55.2**-VP2/3ko-HSPGmut) contained the coding sequence of DARPin 55.2 flanked N-terminally by a $(G_4S)_5$-linker and a myc-tag and C-terminally by a G_4A-linker. Restriction sites SpeI and SfiI on the termini allowed for flexible exchange of DARPins. The construct was inserted into the GH2/3 loop of VP1 encoded in the pRC22-VP2/3ko-HSPGmut plasmid which possessed a disrupted major splice site to prevent VP2 and VP3 expression.

To target AAVs to CD32a receptor, DARPin 55.2 was replaced with the CD32a-specific F11 DARPin by restriction cloning using SpeI and SfiI sites resulting in plasmid pRC22-VP1-**F11**-VP2/3ko-HSPGmut. In order to construct bispecific AAV particles, both DARPins were connected by $(G_4S)_3$-linker in both orientations by overlap-extension PCR. Subsequently, connected DARPins were then inserted in the GH2/3 loop by restriction cloning resulting in the plasmids pRC22-VP1-**F11-55.2**-VP2/3ko-HSPGmut and pRC22-VP1-**55.2-F11**-VP2/3ko-HSPGmut. In combination with the plasmid pRC22-VP1ko-HSPGmut encoding for unmodified VP2 and VP3, these plasmids were used for the generation of CD32a-specific F11-AAV, CD4-specific 55.2-AAV, CD4/CD32a-specific F11-55.2-AAV and 55.2-F11-AAV (see Figure 26).

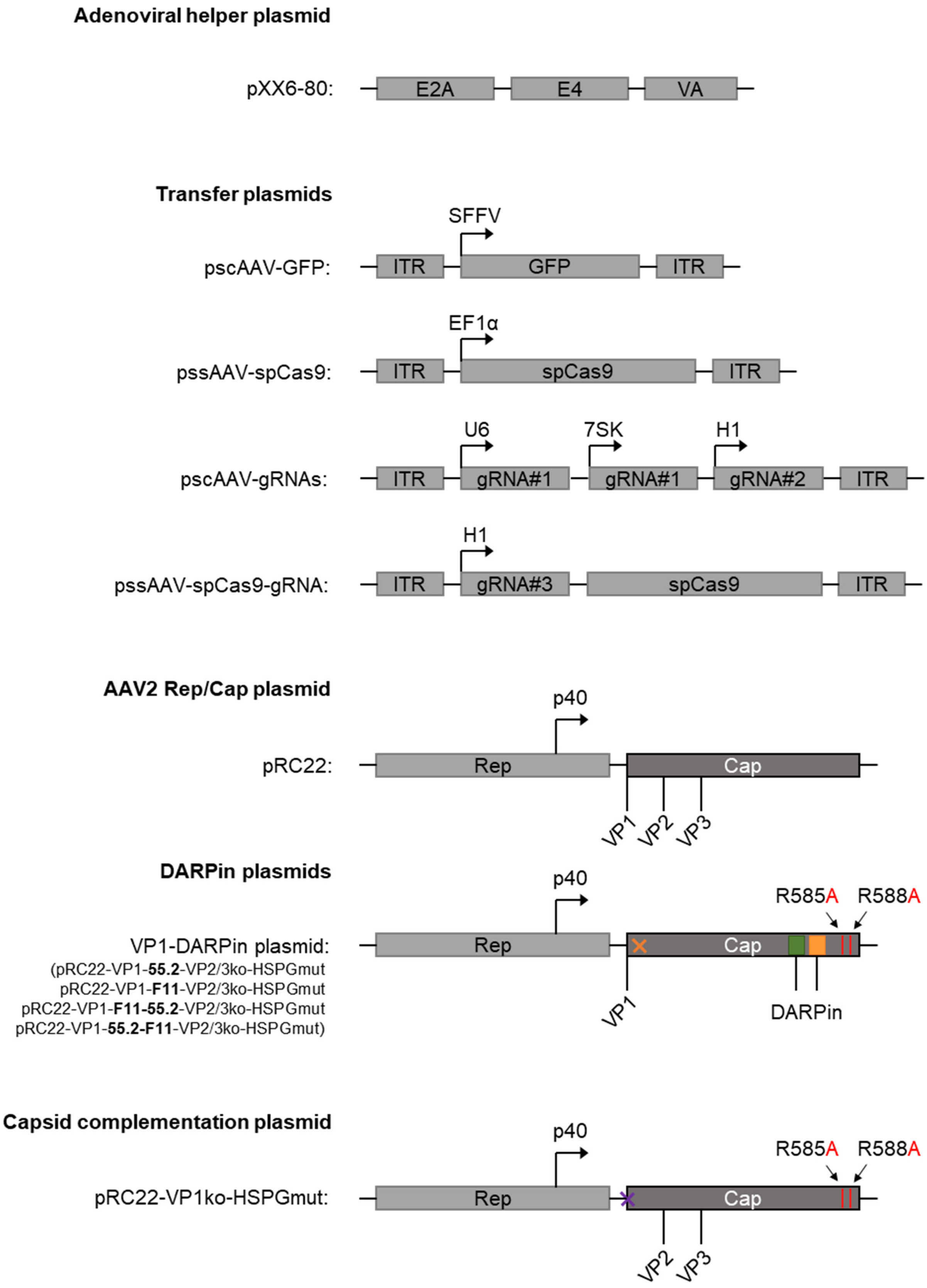

Figure 26: **Schematic representation of plasmids used for the production of AAVs.**
The adenoviral helper plasmid pXX6-80 provided the *E2A*, *E4* and *VA* genes. Transfer plasmids comprised the packaged gene (*GFP*, *spCas9* or *gRNAs*) being flanked by *ITR* sequences. The AAV2 Rep/Cap plasmid was required for the production of AAV2 WT and encoded the Rep and capsid proteins. For the generation of targeted AAVs, one targeting plasmid was combined with the capsid

complementation plasmid pRC22-VP1ko-HSPGmut. The targeting plasmids possessed a disrupted major splice acceptor site leading to the exclusive expression of the VP1 protein. Additionally, one or two DARPins were inserted in the GH2/3 loop resulting in the expression of a VP1-DARPin fusion protein. Point mutations in the HSPG binding domain ablated the recognition of the natural receptor (R585A and R588A). Within the complementation plasmids, the VP1 start codon was mutated preventing VP1 but leading to VP2 and VP3 protein expression.

4.5.2 Structure prediction of targeted AAVs

To predict the presentation of DARPins on the AAV capsid, the AlphaFold artificial intelligence was employed for the protein structure of a single VP protein conjugated to the DARPin. This involved the *in silico* design of the amino acid sequence of the VP protein having either F11 or F11-55.2 within the GH2/3 loop. The accuracy of the predicted structure was evaluated by aligning and superimposing with the X-ray crystal structure of VP3 (PDB: 1LP3). Afterwards, five predicted VP-DARPin protein structures were randomly distributed on an AAV capsid based on the symmetric data of an X-ray resolved structure (PDB: 1LP3) (see Figure 27).

The predicted structure of the VP-F11 structure exhibited only minor deviations from the 1LP3 structure, primarily found in flexible loops being hardly predictable by structure determination methods. Additionally, the PLDDT values, serving as indicator of prediction confidence, were mainly higher than approximately 90, suggesting a high likelihood of an accurate, native structure. Importantly, the DARPin did not alter the overall structure of the VP protein. Conclusively, based on this structural prediction, the insertion of the DARPins into the GH2/3 loop of VP did not alter the VP protein conformation, indicating that the AAV capsid likely tolerated DARPin incorporations.

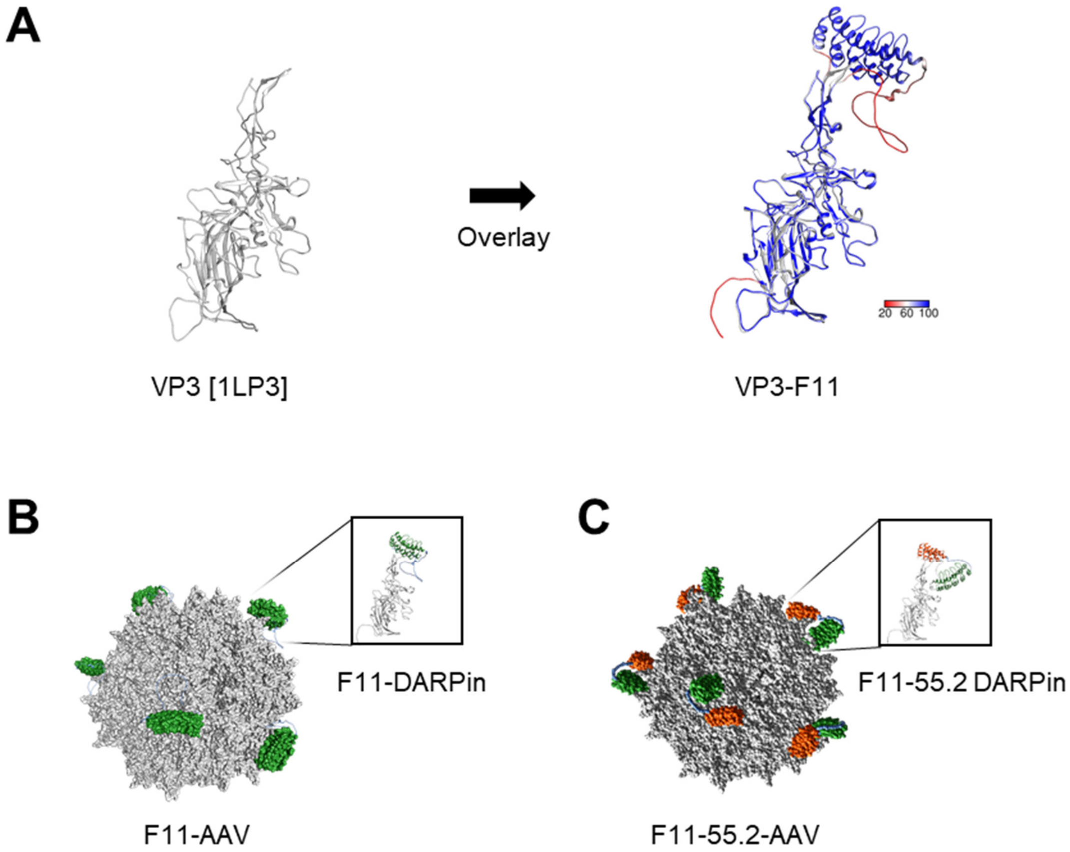

Figure 27: **Capsid structure prediction of DARPin-targeted AAVs using AlphaFold.**
For the computational modelling of the AAV capsid, the DARPin F11 and biDARPin F11-55.2 were *in silico* inserted into the GH2/3 loop of AAV2's VP3 GH2/3 loop. Although the insertion of DARPins in the experiments occurred in the VP1 loop, the smaller VP3 was chosen for this predictive structural analysis to minimize computing time, given that the VP1 N-terminus does not contribute to the capsid surface. **A)** The three dimensional structure of the fusion protein was predicted by AlphaFold (Mirdita et al. 2022) and overlayed on the VP3 structure of AAV2 determined by x-ray crystallography (white, PDB: 1LP3) using Chimera. The bar visualized the confidence intervals of the VP3-F11 structure prediction by AlphaFold based on the predicted local distance difference test (PLDDT). **B-C)** Due to the known abundance of VP1 proteins in the capsid, five **B)** VP3-F11 or **C)** VP3-F11-55.2 structures were randomly overlayed on the AAV2 capsid structure (PDB: 1LP3). Illustration in **C** were adapted from (Theuerkauf et al. 2023).

4.5.3 Biochemical characterization of mono- and bispecific vectors

4.5.3.1 DARPins are incorporated into the capsid and do not affect capsid morphology

To confirm the insertion of the DARPin molecules into the AAV capsid, the produced AAV particles targeting CD4 and/or CD32a were biochemically characterized for DARPin incorporation and capsid morphologies. To demonstrate the incorporation of VP1-DARPin proteins, AAV vector stocks were lyzed and analyzed by western blot (see Figure 28A).

Using an antibody recognizing all three capsid proteins F11-AAV and F11-55.2-AAV exhibited a higher shift in the unmodified VP2 and VP3 proteins compared to AAV2, which was shown before to be related to the point mutations in the HSPG binding site (Hamann et al. 2021). As expected, VP1 of F11-AAV had a higher molecular weight of above 100 kDa, due to the incorporation of the DARPin, than VP1 of AAV2 (87 kDa) (Warrington et al. 2004). The VP1 signal for F11-55.2-AAV (117 kDa) shifted even further according to the incorporation of two DARPins. Furthermore, F11-55.2-AAV showed additional signals at around 100 kDa, which might be related to unintended DARPin modifications of VP2 and VP3, indicating that there is residual protein expression despite the disruption of the major splice acceptor site. The shifted signals of VP proteins of targeted AAVs were further confirmed by staining against the myc-tag which indicated the presence of the DARPins.

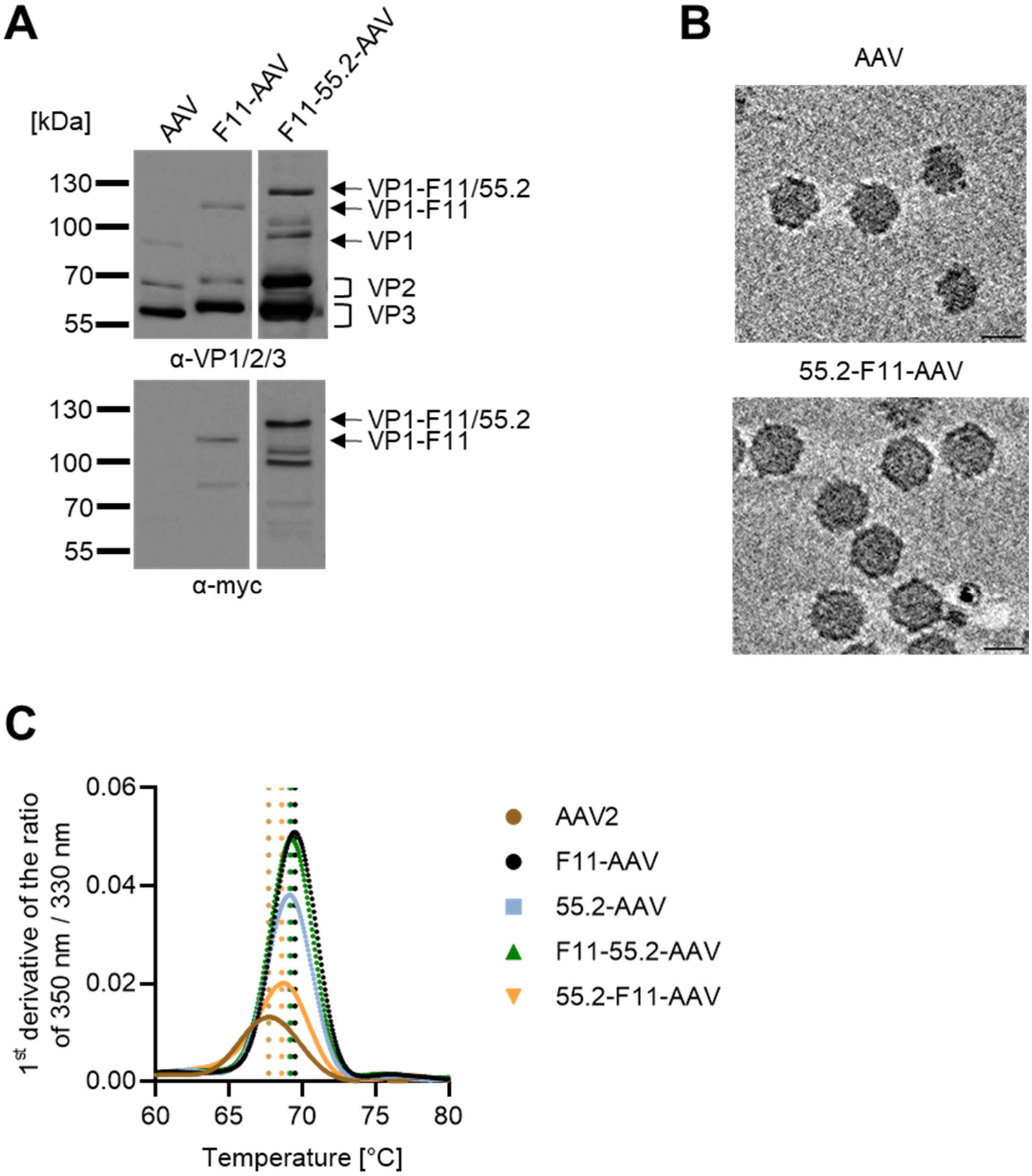

Figure 28: **VP1-DARPin fusion proteins are efficiently incorporated into the capsid and do not affect the capsid morphology.**
A) AAV WT, F11-AAV and F11-55.2-AAV were purified from the cell supernatant of transfected 293T cells and vector particles were concentrated by centrifugation through a 40% sucrose cushion. Particles were then lyzed, separated on a 4-15% polyacrylamide gel and blotted for western blot analysis using anti-VP1/2/3 (upper part) and anti-myc (lower part) antibodies. Markers on the right indicate the signals of the VP1-DARPin constructs and the unmodified VP proteins. **B)** Cryo-electron tomography of the AAV WT and the 55.2-F11-AAV capsids. The scale bar indicates 20 nm. Images were kindly provided by Petr

Chlanda (Heidelberg). **C)** The capsid protein thermal stability of AAV particles was assessed by Prometheus. Fluorescence signals at 330 and 350 nm were determined within a range of 30 to 95°C using a 1.5°C/min ramp rate. Shown is the first derivative of the 350 over 330 nm ratio among the temperature. Data were collected by Fabian John (Paul-Ehrlich-Institut). Illustrations in **A** and **B** were adapted from (Theuerkauf et al. 2023).

Taking into account that the protein folding of the VP1-DARPin fusion protein and subsequent particle assembly is hardly to predict, the next step was to investigate the impact on capsid morphology and stability. For that, the capsid structure of targeted and wild-type AAV were compared using cryo-electron tomography (ET) and thermal stability was assessed in a melting curve. For this purpose, the produced and characterized AAV particles were handed over to Petr Chlanda (Heidelberg) for cryo-ET measurements and to Fabian John (Paul-Ehrlich-Institut) to assess the thermostability.

Using cryo-ET, the morphology of AAV2 and 55.2-F11-AAV capsids were identical at high magnification (see Figure 28B). Furthermore, the melting points of the targeted AAVs were rather alike (68.5 to 69.5°C), than that of AAV2 WT (67.7°C) (see Figure 28C). This difference is likely related to the mutation of the HSPG binding site (Hamann et al. 2021). Overall, the thermal stability analysis showed that there is no decreased thermal stability of capsids having incorporated one or two DARPins and the capsid morphology was not affected.

4.5.3.2 Targeted AAV can be produced with high titer and high full/empty ratio

Having seen the efficient DARPin incorporation and confirmed the capsid integrity of targeted AAV, vector stocks were investigated to determine the effectiveness of an iodixanol gradient to remove vector particles lacking the genome (‘empty’ particles). For that, the produced particles were handed over to Fabian John (Paul-Ehrlich-Institut) for the staining of vector particles and acquisition of electron-microscopy images. Additionally, the genomic titer of the stocks was determined to evaluate whether the DARPin incorporation has any impact on the production yield.

To exclude empty particles from the vector stocks, AAVs were purified by iodixanol gradient centrifugation and the resulting stocks were analyzed for the full/empty ratios of particles by electron microscopy using negative-contrast staining (see Figure 29A). All stocks showed a high percentage of filled particles of up to 99% (see Figure 29B). Interestingly, 55.2-F11-AAV showed significantly less filled particles but still the vast majority of particles were filled (94%). Next, the amount of viral genomes per volume of vector stock was calculated using a qPCR targeting the ITR region. The genomic titer of all stocks was similar at about $1x10^{10}$ genome copies (GC) per µl, which is comparable to the titer of conventional AAV2 preparations (see Figure 29C). For that, the display of one or two DARPins on the capsid did not influence the genome concentration in vector stocks. Taken together, the DARPin insertions did not affect the capsid integrity and genome incorporation.

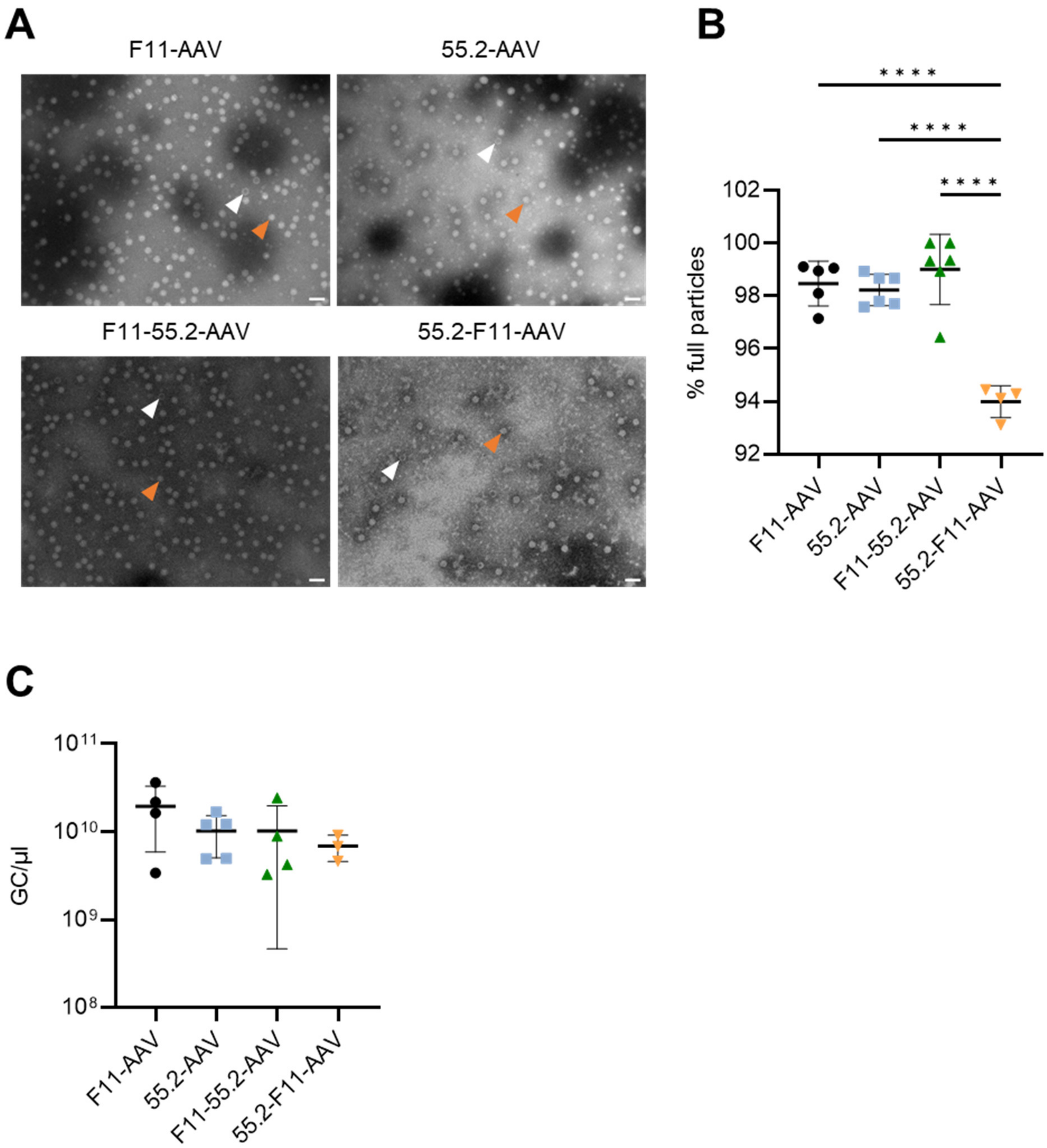

Figure 29: **Targeted AAV stocks have a high full/empty ratio and similar genomic titer.**

A-B) Targeted AAV purified by iodixanol gradient centrifugation were negatively stained with phosphotungstic acid and analyzed by electron microscopy. **A)** Full (white filled) and empty particles (dark center, white border) were identified and exemplarily marked with orange and white arrow heads, respectively. The scale bar indicates 50 nm. **B)** At least four images of one vector batch were counted for the amount of full particles and results were plotted as percent full particles. Statistical differences were calculated by one-way ANOVA, P-value **** < 0.0001. Standard deviation (STD) is reported. Electron microcopy images were kindly provided by Fabian John (Paul-Ehrlich-Institut). **C)** Vector particles were lyzed and DNA was extracted using the Blood & Tissue kit (Qiagen). Vector genome titers were then determined by an ITR-specific qPCR and results were plotted as GC per µl of vector stock. Each symbol represents one vector stock (F11-AAV n=4, 55.2-AAV n=5, F11-55.2-AAV n=4, 55.2-F11-AAV n=3). Statistical analysis with one-way ANOVA did not show significant differences. Standard deviation is reported. Figure is adapted from (Theuerkauf et al. 2023).

4.5.4 Gene delivery by targeted AAV

Having characterized the AAV particle’s biochemical properties, we next evaluated the specificity and gene delivery activity on cell lines. For that, cell lines were generated to express either CD32a, CD4 or a combination of both. SupT1 cells were chosen as target cell line because of their endogenous CD4 expression, named as SupT1-CD4 cells hereinafter. To compare the transduction efficiency to CD32a-targeted AAVs, SupT1-CD4 cells were engineered to additionally express CD32a by transduction with a lentiviral vector encoding the human CD32a protein resulting in SupT1-CD4/CD32a cells. Additionally, SupT1-CD4/CD32a cells were treated by a lentiviral vector transferring a CD4-targeted Cas9 to abolish CD4 expression resulting in the SupT1-CD32a cell line. The expression of the indicated receptors was then verified by flow cytometry using antibodies against CD4 and CD32a (see Figure 30). The engineered cell lines were kindly provided by Elena Herrera-Carrillo (Amsterdam, Netherland).

Flow cytometry confirmed that SupT1-CD4 cells were only positive for CD4 and SupT1-CD4/CD32a cells were uniformly positive for both receptors. The main cell population of SupT1-CD32a showed events for CD32a+ but a small fraction of cells still co-expressed CD4 (4.5%), indicating that CD4 expression was not completely prevented by the Cas9 treatment in these cells. Conclusively, all three SupT1 cell lines stably expressed the desired receptors.

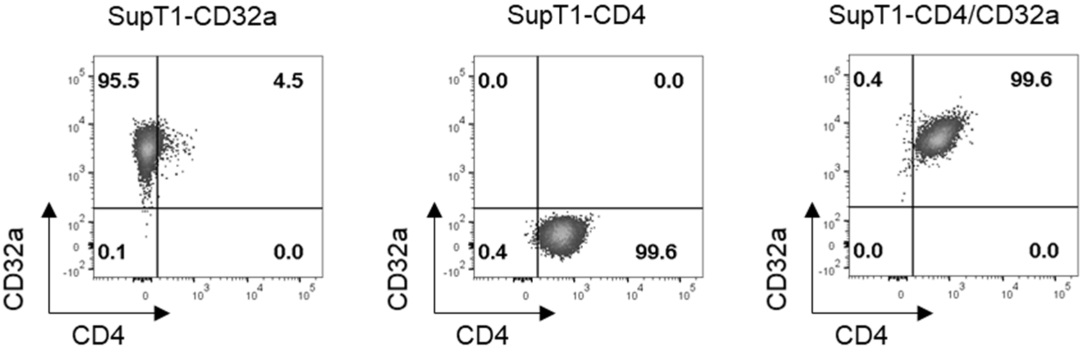

Figure 30: **Receptor expression on SupT1 cell lines.**
SupT1 cells were stained with fluorophore-conjugated antibodies against human CD4 and CD32a and analyzed by flow cytometry. Plots show the percentage of CD32a-expressing cells in relation to the cells expressing CD4. Figure is adapted from (Theuerkauf et al. 2023).

The established cell lines were then used to determine the transduction efficiency of the targeted AAVs. To determine which AAV capsid is most efficient in transducing the different SupT1 cells, equivalent AAV particle numbers were titrated. The percentage of GFP expressing cells three days post transduction was determined by flow cytometry and the transducing units (TU) per 1x10^5 GC were calculated from values showing linear correlation to the dilution factor (see Figure 31 and Table 1).

55.2-AAV transduced the SupT1-CD32a inefficiently, showing only a small fraction of GFP+ cells using highest particle numbers. This might be related to the transduction of the few CD4+ cells within the SupT1-CD32a cells. F11-AAV and F11-55.2-AAV showed similar titers of 11.5 and 13.9 TU/1x10^5 GC, respectively. Surprisingly, 55.2-F11-AAV showed a significant lower titer of 2.1 TU/1x10^5 GC, indicating that the orientation of both DARPins influenced gene delivery. On SupT1-CD4 cells, the titer of 55.2-F11-AAV increased more than 10-fold reaching 23.9 TU/1x10^5 GC. Now the titer was even slightly higher than for F11-55.2-AAV on SupT1-CD4 cells (20.9 TU/1x10^5 GC). 55.2-AAV reached a titer of 8.5 TU/1x10^5 GC, which was surprisingly lower than for the bispecific AAVs. F11-AAV only transduced 3.7% of the cells at highest GC/cell. The highest transduction efficiency was obtained from the transduction of SupT1-CD4/CD32a cells with the bispecific AAVs reaching 52.1 TU/1x10^5 GC for F11-55.2-AAV and 36.4 TU/1x10^5 GC for 55.2-F11-AAV. Both monospecific AAVs showed significant lower transduction efficiencies of 6.8 TU/1x10^5 GC for F11-AAV and 6.6 TU/1x10^5 GC for 55.2-AAV. Interestingly, the transduction efficiency of both monospecific vectors was lower on SupT1-CD4/CD32a compared to the SupT1 cells expressing either CD4 or CD32a. This proofs that SupT1-CD4/CD32a were not intrinsically more permissive for AAV transduction. Overall, the data demonstrate the receptor-dependent transduction with the targeted AAV and reveal a high transduction efficiency of the bispecific vectors on SupT1-CD4/CD32a. Furthermore, both bispecific AAVs show a tendency to transduce SupT1-CD4 better than SupT1-CD32a cells. This effect was most pronounced for 55.2-F11-AAV.

Table 1: Transducing units per 1x10^5 genome copies

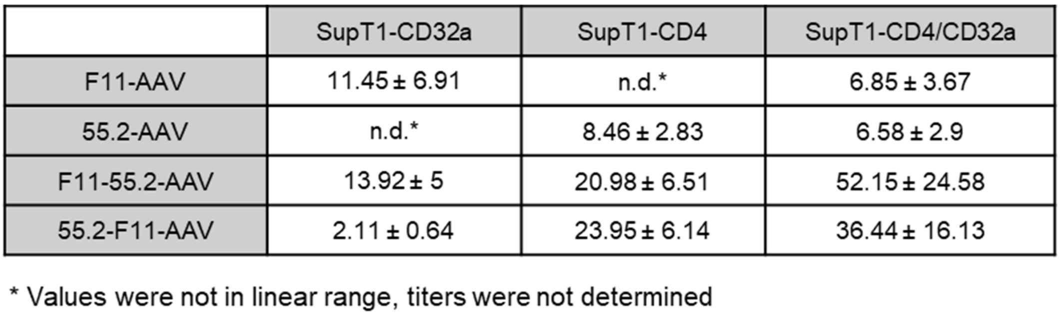

	SupT1-CD32a	SupT1-CD4	SupT1-CD4/CD32a
F11-AAV	11.45 ± 6.91	n.d.*	6.85 ± 3.67
55.2-AAV	n.d.*	8.46 ± 2.83	6.58 ± 2.9
F11-55.2-AAV	13.92 ± 5	20.98 ± 6.51	52.15 ± 24.58
55.2-F11-AAV	2.11 ± 0.64	23.95 ± 6.14	36.44 ± 16.13

* Values were not in linear range, titers were not determined

Table 1 is adapted from (Theuerkauf et al. 2023).

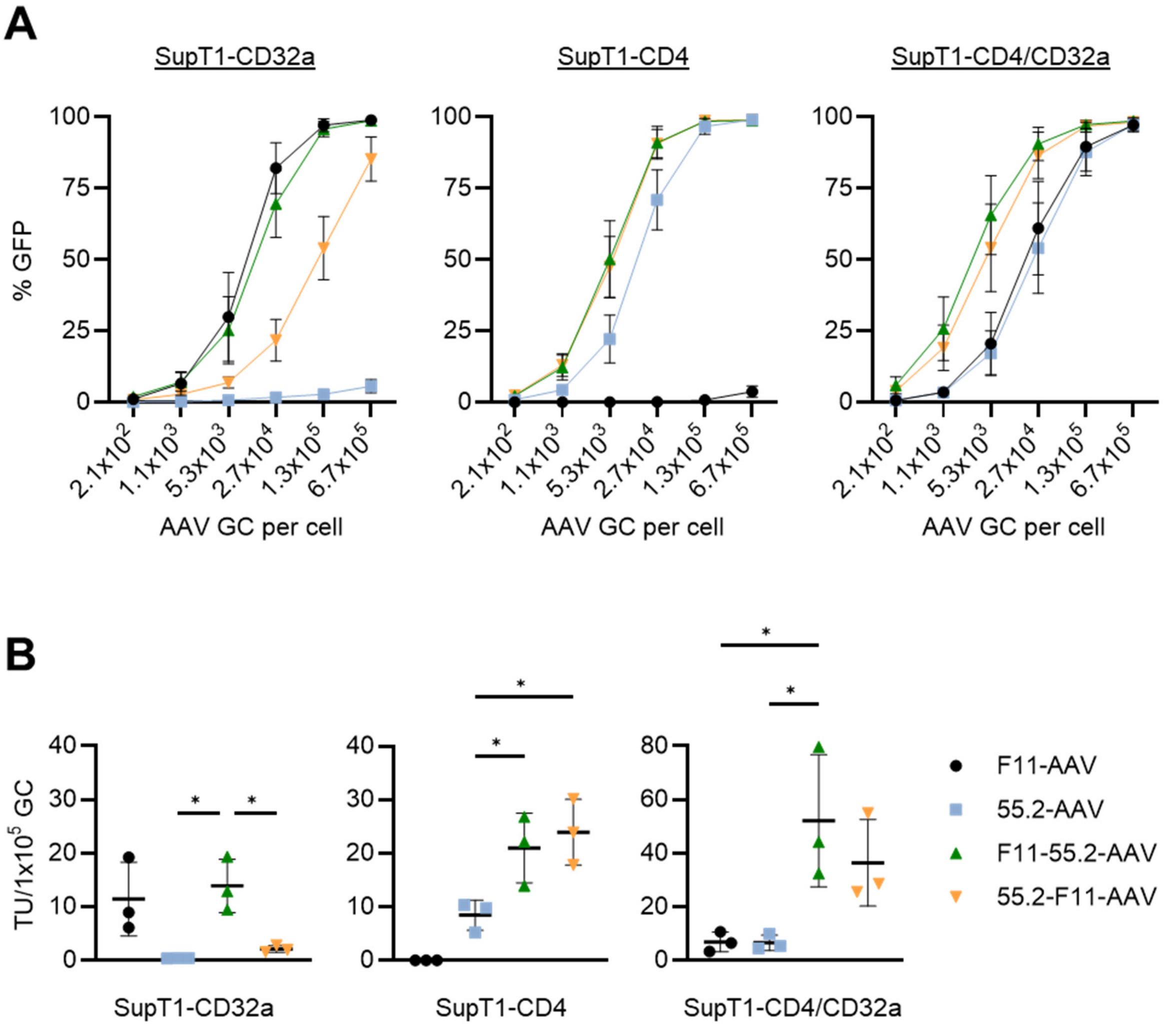

Figure 31: **Titration on SupT1 cell lines expressing CD4, CD32a or both receptors.**
AAV particles were normalized to the same genome copies as determined by qPCR and particles were added to SupT1 cell lines in five-fold dilution series. Three days after transduction SupT1 cells were analyzed for GFP expression by flow cytometry. **A)** The graphs show the percentages of GFP-expressing cells at the indicated AAV GC/cell **B)** Functional titers of the AAV variants were determined based on a linear correlation between the percentage of GFP-expressing cells and the dilution factor. The titer was expressed as transducing units (TU) per 1x10^5 GC. Statistical differences were calculated by one-way ANOVA, p-value * = 0.01-0.05. **A-B)** Bars show the mean of three independent experiments and the STD is reported. **B** is adapted from (Theuerkauf et al. 2023).

4.6 Selective transduction with mono- and bispecific vectors

4.6.1 Selectivity of F11-AAV

Having demonstrated the transduction efficiency of the vectors on individual cell lines, the selectivity of F11-AAV was assessed in mixed cell culture. For that, we mixed SupT1-CD4 off-target cells with SupT1-CD4/CD32a and serially reduced the amount of SupT1-CD4/CD32a cells down to only 1.5% of the total cell population (see Figure 32A). The cell selective transduction with 1.3x10^5 GC per cell was determined three days post transduction by flow cytometry.

In all cocultures, F11-AAV transduced most of the SupT1-CD4/CD32a cells and off-target transduction events were below 1.2% demonstrating high selective transduction even when the target cell population was underrepresented.

Furthermore, the vector masked the epitope recognized by the anti-CD32a antibody, which was most pronounced in cocultures containing less target cells as seen from the decreased mean fluorescence identity (MFI) in the respective channel (see Figure 32B). This can be explained by the fact that as the population of target cells decreases, the number of viral particles per target cell rises and more particles compete for the binding site of the antibody. This further validates that F11-AAV binds and transduces CD32a-expressing cells selectively.

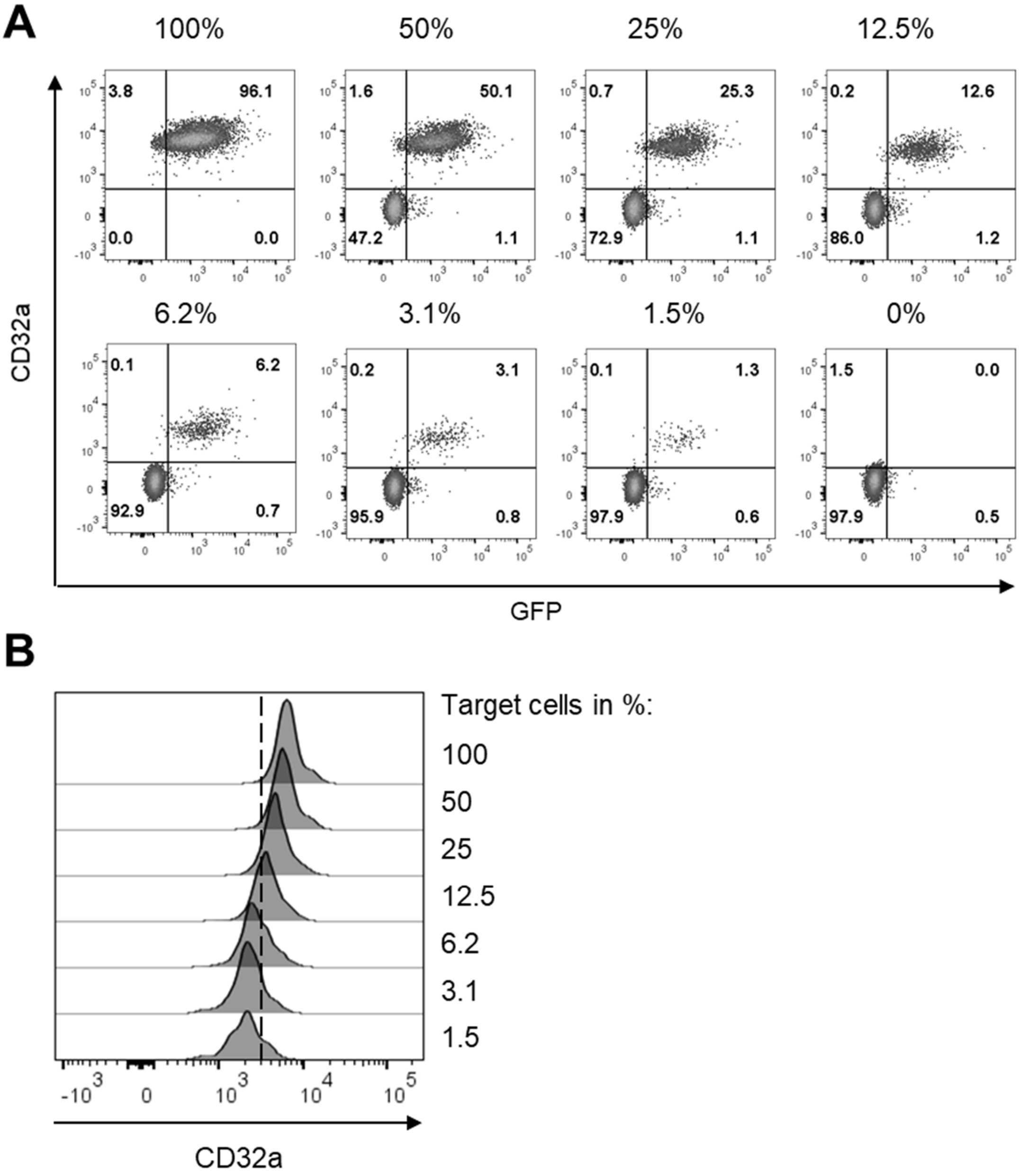

Figure 32: **Selective gene transfer with F11-AAV in SupT1-CD4 and SupT1-CD4/CD32a cocultures.** SupT1-CD4/CD32a cells were serially diluted in SupT1-CD4 cells resulting in six different cocultures ranging from 50% SupT1-CD4/CD32a cells down to 1.5%. Additionally, cell cultures containing only SupT1-CD4/CD32a cells (100%) or only SupT1-CD4 cells (0%) were used. The cell mixtures were then

incubated with 1.3×10^5 GC/cell of F11-AAV for three days and GFP expression was determined by flow cytometry. **A)** Plots show the percentage of CD32a-expressing cells related to cells expressing GFP. **B)** Histograms show the MFI of the CD32a signals pre-gated on CD32a-expressing cells in the different cocultures indicated on the right side.

4.6.2 Bispecific AAVs preferentially transduce cells expressing both receptors

The bispecific vectors already showed higher transduction efficiencies on the SupT1 cells expressing both CD4 and CD32a receptor. Encouraged from these results, the next step was to analyze whether the bispecific AAVs would preferably transduce CD4+/CD32a+ cells in presence of cells expressing only one of the receptors. For this purpose, we mixed SupT1-CD32a, SupT1-CD4 and SupT1-CD4/CD32a at equal ratio and analyzed GFP expression three days post vector exposure (see Figure 33).

When gated on all GFP-positive cells, F11-AAV and 55.2-AAV selectively transduced the CD32a and CD4 population, respectively, revealing below 0.3% off-target transduction. Both bispecific vectors showed a much higher frequency of double-positive cells (56.1% and 48.7%) compared to the monospecific vectors (27.8% and 28.9%). This was also evident when comparing the MFI of GFP+ cells within the CD4+/CD32a+ cell population, indicating that CD4+/CD32a+ cells are transduced more efficiently by the bispecific than the monospecific vectors. Furthermore, the bispecific vectors showed a tendency to transduce CD4+ cells more efficiently than CD32a+ cells. This was especially pronounced for vector 55.2-F11-AAV which showed 49% CD4+ cells compared to only 2.1% CD32a cells among all GFP+ cells (see Figure 33A, right panel). Conclusively, targeted AAVs showed selective transduction of target cells in mixed SupT1 cell cultures. Furthermore, bispecific AAVs exhibited a preference for SupT1-CD4/CD32a cells.

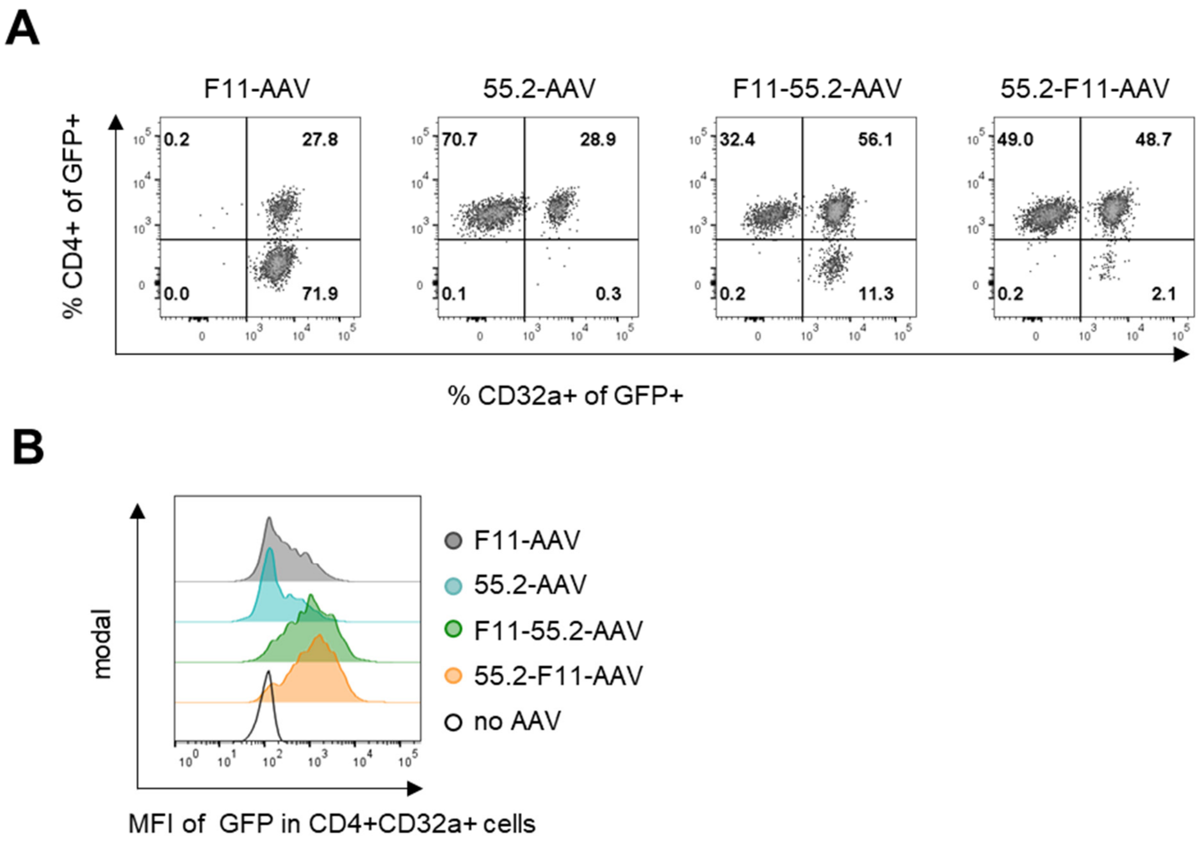

Figure 33: **Selective transduction of target cells present in cocultures of SupT1-CD4, SupT1-CD32a and SupT1-CD4/CD32a cells.**
SupT1-CD4, SupT1-CD32a and SupT1-CD4/CD32a cells were mixed in a 1:1:1 ratio and 2.67x10^4 GC/cell of targeted AAV were added. Three days after transduction, GFP expression in the different cell populations was determined by flow cytometry. **A)** GFP-expressing cells were gated for CD4 versus CD32a expression. **B)** Histograms showing the MFI of GFP in cells expressing both CD4 and CD32a after incubation with targeted AAVs. Untransduced cells served as negative control (no AAV). **A** is adapted from (Theuerkauf et al. 2023).

Next, the selectivity of bispecific vectors for underrepresented double-positive cells was assessed. SupT1-CD4/CD32a cells were serially diluted in a 1:1 coculture of SupT1-CD4 and SupT1-CD32a cells. This way, five different cell mixtures were established covering SupT1-CD4/CD32a cell concentrations, ranging from 25% down to 1.7% (see Figure 34).

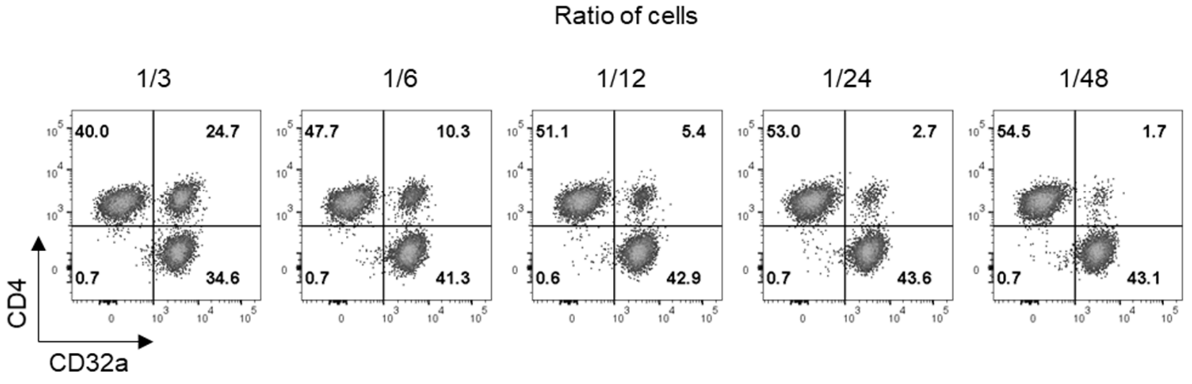

Figure 34: **Cell mixtures to determine specificities of bispecific AAVs.**

SupT1-CD4/CD32a cells were serially diluted in a 1:1 coculture of SupT1-CD4 and SupT1-CD32a cells. The amount of each cell population was determined by flow cytometry three days after coculture setup by staining for the CD4 and CD32a receptors. Figure is adapted from (Theuerkauf et al. 2023).

After setting up the cocultures, the targeted vector particles were added to each of the cell mixtures and GFP expression within CD4+, CD32a+ and CD4+/CD32a+ cells was determined three days later (see Figure 35).

Similar to the findings above, the bispecific AAVs outperformed the monospecific vectors regarding the transduction efficiencies on double-positive cells. There were at least twofold more CD4+/CD32a+ GFP+ cells (between 67.4 to 83.4%) compared to the monospecific vectors (between 28.8 to 42.7%). Furthermore, the significantly increased MFI for bispecific vectors confirmed the preferred transduction of CD4+/CD32a+ cells. In contrast, bispecific vectors were equally efficient on CD4 cells compared to 55.2-AAV showing no significant differences. Surprisingly, the transduction efficiency of F11-AAV on SupT1-CD32a was higher compared to the bispecific vectors. This is in contrast to titration on the SupT1-CD32a cell line shown in Figure 31 and Table 1, showing that at least F11-55.2-AAV had a similar titer as F11-AAV on this cell line. Consequently, these data reveal that bispecific AAVs show highest transduction efficiency on CD4+/CD32a+ cells, even when these are highly underrepresented. Furthermore, CD32a+ cells were less efficiently transduced by the bispecific vectors, while the transduction of CD4+ cells was comparable to the respective monospecific AAVs.

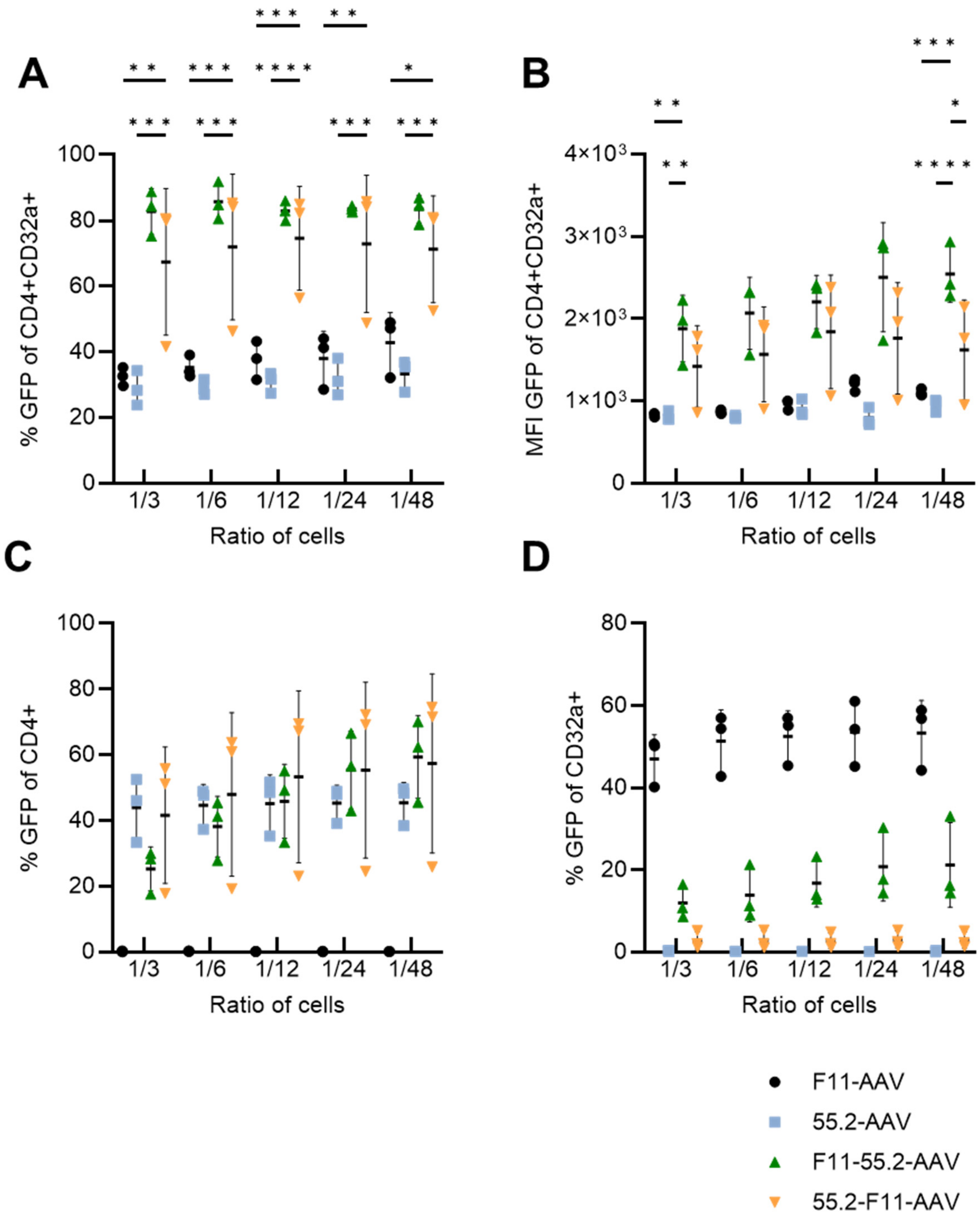

Figure 35: **Bispecific AAVs show highest transduction efficiency on CD4+CD32a+ cells.**
2.67×10^4 GC/cell of the indicated vectors were added to SupT1-CD4 and SupT1-CD32a cocultures containing decreasing amounts of SupT1-CD4/CD32a cells as depicted in Figure 34. The transduction efficiency was determined as percentage of GFP-expressing **A)** SupT1-CD4/CD32a cells, **C)** SupT1-CD4 cells and **D)** SupT1-CD32a cells. **B)** MFI of GFP in SupT-CD4/CD32a cells. Bars show the mean of three independent experiments and the STD is reported. Statistical differences were determined by two-way ANOVA, p-value **** < 0.0001, p-value *** = 0.0001-0.001, p-value ** = 0.001-0.01, p-value * = 0.01-0.05. **A** and **B** are adapted from (Theuerkauf et al. 2023).

To demonstrate the preferred transduction of double-positive cells by the bispecific vectors in the mixed SupT1 cell lines, the ratio of GFP-expressing CD4+/CD32a+ over CD32a+ cells or over CD4+ cells was calculated (see Figure 36).

Based on this data, 55.2-F11-AAV showed up to 30-fold better transduction on double-positive cells compared to the transduction of CD32a+ cells. This effect was reduced but still strong for F11-55.2-AAV reaching a preference of up to 7-fold for CD4+/CD32a+ cells. Even when CD4+/CD32a+ cells were highly underrepresented and only made up 1.7% of the total cell population, F11-55.2-AAV achieved a 4.5-fold preference and 55.2-F11-AAV a 29.3-fold preference for double-positive cells. Importantly, F11-AAV did not prefer the CD4+/CD32a+ cells but rather transduced the CD32a+ cells (relative preference below 1). Also in comparison to CD4+ cells, both bispecific vectors clearly showed a significant preference for the double-positive cells, although the effect was weaker. The relative preferences for CD4+/CD32a+ over CD4+ cells ranged between 3.4-fold and 1.4-fold transduction efficiencies for the bispecific vectors. Notably, also 55.2-AAV preferably transduced the CD4+ cells over CD4+/CD32a+ cells (relative preference below 1).

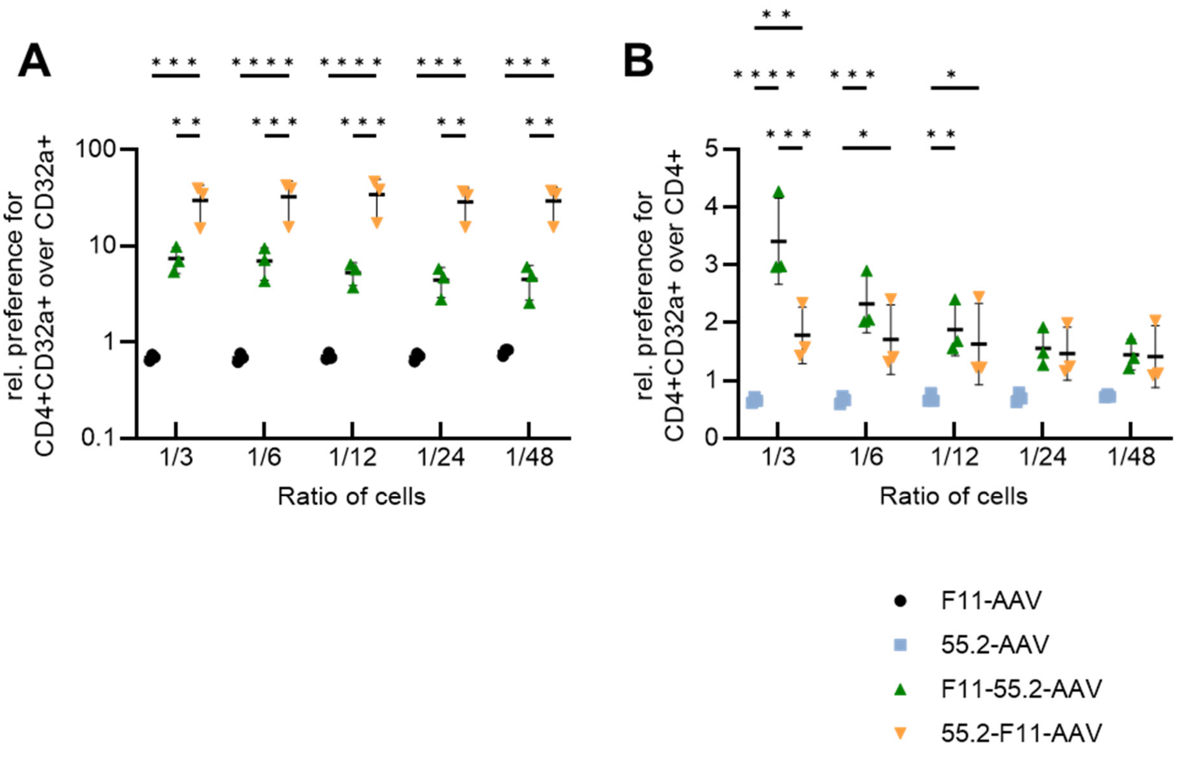

Figure 36: **Bispecific AAV preferably transduce CD4+CD32a+ over cells expressing either CD4 or CD32a.**
2.67x10^4 GC/cell of the indicated vectors were added to SupT1-CD4 and SupT1-CD32a cocultures containing decreasing amounts of SupT1-CD4/CD32a cells as depicted in Figure 34. The ratios of GFP-expressing CD4/CD32a cells over **A)** CD32a cells and over **B)** CD4 cells are shown. Bars show the mean of three independent experiments and the STD is reported. Statistical differences were determined by two-way ANOVA, p-value **** < 0.0001, p-value *** = 0.0001-0.001, p-value ** = 0.001-0.01, p-value * = 0.01-0.05. Figure is adapted from (Theuerkauf et al. 2023).

To demonstrate a higher transduction efficiency of bispecific versus monospecific vectors on SupT1-CD4/CD32a cells, the ratio of percent GFP-expressing cells was calculated. Bispecific vectors reached up to 3-fold higher gene delivery rates (see Figure 37). Importantly, both monospecific vectors had similar transduction efficiencies on these cells (value of 1). Overall, these data sets clearly show the preference of the bispecific vectors for cells expressing both targeted receptors in presence of cells expressing only one of the receptors. This effect was consistent at variable target cell numbers even down to only 1.7%.

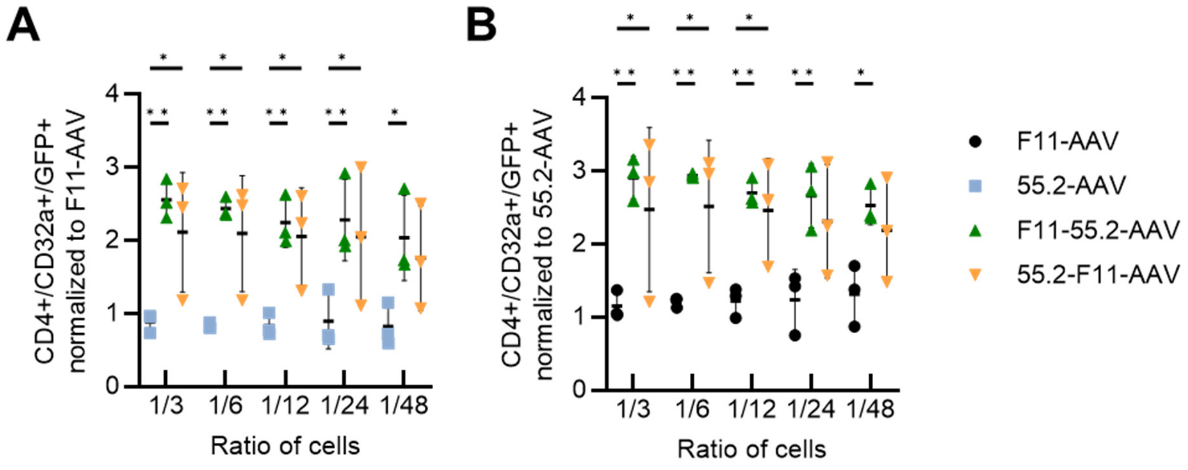

Figure 37: **Bispecific AAV show higher transduction efficiency on SupT1-CD4/CD32a compared to monospecific AAV.**

A-B) 2.67x10^4 GC/cell of the indicated vectors were added to SupT1-CD4 and SupT1-CD32a cocultures containing decreasing amounts of SupT1-CD4/CD32a cells as depicted in Figure 34. Fold-increase GFP expression in SupT1-CD4/CD32a cells with the indicated vectors over **A)** F11-AAV and **B)** 55.2-AAV is shown. Bars show the mean of three independent experiments and the STD is reported. Statistical differences were determined by two-way ANOVA, p-value ** = 0.001-0.01, p-value * = 0.01-0.05.

4.6.3 Low genome copies of bispecific AAVs are sufficient to efficiently transduce CD4+CD32a+ cells

Using the cell mixtures in Figure 34, the efficient transduction of bispecific vectors on double-positive cells was demonstrated. However, once the vectors will be systemically injected in a living organism, vector particles will be heavily diluted in the blood circulation and partially cleared from the system by specialized immune cells and organs. Thus, vector particles need to be active at low genome copies per cell to achieve therapeutic effects. To simulate such a situation, a coculture of only 2% SupT1-CD4/CD32a cells was used and the three vector concentrations 2667, 533 and 107 GC per cell were utilized to assess the specific transduction efficiencies (see Figure 38).

At all bispecific vector doses, a significant better transduction efficiency of the double-positive cells was observed compared to the monospecific vectors and even better than the combination of F11-AAV and 55.2-AAV (see Figure 38A). Furthermore, the relative preference for double-positive cells over CD32a+ cells reached up to 66.4-fold for 55.2-F11-AAV and 27.2-fold for F11-55.2-AAV (see Figure 38C). This was significantly higher than the mixed monospecific vectors, which reached at maximum a 3.8-fold preference. Interestingly, only F11-55.2-AAV showed a preference of SupT1-CD4/CD32a cells over SupT1-CD4 cells greater than the mix group when low AAV concentrations of 533 and 107 per cell were used (see Figure 38D). Concluding from these results, bispecific AAVs also prefer the transduction of CD4/CD32a cells at low genome copies per cell and this preference becomes more pronounced as the genome copies per cell decrease. Importantly, the transduction rates of the bispecific vectors were not reached by the combination of both monospecific AAVs, verifying that the bispecific AAV's transduction properties are especially suited to modify CD4/CD32a cells.

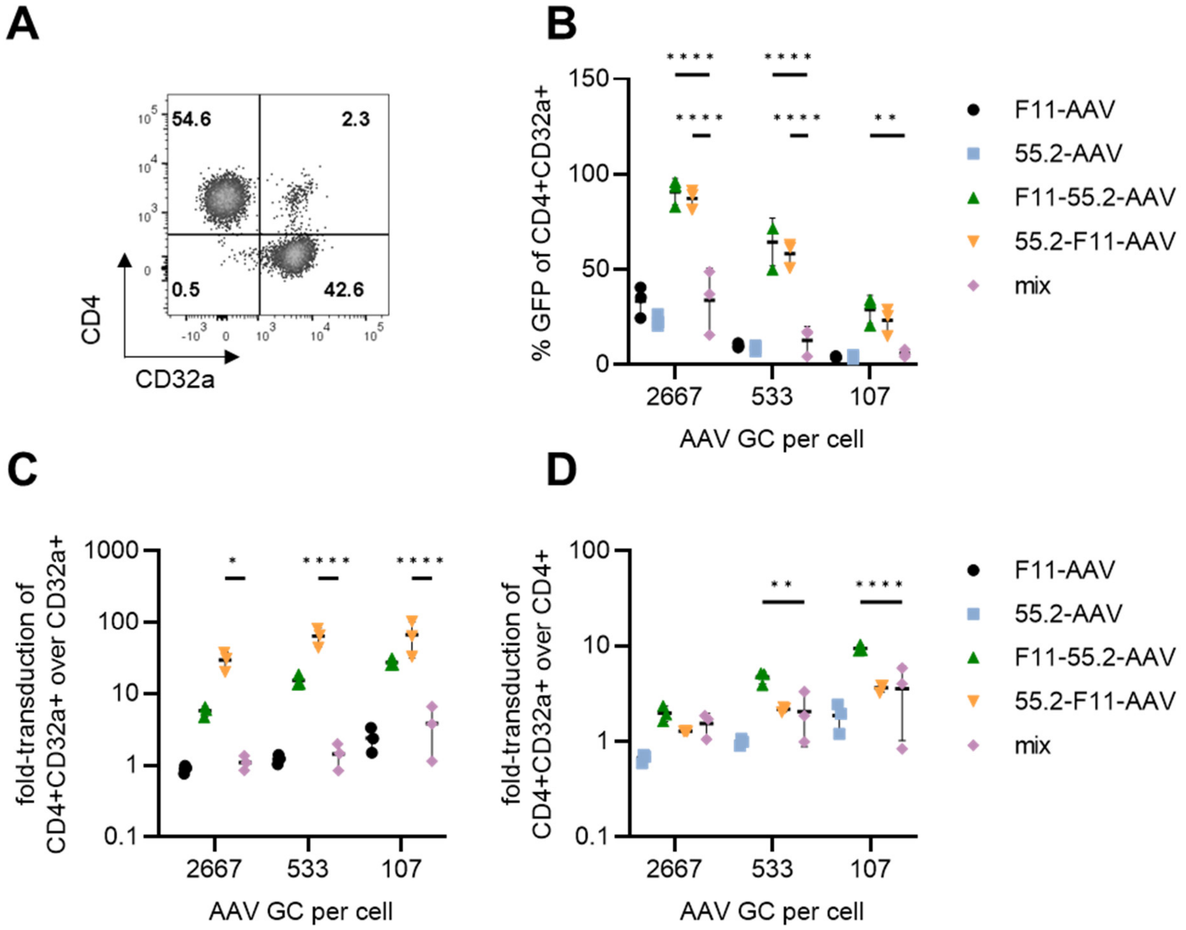

Figure 38: **Bispecific AAV show higher transduction efficiencies on underrepresented SupT1-CD4/CD32a cells compared to a combination of F11-AAV and 55.2-AAV.**

A) Percentages of SupT1-CD4 (upper left quadrant), SupT1-CD32a (lower right quadrant) and SupT1-CD4/CD32a (upper right quadrant) in the coculture used for transduction experiments. Cell lines were identified by CD4- and CD32a-specific staining and subsequent analysis by flow cytometry. **B-D)** The coculture was transduced with F11-AAV, 55.2-AAV, F11-55.2-AAV and 55.2-F11-AAV with the indicated GC/cell. Additionally, a mix of F11-AAV and 55.2-AAV was added to cells containing the double number of particles per cell to match the dosages applied for cells solely transduced with the monospecific vectors. **B)** Percentage of GFP-expressing SupT1-CD4/CD32a cells. **C-D)** The ratios of GFP-expressing CD4/CD32a over **C)** CD32a cells and over **D)** CD4 cells are shown. Bars show the mean of three independent experiments and the STD is reported. Statistical differences were determined by two-way ANOVA, p-value **** < 0.0001, p-value ** = 0.001-0.01, p-value * = 0.01-0.05. Figure is adapted from (Theuerkauf et al. 2023).

4.6.4 Cellular uptake of targeted AAV

Having proved the better transduction efficiency of bispecific AAV on SupT1-CD4/CD32a cells in the aforementioned assays, the results were then verified on the genetic level. For this purpose, SupT1-CD4/CD32a cells were incubated with vector particles at 4°C and all unbound particles were removed (see Figure 39). After allowing endocytosis for 2 to 5 hours at 37°C, the subcellular fractions from cytosol, membrane and nucleus were isolated and AAV genomes within these fractions were quantified by GFP-specific qPCR.

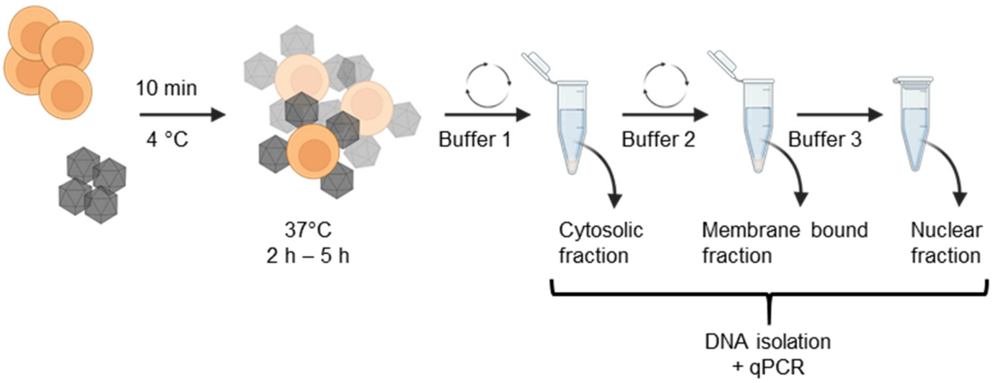

Figure 39: **Endocytosis assay to quantify cell internalization rate of AAV.**
$3x10^{10}$ GC of AAVs were incubated with $1x10^{10}$ SupT1-CD4/CD32a for 10 min at 4°C. Unbound particles were removed by washing steps and bound cells were incubated for 2-5 hours at 37°C. Afterwards, fractions from cytosol, membrane and nucleus were isolated using the subcellular fractionation kit. The amount of GFP sequences within the eluted DNA of each fraction was quantified by qPCR.

Comparing all vector types, we found at both time points significant higher uptake of the F11-55.2-AAV compared to the monospecific vectors (see Figure 40). Also, 55.2-F11-AAV showed a trend for higher genome levels in the fractions, although differences were not significant. This experiment further proved the advantageous cell entry of bispecific vectors on double-positive cells compared to the monospecific counterparts.

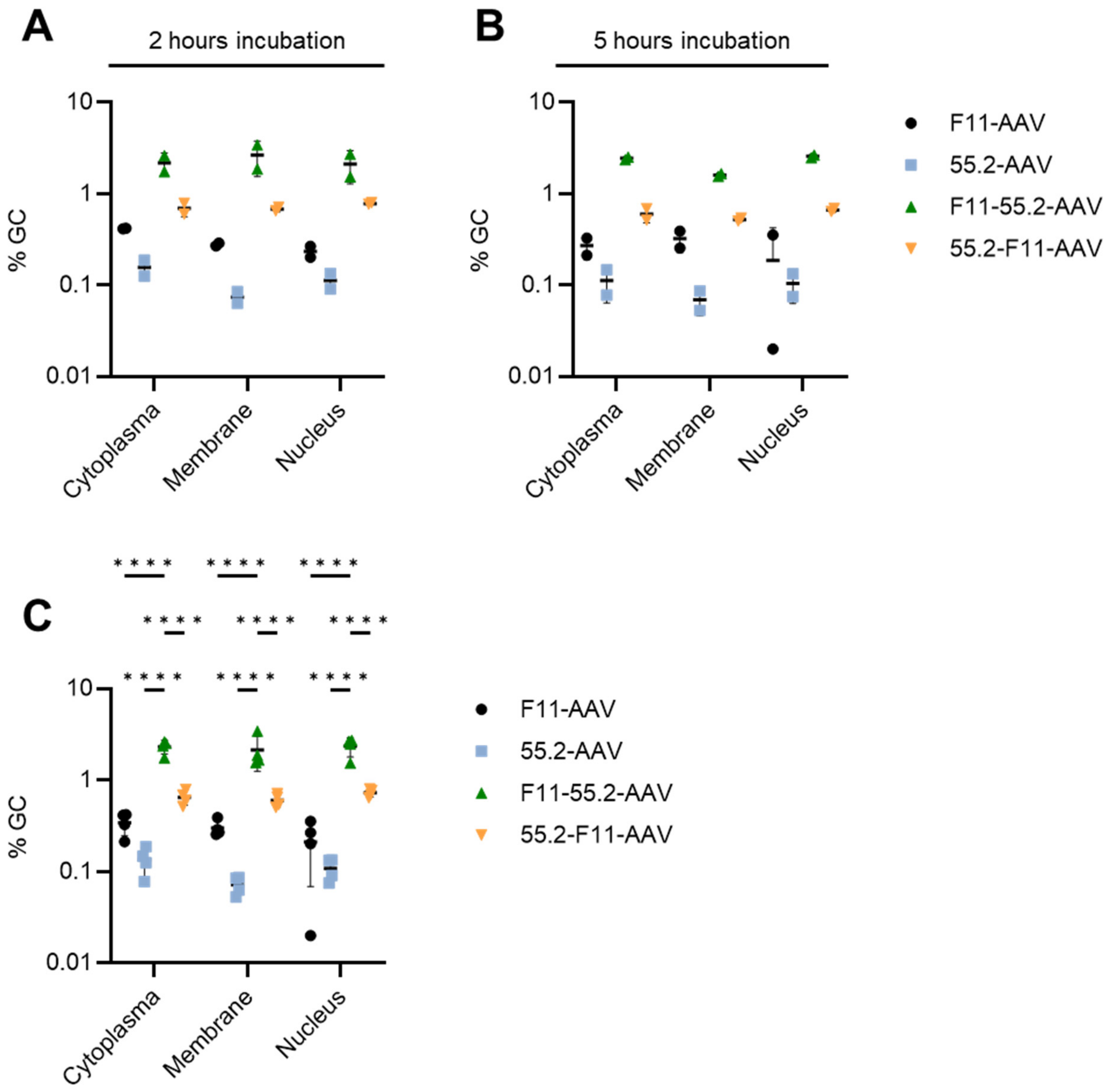

Figure 40: **Bispecific AAVs are more efficiently taken up by CD4+/CD32a+ cells compared to monospecific AAV.**
The indicated AAV were incubated with SupT1-CD4/CD32a cells and GFP sequences in subcellular fractions from cytosol, membrane and nucleus were quantified by qPCR. The percentage of input GC ($3x10^{10}$ GC) after incubation for **A)** 2 and **B)** 5 hours are shown. **C)** Data from both time points were combined. Bars represent means of four independent experiments and the STD is reported. Statistical differences were determined by two-way ANOVA, p-value **** < 0.0001. **C** is adapted from (Theuerkauf et al. 2023).

4.7 Vector tropism in whole blood and primary cells

So far, SupT1 cells served as target cell lines in the previous experiments to determine the specificities of the receptor-targeted AAV. In the next steps, the vector tropism should be verified on primary cells expressing the targeted receptors. First, primary PBMC were mixed with vector particles to assess the binding to CD4 T cells and monocytes (CD4+/CD32a+). Secondly, transduction efficiencies on activated primary T cells were determined. Finally, vectors were added to human whole blood and their ability to transduce the primary cells as well as the spiked SupT1 cells was analyzed.

4.7.1 Binding to PBMC

To assess the binding of the vector particles to primary cells, $5x10^5$ GC per cell were incubated with isolated human PBMC. The cell type and the number of vector-bound cells were determined by flow cytometry using antibodies against the AAV capsid (A20) and against marker of monocytes (CD14+) and CD4 T cells (CD3+ CD4+) (see Figure 41).

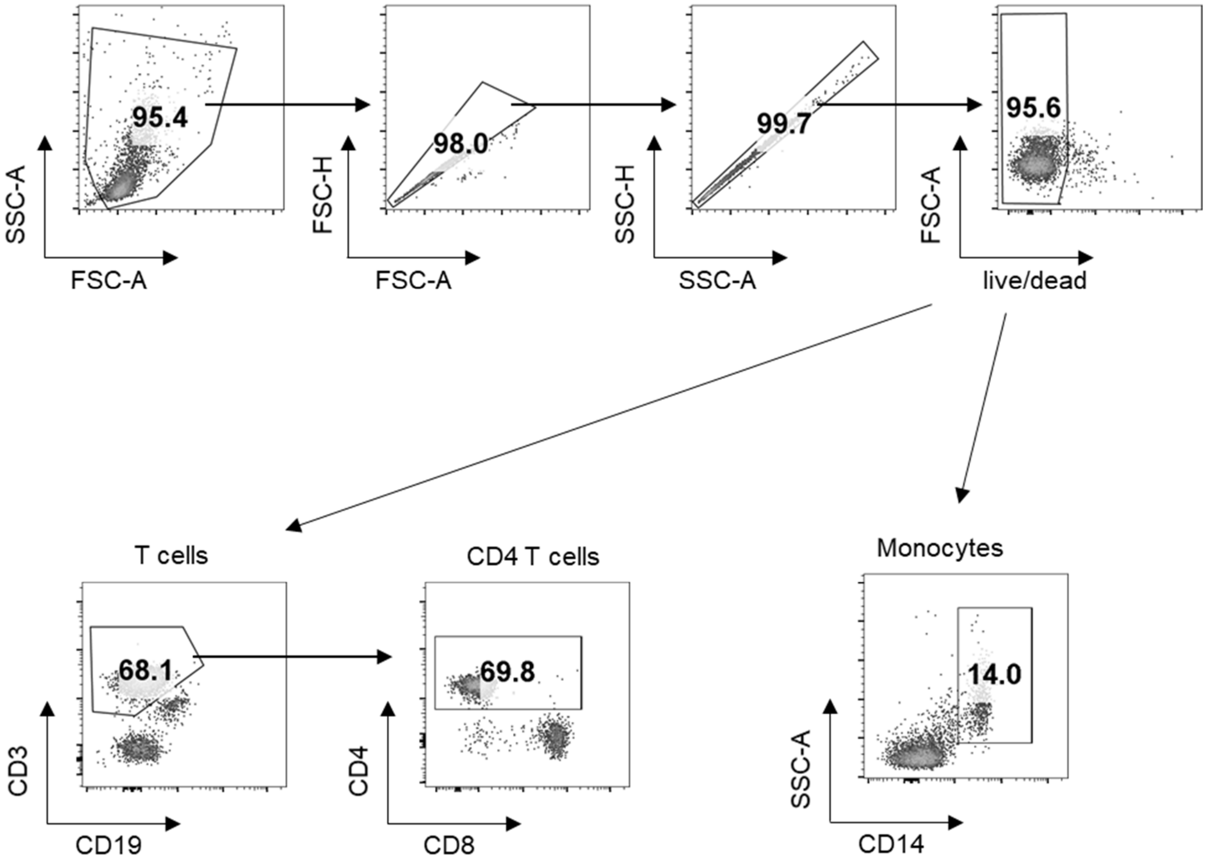

Figure 41: **Gating strategy to identify monocytes and CD4 T cells.**
Viable, single cells were identified in forward (FSC), sideward scatter (SSC) and by staining with a viability dye (upper row). Then, CD4 T cells were identified by CD3 expression (bottom left) followed by CD4 expression (bottom middle). Monocytes were identified by CD14 expression (bottom right). Gating strategy is shown exemplarily for one sample containing cells without vector particles. Figure is adapted from (Theuerkauf et al. 2023).

As expected, the bispecific vectors showed higher vector signals on monocytes, which express CD32a (Alevy et al. 1992) and show dim CD4 expression (Filion et al. 1990), compared to the monospecific vectors (see Figure 42A-B). According to the expression pattern of the targeted receptors on monocytes, F11-AAV showed higher binding to monocytes than 55.2-AAV. Since CD32a expression on CD4 T cells is rare (Darcis et al. 2020; Riechert et al. 2023), binding of F11-AAV was not expected and demonstrated by the flow cytometry data. 55.2-AAV and F11-55.2-AAV bound CD4 T cells with similar efficiencies. Interestingly, a significantly higher amount of 55.2-F11-AAV than of F11-55.2-AAV bound CD4 T cells. A similar trend was seen in the titration of SupT1-CD4 cells showing elevated titer compared to 55.2-AAV and F11-55.2-AAV (Figure 31 and Table 1). Furthermore, while with the applied vector doses, both bispecific vectors bound all CD4 T cells and monocytes, 55.2-AAV only attached to 39.1% and F11-AAV to 78.7% of all monocytes (see Figure 42C). These data prove that the engineered vector particles efficiently bind primary cells and the determined specificities are in line with the tropism as investigated on the SupT1 cell lines.

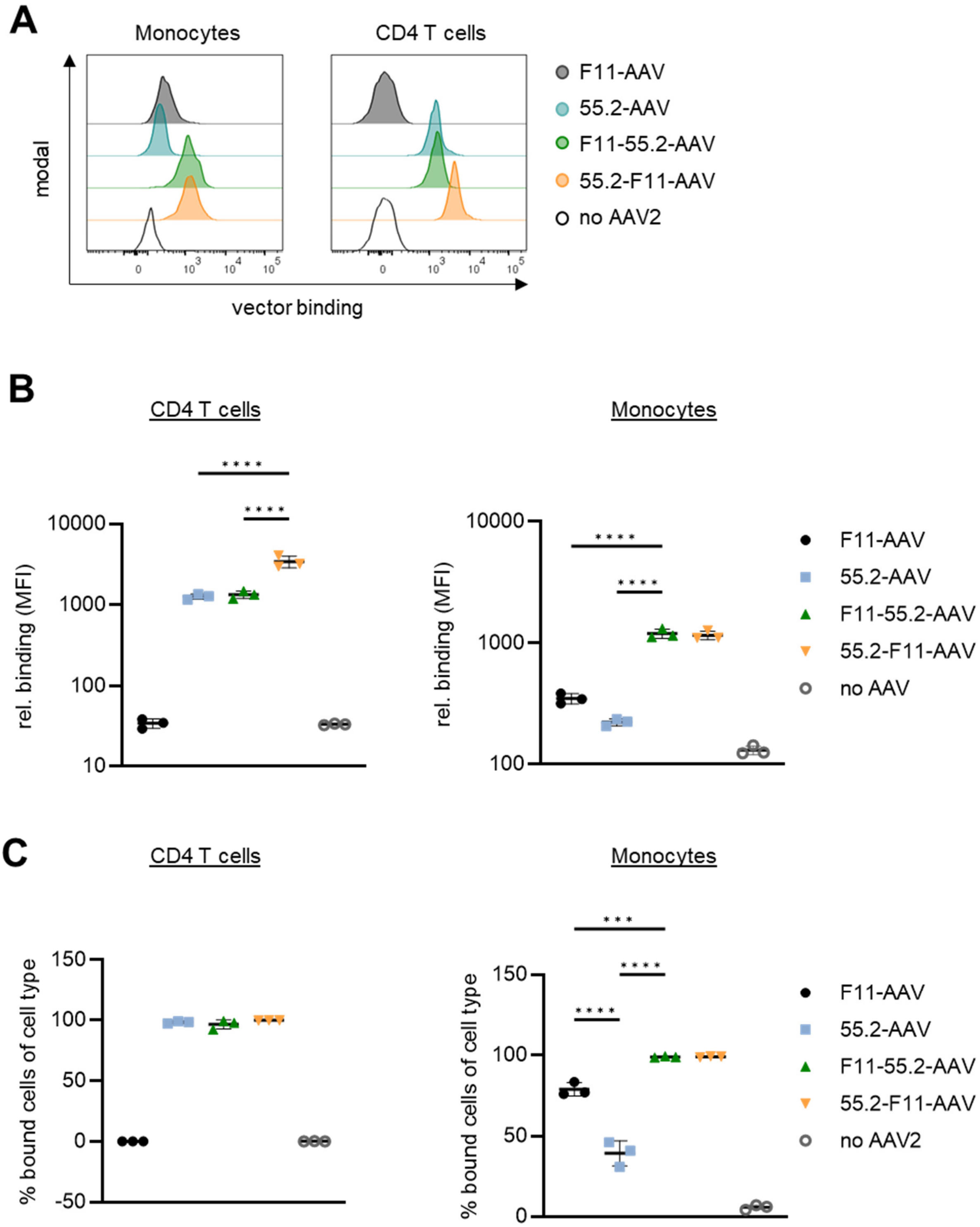

Figure 42: **Vector distribution on primary cells.**

The indicated vectors or medium as control (no AAV2) were incubated with isolated primary cells at 5x10^5 GC/cell for 2 hours. Bound cells were identified by a capsid-specific antibody staining. **A)** Representative histogram plots showing the MFI of capsid-specific signals on monocytes and CD4 T cells for one donor. **B)** MFI of capsid signal on monocytes and CD4 T cells for three donors. **C)** Percentages of bound CD4 T cells and monocytes. Bars represent means of three independent experiments and the STD is reported. Statistical differences were determined by one-way ANOVA, p-value **** < 0.0001, p-value *** = 0.0001-0.001. **A** and **B** are adapted from (Theuerkauf et al. 2023).

4.7.2 Transduction of activated T cells

The transduction efficiencies of the AAVs were further determined on activated T cells. For that, vector particles were serially diluted and added to activated PBMC. GFP expression in CD4 T cells was analyzed three days after transduction (see Figure 43). This data set was kindly provided by Burak Demircan (Paul-Ehrlich-Institut).

All CD4 targeted AAVs showed efficient transduction of CD4 T cells and there were less than 1.2% off-target cells transduced. When 2.5x10^5 GC per cell were used, 55.2-AAV transduced 22.2% and F11-55.2-AAV 23.3% of the CD4 cells. However, there was a trend for a higher transduction efficiency with 55.2-F11-AAV reaching 31.8%. Although this difference was non-significant, it was in line with the binding experiment above showing better attachment of 55.2-F11-AAV to CD4 T cells. Importantly, AAV2 wild type was inefficient in transducing primary cells showing only 1.6% GFP-expressing cells. Overall, re-targeting of AAV using DARPins allowed efficient transduction of primary CD4 T cells, while transduction with AAV2 wild type did only show low efficiencies.

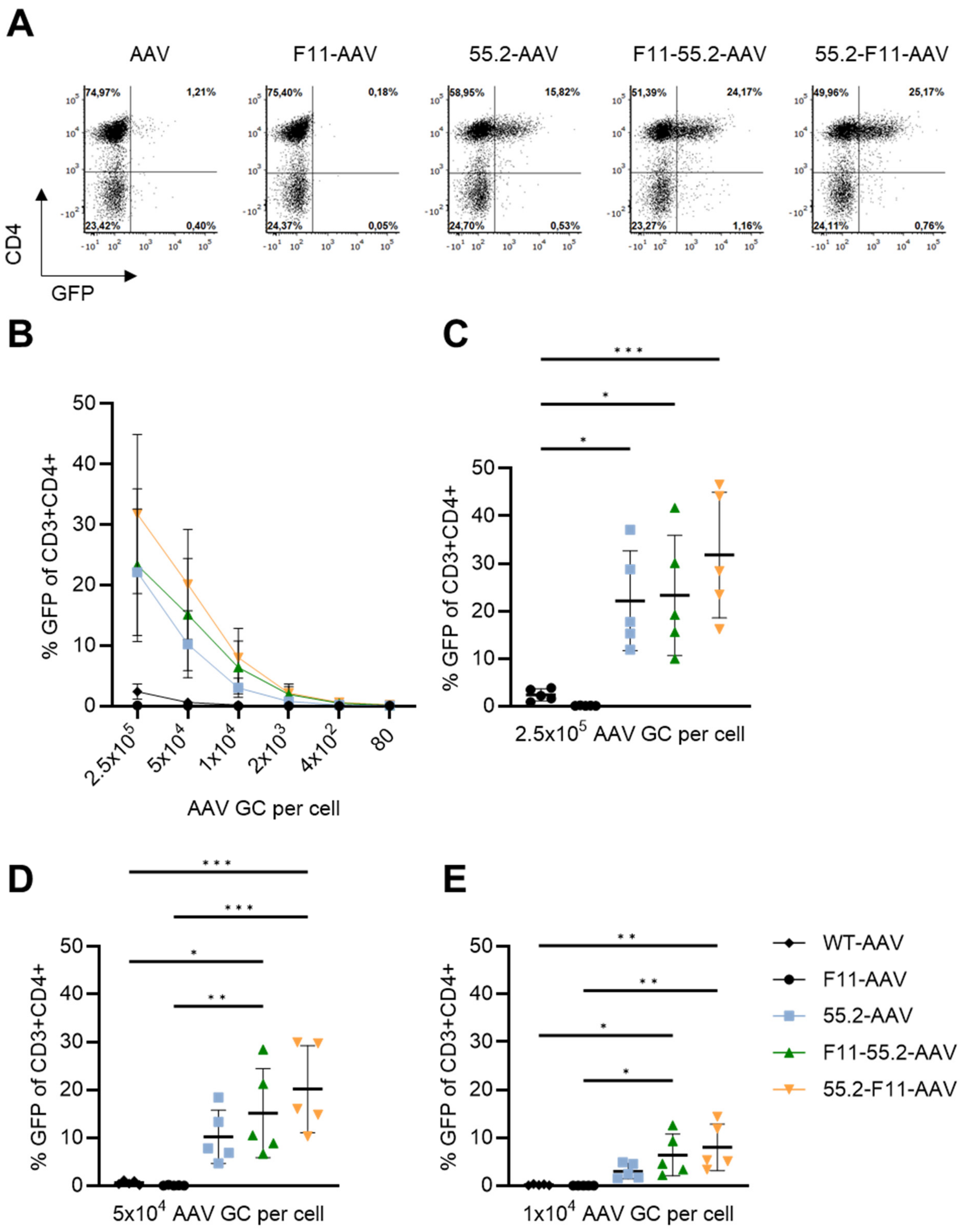

Figure 43: **Transduction of primary cells.**

The indicated amounts of AAV GC were added to activated PBMC and GFP expression was analyzed three days post transduction. **A)** Representative flow cytometry plots showing CD4 expression versus GFP expression after transduction with 5x10^4 AAV GC/cell. **B)** GFP expression in CD3+CD4+ T cells after vector titration. **C-E)** Transduction efficiencies of the indicated vectors at vector dosages **C)** 2.5x10^5 GC/cell, **D)** 5x10^4 GC/cell and **E)** 1x10^4 GC/cell. Bars represent means of five donors and the STD is reported. Statistical differences were determined by one-way ANOVA, p-value *** = 0.0001-0.001, p-value ** = 0.001-0.01, p-value * = 0.01-0.05. Experiments were performed by Burak Demircan (Paul-Ehrlich-Institut).

4.7.3 Transduction of cells in whole blood

Building on the cell-selective binding and transduction experiments on primary cells, the efficiencies of the vectors in human whole blood was analyzed next. Since the number of CD32a-expressing CD4 T cells are rare, 1x10^5 SupT1-CD4/CD32a were spiked into 400 µl whole blood. After six hours of incubation, PBMC and SupT1 cells were isolated and activated. Three days later, GFP expression in primary and SupT1 cells was analyzed. SupT1 cells were identified by the expression of CD32a and a dim CD8 signal (see Figure 44).

For these experiments, we first started with a high number of 4x10^9 GCs (see Figure 45A). At the time point of analysis, all CD4-targeted AAV showed selective transduction of only CD4 T cells. 55.2-AAV and F11-55.2-AAV had similar transduction efficiencies of around 13% GFP expressing CD4 T cells. Again, 55.2-F11-AAV resulted in an increased transduction efficiency of 15.5%. As expected, F11-AAV did not transduce primary T cells in this setting. Notably, both bispecific AAVs showed a highly efficient transduction of the spiked SupT1 cells reaching about 85% of the cells (see Figure 45B). Compared to the bispecific vectors, 55.2-AAV showed decreased transduction efficiency and yielded 59% of GFP-expressing SupT1 cells. To our surprise, transduction with F11-AAV resulted in only 0.3% of the SupT1 cells expressing GFP. This might be related to the high abundance of platelets present in whole blood which are highly positive for CD32a. Thus, F11-AAV had been absorbed by platelets and therefore did not reach the SupT1 cells. Taken together, CD4 targeted vectors showed efficient transduction of primary CD4 T cells in the whole blood assay. Additionally, bispecific AAVs also showed in this experimental setup preferable transduction of the spiked SupT1-CD4/CD32a cells.

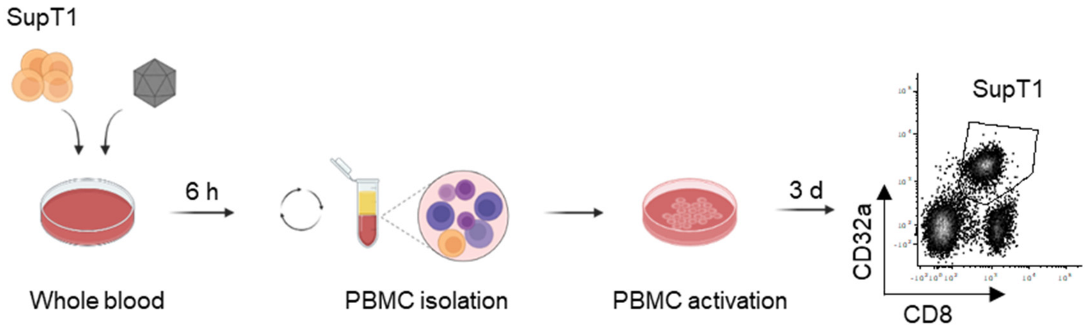

Figure 44: **Whole blood transduction assay.**
1x10^5 SupT1-CD4/CD32a cells were spiked into 400 µl whole blood and AAV vector were added. After 6 hours of incubation mononuclear cells (PBMC and SupT1) were isolated by gradient centrifugation. Cells were then activated for three days and GFP expression was analyzed by flow cytometry. SupT1 cells were identified by gating for CD32a and CD8 expression. Figure is adapted from (Theuerkauf et al. 2023).

After these initial results, the whole blood assay was repeated with a lower dose of 8x10^8 GCs and GFP expression within SupT1 cells was analyzed from three different donors. As seen before, SupT1 cells were most efficiently transduced by the bispecific vectors compared to the monospecific vectors. This time, F11-55.2-AAV showed a significant higher transduction efficiency than 55.2-F11-AAV, indicating that the vector doses used in the initial experiment were too high to differentiate the gene delivery rates between the bispecific vectors. Overall, under this ‘in vivo’-like conditions, bispecific AAV vectors efficiently reached the target cells. Furthermore, the relevance of the bispecific configuration was again highlighted, since F11-AAV was not able to transduce CD32a-expressing SupT1 cells.

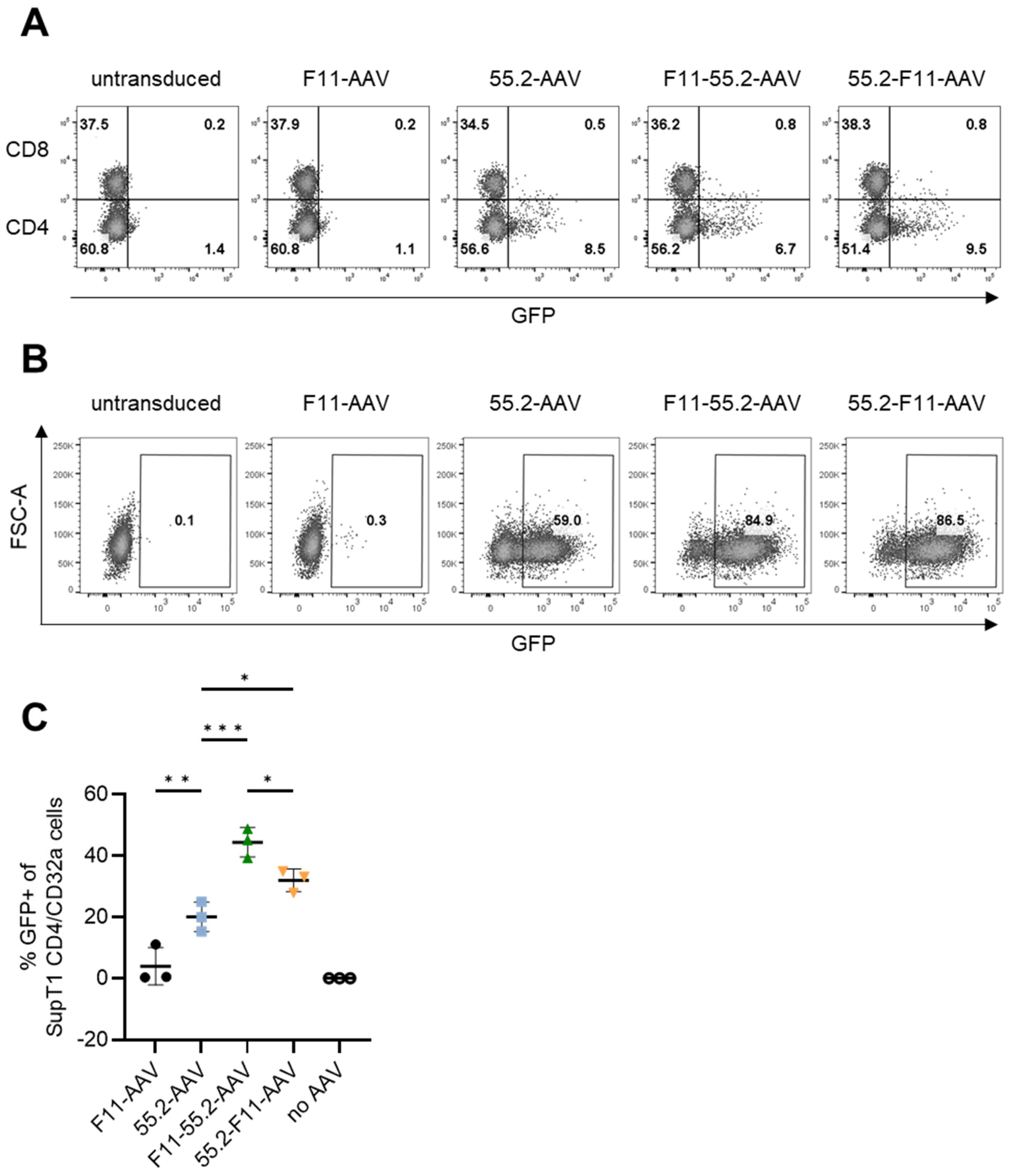

Figure 45: **Transduction efficiency of targeted AAV in whole blood.**
The indicated vectors were added to 400 µl whole blood spiked with SupT1-CD4/CD32a cells. GFP expression in primary and SupT1 cells was analyzed three days after vector addition. **A-B)** Transduction of **A)** primary T cells and **B)** SupT1 cells using 4x10^9 GCs per 400 µl whole blood. **C)** GFP expression in SupT1 cells after transduction with 8x10^8 GCs per 400 µl whole blood. Bars represent means of three independent experiments and the STD is reported. Statistical differences were determined by one-way

ANOVA, p-value *** = 0.0001-0.001, p-value ** = 0.001-0.01, p-value * = 0.01-0.05. **C** is adapted from (Theuerkauf et al. 2023).

4.8 *In vivo* gene delivery

4.8.1 Selective *in vivo* gene delivery by F11-AAV in NSG mice

The preceding chapter demonstrated the selectivity of the novel vectors *in vitro* and validated their distinct transduction profiles. Consequently, the subsequent step involved analyzing the vector selectivity *in vivo*. To obtain initial ideas about targeting human CD32a *in vivo*, NOD.Cg-Prkdc^{scid} Il2rg^{tm1Wjl} (NSG) mice were injected intravenously (i.v.) with a cell mixture of SupT1-CD4/CD32a and CD32a-negative Hut78 cells (see Figure 46). After seven days of cell engraftment, 2x10^{11} GC of F11-AAV were administered i.v. and mice were sacrificed three and seven days after vector injection. On the day of analysis, cells from bone marrow, blood, spleen and liver were isolated and single cell suspensions were stained for flow cytometry analysis.

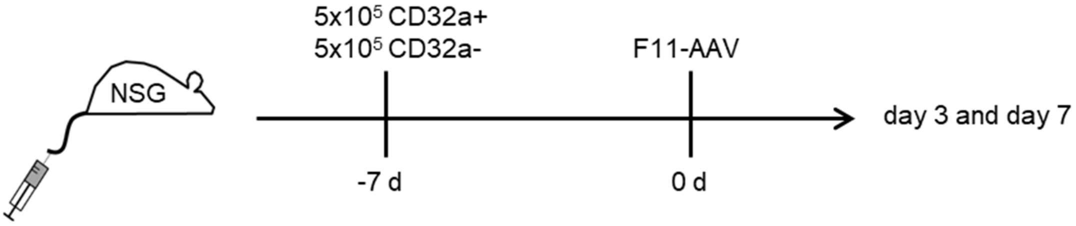

Figure 46: **Experimental setup to assess *in vivo* gene delivery of F11-AAV in SupT1-CD4/CD32a cell-engrafted NSG mice.**
NSG mice were injected i.v. with a cell mix of 5x10^5 SupT1-CD4/CD32a and 5x10^5 CD32a-negativ Hut78 cells. Seven days after cell engraftment, 2x10^{11} F11-AAV GC were injected i.v.. Three and seven days after vector injection, mice were sacrificed and cells from blood, spleen, bone marrow and liver were analyzed for GFP expression by flow cytometry. Figure is adapted from (Theuerkauf et al. 2023).

Using the CD45 marker for human cells, most of the engrafted cells were identified in the bone marrow. As expected, the cell number of CD45+ cells raised from 1.2% on day three to 23.9% on day seven in bone marrow indicating that the injected human cells proliferated within NSG mice (see Figure 47).

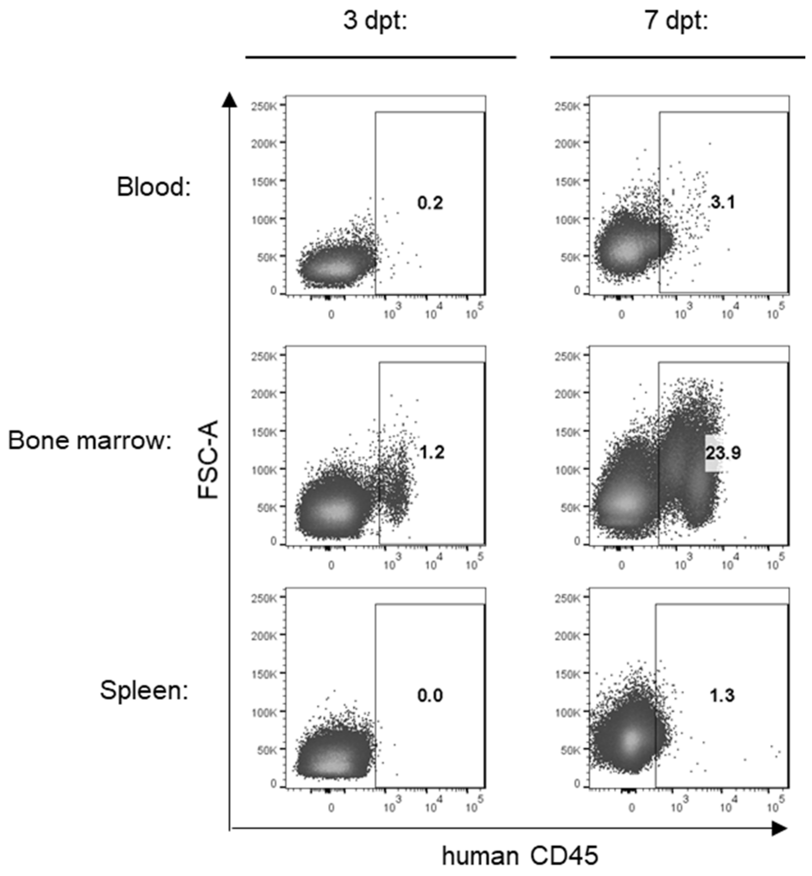

Figure 47: **Cell engraftment within NSG mice injected with a mix of SupT1-CD4/CD32a and HuT78 cells.**
Isolated cells from mice sacrificed on day three (left) and seven (right) after vector administration, were stained for human CD45 and analyzed by flow cytometry.

The flow cytometry analysis from bone marrow cells revealed a high transduction efficiency of CD32a-expressing cells reaching 55.5% GFP expression in vector treated mice. This signal decreased on day seven to 9.6% most likely due to the non-integrating, episomal persistence of the AAV genome. Taking into account that the number of human cells in bone marrow increased 20-fold on day seven, the reduction of GFP+ cells was expected. Furthermore, off-target transduction was close to background levels, indicating that F11-AAV retained its specificity *in vivo*. Additionally, the targeting coefficient was calculated as a ratio of CD32a+ GFP+ over CD32a- GFP+ cells and revealed an on-target efficiency of 29.6 on day three and 15.9 on day seven. Importantly, F11-AAV did not result in any detectable gene transfer in liver three days post injection (Figure 48D). These results demonstrate a highly efficient and selective transduction of F11-AAV *in vivo*.

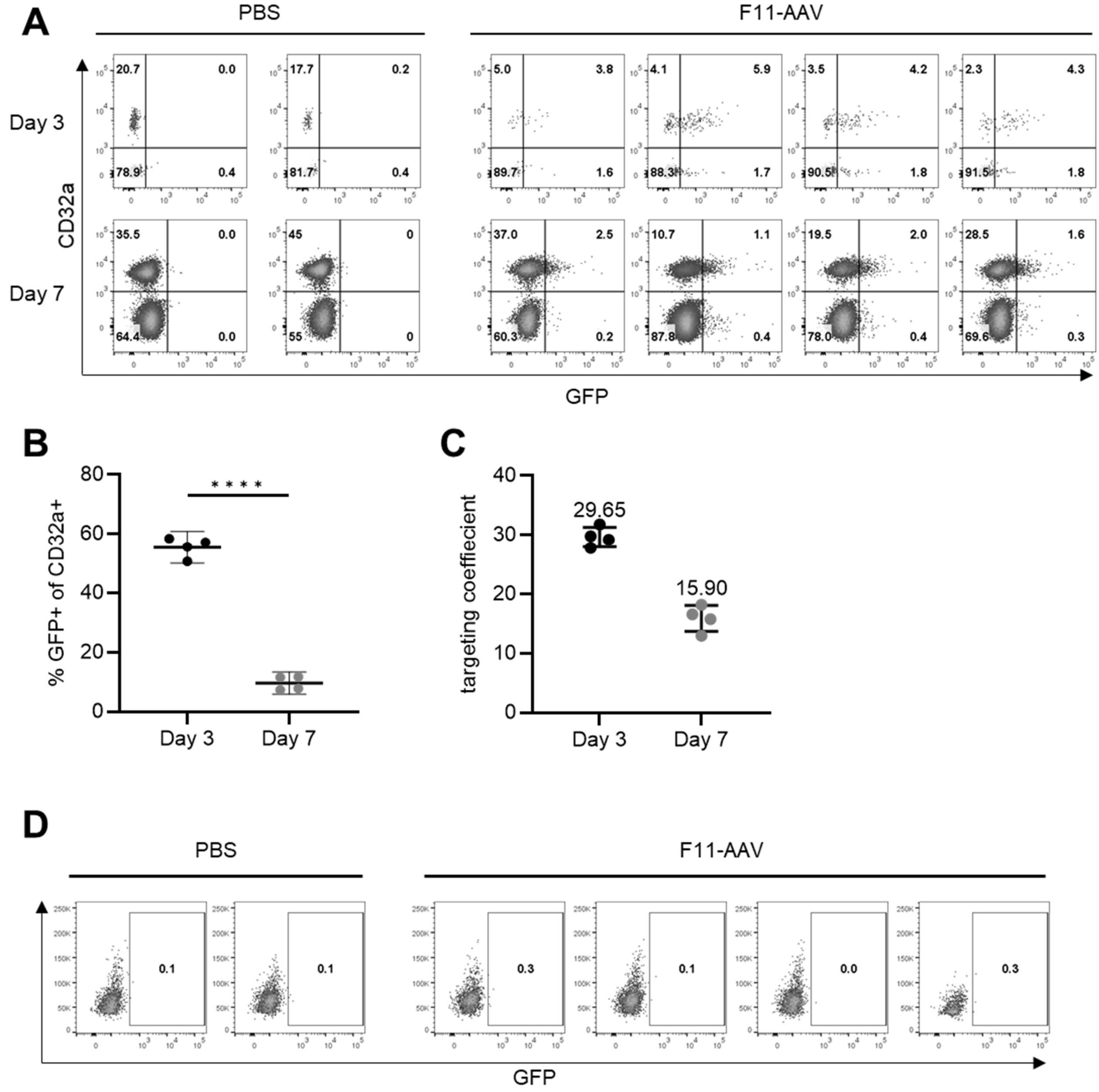

Figure 48: **Highly selective and efficient transduction of CD32a+ cells by F11-AAV *in vivo*.**
A) Bone marrow cells isolated from SupT1-CD4/CD32a and HuT78-transplanted NSG mice three (above) and seven (bottom) days after F11-AAV injection. Shown is the GFP expression among CD32a-expressing cells in PBS- (left) and vector-injected (right) mice. **B)** Percentage of GFP+ cells among CD32a-expressing cells three and seven days after vector injection. Bars represent means of four mice. Statistical differences were calculated by unpaired t-test and the standard deviation is reported, p-value **** < 0.0001. **C)** The targeting coefficient for F11-AAV was determined by calculating the ratio of GFP+ cells among CD32a-positive and CD32a-negative cells three and seven days after vector injection. **D)** GFP expression in liver cells of PBS- and vector-injected mice. Figure is adapted from (Theuerkauf et al. 2023).

4.8.2 *In vivo* biodistribution of bispecific AAVs

Following the highly efficient and selective *in vivo* gene delivery of F11-AAV, the biodistribution of the bispecific AAVs was investigated. For this purpose, NSG mice were transplanted with a cell mix of 1x10^6 SupT1-CD4, 1x10^6 SupT1-CD32a and 1x10^6 SupT1-CD4/CD32a cells i.v. (see Figure 49). Thirteen days after cell injection, 2x10^{11} GC of mono- and bispecific vectors were administered i.v.. Additionally, a mix of $2x10^{11}$ F11-AAV and $2x10^{11}$ 55.2-AAV were injected and animals were sacrificed three days after vector application.

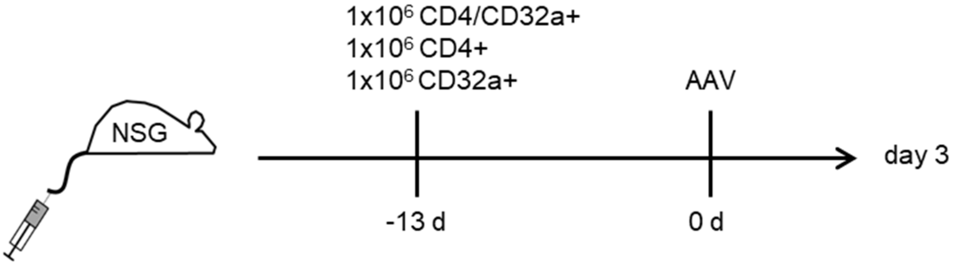

Figure 49: **Experimental setup to analyze the *in vivo* biodistribution of bispecific AAVs in SupT1 cell-engrafted NSG mice.**
NSG mice were i.v. injected with a cell mix of $1x10^6$ SupT1-CD4/CD32a, $1x10^6$ SupT1-CD4 and $1x10^6$ SupT1-CD32a cells. Thirteen days after cell injection, $2x10^{11}$ GC of F11-AAV, 55.2-AAV, F11-55.2-AAV, 55.2-F11-AAV and a combination of F11-AAV and 55.2-AAV were administered i.v.. Mice were sacrificed three days after vector injection. Figure is adapted from (Theuerkauf et al. 2023).

SupT1 cells received from the bone marrow were identified by the expression of CD4 and CD32a in flow cytometry (see Figure 50).

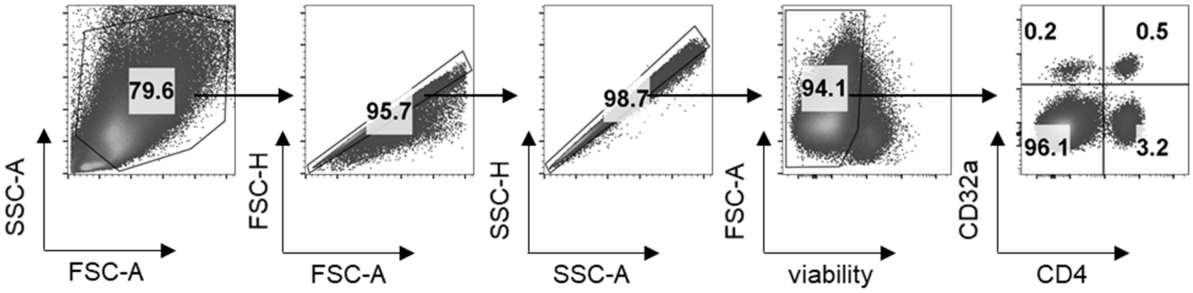

Figure 50: **Gating strategy for the identification of SupT1 cells extracted from bone marrow.**
Viable, single cells were identified in forward (FSC), sideward scatter (SSC) and by staining with a viability dye. SupT1 cell populations were then identified and discriminated by CD4 and CD32a expression. Gating strategy is shown exemplarily for one mouse injected with PBS. Figure is adapted from (Theuerkauf et al. 2023).

Although the SupT1 cells were injected at equal cell numbers, the cells engrafted differently in the bone marrow. SupT1-CD4 cells were most abundant (2.04% of all cells), followed by SupT1-CD4/CD32a cells (0.21% of all cells) and SupT1-CD32a cells (0.04% of all cells). Due to the very low number of human cells in some mice, they were excluded from statistical analysis (marked in red in Figure 51).

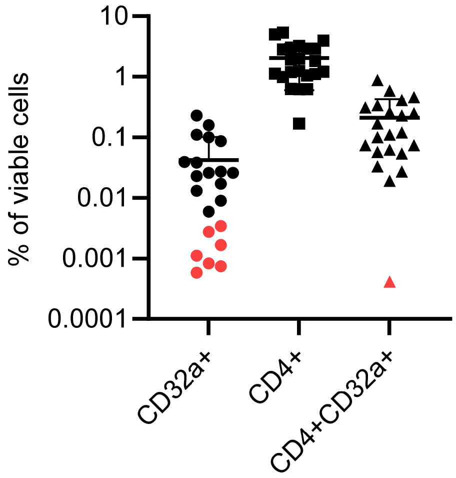

Figure 51: **Engraftment of SupT1 cell lines in the bone marrow of NSG mice.**
Percentages of SupT1-CD32a, SupT1-CD4 and SupT1-CD4/CD32a among all viable cells in the bone marrow of NSG mice analyzed sixteen days after cell injection by flow cytometry. Figure is adapted from (Theuerkauf et al. 2023).

The highest gene delivery rate was determined for F11-55.2-AAV reaching 64.5% of SupT1-CD4/CD32a cells *in vivo* (see Figure 52). This was significantly higher than what was reached by F11-AAV (17.1%) and 55.2-AAV (27.8%) and even the combination of both (mix, 43.7%). This was accompanied by a significantly increased MFI of GFP in CD4+/CD32a+ cells. Notably, the monospecific vectors and the mix group showed higher transduction efficiencies on the cell lines expressing only one of the two receptors compared to the GFP expression in SupT1-CD47CD32a cells. In detail, 55.2-AAV and the mix group transduced 38.4% and 43.4% of the SupT1-CD4 cells, respectively, which was significantly higher than the transduction efficiency of F11-55.2-AAV on these cells (19%). Consequently, F11-55.2-AAV showed a 3.4-fold relative preference for CD4+/CD32a+ cells over CD4+ cells. Furthermore, F11-AAV and both monospecific vectors combined showed transduction efficiencies of 35.7% and 36.4% on SupT1 CD32a cells. F11-55.2 transduced only 4% of the CD32a+ cells and showed a 16.5-fold preference for CD4+/CD32a+ cells. Surprisingly, 55.2-F11-AAV showed substantially less transduction efficiency on all injected cell lines, which was below the levels of the monospecific vectors. Taken together, F11-55.2-AAV transduced the CD4/CD32a cells high efficiently *in vivo*, while the monospecific vectors preferred the transduction of cells expressing only one of the receptors. Remarkably, the high transduction efficiency on double-positive cells was not reached by the combination of both monospecific vectors.

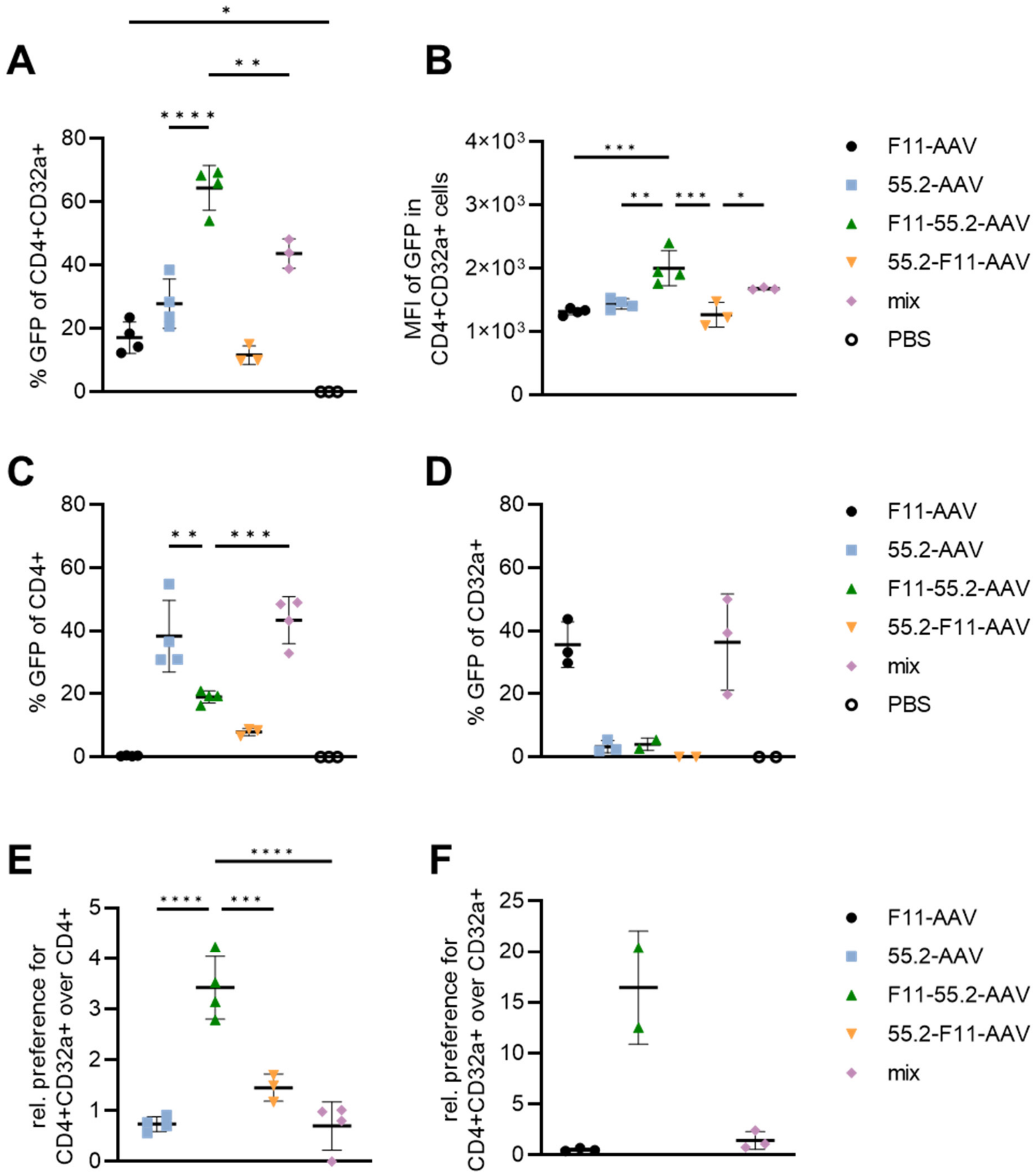

Figure 52: **Bispecific AAVs transduce CD4+CD32a+ cells more efficiently than a mix of F11-AAV and 55.2-AAV *in vivo*.**
SupT1 cell-transplanted NSG mice were analyzed for GFP expression in isolated bone marrow cells three days after injection with the indicated vectors, a mix of F11-AAV and 55.2-AAV or PBS. **A)** GFP expression in SupT1-CD4/CD32a cells. **B)** MFI of GFP in SupT1-CD4/CD32a cells. **C-D)** GFP expression in **C)** SupT1-CD4 and **D)** SupT1-CD32a cells. **E-F)** Ratio of percent GFP expression in SupT1-CD4/CD32a cells over **E)** SupT1-CD4 and over **F)** SupT1-CD32a. Statistical differences were determined by one-way ANOVA and the standard deviation is reported, p-value **** < 0.0001, p-value *** = 0.0001-0.001, p-value ** = 0.001-0.01, p-value * = 0.01-0.05.
N=4 (F11-AAV, 55.2-AAV, F11-55.2-AAV, mix) and n=3 (55.2-F11-AAV, PBS) in **A**, **B,** **C**. N=3 (F11-AAV, 55.2-AAV, mix) and n=2 (F11-55.2-AAV, 55.2-F11-AAV, PBS) in **D**. N=4 (55.2-AAV, F11-55.2-AAV, mix) and n=3 (55.2-F11-AAV) in **E**. N=3 (F11-AAV, mix) and n=2 (F11-55.2-AAV) in **F.** Figure is adapted from (Theuerkauf et al. 2023).

4.9 Cas9 delivery by targeted AAVs protects against HIV replication

Finally, targeted AAV were used to deliver spCas9 into HIV infected SupT1 cells to inhibit virus replication. For this purpose, the Cas9 encoding gene was co-delivered with the coding sequence of three gRNAs targeting the HIV-1 *LTR* and *gag* genes (see Figure 26 for the plasmid design and Figure 53 for the target region on the HIV-1 provirus). Furthermore, the expression of each of the gRNAs was driven by different promoters to minimize the risk of promoter methylation and to avoid homologous sequence on the plasmid which might result in strong secondary structure of the nucleic acids. This combination of gRNAs was validated in a yet unpublished study showing efficient HIV eradication and the transfer plasmids were kindly provided by Dirk Grimm (Heidelberg). For these experiments, the vector particles were produced, characterized and handed over to Elena Herrera-Carrillo and Mariano Molina (Amsterdam, Netherlands) for the HIV inhibition experiment.

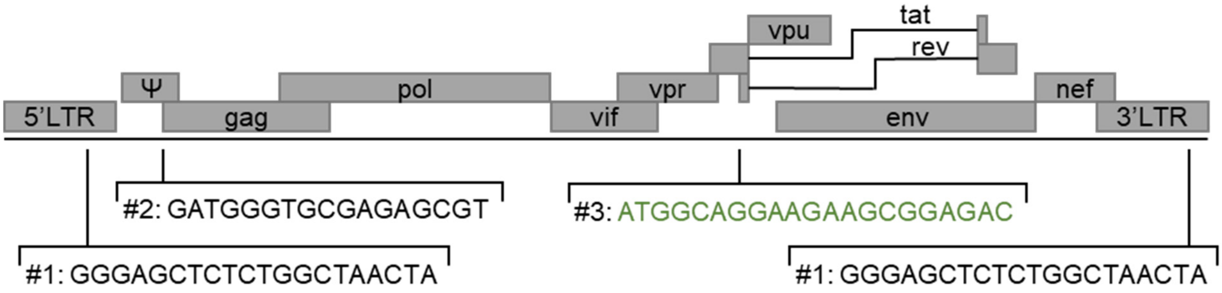

Figure 53: **Schematic illustration of the gRNA binding sites on the HIV-1 provirus.**
gRNA sequence #3 illustrated in green was used in the F11-55.2-AAV-Cas9-gRNA vector, whereas gRNA #1 and #2 were delivered by the F11-AAV-gRNA vector.

Due to the size restrains of the AAV transgenes, the nuclease and the gRNAs were separately packaged into two AAV capsids. Thus, both capsids had to transduce the same infected cell to complement the HIV-guided Cas9 (see Figure 54).

Following this approach, the F11-AAV capsid was assessed to deliver Cas9 as well as the gRNAs into infected SupT1 cells. For that, 2.5x10^5 SupT1-CD4/CD32a cells were transduced with in total 3.6x10^5 GC of F11-AAV-Cas9 and F11-AAV-gRNA. Two hours post-transduction cells were infected with HIV-1 at a MOI of 0.02. The amount of inter- and extracellular HIV capsids twelve days after infection were determined by flow cytometry and ELISA using antibodies against the HIV-capsid protein p24, respectively.

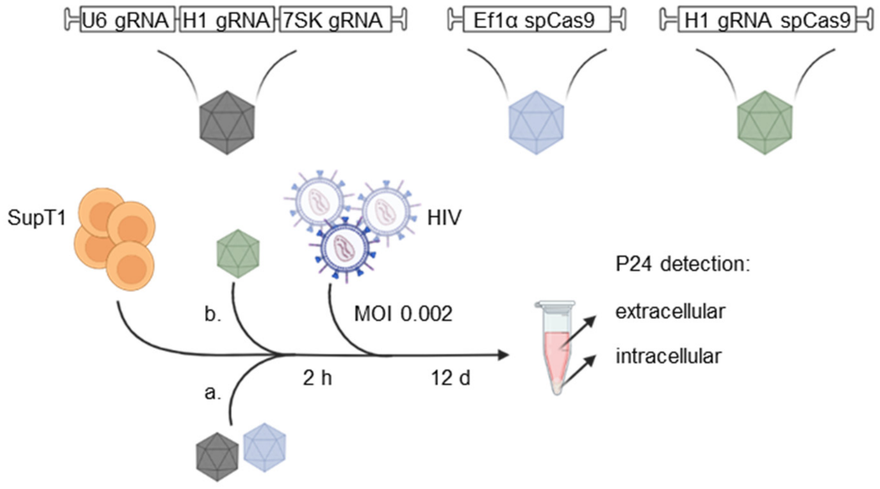

Figure 54: **Experimental setup: Cas9 delivery by F11-AAV and F11-55.2-AAV inhibit HIV replication.**
Two approaches were used to inhibit HIV replication in SupT1-CD4/CD32a cells. In a) SupT1-CD4/CD32a cells were incubated with a combination of two F11-AAVs (in total $3.6x10^5$ GC/cell) transferring *Cas9* (shown in blue) and the *gRNA*s (shown in black). In b) cells were treated with F11-55.2-AAV ($3.6x10^5$ GC/cell) transferring the ‘all-in-one’ cassette (symbolized in green). Two hours post transduction, cells were infected with HIV at a MOI of 0.02. The p24 amounts were subsequently assessed in the supernatant by ELISA and intracellular staining by flow cytometry twelve days after infection. Figure is adapted from (Theuerkauf et al. 2023).

On average, 50% of the infected cells showed intracellular p24 signal and a clear signal was obtained from the supernatant twelve days post infection (see Figure 55). This signal completely vanished and reached background level when the infected cells were incubated with both AAVs transferring the *Cas9* and *gRNAs* demonstrating effective inhibition of HIV replication. Importantly, when infected cells were only treated with F11-AAV-Cas9, the p24 signal remained at high levels similar to the positive controls proofing that the Cas9 itself was not interfering with HIV replication.

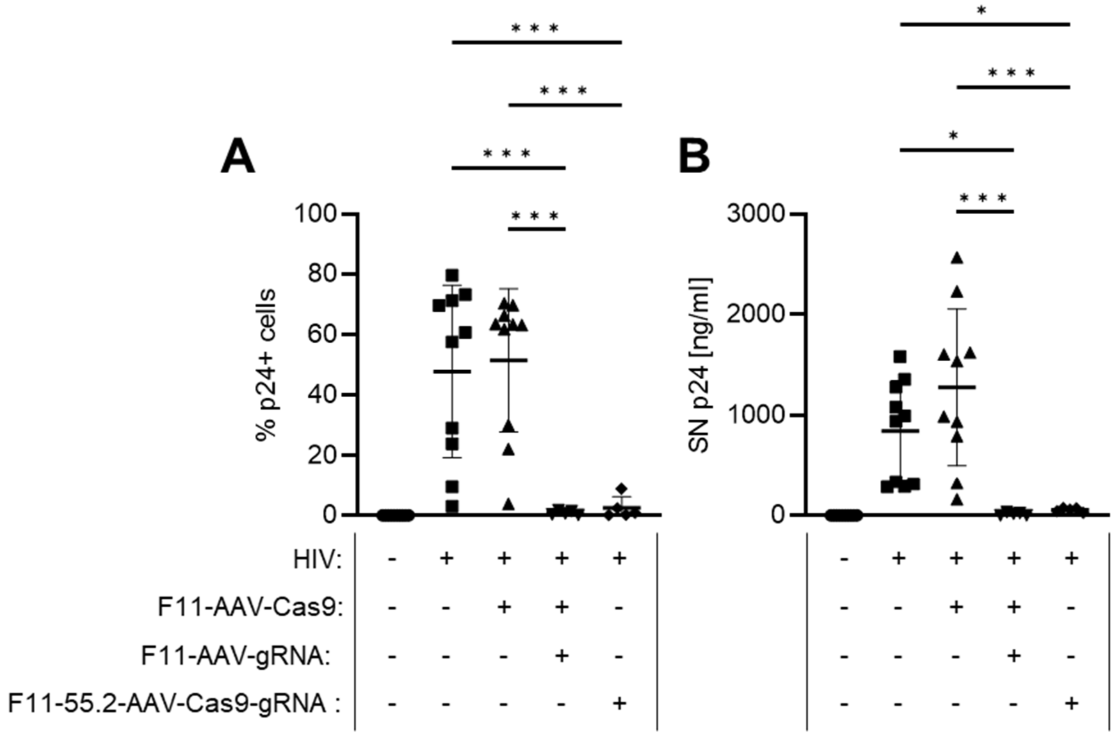

Figure 55: **spCas9 delivered by F11-AAV and F11-55.2-AAV protects against HIV infection.** **A)** Percentage of p24-positive SupT1-CD4/CD32a cells after treatment with the indicated AAV and HIV. **B)** P24 concentration in the supernatant (SN) of cells twelve days after infection. **A-B)** Untreated cells served as control. Bars in the groups untreated, HIV infected and HIV infected + F11-AAV-Cas9 treated represent ten technical replicates. Bars for the groups treated with F11-AAV-gRNA and F11-55.2-AAV-Cas9-gRNA represent five technical replicates. Statistical differences were calculated by one-way ANOVA, p-value *** = 0.0001-0.001, p-value * = 0.01-0.05. The data was generated by Elena Herrera-Carrillo and Mariano Molina at the University of Amsterdam (Netherlands). Figure is adapted from (Theuerkauf et al. 2023).

Then, the anti-HIV strategy was transferred to F11-55.2-AAV. The previous results clearly demonstrate that F11-55.2-AAV has superior gene delivery rates into cells expressing both of the HIV reservoir markers, CD4 and CD32a. Hence, this capsid variant might be the most suitable for genetically modifying reservoir cells. Additionally, although the split cassettes allow for packaging into AAVs, the efficiency for gene editing is lower compared to using a single capsid that packages all essential components (‘all-in-one’ approach) (Ibraheim et al. 2021). To generate a transfer plasmid encoding the Cas9 and one gRNA (Wang et al. 2016), whose size allows for AAV packaging, we exchanged the EF1α- promoter against the recently described miniature H1 promoter. This promoter is only 99 base pairs in size and allows for the transcription of *gRNAs* and *Cas9* by combining RNA polymerase activity II and III (see Figure 26 and Figure 53). This construct was then packaged resulting in the vector F11-55.2-AAV-Cas9-gRNA. Following the workflow as described above, SupT1 cells were transduced with $3.6x10^5$ GC of F11-55.2-AAV-Cas9-gRNA and anti-HIV activity was assessed twelve days after infection with HIV.

Similar to the combined treatment of F11-AAV-Cas9 and F11-AAV-gRNA, intracellular and extracellular p24 signals reached background levels indicating the inhibition of HIV (see Figure

55). Taken together, these results demonstrate the successful delivery of endonuclease to HIV infected cells using the established AAVs targeted against markers of the HIV reservoirs. Additionally, the delivered cassettes showed efficient inhibition of the HIV replication.

5 Discussion

Discussion of Part A: Fusion activity of the SARS-CoV-2 spike protein

5.1 Quantifying the fusion activity

Three fusion assays were established covering not only cell-cell fusion but also particle-cell fusion mediated by the SARS-CoV-2 spike protein, which was either expressed from a plasmid in effector cells or S was incorporated into pseudotyped lentiviral vector systems. The high signal-to-noise ratio of 2-3 orders of magnitude was on one hand due to the reporter complementation design of the established assays. On the other hand, the extreme membrane fusion activity mediated by S was surprising. Syncytia of transfected cells formed very rapidly and covered almost all cells in the cell culture dish. Shortly before the start of this thesis, it was demonstrated that syncytia formation is mediated by S, but sensitive quantitative assays to determine the extent of cell-cell fusions were lacking (Buchrieser et al. 2020). Our cell-cell fusion assays revealed an extraordinary fusion activity of S which was even detectable when S levels on effector cells were below the detection limits of Western blot and flow cytometry analysis. This high fusion activity is most likely due to the high affinity of S and ACE2 being in the low nanomolar range (Walls et al. 2020). This interaction strength is much more pronounced than that of the highly fusogenic measles virus (Navaratnarajah et al. 2008). Moreover, the fusion activity of SARS-CoV-2 is significantly higher than that of SARS, likely due to an optimized fusion reaction. One significant difference is the acquisition of the furin cleavage site between the S1 and S2 subunits (Hoffmann et al. 2020a; Papa et al. 2020; Leroy et al. 2020). While SARS-CoV-2 already pre-activates the fusion mechanism in the host cell by cleavage through furin, complete activation requires TMPRSS2 or cathepsin L on the target cell. In contrast, SARS activation requires the co-expression of both molecules on the target cells. Therefore, the already destabilized S complex of SARS-CoV-2 might allow for an easier S1 and S2 dissociation after initial ACE2 interaction and cleavage at the S2'. This facilitates the following fusion mechanism involving the refolding of the metastable S2 subunit driven by the conformational changes in the HR1 domain leading to the insertion of the fusion peptide into the cell membrane. Following refolding events in the HR2 domain contracts the membranes, leading to the formation of a fusion pore and subsequent cell fusion (Jackson et al. 2022). Along this line the increased affinity in evolved SARS-CoV-2 variants improved the fusion activity. So far, the Delta variant exhibits the highest fusion activity, with a ~4.5-fold higher affinity to ACE2 than the Wuhan variant used in this thesis (Wu et al. 2022).

The cell-cell fusion assay may underestimate the extent of S fusion as the production of the effector cells depends on the transfection efficiency. Therefore, it is possible that not all cells received both the reporter and S-plasmid and S-expressing cells lacking the reporter were introduced into the system. To achieve even higher sensitivity, stable reporter cell lines could be used in which all cells express the reporter at the same level. These cells would only need to be transfected with the S-plasmid, ensuring a more homogenous effector cell population. Furthermore, it would be interesting to transfer this system to cell lines derived from lung tissue, such as Calu-3 or MRC-5 cells, which are closely related to the cells initially targeted by SARS-CoV-2. This would have the advantage of a similar ACE2 expression level to that of these primary cells.

Before publication of the data described in this thesis, established cell-cell fusion assays relied on manual syncytia counting under the microscope (Ou et al. 2020). Although, this method nicely visualizes the extent of S-mediated fusion after a certain time period, it is non-quantitative and subjective. In our experiments, syncytia formation was seen throughout the plate after co-incubation of target and effector cells overnight. However, this assay system is not sufficient to detect subtle differences when assessing neutralizing antibodies. Before the assays established in this thesis was published, two groups used reporter-complementation to analyze SARS-CoV-2 fusion activity (Zhu et al. 2020; Buchrieser et al. 2020). This work was based on the complementation of a split-GFP reporter and at least one order of magnitude less sensitive than the beta-galactosidase reporter system described in this thesis (Zhu et al. 2020).

Various types of viral infection assays have been developed to assess neutralization of antibodies, including plaque-assays and microneutralization assays, which use the authentic virus which is propagated on a susceptible cell line *in vitro*. Although these methods are considered as gold standards, they are often incompatible with a high-throughput screening and require strict biosafety level (BSL) 3 conditions. Therefore, these assay formats are limited to specialized laboratories (Herrlein et al. 2022; Liu et al. 2022). Other assays measure cell-free neutralization which can be performed at lower BSL but are still limited by the binding to recombinant protein in a non-native environment (Fenwick et al. 2021). Pseudotyped viral vector systems were previously proposed utilizing VSV, murine leukemia virus or HIV as vector cores for the incorporating of the envelope proteins of SARS and MERS. Building on them, a pseudotyped system was developed for the SARS-CoV-2 spike protein (Meyrath et al. 2022; Ou et al. 2020; Hoffmann et al. 2020b). The lentiviral vector system used in this study offers the advantage of measuring cell entry neutralization at lower BSL and allow for a highly sensitive readout through the expression of a reporter protein. Furthermore, it is compatible with high-throughput screening. Compared to the LV-based particles described in other studies, our system uses second-generation LV systems. This is achieved by incorporating of self-inactivating LTR regions and the separation of packaging and transfer plasmids. As a result, our system is much safer than first-generation LVs or VSV vector system, which were used for S-pseudotyped particles (Zhu et al. 2020; Zeng et al. 2020). These systems require the co-infection with a helper virus risking the unwanted generation of replication-competent viruses. In addition, virus-like particles displaying S protein, which were used for the FFWO assay, are classified into BSL1 and can be utilized by multiple laboratories. The transduction assay yielded a signal-to-noise ratio of four orders of magnitude which is consistent with published results from other groups (Ou et al. 2020; Zhu et al. 2020).

Although LV and VSV particles possess favorable safety features, they also have limitations. One of them is the difficulty in predicting whether the incorporated glycoprotein is adequately processed in the HEK293T cells used for their production (Meyrath et al. 2022). In our assays, S on VLPs was activated by exogenous trypsin treatment resulting in completely processed S. This is evident in our western blot showing signals corresponding to the full-length S size and the increased, stronger signals for the cleaved S2 subunit after trypsin treatment. It is now known that trypsin cleaves the S1/S2 junction, which is also recognized by furin inside the cell, resulting in the non-covalent association of S1 and S2 (Xia et al. 2020a). The processing had a significant impact on fusion activity indicating that expression in HEK293T cells does not result in a completely mature S. The question of how the S protein mediates cell entry is central to many therapeutic and prophylactic approaches against COVID-19. Although the process is still incompletely understood, it is well established that proteolytic processing of S is crucial for cell entry, and that the availability of proteases determines tropism and entry route. Recently, new studies have revealed that metalloproteases can also activate the S2’ sites in the extracellular milieu (Harte et al. 2022). Our dataset confirms the dependence of S on proteolytic activation and provides a way to increase the potency of the S-LV and VLPs, allowing for more assays to be performed using the same vector stock.

5.2 The SARS-CoV-2 spike protein mediates fusion-from-without (FFWO)

This study demonstrates for the first time the fusion of cells in presence of S-presenting particles and in the absence of a productive infection (see Figure 56). Therefore, S-particles lacking a genome or incorporating a defective genome may still be able to induce cytopathic effects in patients. However, FFWO required at least $5x10^5$ particles per cell ($5x10^8$ particles per $1x10^5$ cells), which is a high number of particles, to achieve a significant signal above background. This was likely related to the diffusion barriers that need to be overcome to allow sufficient contact between particles and cells attached to the plate forming a two-dimensional monolayer. However, in tissues, cells are tightly packed with very limited extracellular milieu. Therefore, it is likely that in patient tissue fewer S-particles may be required to induce syncytia formation, since target cells are in very close proximity. Currently, there is no clinical evidence supporting FFWO mediated by S. However, some reports demonstrated the importance of FFWO *in vivo* after injecting retroviruses (Murphy and Gaulton 2007).

Apart from that, FFWO has so far only been reported for a small number of viruses including HIV, Newcastle disease virus and Herpes simplex virus (HSV). In the case of HSV, a subset of syncytial strains containing two point mutations in glycoprotein B (gB) (V553A and A855V) is able to mediate FFWO. This fusion process depends on the concerted action of the HSV glycoproteins gD and gB and requires the expression of one of the cognate receptors, nectin-1, nectin-2 or HVEM. It was shown that FFWO activity is dependent on the cell type. Cell types that facilitate pH-dependent endocytotic cell entry of HSV do not exhibit FFWO activity, whereas a pH-independent fusion mechanism resulting in the membrane fusion at the plasma membrane promotes FFWO (Weed and Nicola 2017; Roller et al. 2008). This mechanism may be very well transferable to SARS-CoV-2. As stated in the introduction, SARS-CoV-2 enters cells through membrane fusion, which can occur through two pathways. The first pathway involves receptor-mediated endocytosis, followed by endosomal escape through cathepsin L. The second pathway involves the pH-independent fusion at the plasma membrane requiring the activation of the fusion machinery by TMPRSS2. Therefore, it is tempting to speculate that FFWO is mediated by S only if the TMPRSS2-dependent cell entry pathway is chosen. It remains to be proven if this hypothesis is valid for target cells lacking TMPRSS2, as they do not support FFWO.

Unlike the transduction assay, the FFWO assay not only focuses on S particle fusion activity but also examines cell-cell fusion events providing additional insights into S-mediated cell interactions. The neutralization efficiency was notably different between the transduction assays and FFWO. This suggests that a serum neutralizing FFWO will most likely not only prevent the entry of particles into a cell, but also block the viral spread via cell-cell fusion. The FFWO assay developed in this thesis is unique because it combines the neutralization of particle-associated S protein with the neutralization of cell fusion which allows the assessment of two fusion mechanisms in a single readout. Thus, it can be used as a screening platform for highly active fusion inhibitors. Combined with the low safety level (BSL1) and the high signal-to-noise ratio, it can become a valuable assay for preclinical assessment of neutralizing antibodies.

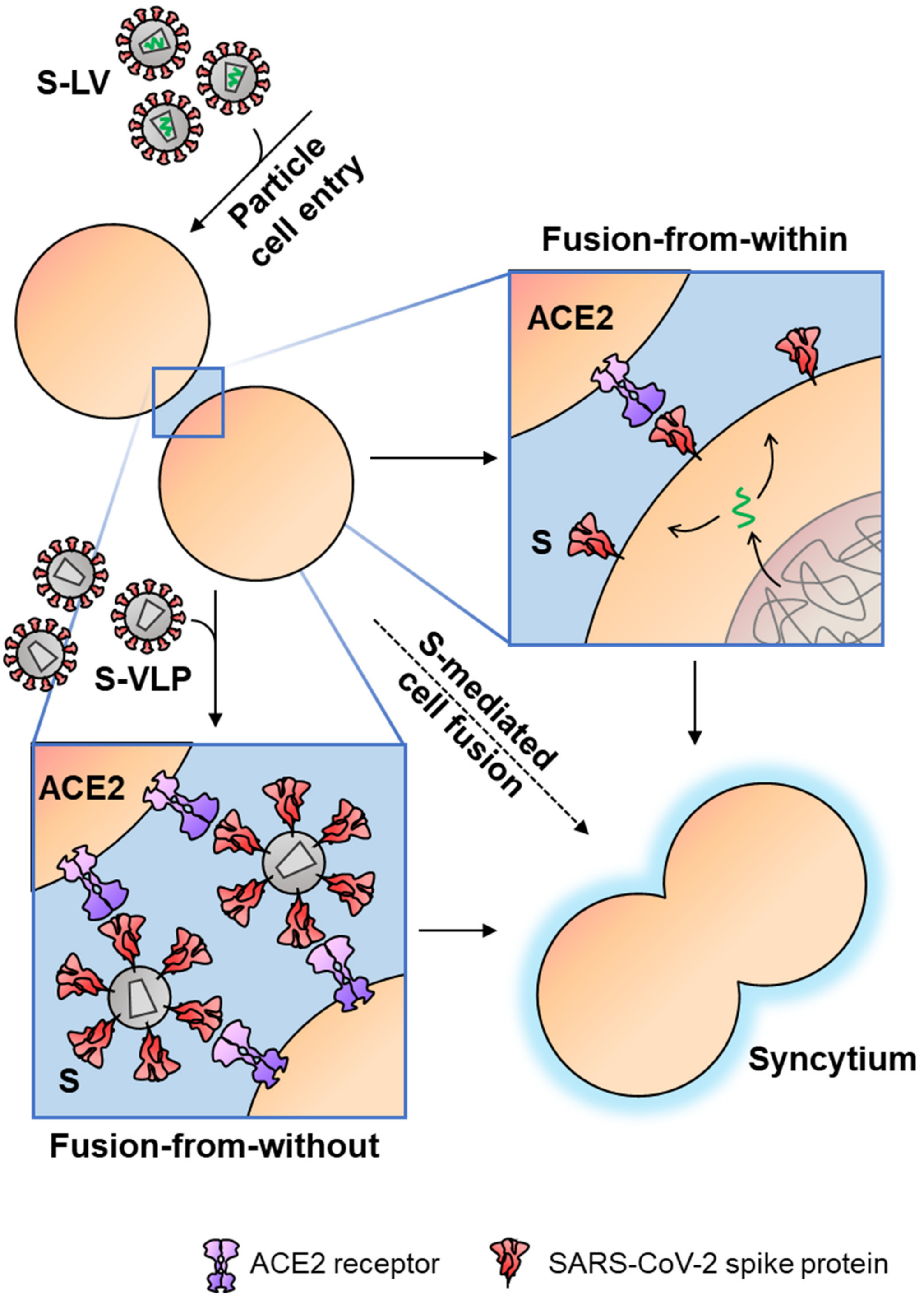

Figure 56: **S-mediated cell fusions.**
In this thesis three assays for the quantification of the SARS-CoV-2 S fusion activity were established. S mediated the cell entry of pseudotyped LVs into ACE2-expressing cells (top). When S-VLPs were incubated with ACE2-expressing target cells, adjacent cells fused forming syncytia in a process known as fusion-from-without (bottom left). Transfected cells expressing S mediate cell fusions with minimal levels of S resulted in fusion-from-within and syncytia formation (right). Figure is adapted from (Theuerkauf et al. 2021).

5.3 SARS-CoV-2 fusion activity and its pathological consequences

Syncytia formation induced by S has been identified in various patient organs, including lung, kidney and heart. These multinucleated cells form irregular cell bodies and present S on the cell surface as demonstrated by histological analysis of tissue biopsies (Bussani et al. 2020). Viral dissemination within a patient can occur either through the secretion of viral particles being susceptible to antibody-mediated neutralization or via cell-cell contacts, which allow the virus to escape immune surveillance. The latter efficient mechanism has been proven for several viruses including measles and HIV (Pedro et al. 2019; Ferren et al. 2019). Studies have shown that cell-to-cell spread results in several orders of magnitude greater efficiency in viral dissemination compared to the spread via cell-free particles. Additionally, as shown for HIV, this mechanism can overcome inhibitory effects of cellular restriction factors, such as tetherin which prevents the release of viral particles by tethering them to the host cell surface (Pedro et al. 2019). Thus, syncytia formation promotes the infection of non-permissive cell types and is considered to be a mechanism for establishing viral reservoir cells (Rajah et al. 2022). The cell fusion activity of SARS-CoV-2 is remarkably strong and can occur with a very low level of S presented on cells as demonstrated in this thesis. This suggests that the virus may be able to evade immune surveillance and increase persistence. Importantly, the cell-cell fusion requires presentation of S on the cell surface which can originate from either the engaging virus transferring S to the plasma membrane after cell fusion and from newly expressed S. When S is transferred from the viral membrane to the cell membrane, it diffuses to distinct locations on the membrane resulting in a low local density of S. After the viral genome is delivered, new S is expressed. However, due to the presence of the ER retention signal, most of the S molecules are prevented from reaching the cell surface. Therefore, the cell surface level of S will be quite low (Zhang et al. 2023). This is adequately reflected in our cell-cell fusion assay, demonstrating fusion activity of effector cells expressing S levels which are below the detection limits of Western blot and flow cytometry. Recently, it was discovered that SARS-CoV-2 remains its high fusion potential in patients by recruiting heparan sulfate (HS) to the attachment site of S- and ACE2-expressing cells. This results in the clustering of ACE2 and S, facilitating a strong concentration of binding partners and subsequent cell fusion (Zhang et al. 2023). It is worth noting that different strains of SARS-CoV-2 possess varying degrees of fusogenicity, with the Delta variant exhibiting the strongest fusion activity (Wu et al. 2022). Interestingly, infection with the Delta variant is associated with a higher risk of hospitalization (Bast et al. 2021).

SARS-CoV-2 is described as a respiratory virus, however the virus spreads quickly to connected organs and causes substantial damage throughout the patient body. The virus infects organs such as the duodenum, small intestines, gall bladder, lung, kidney, testis and heart due to their expression of ACE2. Furthermore, ACE2 is expressed on endothelial cells which increases the risk for thrombosis (Marschalek 2023). Thus, SARS-CoV-2 patients exhibit heterogenous symptoms after experiencing a severe COVID-19 infection. Most of the symptoms are related to inflammatory responses and tissue-destructive processes (Zhang et al. 2023; Marschalek 2023). Moreover, it is suggested that syncytia formation induced by S may play a role in inflammation, thrombosis or lymphopenia. This is based on the frequent observation of multinucleated cells in lung tissue in deceased COVID-19 patients. Additionally, syncytia induced by S rapidly internalize lymphocytes resulting in a cell-in-cell structure which is not observed in other cases of pneumonia (Zhang et al. 2021). Furthermore, S has been shown to induce cell fusion between neurons or glial cells which may contribute to the neurological disorders experienced by long-COVID-19 patients (Martínez-Mármol et al. 2023). An efficient spread via cell fusion is also concerning for the development of therapeutics. Some drugs have been developed for the treatment of HIV patients to prevent particle cell entry, but they show weak efficiency against cell-cell transmissions (Pedro et al. 2019). Therefore, a combination of drugs is required to efficiently prevent the spread and replication of HIV. In this regard, it is concerning that SARS-CoV-2 patient sera and antibodies evaluated in this thesis showed much lower neutralizing efficiency in the cell-cell fusion assays as compared to the particle-cell fusion assays, despite using much higher S amounts in the latter assay. This suggests that S fusion proceeds at low cell surface levels and is difficult to be neutralized with antibodies and sera. The identification of efficient fusion inhibitors is thus of utmost importance. Early on, inhibitors against serine proteases, such as camostat mesylate, were used to inhibit TMPRSS2. However, they did not affect the severity or duration of COVID-19, presumably because SARS-CoV-2 can utilize alternative cell entry pathways. Hydrochloroquine and chloroquine can be used to prevent cell entry via receptor-mediated endocytosis, thereby preventing cathepsin L-mediated endosomal escape (Jackson et al. 2022). The two HS binding drugs Mitoxantrone and Pixantrone showed efficient inhibition of SARS-CoV-2 cell entry and syncytia formation. Intriguingly, both drugs are extensively studied for tumor treatment (Zhang et al. 2023). Initial studies have identified peptide-cholesterol conjugates which specifically bind the HR domains of SARSCoV-2 S showing promising inhibition of the cell fusion activity. These inhibitors can be applied via inhalation, resulting in local rather than systemic effects and therefore reduce the chance of side effects (Xia et al. 2023; Xia et al. 2020b).

Taken together, SARS-CoV-2 exhibits a strong fusion activity which can proceed at minimal levels of SARS-CoV-2. This fusion activity, which is also demonstrated in the FFWO assay, is likely contributing to syncytia formation in patients. The FFWO assay also provides a platform for evaluating neutralizing binders in a preclinical setting. As syncytia formation is associated with the disease progression of COVID-19, it may be relevant to focus on fusion inhibitors preventing or reducing the extend of the fusion activity, since cell-cell fusions are less efficiently neutralized by antibodies.

Discussion of Part B: Targeting strategies for adeno-associated vectors for HIV gene therapy

5.4 Why is bispecific targeting important?

AAV vectors are the prime choice for the delivery of therapeutic genes *in vivo*. Although currently approved gene therapeutics rely on naturally occurring serotypes with their broad tropism, research is focused on engineering the AAV capsid to further restrict tropism to therapy-relevant cells. Specific vectors are expected to substantially reduce the dose that needs to be injected, as these particles are less likely to be lost to off-target cells. Recently, it has been shown that high doses of AAV are associated with severe hepatoxicity which can be fatal for patients (Kishimoto and Samulski 2022). Much progress has been made in the rational engineering of the AAV capsid. This involves the insertion of DARPins or nanobodies being highly specific for the cell surface of choice (Becker et al. 2022). Meanwhile, several receptors have now been successfully targeted, including markers of lymphocytes, endothelial and cancer cells. Nevertheless, this targeting system relies on a single marker defining the target cell population. Many subsets of cell populations are however defined by a combination of several markers. To enable highly specific gene therapy, this thesis focused on the development of AAV vectors recognizing two surface markers and preferentially transfer the gene of interest into cells expressing both receptors. Such a vector system was not described before.

5.5 Display of two DARPins results in novel bispecific vectors without structural impairments

The AAV capsid is a highly rigid, ordered and symmetric structure which is essential for the stability and protection of the viral genome. AAV vectors lack a membranous envelope, so targeting ligands must be incorporated directly into the capsid structure without interfering with assembly and gene delivery processes. The alignment of several AAV Cap sequences and the availability of high-resolution structures of the capsids have identified multiple hypervariable regions being exposed on the surface. These regions were proposed to allow for the insertion of targeting ligands (Hoffmann et al. 2023). Among them, the GH2/GH3 loop has been shown to tolerate the insertion of DARPins and was used in this study (Günther et al. 2023; Michels et al. 2021). Alternatively, the GH12/GH13 loop containing the RBD for HSPG was identified as an insertion site, especially for randomized peptide libraries (Becker et al. 2022).

DARPins are well-suited for the re-targeting of AAVs due to their small size, aggregation resistance and high affinity for the selected receptor. DARPins have been used previously for multivalent interaction with cell types by connecting them on the genetic level using flexible or rigid linkers. Such multispecific fusion proteins were for example used as T cell engagers to crosslink malignant tumor cells with engaging T cells resulting in the killing of the tumor cells (Bianchi et al. 2022). The combination of three different DARPins targeting the RBD domain of SARS-CoV-2 blocks its interaction with ACE2 and is currently tested in clinical trials (Rothenberger et al. 2022). The simple and modular structure of DARPins enables their flexible use in vector systems, allowing for straightforward exchange between DARPins of various specificities.

With the CD4- and CD32a-specific DARPins, we generated vectors targeting each receptor individually and also connected both DARPins to generate bispecific vectors. Among the monospecific vectors, F11-AAV is the first viral vector system which uses CD32a as entry receptor. The DARPins were successfully incorporated into the GH2/GH3 loop of AAV2's capsid and did not interfere with the uptake of the viral genome. Remarkably, the capsid integrity remained intact even after the insertion of the large bispecific construct, as determined by cryo-electron tomography (cryo-ET). Because the DARPins were only inserted into the VP1 capsid protein, there were on average five insertions per particle randomly distributed over the capsid. Furthermore, flexible linkers were used to flank DARPins and prevent steric hindrance during protein folding. Thus, it was not surprising that the DARPin molecule could not be visualized being exposed on the capsid through high-resolution cryo-EM, which requires the averaging of many particles in similar orientations. Therefore, to resolve the DARPin structure exposed on the capsid, the DARPin would have to be displayed symmetrically, requiring the insertion at multiple positions in the capsid. The biochemical characterization and specific gene transfer by the targeted vectors prove the value of the GH2/GH3 loop of VP1 as a site for the insertion of DARPins.

5.6 Bispecific AAVs follow logic AND-gating in target receptor usage

The most important finding of our study was the clear preference of bispecific AAVs for cells expressing both receptors over those expressing only one of the two. This preference came with some surprise, since in the few previous studies incorporating two DARPins with different specificities into viral particles did not follow AND- but OR-gating. This was the case for oncolytic measles viruses having DAPRins specific for EpCam and Her2/*neu* incorporated. The rationale behind this targeting strategy was to prevent the loss of activity on tumor cells in case of downregulation of one of the targeted tumor antigens. The oncolytic measles virus infected all target cell lines equally efficient, single- and double-positive cells. As a result, these bispecific viruses were expected to exhibit persistent killing efficiency against tumor cells compared to monospecific viruses (Friedrich et al. 2013). According to this study, it was expected to be unlikely that a vector incorporating multiple binders could be engineered to preferentially target cell populations defined by two markers and thus exhibit a narrowed tropism.

Targeting systems requiring the simultaneous expression of two receptors on the cell surface follow the Boolean AND-gate strategy. Such a system was developed for chimeric antigen receptor (CAR)-T cells. T cell activation in this instance depends on the input of two antigens which are co-expressed on the tumor cell. Each input signal alone must not be sufficient to induce the killing mechanism but must exceed a threshold of activation signals once the second target is bound (Hamieh et al. 2023). For instance, a CAR design recognizes the targeted antigen but contains an inefficient CD3ξ chain that exhibits impaired signal transduction. A second costimulatory receptor co-expressed on the same T cells compensates for the activation signal once its antigen is bound. Both antigens bound exceed the threshold required for activation via CD3 and costimulatory domains, resulting in the secretion of perforin and granzyme B mediating the killing of the tumor cell (Kloss et al. 2013). Since this AND-gated targeting strategy relies on the activation machinery of CARs, it is rather not transferable to viral vector systems. Instead, the AND-gated binding behavior of multispecific antibodies might be more comparable. These designs rely on the binding strength (affinity) towards the individual antigens. Bi- and trispecific antibodies have been developed as T cell engagers. One of the binding sites targets CD3 on T cells leading to T cell activation, while the other binding regions recognize tumor antigens. To preferentially target tumor cells expressing both of the antigens and omit unwanted binding to healthy cells expressing only one receptor, low-affinity binders are used (Mazor et al. 2015). Consequently, a stable interaction towards the tumor cell is only possible if both antigens are bound due to the increased avidity. Once both tumor antigens are bound, the killing process is initiated requiring costimulatory signals and cytokine secretion (Herrmann et al. 2018; Tapia-Galisteo et al. 2023; Schubert et al. 2014; Mazor et al. 2017). Similar to bispecific antibodies, also the preferential binding of bispecific AAVs may be due to an increase in multiple attachment points on the cell surface.

To evaluate the specific targeting of CD4/CD32a-expressing cells by bispecific AAV, SupT1 cells were engineered to express CD4 and CD32a mimicking HIV reservoir cells (Descours et al. 2017). These SupT1 cells were then diluted into cell lines or primary cells expressing only one of the targeted receptors to achieve highly underrepresented double-positive cells. These included complex primary cell mixtures such as human whole blood and systemically injected target cells in a mouse model. The preference for CD4/CD32a cells was highest over CD32a-expressing cells when a low dose of vector particles was applied, reaching a maximum of 66-fold. Interestingly, the preference over CD32a-expressing cells was much higher than for CD4+ cells. This might be related to the higher affinity of the 55.2 DARPin towards CD4 than the interaction of F11 to CD32a.

Furthermore, F11-AAV exhibited low transduction efficiency on target cells spiked into human whole blood, most likely due to the recognition and binding of platelets which highly express CD32a. In contrast, bispecific AAV were detargeted from platelets only expressing CD32a and preferred double-positive cells. Remarkably, after injection into mice, even the combined injection of both monospecific vectors resulted in significantly 1.5-fold lower transduction efficiency for double-positive cells than what was achieved with bispecific vectors. Even in this setup, bispecific vectors also showed lower transduction efficiency on single-positive cells compared to the monospecific vectors. The highest efficiency was observed on double-positive cells, demonstrating that bispecific vectors are especially well-suited to transduce these cells.

5.7 How can the preference of bispecific AAVs for cells expressing both receptors be explained?

AAV vectors differ substantially from oncolytic measles viruses in terms of size and the number of incorporated targeting ligands. While oncolytic measles viruses, which are about 120 nm in size, incorporate several hundred of targeting ligands (Cox and Plemper 2017), the non-enveloped AAV used in this study incorporate on average five modified VP1 molecules. As explained above, the DARPins are randomly distributed over the surface of the capsid, which implies that not all DARPins can simulteanously face the cell surface for cell attachment. Furthermore, the linker length selected for separating the DARPins only covers a maximum distance of 50 Å when stretched out (Jost et al. 2013). Hence, it is unlikely that CD4 and CD32a are positioned closely enough on the cell surface for a single VP protein to bind both receptors. As a result, less than half of the approximately ten available binding sites are practically available for the cell interaction. While it is likely that measles virus will bind to all available receptors in close proximity, AAV vectors can only interact with a few of them. This makes AAV more comparable to the binding of multispecific antibodies. Therefore, the preference for double-positive cells may be the result of an increased avidity effect.

Given the similar binding behavior of bispecific AAV to antibodies, it will be interesting to identify parameters most relevant for the binding and cell entry behavior. Mechanistic model calculations have identified that, apart from the individual affinities of bispecific antibodies for the cognate receptors, the internalization rate of intermediate states also plays a role. This suggests that the recycling rate of receptors is important. Furthermore, the spatial orientation of both receptors on the cell surface likely contributes (Kareva et al. 2018; Kareva et al. 2021). Current models propose a two-step binding process. Firstly, a targeting ligand with the highest affinity is bound which anchors the bispecific molecule on the cell surface. This restricts the spatial freedom of the second binding moiety keeping the ligand close to the binding epitope. As a result, the apparent affinity to the second target, which is in close proximity, is increased facilitating an easier interaction. When both targets are bound, the overall binding strength is much stronger than to only one receptor. This significantly delays dissociation processes and results in a longer presence of vector particles on the cell surface (Kareva et al. 2022). In turn, subsequent internalization processes have more time for their initiation resulting in a higher likelihood for vector internalization (see Figure 57).

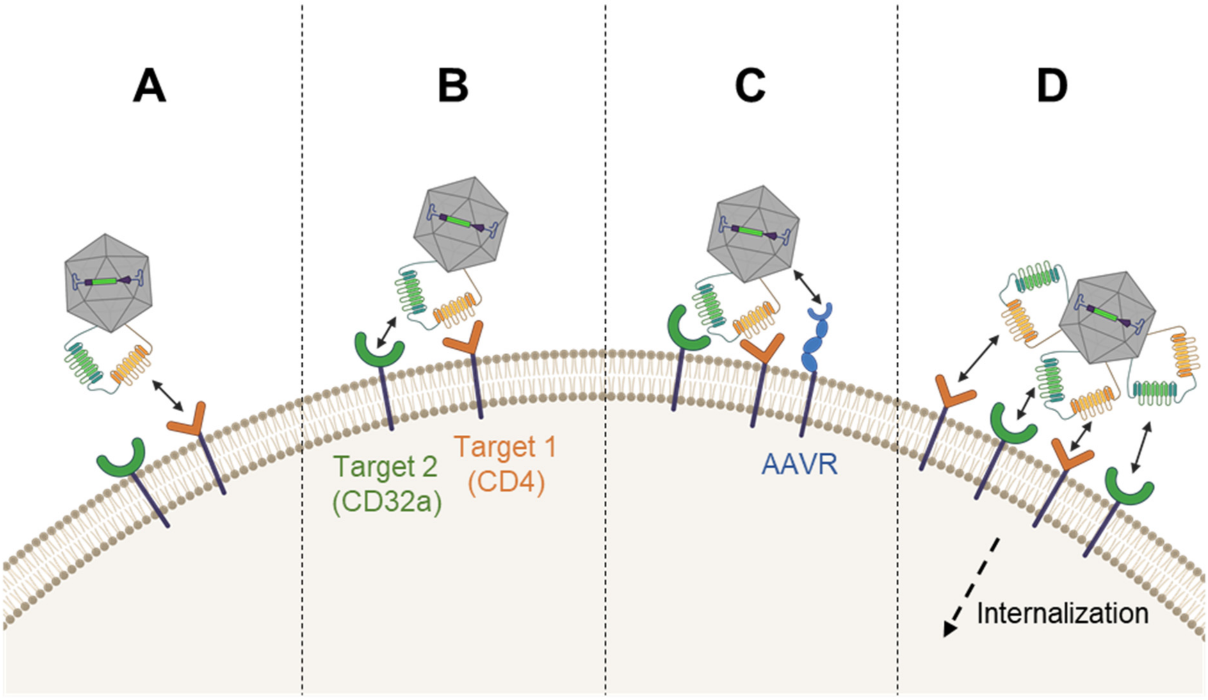

Figure 57: **Binding model for bispecific AAV.**
A) The bispecific AAVs used in this thesis will most likely first interact with the CD4 receptor of a target cell that expresses both CD4 and CD32a receptors. This is due to the high affinity of 55.2 towards CD4. **B)** Once CD4 is bound, the bispecific AAV is anchored on the membrane facilitating the binding to CD32a, despite F11 having a lower affinity for CD32a compared to the CD4 interaction. **C)** After both target receptors are bound, the vector needs to bind to the AAVR to mediate cell entry and intracellular trafficking. This binding site is located on the three-fold axis of the AAV2 capsid (Zhang et al. 2019) and binding occurs independently from the displayed DARPins (Hartmann et al. 2019). **D)** Multiple VP1 molecules are incorporated into the capsid resulting in the display of many DARPins that can interact with multiple receptors on the cell surface. This interaction has high-avidity resulting in a stronger binding to the cell surface than a monospecific AAVs. As a result, particles remain on the cell surface a longer period of time increasing the likelihood of successful cell entry and gene delivery.

While the bispecific vector particles described in this thesis exhibit a preference for double-positive cells are not absolutely selective. As previously mentioned, the activity of multispecific antibodies on single-positive cells can be substantially reduced by using binders with lower affinity. This approach may be transferable to the targeting of AAVs. Indeed, the tropism of the vector was influenced by the affinities towards the targeted receptor and the orientation of the DARPins within a single VP protein. The stronger affinity towards the CD4 receptor mediated by the 55.2 DARPin with an affinity of 0.84 nM compared to F11 (6.1 nM) resulted in a preference for CD4 over CD32a-expressing cells (Theuerkauf et al. 2023). Furthermore, DARPins positioned at the N-terminus showed better binding and transduction of their cognate target cells. As demonstrated in the *in vivo* experiment, the lower affinity of F11 was partially compensated by positioning it at the N-terminus. Interestingly, when F11 was positioned at the C-terminus in the bispecific construct, it showed low activity after being injected into mice.

After initial attachment to the cells by receptor-targeted and unmodified AAV, cell entry depends on the interaction with a co-receptor which is in most cases the AAVR (Pupo et al.

2022). AAV2 WT exhibits a high affinity for HSPG of about 0.1 nM (Zhang et al. 2013), while binding to AAVR is less affine, approximately 150 nM (Pillay et al. 2016). Interestingly, it was shown before that retargeting of AAVs is most efficient and specific when using high-affinity binders. In contrast, lentiviral vectors also tolerate binders with lower affinity (Hartmann et al. 2018). Taking into consideration that the affinity attenuation in antibodies allows for the design of AND-gated binding, it is tempting to speculate that lower affine DARPins in bispecific AAV might optimize the binding behavior. To improve the selectivity for double-positive cells, CD4-specific DARPin with lower affinity can be selected, which would prevent the CD4-preference of the bispecific vector. In literature, AND-gated antibodies usually exhibit a binding strength of 60-80 nM towards their targeted receptors (Mazor et al. 2015). Although the individual binding strength of the DARPins would be reduced, which is contradictory to the requirement for strong binders in the context of AAV targeting, the necessary overall binding strength towards the cell might be compensated by the simultaneous interaction with both receptors.

5.8 HIV gene therapy

Application for bispecific AAVs are plentiful, reaching from basic gene function studies to applied therapies. Especially promising is the targeting of the HIV reservoir cells which express a combination of several markers distinguishing them from healthy cells. In this thesis, an 'all-in-one' vector F11-55.2-AAV efficiently packaged and delivered the endonuclease Cas9 along with a gRNA specific for the HIV provirus into HIV-infected cells, preventing HIV replication.

The use of split-AAV for the delivery showed remarkable efficiency and the advantage of delivering three gRNAs which was shown to successfully prevent the generation of escape mutants (Das et al. 2019). Nevertheless, transitioning to an 'all-in-one' vector system is promising for *in vivo* delivery. Unlike the split-AAV system, the all-in-one vector eliminates the need for simultaneous transduction by at least two particles after systemic injections. However, this comes at the cost of packaging only a single gRNA, in order to avoid exceeding the packaging capacity of the AAVs. While this might provoke the emergence of escape mutants, the most efficient system would need to be identified in long-lasting experiments ensuring the absence of replication of escape mutants. Several other nucleases can be used for the delivery by AAVs, including saCas9 which is 1 kb smaller in size and may accommodate the addition of gRNAs and promoter sequences (Yin et al. 2017). However, saCas9 is dependent on a less flexible DNA recognition site (PAM) to induce the double-strand break which limits the variety of useable gRNAs (Ran et al. 2015).

CD32a co-expressed on CD4 T cells was proposed as a marker for HIV reservoir cells showing highly enriched replication-competent HIV DNA (Descours et al. 2017). Some studies have challenged these results reporting no enrichment of HIV CD32a cells or even questioning the existence of CD32a+ CD4+ T cells (Badia et al. 2018; Osuna et al. 2018). These contradictory results may be due to different timing of cART treatment initiation, duration and continuous immune activation leading to a diversified phenotype (Adams et al. 2021). Furthermore, during the purification of the minor cell population, technical difficulties can led to contaminations with platelets or monocytes, which are known to express a high level of CD32a. Nevertheless, numerous studies have confirmed the role of CD32a as a reservoir marker by using independent and adapted purification methods allowing for the isolation of pure CD32a+CD4+ cells (Darcis et al. 2020). CD32a is a promising marker owing to its expression during both latent and transcriptionally active HIV replication (Darcis et al. 2020; Abdel-Mohsen et al. 2018) and its presence in tissue harboring reservoir cells, such as lymph nodes, the gastrointestinal tract and cervical tissue (Vásquez et al. 2019; Cantero-Pérez et al. 2019). Additionally, a large fraction of CD32a-expressing cells becomes reactivated either naturally or through stimulation using latency reversal agents (Astorga-Gamaza et al. 2022).

Having proved the co-expression of CD32a on primary CD4 T cells, it was rarely possible to detect CD32a mRNA in these cells. This raised the question of the origin of the CD32a presence on CD4 T cells. Follow up studies revealed a CD32-driven trogocytosis process that results in the transfer of membrane patches from monocytes to CD4 T cells. The authors suggested that CD32a, along with other surface proteins, is actively transferred through cell-cell contacts and modifies the function of the recipient cell. CD4 T cells not only exhibit altered adhesion and migration properties, but also an increased susceptibility to HIV infections. The mechanism by which the transfer of membrane patches increases the binding probability of HIV to the modified T cells is not entirely clear. However, the authors speculate that the transfer of certain lipid rafts or integrins provides multiple rather unspecific attachment sites for HIV. This increases the viral load on specific membrane sites raising the likelihood of an infection. Furthermore, this study revealed that the presence of antibodies developed during HIV infection target certain T cell epitopes. The Fc domains of these autoantibodies can subsequently interact with the CD32a receptors present on monocytes, facilitating the crosslink between T cells and monocytes and thereby enhancing the trogocytosis effect. This is in line with studies in non-human primates showing elevated levels of CD32a after SIV infection. Thus, it was concluded that HIV hijacks the CD32-mediated trogocytosis process to create a favourable microenvironment for HIV binding (Albanese et al. 2023).

Identifying the size of the HIV reservoir remains challenging due to the highly dynamic composition of reservoir cells. Various assays and techniques have been proposed to identify reservoir cells including the universally accepted viral outgrowth-assay (VOA) which provides reliable information of an inducible and replication-competent provirus. However, recent estimates have calculated a frequency of reservoir cells in patient blood of 1 in 1 million, which is in many cases too low for the VOA assay (Dufour et al. 2020). Additional assays rely on next-generation sequencing techniques aiming to identify a non-truncated HIV sequence on RNA level implying an inducible provirus. However, as stated by others, latency of HIV can be maintained on post-transcriptional level which limits the informative value of sequencing techniques (Pasternak and Berkhout 2018). Alternatively, single-cell RNA sequencing was used to identify upregulated receptors on the surface of HIV reservoir cells. This approach is especially promising since the single-cell analysis is required to analyze the quite heterogeneous cell composition of reservoir cells.

Wu et al. described a single-cell assay for transposase accessible chromatin-sequencing (scATACseq) (Wu et al. 2023). This technique tags accessible DNA fragments with specific adaptors for detecting the provirus by sequencing combined with cell surface protein profiling. The results revealed highly heterogeneous cell surface receptor combinations, which mark reservoir cells. Although many of the previously established markers were detectable, such as PD-1, CXCR5, CCR6, CTLA-4, CD69, OX40, CD2, Lag-3, TIGIT, CD20 and CD161, none of them alone predict the presence of integrated HIV. Nevertheless, the combination of markers or their relative expression levels proved to be more reliable for predicting a reservoir cell. For instance, activation and T follicular helper cell markers (CD71, ICOS, HLA-DR and PD-1) were differentially expressed in the CD4 population isolated from lymph nodes (Wu et al. 2023). Notably, CD32a was also found to be upregulated in this single-cell study. It is important to note that this analysis is limited to the identification of HIV in actively transcribed DNA regions while latent integrated proviruses might also reside in non-accessible DNA regions. Furthermore, this method is unable to assess the integrity of the HIV sequences and therefore cannot distinguish replication-competent proviruses. In another study from Sun et al., phenotypical and proviral sequencing was used to identify surface marker enrichment in reservoir cells (Sun et al. 2023). After receiving a highly diversified phenotype the authors conclude that the receptor composition reflects the consequences of immune selection providing selective advantages for certain HIV clones, rather than a virus-mediated change in receptor expression profile.

HIV reservoir cells are extremely rare in patients with frequencies ranging between 0.012% (Descours et al. 2017) to 0.074% (Darcis et al. 2020) of CD4 T cells in human peripheral blood. Therefore, it is crucial to use highly specific and efficient vector stocks to target these cells. Bispecific AAVs may be the most suitable option for this task, since they are especially selective on underrepresented cells and show high efficiency on cells expressing two surface markers of reservoir cells. Furthermore, their high activity in human whole blood and successful gene delivery after systemic injection into NSG mice qualifies them for *in vivo* gene therapy. It is important to note that HIV infection mediates downregulation of CD4 which would interfere with the targeting system. However, CD4 is still expressed on reservoir cells in ART-treated patients (Dubé et al. 2023). Although these vectors show promise for HIV gene therapy and AAV vectors in general have been used to treat patients with various diseases, these novel vectors would need to be tested for safe application in humans. One concern for bispecific

AAVs may be the unwanted crosslinking of immune cells which could lead to immune activation and exhaustion. The true potential of these vectors will need to be tested on patient blood delivering an HIV-guided Cas9 nuclease.

Taking into account the significant variation in cell surface markers both within and between patients, the use of bispecific AAVs targeted to a patient's individual surface marker composition shows promise. This approach would involve developing a patient specific therapy. It may be feasible to perform single-cell RNA-sequencing on patient's blood cells to identify the differentially upregulated receptors from a panel of candidates. The bispecific vector system is modular and easily adaptable to target a variety of different cell surface receptor pairs. Moreover, not only DARPins may be suitable for bispecific targeting of AAV. Nanobodies, which are currently extensively studied, may also be suitable for retargeting AAVs, thus expanding the range of potential binders. Therefore, targeting ligands can be exchanged for the surface markers being upregulated as identified by RNA-seq to deliver the therapeutic cassette.

Apart from targeting HIV reservoir cells, bispecific AAVs have potential application in various assays. Among them, targeting specific subsets of T cells for the delivery of CARs might be useful to harness specific T cell properties. For instance, the combination of CD3 and CD62L targeting may be used to modify naïve T cells, which exhibit a less exhausted phenotype, hoping to achieve a long-lasting killing activity (Kapitza et al. 2023). Furthermore, NK-T cells classified by CD8 and CD56 expression exhibit potent killing efficiency for solid tumors, thus CAR delivery into these cells may have advantages in tumor control (Bashiri Dezfouli et al. 2021). Lastly, tumor cells are usually identified by the upregulation of several markers. Bispecific AAV can selectively deliver suicide cassettes or enable the secretion of checkpoint inhibitors to attract immune cells (Reul et al. 2019; Strecker et al. 2022).

6 Material and Methods

6.1 Material

6.1.1 Cell lines and bacteria

Name	Description	Culture medium	Source
Calu-3	Derived from lung adenocarcinoma	MEM + 10% FCS + 2 mM L-glutamine + 1x non-essential amino acids and 1x sodium pyruvate	AddexBio
E. Coli Top10	Highly transformable laboratory strain of Escherichia coli (E. coli)	LB medium	Life technology
HEK293T	Human embryonic kidney cell line, transformed to express the SV40 large T antigen	DMEM + 10% FCS + 2mM L-glutamine	ATCC
Lenti-X 293T	Human embryonic kidney cell line, transformed to express the SV40 large T antigen. Selected clone for high LV production yields.	DMEM + 10% FCS + 2mM L-glutamine	Takara Bio
MRC-5	Fibroblastic cell line derived from human lung	MEM + 10% FCS + 2 mM L-glutamine and 1x non-essential amino acids	ATCC
NEBStable Competent *E. coli*	Used for the production of AAV transfer plasmids	Outgrowth medium	New England Biolabs
SupT1-CD32	T-Cell Lymphoblastic Lymphoma cell line, engineered for the expression of CD32a under CMV promoter control and abolished CD4 expression	Advanced RPMI + 4% FCS + 2mM L-glutamine + 4 µg/ml puromycin	Elena Herrera-Carrillo

SupT1-CD4	T-Cell Lymphoblastic Lymphoma cell line	Advanced RPMI + 4% FCS + 2mM L-glutamine	DSMZ
SupT1-CD4-CD32a	T-Cell Lymphoblastic Lymphoma cell line, engineered for the expression of CD32a under CMV promoter control	Advanced RPMI + 4% FCS + 2mM L-glutamine + 4 µg/ml puromycin	Elena Herrera-Carrillo
Vero E6	Simian kidney cells isolated from African green monkey	DMEM + 10% FCS + 2mM L-glutamine	ATCC
Vero-GFP	Simian kidney cells isolated from African green monkey, engineered for GFP-expression under SFFV promoter control by LV transduction	DMEM + 10% FCS + 2mM L-glutamine + 10 µg/ml puromycin	This thesis

6.1.2 Consumables

Name	Supplier
1.4 ml	Micronic
500 ml Rapid-Flow Bottle Top Filter, 0.45 µm SFCE	Thermo Fisher Scientific
AmershamTM Hybond-ECL, nitrocellulose membrane	GE Healthcare
Amicon Ultra-4 50 kDa cut-off size exclusion filters	Sigma Aldrich
BD Vacutainer® CPT™ blood collection tubes	BD Biosciences
Cell culture, 15 cm dish	VWR
Cell strainer, 70 µm	Corning
Centrifuge tubes, 225 ml	VWR
chamber slides	Thermo Fisher Scientific
Cryovial	Greiner Bio-One
Insulin syringes, U-100; 0.33 mm (29G) × 12.7 mm	BD Biosciences

Micro-centrifuge tubes, 1.5 ml and 2 ml	Eppendorf
Pasteur pipet, glass	VWR
PCR tubes, 0.2 ml	Eppendorf
Petri dish, 10 cm	Greiner Bio-One
Pipet tips, filtered (10 µl, 100 µl, 300 µl, 1000 µl)	Biozym
Serological pipets (5 ml, 10 ml, 25 ml)	Greiner Bio-One
Syringe filters, Minisart, PTFE (0.45 µm, 0.2 µm)	Sartorius
Tissue culture flask (T25, T75, T125)	Greiner Bio-One
Tissue culture plates (6-, 12-, 24-, 48-, 96-well)	Thermo Fisher Scientific
Whatman™ filter paper	Whatman

6.1.3 Kits

Name	Supplier
DNeasy 96 Blood and Tissue kit	Qiagen
DNeasy Blood and Tissue kit	Qiagen
Fixable Viability Dye, eFluorTM 780	Thermo Fisher Scientific
Galactostar assay kit	Thermo Fisher Scientific
GeneJet® Gel Extraction Kit	Thermo Fisher Scientific
GeneJet® Mini Prep Kit	Thermo Fisher Scientific
Light Cycler 480 Probes Master mix	Roche Diagnostics
NucleoBond® Xtra Midi Kit	Macherey-Nagel
Pierce™ ECL wester blotting substrate	Thermo Fisher Scientific
subcellular fractionation kit	Thermo Fisher Scientific

6.1.4 Chemicals and reagents

Name	Supplier
1 kb Plus DNA ladder	New England Biolabs
2log ladder	New England Biolabs
30% acrylamide solution (Rotiphorese® Gel 30)	Carl Roth
Agarose	Biozym
Ampicillin	Roche
BD PharmLyse™	BD Biosciences
BD Vacutainer® CPT™ blood collection tubes	BD Bioscencie

Bromophenol blue	Merck Millipore
Dimethyl sulfoxid (DMSO)	Sigma Aldrich
Dithiotreitol (DTT)	Sigma Aldrich
DNA loading dye, purple (6x)	New England Biolabs
Fc receptor blocking reagent, human	Miltenyi Biotec
Formaldehyde	Sigma Aldrich
Histopaque®-1077	Sigma Aldrich
Human off-the-clot sera	PAN Biotech
Iodixanol (Optiprep™)	STEMCELL Technologies
Midori Green Direct DNA loading dye	Nippon Genetics
PageRuler™ Plus Prestained Protein ladder	Thermo Fisher Scientific
Penicillin/streptomycin	Paul-Ehrlich-Institut
Poloxamer 188	Sigma Aldrich
Polyethylenimine, branched (PEI)	Sigma Aldrich
protease inhibitor cocktail	Roche
Puromycin	Life Technologies
Sucrose	Sigma Aldrich
Tween-20	Sigma Aldrich

6.1.5 Enzymes and cytokines

Name	Supplier
Antarctic Phosphatase	New England Biolabs
Benzonase	Sigma Aldrich
Human IL-15, premium grade	Miltenyi Biotec
Human IL-7, premium grade	Miltenyi Biotec
Q5® High Fidelity DNA Polymerase	New England Biolabs
Restriction enzymes	New England Biolabs
Standard T4 DNA ligase	Thermo Fisher Scientific
Trypsin (Melnick, 2.5% solution)	Paul-Ehrlich-Institut
Vent® DNA Polymerase	New England Biolabs

6.1.6 Antibodies

Name	Clone	Application	Dilution	Supplier
SARS-CoV-2 spike protein detection				
Mouse anti-SARS-CoV-2 spike antibody	1A9	Flow cytometry Western blot	1:100 1:1000	GeneTex

Anti-mouse IgG1	REA1017	Flow cytometry	1:100	Miltenyi Biotec
Anti-P24	38/8.7.47	Western blot	1:1000	Gentaur
Rabbit anti-mouse-HRP	polyclonal	Western blot	1:2000	Dako
Anti-GAPDH-HRP	14C10	Western blot	1:1000	Cell Signaling

AAV whole blood transduction assay

Anti-human CD8	REA734	Flow cytometry	1:100	Miltenyi Biotec
Anti-human CD3	BW264/56	Flow cytometry	1:100	Miltenyi Biotec
Anti-human CD4	L200	Flow cytometry	1:100	BD Biosciences
Anti-human CD32	Fun-2	Flow cytometry	1:100	Biolegend

AAV binding to PBMC

Mouse anti-AAV2	A20	Flow cytometry	2 µl per sample	Progen
anti-mouse IgG	polyclonal	Flow cytometry	1:50	Jackson immune research
Anti-human CD4	VIT4	Flow cytometry	1:100	Miltenyi Biotec
Anti-human CD14	TÜK4	Flow cytometry	1:100	Miltenyi Biotec
Anti-human CD8	BW135/80	Flow cytometry	1:100	Miltenyi Biotec
Anti-human CD3	BW264/56	Flow cytometry	1:100	Miltenyi Biotec

Transduction of cocultured SupT1 cells with AAV

Anti-human CD4	VIT4	Flow cytometry	1:100	Miltenyi Biotec
Anti-human CD32	Fun-2	Flow cytometry	1:100	Biolegend

***In vivo* experiments**

Anti-human CD45	5B1	Flow cytometry	1:100	Miltenyi Biotec
Anti-human CD4	VIT4	Flow cytometry	1:100	Miltenyi Biotec
Anti-human CD32	Fun-2	Flow cytometry	1:100	Biolegend

Detection of AAV VP proteins

Anti-AAV VP1/VP2/VP3/	B1	Western blot	1:50	Progen
Anti-myc tag	Myc.A7	Western blot	1:1000	Abcam
Rabbit anti-mouse-HRP	polyclonal	Western blot	1:2000	Dako

6.1.7 Devices

Name	Supplier
70Ti, SW40 rotor	Beckman coulter
Cell incubator BBD6220	Heraeus, Thermo Fisher Scientific Scientific
Centrifuge multifuge X3	Heraeus, Thermo Fisher Scientific Scientific
gentleMACS Dissociator	Miltenyi Biotec
human off-the-clot sera	PAN Biotech
LightCycler 480 II Real-Time PCR System	Roche Diagnostics
Luna-FI cell counter	Logos Biosystems
MACSQuant Analyzer 10x	Miltenyi Biotec
MicroChemi imaging system	DNR Bio-Imaging systems
Micropipets research plus®	Eppendorf
Mini-Protean® 3 cell chamber system	Bio-Rad
Mr. Frosty™	Nalgene
Multichannel pipets	Thermo Fisher Scientific
NanoDrop 2000c spectrophotometer	Thermo Fisher Scientific
NanoSight NS300	Malvern
Nitrogen tank Chronos, Apollo	Messer
Orion II plate luminometer	Berthold Systems
Preperative ultracentrifuge	Beckman coulter
Prometheus	Nanotemper
Revolve microscope	ECHO A BICO COMPANY
SP8 Lightning laser scanning microscope	Leica
Trans-Blot® SD semi-dry transfer cell	Bio-Rad
Viaflo multichannel pipette	Integra Biosciences

6.1.8 Buffer and solution

Buffer	Composition
20% sucrose in PBS	20% (w/v) sucrose in PBS w/o Mg2+/Ca2+
40% sucrose in TNE buffer	40% (w/v) sucrose in TBS, 100 mM EDTA
AAV lysis buffer	50 mM Tris-HCL (pH 8.5), 150 mM NaCl, 1 mM $MgCl_2$ in H_2O
Anode buffer I	20% Ethanol (v/v), 300 mM Tris
Anode buffer II	20% Ethanol (v/v), 25 mM Tris
Cathode buffer	20% Ethanol (v/v), 40 mM 6-Aminohexanoic acid

Fetal calve serum (FCS)	Sigma Aldrich
Fixation buffer for flow cytometry	1% PFA in PBS w/o Mg^{2+}/Ca^{2}
Non-essential amino acids	Gibco
PBS M/K	2.5 mM KCl, 1 mM $MgCl_2$ in PBS
RIPA buffer	50 mM Tris/HCl (pH 8), 150 mM NaCl, 1% NP-40, 0.5% sodium desoxycholat (w/v), 0.1% SDS (w/v)
Sample buffer (4x)	250 mM Tris/HCl (pH 6.8), 4% SDS (w/v), 20% glycerin (v/v), 0.2% bromophenol blue (v/v), 10% β-mercaptoethanol, 800 mM DTT in H_2O
SDS running buffer	25 mM Tris, 192 mM glycine, 1% SDS in dH2O
Sodium pyruvate	Gibco
TAE buffer	40 mM Tris, 20 mM acetic acid, 1 mM EDTA in dH2O
TBS-T buffer	50 mM Tris(hydroxymethyl)-aminomethan, 150 mM NaCl, 25% HCl, 0.1% Tween-20 in dH2O
TE buffer	10 mM Tris-HCl, 1 mM EDTA in dH_2O
Transfection reagent	18 mM branched polyethyleneimine in H2O
Urea denaturation buffer (2x)	200 mM Tris/HCl (pH 8), 5% SDS, 8 M urea 0.1 mM EDTA, 0.03% bromophenol blue, 2.5% dithiothreitol in H_2O
Wash buffer for flow cytometry staining	2% FCS, 0.1% NaN_3 in PBS w/o Mg^{2+}/Ca^{2+}

6.1.9 Culture media

Media	Supplier
4Cell® NutriT-media	Sartorius
Advanced Roswell Park Memorial Institute (RPMI) 1640 medium	Gibco
Dulbecco's Modified Eagle's Medium High Glucose (DMEM)	Biowest
Freezing medium	10% DMSO, 90% FBS
LB medium	Paul-Ehrlich-Institut
Minimal Essential Medium Eagle (MEM) media	Gibco

SOC medium	KCl, 10 mM $MgCl_2$, 10 mM $MgSO_4$, 20 mM glucose in dH2O

6.1.10 Plasmids

Name	Description	Source
pCG-SARS-CoV-2-SΔ19	Encodes the truncated codon-optimized SARS-CoV-2 spike protein sequence (Wuhan HU-1)	This thesis
pCG-SARS-CoV-2-S	Encodes the codon-optimized SARS-CoV-2 spike protein sequence (Wuhan HU-1)	Karl-Klaus Conzelmann
pCMV-LacZ	Transfer plasmid for lentiviral vectors encoding the β-galactosidase under the control of the CMV promoter	This thesis
pMD2.G	Encodes the glycoprotein G of VSV	D. Trono
pCMV-SP-Myc-ACE2	Encodes the human ACE2 under the control of the CMV promoter	Sino Biological
pCDNA3.1 (+)	Empty plasmid, CMV promoter followed by multiple cloning site	Thermo Fisher Scientific
pCMV-α	Encodes for the Alpha-fragment of the β-galactosidase under the control of the CMV promoter	(Holland et al. 2004)
pCMV-ω	Encodes for the Omega-fragment of the β-galactosidase under the control of the CMV promoter	(Holland et al. 2004)

pCG-NiV-Gmut-L3-CD32a.F11	Encodes NiV-GΔ34 fused to the F11 DARPin	Vanessa Riechert
pRC22-VP1-55.2-VP2/3ko-HSPGmut	Encodes Rep proteins of AAV2 and the VP1 protein containing DARPin 55.2 in the GH2/GH3 loop	Luca Zinser
pRC22-VP1-F11-VP2/3ko-HSPGmut	Encodes Rep proteins of AAV2 and the VP1 protein containing DARPin F11 in the GH2/GH3 loop	This thesis
pRC22-VP1-F11-55.2-VP2/3ko-HSPGmut	Encodes Rep proteins of AAV2 and the VP1 protein containing DARPins F11 and 55.2 in the GH2/GH3 loop	This thesis
pRC22-VP1-55.2-F11-VP2/3ko-HSPGmut	Encodes Rep proteins of AAV2 and the VP1 protein containing DARPins 55.2 and F11 in the GH2/GH3 loop	This thesis
pRC22-VP1ko-HSPGmut	Encodes Rep proteins, VP2 and VP3 of AAV2	Dorothee Günther
pssAAV-gRNA	AAV single-stranded transfer plasmid coding for three gRNAs which guide spCas9 to the HIV provirus. Expression of the gRNAs is driven by U6, 7SK and H1 promoters	Dirk Grimm
pssAAV-spCas9	AAV single-stranded transfer plasmid coding for spCas9 under the control of the Ef1α promoter	Dirk Grimm
plentiCas9-H1-99-gTATREV-U6-gGAG1-EGFP	Transfer plasmid for lentiviral vector encoding	Elena Herrera-Carrillo

	two gRNAs specific for the HIV provirus under the control of U6 and H1 promoter. The same H1 promoter also drives the expression of spCas9 and GFP connected by a P2A site.	
pssAAV-spCas9-gRNA	AAV single-stranded transfer plasmid coding for one gRNA specific for the HIV provirus and spCas9 under the control of the H1 promoter.	This thesis
pXX6-80	Adenoviral helper plasmid encoding the adenoviral genes VA, E2A and E4	Hildegard Bünning
pRC22 Rep/Cap plasmid	Encodes AAV2 Rep and Cap proteins	Hildegard Bünning
pscAAV-GFP	AAV self-complementary transfer plasmid encoding GFP under the control of the SFFV promoter	Robert Münch

6.1.11 Software

Name	Company
BioRender	Science Suite Inc.
Chimera 1.13.1	UCSF
Citavi 6	Swiss Academic Software
FCS Express, Version 6	De Novo Software
FlowJo, Version 10	FlowJo LLC
GraphPad Prism 8	GraphPad Software
ImageJ (Fiji)	ImageJ
Intas Gel Doc	Intas
LAS X	Leica
LightCycler® Software 4.1	Roche

Microsoft Office 2016	Microsoft
NTA, version 3.3	Malvern Pananalytic
SnapGene 4.0.6	SnapGene

6.2 Methods

6.2.1 Molecular biology and protein biochemistry

6.2.1.1 Molecular cloning

Karl-Klaus Conzelmann (Munich) kindly provided the expression plasmid for codon-optimized SARS-CoV-2 S with a C-terminal HA tag, designated as pCG-SARS-CoV-2-S (Hennrich et al. 2021). The plasmid pCG-SARS-CoV-2-SΔ19, encoding the truncated S variant, was created by PCR amplification of the S sequence. This process involved inserting PacI and SpeI restriction sites, along with a stop codon, using primer 1 and primer 2. The resulting PCR fragment was incorporated into the pCG backbone through restriction cloning.

For the lentiviral vector, transfer plasmid pCMV-LacZ, the CMV promoter region and the lacZ coding sequence were amplified by PCR adding restriction sites EcoRI and Bsu361. This fragment was subsequently inserted into the pSEW plasmid (Funke et al. 2008) and replaced to original SSFV promoter. Expression plasmids pCMV-α and pCMV-ω, encoding the beta-galctosidase fragments, were described previously (Holland et al. 2004). The expression plasmid for N-terminally myc-tagged hACE2 (pCMV-SP-Myc-ACE2) was bought from Sino Biological (HG10108-NM).

Targeting plasmids for the production of AAVs containing DARPin F11 or bispecific 55.2 and F11 within the GH2/GH3 loop of VP1 were generated as following: DARPin sequence of F11 was amplified by PCR from plasmid pCG-NiV-Gmut-L3-CD32a.F11 (kindly provided by Vanessa Riechert (Paul-Ehrlich-Institut)) using primer 3 and primer 4 adding SfiI and SpeI restriction sites. This PCR fragment was then inserted into pRC22-VP1-55.2-VP2/3ko-HSPGmut which was kindly provided by Luca Zinser (Paul-Ehrlich-Institut) via SfiI and SpeI restriction cloning leading to plasmid pRC22-VP1-F11-VP2/3ko-HSPGmut.

For bispecific AAVs, both DARPins were connected by a $(G_4S)_3$-linker. For the generation of pRC22-VP1-**F11-55.2**-VP2/3ko-HSPGmut, overlap extension PCR was used to amplify the F11 sequence from pRC22-VP1-F11-VP2/3ko-HSPGmut adding $(G_4S)_3$-linker C-terminally using primer 5 and primer 6, 55.2 was amplified from pRC22-VP1-55.2-VP2/3ko-HSPGmut adding complementary linker sequences using primer 7 and primer 8. PCR fragments were then combined and used as template for the extension PCR using primer 5 and primer 8. The resulting PCR product was cloned into pRC22-VP1-F11-VP2/3ko-HSPGmut via SfiI and SpeI restriction cloning, resulting in an intermediate plasmid. Subsequently, the N-terminal linker was shortened to a $(G_4S)_2$-linker. For that, a shorter linker region of the intermediate plasmid was amplified using primer 9 and primer 10, adding the AgeI restriction site C-terminally. The PCR fragment was then inserted into pRC22-VP1-F11-VP2/3ko-HSPGmut via Bsiwi and AgeI restriction cloning resulting in pRC22-VP1-**F11-55.2**-VP2/3ko-HSPGmut. pRC22-VP1-**55.2-F11**-VP2/3ko-HSPG was generated accordingly using primer 11 and 12 for the amplification of 55.2, and primer 13 and 14 for F11 amplification. Extension PCR was performed using primer 11 and 14. The PCR fragment was then inserted into the backbone of pRC22-VP1-**F11-55.2**-VP2/3ko-HSPGmut resulting in pRC22-VP1-**55.2-F11**-VP2/3ko-HSPG using SfiI and SpeI restriction cloning.

Point mutations in the targeting plasmids prevented the expression of VP2 and VP3 from these plasmids. VP2 and VP3 expression were complemented from the pRC22-VP1ko-HSPGmut plasmid, which contained a point mutation in the VP1 start codon and was kindly provided by Dorothee Günther (Paul-Ehrlich-Institut). Additionally, all plasmids coding for VP protein contained point mutation in the AAV2 binding site for HSPG resulting in the amino acid exchanges R585A and R588A.

The plasmids pssAAV-gRNA and pssAAV-spCas9 were kindly provided by Dirk Grimm (Heidelberg). The EF1α promoter in pssAAV-spCas9 was replaced with the miniature H1 promoter (Gao et al. 2021), followed by the coding sequence of the gRNA (GTCTCCGCTTCTTCCTGCCAT). For that, the H1 promoter and the gRNA sequence was excised from the plentiCas9-H1-99-gTATREV-U6-gGAG1-EGFP, which was kindly provided by Elena Herrera-Carrillo (Amsterdam, Netherland), and inserted into the backbone of pssAAV-spCas9 using PacI and AfeI restriction cloning. This modification resulted in the plasmid pssAAV-spCas9-gRNA, which was used for the production of F11-55.2-AAV-Cas9-gRNA.

Table 2: Primer sequences.

Primer	Number	Sequence (5’-3’)
PacI-S for	1	TTATTAATTAAATGTTCGTGTTTCTGGTG
SΔ19-SpeI rev	2	TATACTAGTTCTAGCAGCAGCTGCC
SfiI-F11 for	3	TGAAGACTAGTCGCACCGCCACCGCCCGCTGCTGCCTTTTGCAGCAC
F11-SpeI rev	4	CCATCACCAACTGCTTTCTG
SfiI-F11 for	5	GGCGGCCCAGCCGGCCAAGGACCTGGG
F11-linker rev	6	TACCCAGGTCCATGCTACCGCCACCGCCGCTACCGCCACCGCCCGAACCGCCACCGCCCGCTGCTGCCTT
Linker-55.2 for	7	AAGGCAGCAGCGGGCGGTGGCGGTTCGGGCGGTGGCGGTAGCGGCGGTGGCGGTAGCATGGACCTGGGTA
55.2-SpeI rev	8	AAGACTAGTCGCACCGCCACCGCCATTAAGCTTTTGCAGGATTTCAGCCAGG

Bsiwi-VP-linker for	9	CTCCCGTACGTCCTCGG
VP-linker-AgeI rev	10	TTAACCGGTGCTACCGCCACCGCCGCTACCGCCACCGCCCGATCGACTTGGAGTGTTTGTTCTGCTC
SfiI-55.2 for	11	GGCGGCCCAGCTGGCCGGTATGGACCTGG
55.2-linker rev	12	TTACCCAGGTCCGAACCGCCACCGCCCGAACCGCCACCGCCCGAACCGCCACCGCCATTAAGCTTTTGCAG
Linker-F11 for	13	CTGCAAAAGCTTAATGGCGGTGGCGGTTCGGGCGGTGGCGGTTCGGGCGGTGGCGGTTCGGACCTGGG
F11-SpeI rev	14	AAGACTAGTCGCACCGCCACCGCCCGCTGCTG

6.2.1.2 Restriction digest of DNA

DNA digests were performed to verify the correctness of plasmids or for subsequent cloning work. Digestion conditions were chosen according to the vendor of the selected restriction enzyme. Reactions were incubated for 2-4 h and the DNA was then analyzed on an agarose gel.

6.2.1.3 Polymerase chain reaction

Polymerase chain reaction (PCR) was used to amplify DNA fragments for molecular cloning. Q5® High Fidelity DNA Polymerase or Vent® DNA Polymerase, and sequence-specific primers were used to amplify and append the sequence to introduce linker or restriction sites. The PCR reaction was set up as described by the manufacturer of the polymerases. PCR products were analyzed and if necessary excised from agarose gels.

6.2.1.4 Agarose gel electrophoresis

To analyze DNA digestion and to recover DNA fragments of interest, agarose gel electrophoresis was performed. 0.8-1.2% agarose was dissolved in heated TAE buffer. Samples and marker (2log ladder or 1 kb Plus DNA ladder, 6 µl per lane) were mixed with loading dye and Midori Green to visualize the DNA. Gels were run at 100 V and DNA fragments were visualized using a FastGene Blue-Green LED Illuminator table.

6.2.1.5 DNA purification after gel electrophoresis or PCR

For the extraction of DNA from agarose gels, the fragment of interest was excised and dissolved in the binding buffer of the GeneJet® Gel Extraction Kit. Following the manufacturer's instructions, DNA was eluted in 30 µl water, stored at -20°C or directly used for further cloning steps.

6.2.1.6 DNA ligation and dephosphorylation

For the ligation of DNA with compatible ends, the fragment containing the antibiotic resistance cassette was dephosphorylated using 5 units of Antarctic Phosphatase and incubated for 1 h at 37°C. The phosphatase was then heat-inactivated at 80°C for 2 min prior to ligation. For ligation, the T4 DNA ligase was used. Backbone DNA was mixed with insert DNA at a molecular weight ratio of 1:3. The reaction was incubated for 1 h at 22°C and subsequently used for the transformation of competent bacteria.

6.2.1.7 Transformation of chemically competent bacteria

For the transformation of the *E. Coli* Top10 strand with ligated plasmids, bacteria were thawed from -80°C on ice for 20 min. 10 µl of ligation product was then added to the cells and bacteria were heat-shocked for one minute at 42°C. After the heat-shock, bacteria were cooled on ice for 3 min and 900 µl of SOC medium was added followed by 1 h incubation at 37°C while shaking at 600 rpm. 100 µl of the transformation was added to agar plates containing an appropriate antibiotic and incubated overnight. For retransformation, 1 µl of plasmid DNA was added to bacteria for 5 min at 37°C and transferred to an antibiotic-containing agar plate for overnight incubation at 37°C. On the following day, clones were picked and LB medium containing the corresponding antibiotics were inoculated. Cultures were grown overnight at 37°C with constant shaking at 180 rpm and harvested on the next day.

For the generation and amplification of AAV transfer plasmids, the incubation temperature was lowered from 37°C to 30°C, minimizing the risk of homologous recombination due to the repetitive ITR regions. In some cases, NEB® Stable Competent E. coli were used instead of the Top10 strain.

6.2.1.8 Plasmid DNA preparation

For small-scale plasmid purification from a cell culture volume of 5 ml, cells were centrifuged at 13,000 rpm for 1 min. DNA was extracted from the cell pellet following the instructions of the GeneJet® Mini Prep Kit. DNA was eluted in 50 µl of water and DNA concentration was determined by UV/Vis spectroscopy using a NanoDrop 2000 spectrophotometer. For large-scale plasmid purification, a bacteria culture volume of 250 ml was centrifuged at 4600 rpm for 20 min. DNA was extracted following the instructions of the Macherey-Nagel® NucleoBond® Xtra Midi Kit. DNA was eluted in 250 µl TE buffer and DNA concentration was adjusted to 1 mg/ml using the spectrophotometer. DNA was stored at -20°C.

6.2.1.9 DNA sequencing

DNA isolated from selected bacterial clones were analyzed for their DNA sequence utilizing the sequencing service of GATC Services Eurofins Genomics. For that 400-800 ng DNA was mixed with 2.5 µM of a compatible primer. Sequences were aligned to a reference plasmid map using SnapGene.

6.2.1.10 SDS-polyacrylamide gel electrophoresis

Sodium dodecyl sulfate-polyacrylamide gel electrophoresis (SDS-PAGE) was used to separate denatured proteins according to their molecular weight. For the detection of S in cell lysates, cells were detached by trypsin treatment, counted in a hemocytometer and 2x10^5 cells/lane were lysed in RIPA buffer supplemented with protease inhibitors for 1 h at 4°C. Following this, cell lysates were cleared by centrifugation and incubated with sample buffer at 95°C for 10 min. For the detection of S in vector particles, a defined number of particles were denatured at 95°C for 10 min in urea denaturation buffer. To analyze the impact of trypsin treatment on S-VLPs, 2x10^9 particles were incubated with 8 mg/ml trypsin for the indicated time period and immediately denatured at 95°C for 10 min in urea denaturation buffer. AAV vectors were lysed in urea denaturation buffer at 95°C for 10 min. Proteins were then either separated on a 10% or 4-15% gradient SDS polyacrylamide gel. Gradient gels were cast by aspirating 5 ml of the 15% polyacrylamide solution and then 5 ml of the 4% polyacrylamide solution into a serological 10 ml pipette. Both solutions were mixed by introducing a single air bubble at the tip of the pipette. 10 ml of the mixed solution were then transferred to the glass plates of the Mini-Protean® 3 cell chamber system. After polymerization, samples were separated at 80 V for 15 min and thereafter at 120 V.

Table 3: Composition of SDS polyacrylamide gels.

	5% stacking gel	10% resolving gel	4% for gradient gel	15% for gradient gel
30% acrylamide solution	750 µl	3 ml	1.6 ml	6 ml
H_2O	2.85 ml	2.5 ml	7.94 ml	1.32 ml
1 M Tris, pH 8.8	-	3.4 ml	-	4.5 ml
1 M Tris, pH 6.8	850 µl	-	2.28 ml	-
10% SDS	45 µl	90 µl	120 µl	120 µl
20% APS	37.5 µl	45 µl	60 µl	60 µl
TEMED	2 µl	7 µl	4.8 µl	4.8 µl

6.2.1.11 Western Blot

After separation by SDS-PAGE, proteins were transferred onto nitrocellulose membranes and analyzed by antibody staining. A discontinuous buffer system was used for the protein transfer onto nitrocellulose membranes. Whatman™ filter papers were soaked in cathode buffer, anode buffer I or anode buffer II. Then six filter papers soaked in cathode buffer were overlaid on the polyacrylamide gel followed by the nitrocellulose membrane, two filter papers incubated in anode buffer II and four filter papers soaked in anode buffer I. Proteins were transferred at 25 V for one hour using the Trans-Blot® SD semi-dry transfer cell. Thereafter, the membrane was blocked for 1 h in 10% horse serum. Antibodies used for the following immunostaining were diluted in TBS-T supplemented with 5% horse serum. For the detection of P24 and S, membranes were incubated with mouse anti-p24 (Clone 38/8.7.47, 1:1000, Gentaur) and the upper part was incubated with mouse anti-SARS-CoV-2 spike (Clone: 1A9, 1:1000, GeneTex) at 4°C overnight. On the following day, membranes were exposed to the secondary antibody rabbit anti-mouse conjugated to horseradish peroxidase (HRP) (1:2000, Dako) for 90 min at RT. For the detection of GAPDH, rabbit anti-GAPDH conjugated to HRP (1:1000, Cell Signaling) was used. For the detection of VP proteins and the conjugated myc-tag, mouse anti-AAV VP1/VP2/VP3 (Clone B1, 1:50, Progen) and mouse anti-myc tag (Clone Myc.A7, 1:1000, Abcam) were incubated with the membranes overnight at 4°C. Subsequently, the membranes were subjected to incubation with the secondary antibody as stated above for 2 h at RT.

Signals in Western blots were detected using the Pierce^{TM} ECL western blotting substrate and visualized on the MicroChemi imaging system. Image contrasts were adjusted retaining relative signal strength using ImageJ (Fiji).

6.2.2 Cell culture and virological methods

6.2.2.1 Generation and cultivation of cell lines

HEK293T (ATCC CRL-11268 or Lenti-X 293T from Takara Bio) and Vero E6 (ATCC) were cultivated in Dulbecco’s Modified Eagle’s Medium High Glucose (DMEM) supplemented with 10% fetal calve serum (FCS) and 2 mM L-glutamine.

For the generation of 293T-ACE2 and 293T-mock cells, HEK293T cells were seeded in T75 flasks and transfected with a mix combining 1 ml media supplemented with 60 µl of 18 mM PEI with 1 ml media containing 15 µg DNA of the pCMV-SP-Myc-ACE2 plasmid (for 293T-ACE2 cells) or pCDNA3.1 (+) (for 293T-mock cells). Media was exchanged 5 h after transfection and cells were used three days later for the transduction assay.

Vero-GFP cells were transduced with a VSVG-LV transferring eGFP under the control of the SFFV promoter. These cells were cultivated with DMEM supplemented with 10% fetal calve serum (FCS), 2 mM L-glutamine and 10 µg/ml puromycin.

SupT1-CD4 cells (DSMZ, ACC140) were maintained in advanced Roswell Park Memorial Institute (RPMI) 1640 medium supplemented with 4% FCS and and 2 mM L-glutamine. The SupT1-CD32a and SupT1-CD4/CD32a cell lines were generated and provided by Elena Herrera-Carrillo (Amsterdam, Netherlands). SupT1-CD32a and SupT1-CD4/CD32a were cultured in advanced RPMI supplemented with 4% FCS, 2 mM L-glutamine and 4 µg/ml puromycin.

MRC-5 cells (ATCC) were cultured in Minimal Essential Medium Eagle (MEM) supplemented with 10% FCS, 2 mM L-Glutamin and1x non-essential amino acids. Calu-3 cells (AddexBio) were cultured in MEM supplemented with 10% FCS, 2 mM L-Glutamin, 1x non-essential amino acids and 1x sodium pyruvate.

HEK293T and Vero E6 cells were subcultured twice a week at ratios between 1:8 and 1:10. SupT1 cells were subcultured twice a week at a ratio of 1:5. MRC-5 and Calu-3 were subcultured every two weeks at ratios between 1:2 and 1:3 and media was exchanged twice a week.

6.2.2.2 Primary cells

Human peripheral blood mononuclear cells (PBMC) were obtained from either healthy donors with informed consent or buffy coats acquired from DRK Blutspendedienst (Frankfurt, Germany) under the ethical approval of the Frankfurt University Hospital committee. The isolation of PBMC involved their separation from plasma and red blood cells through Histopaque® gradient centrifugation. For this, 25 ml of blood were mixed with 25 ml of PBS. 25 ml of the diluted blood were added on top of 15 ml Histopaque® and centrifuged at 1800 rpm in a swinging bucket rotor without breaks. After centrifugation, cells right above the Histopaque® layer were isolated, transferred to a new tube and filled up with PBS in order to wash cells. After centrifugation, PBS was added again and cells were centrifuged at 200 x g for 10 min to remove platelets. Remaining erythrocytes were lyzed by incubation in 0.86% ammonium chloride at 37°C for 10 min. PBMC were washed, aliquoted and frozen in FCS + 10% dimethyl sulfoxid (DMSO) in the gas phase of liquid nitrogen.

For T cell activation, cells were activated with anti-CD3 (1 µg/ml, Miltenyi Biotec) antibody coated on a plate and anti-CD28 (3 µg/ml, Miltenyi Biotec) was added to NutriT-media supplemented with 0.5% penicillin/streptomycin, 25 U/ml interleukin-7 (IL-7) and 50 U/ml interleukin-15 (IL-15). Cells were used for transduction experiments three days after activation.

6.2.2.3 Cryopreservation and thawing of cells

For cryopreservation, an appropriate number of cells was centrifuged and washed once using 10 ml of PBS and centrifugation at 300 x g for 5 min. The pellet was suspended in 1 ml freezing media consisting of FCS supplemented with 10% DMSO. Samples were then frozen in a Mr. Frosty™ container at -80°C for 24 h. Cells were then transferred to the gas phase of liquid nitrogen for long-term storage.

Cells were thawed quickly at 37°C in a water bath. Cell suspension was then transferred to 15 ml tubes with 12 ml pre-warmed medium and centrifuged at 300 x g for 5 min to remove remaining freezing medium. After centrifugation, cells were suspended in medium and transferred to an appropriate cell culture flask.

6.2.2.4 Production of LV and VLP vectors

For the production of lentiviral vectors, 2.2 - 2.5x10^7 HEK293T cells were seeded into T175 flasks. On the day of transfection, cell culture medium was replaced with 12 ml of DMEM media containing 15% FCS and 2 mM L-glutamine. For transfection, 35 µg of plasmid DNA was mixed into 2.3 ml DMEM per flask and added to 2.2 ml DMEM supplemented with 140 µl PEI solution. The plasmid-PEI mix was mixed thoroughly, incubated for 20 min and added to the seeded HEK293T cells. The media was changed to DMEM supplemented with 10% FCS and 2 mM L-glutamine 5 h after transfection.

For the production of S-LV, the plasmids encoding S (pCG-SARS-CoV-2-SΔ19 or pCG-SARS-CoV-2-S), transfer plasmid (pCMV-LacZ) and the packaging plasmid pCMVd8.9 were mixed in a ratio of 35:100:65. VSV-G pseudotyped LVs were produced accordingly using pMD2.G instead of the S encoding plasmid. For VLPs, the transfer plasmid was omitted, but the total amount of plasmid and the ratio of packaging to envelope plasmid were retained. 48 h after transfection, the cell culture medium was collected and filtered (0.45 µM). Particles were concentrated by centrifugation through a 20% sucrose cushion at 4,500 x g overnight. The pellet was suspended in PBS resulting in a 300-fold concentrated vector stock. The vector stocks were divided into aliquots and stored at -80°C.

6.2.2.5 Nanoparticle tracking analysis of S-LV, VSVG-LV, S-VLP and bald-VLP

Particle numbers and size distribution were evaluated through nanoparticle tracking analysis conducted with the NanoSight NS300. LVs and VLPs were diluted in 0.2 µm-filtered PBS to obtain a particle concentration of 30-60 particles per frame. Particles were measured in continuous flow using a syringe pump and data were obtained from technical quadruplicates.

6.2.2.6 Titration of LVs

5 µl of VSV-LV or SΔ19-LV were serially 5-fold diluted and 100 µl of the diluted vector was added to $1x10^4$ target cells seeded one day before in 100 µl of medium. β-galactosidase activity was measured three days after transduction.

6.2.2.7 Fusion assays and neutralization

HEK293T cells were transfected in T75 flasks. On the day of transfection, cell culture medium was replaced with 4.3 ml of DMEM medium containing 15% FCS and 2 mM L-glutamine. For this, a transfection mix was used combining 1 ml medium supplemented with 60 µl of 18 mM PEI with 1 ml medium containing 15 µg DNA.

For the cell-cell fusion assay, the transfection mix for effector cells contained a mixture of pCG-SARS-CoV-2-SΔ19 and pCMV-α, and target cells received a mix of pCMV-SP-Myc-ACE2 and pCMV-ω in a ratio of 1:1. For the FFWO assay, the transfection mix for one target cell population contained pCMV-SP-Myc-ACE2 and pCMV-α, while the other contained pCMV-SP-Myc-ACE2 and pCMV-ω at a ratio of 1:1. The total plasmid amounts for effector cells receiving reduced amounts of S-plasmid were compensated using an empty plasmid (pCDNA3.1 (+)). After mixing thoroughly and incubating for 20 min, 2 ml of the transfection mix was added to the cells. The medium was exchanged 5 h after transfection. Cells were detached two days after transfection by trypsin or PBS/EDTA treatment. Cells were counted using a Luna-FI cell counter, pelleted at 300 x g for 5 min and resuspended in a cell density of $5x10^4$ in 20 µl.

Cocultures were setup in V-bottom plates at $1x10^5$ cells per well in 40 µl. To allow for close cell-to-cell contacts cocultures were centrifuged for a short period of time (300 x g for 30 s). For the FFWO assay the indicated VLPs were added to the coculture and mixed before centrifugation. For trypsin treatment of VLPs used for the FFWO assay, a final concentration of 2.5 mg/ml trypsin was added to VLPs in PBS for the indicated time period. Trypsin was then inactivated by FCS in the cell culture medium after adding the treated VLPs to the target cells. For the transduction of target cells with LVs, $2x10^4$ cells/well were seeded into a flat-bottom 96-well plate. After attachment of the adherent cells overnight, 0.2 µl of S-LV or VSVG-LV were added to cells.

For FFWO neutralization, $5x10^8$ particles/well were incubated with antibodies or sera for 30 min in the incubator before addition to the coculture. LV particles were incubated for 30-60 min with antibody or sera. For neutralization of cell-cell fusions, effector cells were incubated for 30 min with sera or antibody before mixing with target cells.

6.2.2.8 Sera and S-neutralizing antibodies

Sera were obtained with informed consent and received approval from the local ethics committee at Frankfurt University Hospital. The sera originated from two convalescent patients previously diagnosed with SARS-CoV-2 through PCR testing of throat swabs approximately four months prior to donation. Both patients had experienced mild symptoms during their illness. As a negative control, a commercially available pool of human off-the-clot sera (PAN Biotech) was used. For positive controls, a commercially available neutralizing antibody against SARS-CoV-2 (Clone 001, Sino Biological, 40592-R001) and the corresponding normal control (Clone CR1, Sino Biological) were used.

6.2.2.9 Luminescence assay to determine beta-galactosidase activity

To quantify reporter-complementation after employing the FFWO, cell-cell fusion assays or to determine reporter expression after transduction with LVs, cells were pelleted in V-bottom plates at 300 x g for 5 min. The supernatant was removed and 50 µl/well of lysis buffer, which is a component of the Galactostar assay kit, was added. Plates were then agitated on an orbital shaker at 450 rpm at RT for 10 min and subsequently frozen at -80°C.

The activity of the beta-galactosidase reporter was quantified using the Galactostar assay kit. Frozen samples were thawed at RT and mixed thoroughly on an orbital shaker. 10 µl of the lysates was incubated with 50 µl of the Galactostar working solution in white flat-bottom plates. After an incubation of 30-60 min at RT in the dark, luminescence was measured on an Orion II plate luminometer (Berthold Systems) with an exposure time of 0.1 s per well.

6.2.2.10 Cell staining for laser scanning microscopy

To analyze syncytia formation mediated by S, Vero E6 cells stably expressing GFP, were generated through LV-mediated transduction followed by puromycin selection. HEK293T cells were co-transfected with plasmids encoding RFP and either SΔ19 or full-length S. $5x10^4$ transfected HEK293T cells were seeded in chamber slides and allowed to attach overnight. The following day, $5x10^4$ Vero-GFP cells were added. Seven hours after co-culture set up, the cells were fixed with 4% paraformaldehyde (PFA), permeabilized using 0.5% Triton X-100 in PBS and blocked with 1% BSA/PBS for 15 min. Subsequently, the cells were stained with phalloidin-Atto633 (1:500, Sigma Aldrich) and HOECHST3342 (1:10,000, Sigma Aldrich) for 1 h at RT before being imaged on an SP8 Lightning laser scanning microscope (Leica) equipped with a HC PL APO CS2 40x/1.30 lens.

6.2.2.11 Infection of Vero and 293T cells with SARS-CoV-2

Bevan Sawatsky (Paul-Ehrlich-Institut) infected 293T and Vero cells with SARS-CoV-2 (Wuhan Hu-1 strain (Hennrich et al. 2021)) at a MOI of 1. After inactivation, the samples were received and prepared for SDS-PAGE followed by Western blot analysis to determine S levels in cells.

6.2.2.12 Antibody staining for flow cytometry

For S-mediated fusion assays, $1x10^5$ HEK293T effector cells were stained for surface expression of the S protein. Cell suspensions were washed in a wash buffer. The S protein was stained using the mouse IgG1 anti-SARS-CoV-2 spike antibody (Clone 1A9, 1 µl per $1x10^5$ cells, GeneTex) for 45 min at 4°C. This was followed by incubation with the secondary antibody anti-IgG1-PE (Clone REA1017, 1 µl per $1x10^5$ cells, Miltenyi Biotec) for 30 min at 4°C. Viability of the cells was assessed using a fixable viability dye eFluor780 (1:1000, eBioscience). Lastly, cells were fixed in 1% PFA in PBS and analyzed by flow cytometry using the MACSQuant Analyzer 10x (Miltenyi Biotec).

For the staining of cells incubated with AAV vectors, up to $5x10^5$ cells were transferred to micronic tubes and washed twice with wash buffer prior to staining. Cells in the whole blood assay, *in vitro* transduced SupT1 cells and cells used for the binding assay underwent staining using a mix of fluorophore conjugated antibodies and the viability dye eFluor780 for 20 min at 4°C. Cells isolated from mice were treated with anti-mouse FC block (Miltenyi Biotec) to prevent unspecific binding of antibodies prior to the antibody staining. All cells were washed twice in wash buffer and were fixed in 1% PFA in PBS before being analyzed by flow cytometry using the MACSQuant Analyzer 10x (Miltenyi Biotec).

6.2.2.13 Production of AAV vectors

AAV2 and receptor-targeted AAVs were produced by transient transfection of HEK293T cells. For this, 1.8 - $2x10^7$ of HEK293T cells were seeded in a 15 cm dish 24 h before transfection and the cell culture medium was replaced with 12 ml of DMEM media containing 15% FCS and 2 mM L-glutamine, on the next morning. The transfection mix comprised 30 µg of total DNA per dish, combined in 2 ml of DMEM without supplements. This mixture was then combined with 1.9 ml of DMEM supplemented with 120 µl of 18 mM polyethylenimine (PEI) solution, mixed thoroughly and incubated for 20 min. Subsequently, 4 ml of the transfection mix per dish was added to the seeded HEK293T cells and the medium was changed after 5 h to 18 ml DMEM supplemented with 10% FCS and 2 mM L-glutamine.

To produce AAV2, a mixture consisting of the helper plasmid pXX6-80, Rep/Cap plasmid pRC22 and the self-complementary transfer plasmid pscAAV-GFP was combined in a ratio of 60:20:20. For the production of targeted vectors, pXX6-80, transfer-, complementary- and targeting-plasmids were mixed in a ratio of 15:5:5:5.

48 h after transfection, cells from five to ten dishes were scraped off, pelleted at 1,800 x g for 30 min at 4°C and the pellet was lysed using Tris/HCl/NaCl (pH 8.5). The lysate underwent three freeze-thaw cycles in liquid nitrogen and was subsequently digested with Benzonase (50 U/ml) for 30 min at 37°C. The lysate was centrifuged at 3,700 x g for 20 min at 4°C and the supernatant was loaded onto a gradient containing 4 ml 15%, 2 ml 25%, 1.6 ml 40% and up to 2.8 ml 60% iodixanol layered on top of each other (see Table 4). After centrifugation for 2 h at 290,000 x g in a 70Ti rotor, full AAV particles were harvested from the 40% iodixanol layer. In some cases, AAV vectors were buffer-exchanged to PBS supplemented with 0.001% Pluronic (Poloxamer 188) by ultrafiltration in Amicon Ultra-4 50 kDa cut-off size exclusion filters and centrifugation at 2000 x g. For Western Blot analysis, cell culture media of transfected cells in one 15 cm dish were collected (~18 ml), filtered (0.45 µm) and digested with 50 U/ml Benzonase. AAV vectors were then pelleted by centrifugation through a 40% sucrose cushion in TNE buffer at 100,000 x g for 16 h. The pellet was suspended in 300 µl PBS resulting in a 60-fold concentrated vector stock which was aliquoted and stored at -80°C.

Table 4: Composition of the iodixanol layers for AAV gradient purification

	15% iodixanol	25% iodixanol	40% iodixanol	60% iodixanol
PBS (10x)	400 µl	300 µl	300 µl	-
NaCl (5 M)	800 µl	-	-	-
$MgCl_2$ (1 M)	4 µl	3 µl	3 µl	3 µl
KCl (1 M)	10 µl	8 µl	8 µl	8 µl
Phenol red (0.5%)	15 µl	12 µl	-	12 µl
H_2O	1.77 ml	1.43 ml	690 µl	-
Optiprep^{TM} (60%)	1 ml	1.25 ml	2 ml	3 ml

6.2.2.14 Analysis of AAV vector genome copies

To analyze the AAV vector genome copies using qPCR, 3 µl of vector stocks were lyzed and DNA isolated following the instructions of the DNeasy Blood and Tissue kit (Qiagen). The elution of DNA was performed in 200 µl in elution buffer and 5 µl was used for qPCR using ITR-specific primers (5′GGAACCCCTAGTGATGGAGTT3′, 5′CGGCCTCAGTGAGCGA3′)

along with a probe (5′6FAM-CACTCCCTCTCTGCGCGCTCG-TAMRA3’). 200 nM of primer and probe were mixed with template DNA and 15 µl of 1x LightCycler 480 Probes Master mix. Signal amplification was measured on the LightCycler 480 II Real-Time PCR System from Roche.

6.2.2.15 Cryo-electron tomography

To analyze the capsid morphology of DARPin-modified AAVs, targeted AAV were produced and characterized. These particles were transferred to Petr Chlanda (Heidelberg) for cryo-ET analysis. The image contrast of the received images was optimized using ImageJ (Fiji).

6.2.2.16 Electron-microscopy

To analyze the full-empty ratios of the produced AAV stocks, AAVs were handed over to Fabian John (Paul-Ehrlich-Institut) for negative contrast staining and acquisition of the images. Image contrast was optimized using ImageJ (Fiji). Then full and empty particles were counted from at least four images per vector stock.

6.2.2.17 Thermostability of AAVs

To assess the thermostability of DARPin modified capsids, AAV vectors were produced, characterized and transferred to Fabian John (Paul-Ehrlich-Institut) for measurement at the Prometheus (Nanotemper). Received data were visualized in GraphPad Prism.

6.2.2.18 Transduction with AAV vectors

AAV vectors were diluted in cell culture media to the desired number of genome copies as determined by qPCR. 100 µl of the diluted AAVs were added to cells seeded in 100 µl of media and mixed by pipetting. GFP expression was analyzed by flow cytometry three days after vector addition.

6.2.2.19 Titration of AAV vector stocks

To determine the gene transfer activity of produced vector stocks, AAVs were titrated on SupT1 cells. Equal genome copies of AAV vector stocks were serially diluted 5-fold in cell culture media and 100 µl of the dilution was added to target cells seeded in 100 µl of media. Suspension cells incubated with vector particles were mixed by pipetting and cultured for three days until GFP expression was determined by flow cytometry. Afterwards, values for the percentage of GFP-expressing cells showing linear correlation to the dilution factor were used to determine transducing units (TU) per 1x10^5 genome copies (GC) using the equations 1 and 2:

$$1)\ TU\ per\ 1\times10^5\ GC = \frac{\frac{\%\ GFP}{100}}{initial\ GC} \times seeded\ cell\ number\ \times dilution\ factor\ \times\ scaling\ factor$$

$$2)\ scaling\ factor = \frac{initial\ GC}{1\times10^5}$$

6.2.2.20 Transduction of cocultured SupT1 cells

Cocultures of SupT1 cells were prepared by mixing CD4-, CD32a- and CD4/CD32a-expressing cells in a ratio of 1:1:1 at a cell concentration of 3x10^4 cells/100 µl. For serial dilution, half of the 1:1:1 coculture was added to a 1:1 coculture of SupT1-CD4 and SupT1-CD32a cells resulting in a twofold dilution of the SupT1-CD4/CD32a cells, and so on. For cocultures containing 2% double-positive cells, 600 SupT1-CD47CD32a were mixed with 1.47x10^4 each of SupT1-CD32a and SupT1-CD4 cells at a cell concentration of 3x10^4 cells/100 µl. After that, 100 µl of each coculture was seeded and transduced with AAVs.

6.2.2.21 Subcellular fractionation

A total of 1x10^{10} SupT1-CD4/CD32a cells were pre-chilled for 10 min at 4°C, followed by incubation with 3x10^{10} genome copies of the respective AAV stock for 10 min at 4°C. Unbound particles were removed by washing in PBS and in 1 ml medium. Subsequently, cells were transferred to 48-well plates and incubated for 2 h at 37°C to enable vector endocytosis. After incubation, cells were washed again with PBS and processed using the subcellular fractionation kit. DNA was isolated from all fractions using the DNeasy 96 Blood and Tissue kit (Qiagen) and eluted in 200 µl elution buffer. For quantification, 5 µl of the eluate was used to determine the amount of GFP-encoding vector genomes by qPCR using primers 5′ATCATGGCCGACAAGCAGAA3′, 5′TCTCGTTGGGGTCTTTGCTC3′ and probe 5′Cy5-CGGCCCCGTGCTGCTGCCCGA-BHQ3-3’. 200 nM of primer and probe were mixed with template DNA and 15 µl of 1x Light Cycler 480 Probes Master Mix. Signal amplification was measured at the LightCycler 480 II Real-Time PCR System from Roche.

6.2.2.22 AAV binding assay on non-activated PBMC

PBMCs were thawed, washed twice in RPMI media and $1x10^5$ cells in 50 µl were incubated $5x10^{10}$ AAV GC in a total volume of 100 µl. Cells were incubated for 2 h at 37°C and thoroughly mixed every 30 min to allow for vector binding. After incubation, cells were washed twice in wash buffer and incubated in anti-human Fc block to prevent unspecific binding of the antibodies. Then, cells were washed twice and incubated with anti-AAV2 (Clone A20, 2 µl per sample, Progen) for 30 min at 37°C. This was followed by one washing step prior to the incubation with the secondary antibody anti-mouse IgG conjugated to AlexaFluor647 (0.5 µl/sample, Jackson ImmunoResearch) for 20 min at 4°C to detect AAV bound cells. Three wash steps were used to ensure the absence of unbound secondary antibody, followed by incubation with conjugated antibodies as described in the chapter 'Antibody staining for flow cytometry'.

6.2.2.23 Transduction of primary cells with AAV vectors

AAV vector stocks were produced, characterized and transferred to Burak Demircan (Paul-Ehrlich-Institut) for titration on primary activated PBMC. After transduction, cells were analyzed by flow cytometry and results were visualized by GraphPad Prism.

6.2.2.24 Whole blood assay

400 µl of human whole blood from healthy anonymous donors were collected in BD Vacutainer® CPT™ blood collection tubes containing 0.1 M sodium citrate to inhibit blood coagulation. In a 48-well plate blood was combined with $1x10^4$ SupT1-CD4/CD32a cells and $8x10^8$ GC of the respective AAV and the mixture was agitated at 400 rpm for 6 h in an incubator to allow for cell entry of the vector particles. Following this, the blood was diluted with 600 µl PBS and layered on 800 µl Histopaque®. After centrifugation for 30 min at 1800 x g at RT, mononuclear cells and SupT1 cells were isolated from a layer on top of the Histopaque®. The cells were washed twice in PBS and platelets were removed by slow centrifugation at 200 x g for 10 min. These washing steps also ensure the removal of extracellular AAV particles. After centrifugation the pellet was suspended in 200 µl NutriT supplemented with IL-7, IL-15 and anti-CD28 antibodies and transferred to anti-CD3 coated 48-well plates for T-cell activation.

6.2.2.25 Inhibition of HIV replication

The AAVs F11-AAV-Cas9, F11-AAV-gRNA and F11-55.2-AAV-Cas9-gRNA were produced, characterized and transferred to Elena Herrera-Carrillo and Mariano Molina at the University of Amsterdam (Netherlands) for performing the HIV inhibition experiment. Received data was visualized in GraphPad Prism.

6.2.3 Animal experiments

All animal experiments were performed in accordance with the regulations of the German animal protection law and the respective European Union guidelines under authorization of the local authority (F107/2007). Four- to five-week-old NSG (NOD.Cg-Prkdc^{scid} Il2rg^{tm1Wjl}) mice were purchased from Charles River and housed in individually ventilated cages. Mice were taken into an experiment earliest one week after arrival. Mice were monitored regularly.

6.2.3.1 Cell and vector administration

SupT1 and Hut78 cells were thawed at least one week before injection and subcultured twice. On the day of injection, the cells were washed twice and counted using the Luna-Fl cell counter. Cells were mixed in equal ratios and resuspended in an appropriate amount of PBS. For the intravenous (i.v.) injection, mice were restrained and 200 µl cell-containing PBS was injected into the tail vein of each mouse.

After cell engraftment, the mice were injected i.v. with AAV vectors. For that, the vector stocks were thawed on ice and equilibrated at RT. The required vector volume was adjusted with PBS for the injection of 200 µl solution per mouse.

6.2.3.2 Blood cell sampling

Mice were anesthetized with 3% isoflurane and blood was taken retroorbitally using thin glass capillaries. Blood was then quickly transferred to collection tubes containing heparin to prevent blood clogging. Cells within the blood were then centrifuged and washed once with 1 ml PBS and centrifuged at 300 x g for 3 min. Erythrocytes were then lysed by resuspending the pellet in 10 ml of BD pharm lysing solution for 10 min at RT. Cells were washed twice before staining for flow cytometry analysis.

6.2.3.3 Isolation of single cells from bone marrow

After blood collection, anesthetized mice were killed by cervical dislocation. Hip bones, femur and tibia were removed and stored in RPMI at RT until further processing. Cells were isolated from bones by cutting open both ends and centrifuging at 7000 rpm for 3 min in a perforated 0.5 ml tube stacked in a 1.5 ml tube. Cell pellets were suspended in 1 ml PBS and large cell clusters were removed by filtration through a cell strainer (70 µm). Cells were transferred to 50 ml tubes and washed with 13 ml PBS. Erythrocytes were then lysed by resuspending the pellet in 5 ml of BD pharm lysing solution for 15 min at RT. Cells were washed twice and counted before being processed for flow cytometry staining or freezing in FCS supplemented with 10% DMSO.

6.2.3.4 Single cell isolation from spleen

Spleens were isolated from sacrificed mice and kept in RPMI until further processing. Single cells were prepared by grinding the spleen through a 70 µm cell strainer. To recover most of the spleen cells, the cell strainer was washed several times with PBS and single cells were transferred to 50 ml tubes. Cells were centrifuged at 300 x g for 5 min and the pellet was treated with 5 ml of BD pharm lysing solution for 6 min at RT. Cells were washed twice and counted before being processed for flow cytometry staining or freezing in FCS supplemented with 10% DMSO.

6.2.3.5 Single cell isolation from liver

Liver lobes were isolated from sacrificed mice and the gallbladder was removed. Single cells were prepared by according to the instructions of the liver dissociation kit from Miltenyi Biotec using the gentleMACS Dissociator. After dissociation of liver tissue cells were filtered through a 70 µm cell strainer. Cells were washed twice and counted before processed for flow cytometry staining or freezing in FCS supplemented with 10% DMSO.

6.2.4 Statistical analysis

Statistical analysis was carried out in GraphPad Prism 8. Statistical tests are indicated within each figure legends and differences were considered statistically significant at $p<0.05$.

7 References

Abdel-Mohsen, Mohamed; Kuri-Cervantes, Leticia; Grau-Exposito, Judith; Spivak, Adam M.; Nell, Racheal A.; Tomescu, Costin et al. (2018): CD32 is expressed on cells with transcriptionally active HIV but does not enrich for HIV DNA in resting T cells. In *Sci Transl Med* 10 (437). DOI: 10.1126/scitranslmed.aar6759.

Abdul, Fabien; Ribaux, Pascale; Caillon, Aurélie; Malézieux-Picard, Astrid; Prendki, Virginie; Vernaz, Nathalie et al. (2022): A Cellular Assay for Spike/ACE2 Fusion: Quantification of Fusion-Inhibitory Antibodies after COVID-19 and Vaccination. In *Viruses* 14 (10). DOI: 10.3390/v14102118.

Adams, Philipp; Fievez, Virginie; Schober, Rafaëla; Amand, Mathieu; Iserentant, Gilles; Rutsaert, Sofie et al. (2021): CD32+CD4+ memory T cells are enriched for total HIV-1 DNA in tissues from humanized mice. In *iScience* 24 (1), p. 101881. DOI: 10.1016/j.isci.2020.101881.

Ahn, Ji Hoon; Kim, JungMo; Hong, Seon Pyo; Choi, Sung Yong; Yang, Myung Jin; Ju, Young Seok et al. (2021): Nasal ciliated cells are primary targets for SARS-CoV-2 replication in the early stage of COVID-19. In *The Journal of clinical investigation* 131 (13). DOI: 10.1172/JCI148517.

Albanese, Manuel; Chen, Hong-Ru; Gapp, Madeleine; Muenchhoff, Maximilian; Yang, Hsiu-Hui; Petterhoff, David et al. (2023): Autoantibody-Enhanced, CD32-Driven Trogocytosis Creates Functional Plasticity of Immune Cells and is Hijacked by HIV-1 to Infect Resting CD4 T Cells.

Alevy, Y. G.; Tucker, J.; Mohanakumar, T. (1992): CD32A (Fc gamma RIIa) mRNA expression and regulation in blood monocytes and cell lines. In *Mol. Immunol.* 29 (11), pp. 1289–1297. DOI: 10.1016/0161-5890(92)90165-t.

Apaa, Ternenge; Withers, Amy J.; Staley, Ceri; Blanchard, Adam; Bennett, Malcolm; Bremner-Harrison, Samantha et al. (2023): Sarbecoviruses of British horseshoe bats; sequence variation and epidemiology. In *J. Gen. Virol* 104 (6). DOI: 10.1099/jgv.0.001859.

Astorga-Gamaza, Antonio; Grau-Expósito, Judith; Burgos, Joaquín; Navarro, Jordi; Curran, Adrià; Planas, Bibiana et al. (2022): Identification of HIV-reservoir cells with reduced susceptibility to antibody-dependent immune response. In *eLife* 11. DOI: 10.7554/eLife.78294.

Badia, Roger; Ballana, Ester; Castellví, Marc; García-Vidal, Edurne; Pujantell, Maria; Clotet, Bonaventura et al. (2018): CD32 expression is associated to T-cell activation and is not a marker of the HIV-1 reservoir. In *Nature communications* 9 (1), p. 2739. DOI: 10.1038/s41467-018-05157-w.

Badraoui, Riadh; Alrashedi, Mousa M.; El-May, Michèle Véronique; Bardakci, Fevzi (2021): Acute respiratory distress syndrome: a life threatening associated complication of SARS-CoV-2 infection inducing COVID-19. In *J. Biomol. Struct. Dyn.* 39 (17), pp. 6842–6851. DOI: 10.1080/07391102.2020.1803139.

Baker, Rachel E.; Mahmud, Ayesha S.; Miller, Ian F.; Rajeev, Malavika; Rasambainarivo, Fidisoa; Rice, Benjamin L. et al. (2022): Infectious disease in an era of global change. In *Nat. Rev. Microbiol.* 20 (4), pp. 193–205. DOI: 10.1038/s41579-021-00639-z.

Bar-On, Yinon M.; Flamholz, Avi; Phillips, Rob; Milo, Ron (2020): SARS-CoV-2 (COVID-19) by the numbers. In *eLife* 9. DOI: 10.7554/eLife.57309.

Barré-Sinoussi, F.; Chermann, J. C.; Rey, F.; Nugeyre, M. T.; Chamaret, S.; Gruest, J. et al. (1983): Isolation of a T-lymphotropic retrovirus from a patient at risk for acquired immune deficiency syndrome (AIDS). In *Science* 220 (4599), pp. 868–871. DOI: 10.1126/science.6189183.

Baselga, Marta; Güemes, Antonio; Alba, Juan J.; Schuhmacher, Alberto J. (2022): SARS-CoV-2 Droplet and Airborne Transmission Heterogeneity. In *J. Clin. Med.* 11 (9). DOI: 10.3390/jcm11092607.

Bashiri Dezfouli, Ali; Yazdi, Mina; Pockley, Alan Graham; Khosravi, Mohammad; Kobold, Sebastian; Wagner, Ernst; Multhoff, Gabriele (2021): NK Cells Armed with Chimeric Antigen Receptors (CAR): Roadblocks to Successful Development. In *Cells* 10 (12). DOI: 10.3390/cells10123390.

Bast, Elizabeth; Tang, Fei; Dahn, Jason; Palacio, Ana (2021): Increased risk of hospitalisation and death with the delta variant in the USA. In *Lancet Infect. Dis.* 21 (12), pp. 1629–1630. DOI: 10.1016/S1473-3099(21)00685-X.

Becker, Jonas; Fakhiri, Julia; Grimm, Dirk (2022): Fantastic AAV Gene Therapy Vectors and How to Find Them-Random Diversification, Rational Design and Machine Learning. In *Pathogens* 11 (7). DOI: 10.3390/pathogens11070756.

Belouzard, Sandrine; Chu, Victor C.; Whittaker, Gary R. (2009): Activation of the SARS coronavirus spike protein via sequential proteolytic cleavage at two distinct sites. In *Proceedings of the National Academy of Sciences of the United States of America* 106 (14), pp. 5871–5876. DOI: 10.1073/pnas.0809524106.

Bender, Ruben R.; Muth, Anke; Schneider, Irene C.; Friedel, Thorsten; Hartmann, Jessica; Pluckthun, Andreas et al. (2016): Receptor-Targeted Nipah Virus Glycoproteins Improve

Cell-Type Selective Gene Delivery and Reveal a Preference for Membrane-Proximal Cell Attachment. In *PLoS Pathog* 12 (6), e1005641. DOI: 10.1371/journal.ppat.1005641.

Bianchi, Matteo; Reichen, Christian; Fischer, Stefanie; Grübler, Yvonne; Eggenschwiler, Aline; Marpakwar, Rajlakshmi et al. (2022): MP0533: A Multispecific Darpin CD3 Engager Targeting CD33, CD123, and CD70 for the Treatment of AML and MDS Designed to Selectively Target Leukemic Stem Cells. In *Blood* 140 (Supplement 1), pp. 2251–2252. DOI: 10.1182/blood-2022-163075.

Bryant, Laura M.; Christopher, Devin M.; Giles, April R.; Hinderer, Christian; Rodriguez, Jesse L.; Smith, Jenessa B. et al. (2013): Lessons learned from the clinical development and market authorization of Glybera. In *Hum Gene Ther Clin Dev* 24 (2), pp. 55–64. DOI: 10.1089/humc.2013.087.

Buchrieser, Julian; Dufloo, Jérémy; Hubert, Mathieu; Monel, Blandine; Planas, Delphine; Rajah, Maaran Michael et al. (2020): Syncytia formation by SARS-CoV-2-infected cells. In *EMBO J*, e106267. DOI: 10.15252/embj.2020106267.

Bussani, Rossana; Schneider, Edoardo; Zentilin, Lorena; Collesi, Chiara; Ali, Hashim; Braga, Luca et al. (2020): Persistence of viral RNA, pneumocyte syncytia and thrombosis are hallmarks of advanced COVID-19 pathology. In *EBioMedicine* 61, p. 103104. DOI: 10.1016/j.ebiom.2020.103104.

Cantero-Pérez, Jon; Grau-Expósito, Judith; Serra-Peinado, Carla; Rosero, Daniela A.; Luque-Ballesteros, Laura; Astorga-Gamaza, Antonio et al. (2019): Resident memory T cells are a cellular reservoir for HIV in the cervical mucosa. In *Nat Commun* 10 (1), p. 4739. DOI: 10.1038/s41467-019-12732-2.

Chomont, Nicolas; El-Far, Mohamed; Ancuta, Petronela; Trautmann, Lydie; Procopio, Francesco A.; Yassine-Diab, Bader et al. (2009): HIV reservoir size and persistence are driven by T cell survival and homeostatic proliferation. In *Nat Med* 15 (8), pp. 893–900. DOI: 10.1038/nm.1972.

Clavel, F.; Charneau, P. (1994): Fusion from without directed by human immunodeficiency virus particles. In *Journal of Virology* 68 (2), pp. 1179–1185. DOI: 10.1128/JVI.68.2.1179-1185.1994.

Colby, Donn J.; Trautmann, Lydie; Pinyakorn, Suteeraporn; Leyre, Louise; Pagliuzza, Amélie; Kroon, Eugène et al. (2018): Rapid HIV RNA rebound after antiretroviral treatment interruption in persons durably suppressed in Fiebig I acute HIV infection. In *Nat Med* 24 (7), pp. 923–926. DOI: 10.1038/s41591-018-0026-6.

Cox, Robert M.; Plemper, Richard K. (2017): Structure and organization of paramyxovirus particles. In *Curr Opin Virol* 24, pp. 105–114. DOI: 10.1016/j.coviro.2017.05.004.

Craigie, Robert; Bushman, Frederic D. (2012): HIV DNA integration. In *Cold Spring Harb. Perspect. Med.* 2 (7), a006890. DOI: 10.1101/cshperspect.a006890.

Cureton, David K.; Massol, Ramiro H.; Saffarian, Saveez; Kirchhausen, Tomas L.; Whelan, Sean P. J. (2009): Vesicular stomatitis virus enters cells through vesicles incompletely coated with clathrin that depend upon actin for internalization. In *PLoS Pathog.* 5 (4), e1000394. DOI: 10.1371/journal.ppat.1000394.

Darcis, Gilles; Berkhout, Ben; Pasternak, Alexander O. (2019): The Quest for Cellular Markers of HIV Reservoirs: Any Color You Like. In *Front Immunol* 10, p. 2251. DOI: 10.3389/fimmu.2019.02251.

Darcis, Gilles; Kootstra, Neeltje A.; Hooibrink, Berend; van Montfort, Thijs; Maurer, Irma; Groen, Kevin et al. (2020): CD32+CD4+ T Cells Are Highly Enriched for HIV DNA and Can Support Transcriptional Latency. In *Cell reports* 30 (7), 2284-2296.e3. DOI: 10.1016/j.celrep.2020.01.071.

Das, Atze T.; Binda, Caroline S.; Berkhout, Ben (2019): Elimination of infectious HIV DNA by CRISPR-Cas9. In *Curr Opin Virol* 38, pp. 81–88. DOI: 10.1016/j.coviro.2019.07.001.

Descours, Benjamin; Petitjean, Gaël; López-Zaragoza, José-Luis; Bruel, Timothée; Raffel, Raoul; Psomas, Christina et al. (2017): CD32a is a marker of a CD4 T-cell HIV reservoir harbouring replication-competent proviruses. In *Nature* 543 (7646), pp. 564–567. DOI: 10.1038/nature21710.

Dubé, Mathieu; Tastet, Olivier; Dufour, Caroline; Sannier, Gérémy; Brassard, Nathalie; Delgado, Gloria-Gabrielle et al. (2023): Spontaneous HIV expression during suppressive ART is associated with the magnitude and function of HIV-specific CD4+ and CD8+ T cells. In *Cell Host Microbe* 31 (9), 1507-1522.e5. DOI: 10.1016/j.chom.2023.08.006.

Dudek, Amanda M.; Zabaleta, Nerea; Zinn, Eric; Pillay, Sirika; Zengel, James; Porter, Caryn et al. (2020): GPR108 Is a Highly Conserved AAV Entry Factor. In *Mol. Ther.* 28 (2), pp. 367–381. DOI: 10.1016/j.ymthe.2019.11.005.

Dufour, Caroline; Gantner, Pierre; Fromentin, Rémi; Chomont, Nicolas (2020): The multifaceted nature of HIV latency. In *The Journal of clinical investigation* 130 (7), pp. 3381–3390. DOI: 10.1172/JCI136227.

Eichhoff, Anna Marei; Börner, Kathleen; Albrecht, Birte; Schäfer, Waldemar; Baum, Natalie; Haag, Friedrich et al. (2019): Nanobody-Enhanced Targeting of AAV Gene Therapy Vectors. In *Mol Ther Methods Clin Dev* 15, pp. 211–220. DOI: 10.1016/j.omtm.2019.09.003.

Einkauf, Kevin B.; Osborn, Matthew R.; Gao, Ce; Sun, Weiwei; Sun, Xiaoming; Lian, Xiaodong et al. (2022): Parallel analysis of transcription, integration, and sequence of single HIV-1 proviruses. In *Cell* 185 (2), 266-282.e15. DOI: 10.1016/j.cell.2021.12.011.

Elmore, Zachary C.; Patrick Havlik, L.; Oh, Daniel K.; Anderson, Leif; Daaboul, George; Devlin, Garth W. et al. (2021): The membrane associated accessory protein is an adeno-associated viral egress factor. In *Nat. Commun.* 12 (1), p. 6239. DOI: 10.1038/s41467-021-26485-4.

EU gets first hemophilia B gene therapy (2023). In *Nat. Biotechnol.* 41 (4), p. 438.

Falke, D.; Knoblich, A.; Müller, S. (1985): Fusion from without induced by herpes simplex virus type 1. In *Intervirology* 24 (4), pp. 211–219. DOI: 10.1159/000149645.

Fan, Minghui; Berkhout, Ben; Herrera-Carrillo, Elena (2022): A combinatorial CRISPR-Cas12a attack on HIV DNA. In *Mol Ther Methods Clin Dev* 25, pp. 43–51. DOI: 10.1016/j.omtm.2022.02.010.

Fan, Xiaoyi; Cao, Duanfang; Kong, Lingfei; Zhang, Xinzheng (2020): Cryo-EM analysis of the post-fusion structure of the SARS-CoV spike glycoprotein. In *Nat Commun* 11 (1), p. 3618. DOI: 10.1038/s41467-020-17371-6.

Fauci, Anthony S. (2003): HIV and AIDS: 20 years of science. In *Nat. Med.* 9 (7), pp. 839–843. DOI: 10.1038/nm0703-839.

Fenwick, Craig; Turelli, Priscilla; Pellaton, Céline; Farina, Alex; Campos, Jérémy; Raclot, Charlène et al. (2021): A high-throughput cell- and virus-free assay shows reduced neutralization of SARS-CoV-2 variants by COVID-19 convalescent plasma. In *Sci Transl Med* 13 (605). DOI: 10.1126/scitranslmed.abi8452.

Ferren, Marion; Horvat, Branka; Mathieu, Cyrille (2019): Measles Encephalitis: Towards New Therapeutics. In *Viruses* 11 (11). DOI: 10.3390/v11111017.

Filion, Lionel G.; Izaguirre, Carlos A.; Garber, Gary E.; Huebsh, Lothar; Aye, Maung T. (1990): Detection of surface and cytoplasmic CD4 on blood monocytes from normal and HIV-1 infected individuals. In *J. Immunol. Methods* 135 (1-2), pp. 59–69. DOI: 10.1016/0022-1759(90)90256-u.

Finkelshtein, Danit; Werman, Ariel; Novick, Daniela; Barak, Sara; Rubinstein, Menachem (2013): LDL receptor and its family members serve as the cellular receptors for vesicular stomatitis virus. In *Proc Natl Acad Sci U S A* 110 (18), pp. 7306–7311. DOI: 10.1073/pnas.1214441110.

Finzi, D.; Hermankova, M.; Pierson, T.; Carruth, L. M.; Buck, C.; Chaisson, R. E. et al. (1997): Identification of a reservoir for HIV-1 in patients on highly active antiretroviral therapy. In *Science* 278 (5341), pp. 1295–1300. DOI: 10.1126/science.278.5341.1295.

Friedrich, Katrin; Hanauer, Jan Rh; Prüfer, Steffen; Münch, Robert C.; Völker, Iris; Filippis, Christodoulos et al. (2013): DARPin-targeting of measles virus: unique bispecificity, effective oncolysis, and enhanced safety. In *Mol. Ther.* 21 (4), pp. 849–859. DOI: 10.1038/mt.2013.16.

Fromentin, Rémi; Chomont, Nicolas (2021): HIV persistence in subsets of CD4+ T cells: 50 shades of reservoirs. In *Semin. Immunol.* 51, p. 101438. DOI: 10.1016/j.smim.2020.101438.

Fromentin, Rémi; DaFonseca, Sandrina; Costiniuk, Cecilia T.; El-Far, Mohamed; Procopio, Francesco Andrea; Hecht, Frederick M. et al. (2019): PD-1 blockade potentiates HIV latency reversal ex vivo in CD4+ T cells from ART-suppressed individuals. In *Nat Commun* 10 (1), p. 814. DOI: 10.1038/s41467-019-08798-7.

Funke, Sabrina; Maisner, Andrea; Mühlebach, M. D.; Koehl, Ulrike; Grez, Manuel; Cattaneo, Roberto et al. (2008): Targeted cell entry of lentiviral vectors. In *Mol Ther* 16 (8), pp. 1427–1436. DOI: 10.1038/mt.2008.128.

Gao, Guangping; Vandenberghe, Luk H.; Alvira, Mauricio R.; Lu, You; Calcedo, Roberto; Zhou, Xiangyang; Wilson, James M. (2004): Clades of Adeno-associated viruses are widely disseminated in human tissues. In *Journal of Virology* 78 (12), pp. 6381–6388. DOI: 10.1128/JVI.78.12.6381-6388.2004.

Gao, Zongliang; van der Velden, Yme Ubeles; Fan, Minghui; van der Linden, Cynthia Alyssa; Vink, Monique; Herrera-Carrillo, Elena; Berkhout, Ben (2021): Engineered miniature H1 promoters with dedicated RNA polymerase II or III activity. In *J Biol Chem* 296, p. 100026. DOI: 10.1074/jbc.RA120.015386.

Geoffroy, Marie-Claude; Salvetti, Anna (2005): Helper functions required for wild type and recombinant adeno-associated virus growth. In *CGT* 5 (3), pp. 265–271. DOI: 10.2174/1566523054064977.

Ghosh, Sourish; Dellibovi-Ragheb, Teegan A.; Kerviel, Adeline; Pak, Eowyn; Qiu, Qi; Fisher, Matthew et al. (2020): β-Coronaviruses Use Lysosomes for Egress Instead of the Biosynthetic Secretory Pathway. In *Cell* 183 (6), 1520-1535.e14. DOI: 10.1016/j.cell.2020.10.039.

Ghosn, Jade; Taiwo, Babafemi; Seedat, Soraya; Autran, Brigitte; Katlama, Christine (2018): HIV. In *Lancet* 392 (10148), pp. 685–697. DOI: 10.1016/S0140-6736(18)31311-4.

Grieger, Joshua C.; Choi, Vivian W.; Samulski, R. Jude (2006): Production and characterization of adeno-associated viral vectors. In *Nat Protoc* 1 (3), pp. 1412–1428. DOI: 10.1038/nprot.2006.207.

Grosse, Stefanie; Penaud-Budloo, Magalie; Herrmann, Anne-Kathrin; Börner, Kathleen; Fakhiri, Julia; Laketa, Vibor et al. (2017): Relevance of Assembly-Activating Protein for Adeno-associated Virus Vector Production and Capsid Protein Stability in Mammalian and Insect Cells. In *J. Virol.* 91 (20). DOI: 10.1128/JVI.01198-17.

Günther, D. M.; Kovacs, R.; Wildner, F.; Salivara, A.; Thalheimer, F. B.; Fries, P. et al. (2023): Substantially improved gene transfer to interneurons with second-generation glutamate-receptor targeted DART-AAV vectors. In *J Neurosci Methods*, p. 109981. DOI: 10.1016/j.jneumeth.2023.109981.

Gupta, Ravindra Kumar; Peppa, Dimitra; Hill, Alison L.; Gálvez, Cristina; Salgado, Maria; Pace, Matthew et al. (2020): Evidence for HIV-1 cure after CCR5Δ32/Δ32 allogeneic haemopoietic stem-cell transplantation 30 months post analytical treatment interruption: a case report. In *Lancet HIV* 7 (5), e340-e347. DOI: 10.1016/S2352-3018(20)30069-2.

Hahn, B. H.; Shaw, G. M.; Cock, K. M. de; Sharp, P. M. (2000): AIDS as a zoonosis: scientific and public health implications. In *Science* 287 (5453), pp. 607–614. DOI: 10.1126/science.287.5453.607.

Hamann, Martin V.; Beschorner, Niklas; Vu, Xuan-Khang; Hauber, Ilona; Lange, Ulrike C.; Traenkle, Bjoern et al. (2021): Improved targeting of human CD4+ T cells by nanobody-modified AAV2 gene therapy vectors. In *PLoS ONE* 16 (12), e0261269. DOI: 10.1371/journal.pone.0261269.

Hamieh, Mohamad; Mansilla-Soto, Jorge; Rivière, Isabelle; Sadelain, Michel (2023): Programming CAR T Cell Tumor Recognition: Tuned Antigen Sensing and Logic Gating. In *Cancer Discov* 13 (4), pp. 829–843. DOI: 10.1158/2159-8290.CD-23-0101.

Harte, James V.; Wakerlin, Samantha L.; Lindsay, Andrew J.; McCarthy, Justin V.; Coleman-Vaughan, Caroline (2022): Metalloprotease-Dependent S2'-Activation Promotes Cell-Cell Fusion and Syncytiation of SARS-CoV-2. In *Viruses* 14 (10). DOI: 10.3390/v14102094.

Hartmann, Jessica; Münch, Robert C.; Freiling, Ruth-Therese; Schneider, Irene C.; Dreier, Birgit; Samukange, Washington et al. (2018): A Library-Based Screening Strategy for the Identification of DARPins as Ligands for Receptor-Targeted AAV and Lentiviral Vectors. In *Mol Ther Methods Clin Dev* 10, pp. 128–143. DOI: 10.1016/j.omtm.2018.07.001.

Hartmann, Jessica; Thalheimer, Frederic B.; Höpfner, Felix; Kerzel, Thomas; Khodosevich, Konstantin; García-González, Diego et al. (2019): GluA4-Targeted AAV Vectors Deliver

Genes Selectively to Interneurons while Relying on the AAV Receptor for Entry. In *Mol Ther Methods Clin Dev* 14, pp. 252–260. DOI: 10.1016/j.omtm.2019.07.004.

Hastie, Eric; Samulski, R. Jude (2015): Adeno-associated virus at 50: a golden anniversary of discovery, research, and gene therapy success--a personal perspective. In *Hum. Gene Ther.* 26 (5), pp. 257–265. DOI: 10.1089/hum.2015.025.

Haworth, Kevin G.; Peterson, Christopher W.; Kiem, Hans-Peter (2017): CCR5-edited gene therapies for HIV cure: Closing the door to viral entry. In *Cytotherapy* 19 (11), pp. 1325–1338. DOI: 10.1016/j.jcyt.2017.05.013.

Hennrich, Alexandru A.; Sawatsky, Bevan; Santos-Mandujano, Rosalía; Banda, Dominic H.; Oberhuber, Martina; Schopf, Anika et al. (2021): Safe and effective two-in-one replicon-and-VLP minispike vaccine for COVID-19: Protection of mice after a single immunization. In *PLoS Pathog.* 17 (4), e1009064. DOI: 10.1371/journal.ppat.1009064.

Herrlein, Marie-Luise; Hein, Sascha; Zahn, Tobias; Mhedhbi, Ines; Raupach, Jan; Husria, Younes et al. (2022): Comparative Investigation of Methods for Analysis of SARS-CoV-2-Spike-Specific Antisera. In *Viruses* 14 (2). DOI: 10.3390/v14020410.

Herrmann, Monika; Krupka, Christina; Deiser, Katrin; Brauchle, Bettina; Marcinek, Anetta; Ogrinc Wagner, Ana et al. (2018): Bifunctional PD-1 × αCD3 × αCD33 fusion protein reverses adaptive immune escape in acute myeloid leukemia. In *Blood* 132 (23), pp. 2484–2494. DOI: 10.1182/blood-2018-05-849802.

Hoffmann, Mareike D.; Zdechlik, Alina C.; He, Yungui; Nedrud, David; Aslanidi, George; Gordon, Wendy; Schmidt, Daniel (2023): Multiparametric domain insertional profiling of adeno-associated virus VP1. In *Mol. Ther. Methods. Clin. Dev.* 31, p. 101143. DOI: 10.1016/j.omtm.2023.101143.

Hoffmann, Markus; Kleine-Weber, Hannah; Pöhlmann, Stefan (2020a): A Multibasic Cleavage Site in the Spike Protein of SARS-CoV-2 Is Essential for Infection of Human Lung Cells. In *Mol. Cell* 78 (4), 779-784.e5. DOI: 10.1016/j.molcel.2020.04.022.

Hoffmann, Markus; Kleine-Weber, Hannah; Schroeder, Simon; Krüger, Nadine; Herrler, Tanja; Erichsen, Sandra et al. (2020b): SARS-CoV-2 Cell Entry Depends on ACE2 and TMPRSS2 and Is Blocked by a Clinically Proven Protease Inhibitor. In *Cell*. DOI: 10.1016/j.cell.2020.02.052.

Holland, Anne U.; Munk, Carsten; Lucero, Ginger R.; Nguyen, Lucia D.; Landau, Nathaniel R. (2004): α-Complementation assay for HIV envelope glycoprotein-mediated fusion. In *Virology* 319 (2), pp. 343–352. DOI: 10.1016/j.virol.2003.11.012.

Hütter, Gero; Thiel, Eckhard (2011): Allogeneic transplantation of CCR5-deficient progenitor cells in a patient with HIV infection: an update after 3 years and the search for patient no. 2. In *AIDS* 25 (2), pp. 273–274. DOI: 10.1097/QAD.0b013e328340fe28.

Ibraheim, Raed; Tai, Phillip W. L.; Mir, Aamir; Javeed, Nida; Wang, Jiaming; Rodríguez, Tomás C. et al. (2021): Self-inactivating, all-in-one AAV vectors for precision Cas9 genome editing via homology-directed repair *in vivo*. In *Nat Commun* 12 (1), p. 6267. DOI: 10.1038/s41467-021-26518-y.

Jackson, Cody B.; Farzan, Michael; Chen, Bing; Choe, Hyeryun (2022): Mechanisms of SARS-CoV-2 entry into cells. In *Nature reviews. Molecular cell biology* 23 (1), pp. 3–20. DOI: 10.1038/s41580-021-00418-x.

Jensen, Björn-Erik Ole; Knops, Elena; Cords, Leon; Lübke, Nadine; Salgado, Maria; Busman-Sahay, Kathleen et al. (2023): In-depth virological and immunological characterization of HIV-1 cure after CCR5Δ32/Δ32 allogeneic hematopoietic stem cell transplantation. In *Nat Med* 29 (3), pp. 583–587. DOI: 10.1038/s41591-023-02213-x.

Johns Hopkins University of Medicine (2023): Coronavirus resource center. Available online at https://coronavirus.jhu.edu/map.html, updated on 10/3/2023, checked on 2/4/2024.

Jost, Christian; Schilling, Johannes; Tamaskovic, Rastislav; Schwill, Martin; Honegger, Annemarie; Plückthun, Andreas (2013): Structural basis for eliciting a cytotoxic effect in HER2-overexpressing cancer cells via binding to the extracellular domain of HER2. In *Structure* 21 (11), pp. 1979–1991. DOI: 10.1016/j.str.2013.08.020.

Kapitza, Laura; Ho, Naphang; Kerzel, Thomas; Frank, Annika M.; Thalheimer, Frederic B.; Jamali, Arezoo et al. (2023): CD62L as target receptor for specific gene delivery into less differentiated human T lymphocytes. In *Front Immunol* 14, p. 1183698. DOI: 10.3389/fimmu.2023.1183698.

Kareva, Irina; Zutshi, Anup; Gupta, Pawan; Kabilan, Senthil (2021): Bispecific antibodies: A guide to model informed drug discovery and development. In *Heliyon* 7 (7), e07649. DOI: 10.1016/j.heliyon.2021.e07649.

Kareva, Irina; Zutshi, Anup; Kabilan, Senthil (2018): Guiding principles for mechanistic modeling of bispecific antibodies. In *Prog. Biophys. Mol. Biol.* 139, pp. 59–72. DOI: 10.1016/j.pbiomolbio.2018.08.011.

Kareva, Irina; Zutshi, Anup; Rhoden, John; Kabilan, Senthil (2022): Practical guide to calculating impact of avidity in models of bispecific antibodies with two membrane-bound targets.

Kern, A.; Schmidt, K.; Leder, C.; Müller, O. J.; Wobus, C. E.; Bettinger, K. et al. (2003): Identification of a heparin-binding motif on adeno-associated virus type 2 capsids. In *J. Virol.* 77 (20), pp. 11072–11081.

Kishimoto, Takashi Kei; Samulski, Richard Jude (2022): Addressing high dose AAV toxicity - 'one and done' or 'slower and lower'? In *Expert Opin Biol Ther* 22 (9), pp. 1067–1071. DOI: 10.1080/14712598.2022.2060737.

Kloss, Christopher C.; Condomines, Maud; Cartellieri, Marc; Bachmann, Michael; Sadelain, Michel (2013): Combinatorial antigen recognition with balanced signaling promotes selective tumor eradication by engineered T cells. In *Nat. Biotechnol.* 31 (1), pp. 71–75. DOI: 10.1038/nbt.2459.

Lamerton, Rachel E.; Marcial-Juarez, Edith; Faustini, Sian E.; Perez-Toledo, Marisol; Goodall, Margaret; Jossi, Siân E. et al. (2022): SARS-CoV-2 Spike- and Nucleoprotein-Specific Antibodies Induced After Vaccination or Infection Promote Classical Complement Activation. In *Front Immunol* 13, p. 838780. DOI: 10.3389/fimmu.2022.838780.

Lamp, Boris; Dietzel, Erik; Kolesnikova, Larissa; Sauerhering, Lucie; Erbar, Stephanie; Weingartl, Hana; Maisner, Andrea (2013): Nipah virus entry and egress from polarized epithelial cells. In *J. Virol.* 87 (6), pp. 3143–3154. DOI: 10.1128/JVI.02696-12.

Lan, Jun; Ge, Jiwan; Yu, Jinfang; Shan, Sisi; Zhou, Huan; Fan, Shilong et al. (2020): Structure of the SARS-CoV-2 spike receptor-binding domain bound to the ACE2 receptor. In *Nature* 581 (7807), pp. 215–220. DOI: 10.1038/s41586-020-2180-5.

Lee, Frederick J.; Amin, Janaki; Carr, Andrew (2014): Efficacy of initial antiretroviral therapy for HIV-1 infection in adults: a systematic review and meta-analysis of 114 studies with up to 144 weeks' follow-up. In *PLoS ONE* 9 (5), e97482. DOI: 10.1371/journal.pone.0097482.

Leroy, Héloïse; Han, Mingyu; Woottum, Marie; Bracq, Lucie; Bouchet, Jérôme; Xie, Maorong; Benichou, Serge (2020): Virus-Mediated Cell-Cell Fusion. In *Int J Mol Sci* 21 (24). DOI: 10.3390/ijms21249644.

Liu, Kuan-Ting; Han, Yi-Ju; Wu, Guan-Hong; Huang, Kuan-Ying A.; Huang, Peng-Nien (2022): Overview of Neutralization Assays and International Standard for Detecting SARS-CoV-2 Neutralizing Antibody. In *Viruses* 14 (7). DOI: 10.3390/v14071560.

Marschalek, Rolf (2023): SARS-CoV-2: The Virus, Its Biology and COVID-19 Disease-Counteracting Possibilities. In *Front. Biosci. (Landmark Ed)* 28 (10), p. 273. DOI: 10.31083/j.fbl2810273.

Martínez-Mármol, Ramón; Giordano-Santini, Rosina; Kaulich, Eva; Cho, Ann-Na; Przybyla, Magdalena; Riyadh, Md Asrafuzzaman et al. (2023): SARS-CoV-2 infection and viral fusogens cause neuronal and glial fusion that compromises neuronal activity. In *Sci. Adv.* 9 (23), eadg2248. DOI: 10.1126/sciadv.adg2248.

Mazor, Yariv; Hansen, Anna; Yang, Chunning; Chowdhury, Partha S.; Wang, Jihong; Stephens, Geoffrey et al. (2015): Insights into the molecular basis of a bispecific antibody's target selectivity. In *mAbs* 7 (3), pp. 461–469. DOI: 10.1080/19420862.2015.1022695.

Mazor, Yariv; Sachsenmeier, Kris F.; Yang, Chunning; Hansen, Anna; Filderman, Jessica; Mulgrew, Kathy et al. (2017): Enhanced tumor-targeting selectivity by modulating bispecific antibody binding affinity and format valence. In *Sci Rep* 7, p. 40098. DOI: 10.1038/srep40098.

McCarty, Douglas M. (2008): Self-complementary AAV vectors; advances and applications. In *Mol Ther* 16 (10), pp. 1648–1656. DOI: 10.1038/mt.2008.171.

McCune, J. M. (2001): The dynamics of CD4+ T-cell depletion in HIV disease. In *Nature* 410 (6831), pp. 974–979. DOI: 10.1038/35073648.

McGary, Colleen S.; Deleage, Claire; Harper, Justin; Micci, Luca; Ribeiro, Susan P.; Paganini, Sara et al. (2017): CTLA-4+PD-1- Memory CD4+ T Cells Critically Contribute to Viral Persistence in Antiretroviral Therapy-Suppressed, SIV-Infected Rhesus Macaques. In *Immunity* 47 (4), 776-788.e5. DOI: 10.1016/j.immuni.2017.09.018.

Mendoza, Pilar; Jackson, Julia R.; Oliveira, Thiago Y.; Gaebler, Christian; Ramos, Victor; Caskey, Marina et al. (2020): Antigen-responsive CD4+ T cell clones contribute to the HIV-1 latent reservoir. In *J Exp Med* 217 (7). DOI: 10.1084/jem.20200051.

Menéndez-Arias, Luis; Delgado, Rafael (2022): Update and latest advances in antiretroviral therapy. In *Trends in pharmacological sciences* 43 (1), pp. 16–29. DOI: 10.1016/j.tips.2021.10.004.

Meyrath, Max; Szpakowska, Martyna; Plesseria, Jean-Marc; Domingues, Olivia; Langlet, Jérémie; Weber, Bernard et al. (2022): Nanoluciferase-based cell fusion assay for rapid and high-throughput assessment of SARS-CoV-2-neutralizing antibodies in patient samples. In *Methods Enzymol.* 675, pp. 351–381. DOI: 10.1016/bs.mie.2022.07.015.

Michels, Alexander; Frank, Annika M.; Günther, Dorothee M.; Mataei, Mehryad; Börner, Kathleen; Grimm, Dirk et al. (2021): Lentiviral and adeno-associated vectors efficiently transduce mouse T lymphocytes when targeted to murine CD8. In *Mol Ther Methods Clin Dev* 23, pp. 334–347. DOI: 10.1016/j.omtm.2021.09.014.

Mirdita, Milot; Schütze, Konstantin; Moriwaki, Yoshitaka; Heo, Lim; Ovchinnikov, Sergey; Steinegger, Martin (2022): ColabFold: making protein folding accessible to all. In *Nat. Methods* 19 (6), pp. 679–682. DOI: 10.1038/s41592-022-01488-1.

MS, Gottlieb; HM, Schanker; PT, Fan; A, Saxon; JD, Weisman (1996): Pneumocystis pneumonia--Los Angeles. 1981. In *MMWR Morb. Mortal. Wkly. Rep.* 45 (34), pp. 729–733.

Münch, Robert C.; Janicki, Hanna; Völker, Iris; Rasbach, Anke; Hallek, Michael; Büning, Hildegard; Buchholz, Christian J. (2013): Displaying high-affinity ligands on adeno-associated viral vectors enables tumor cell-specific and safe gene transfer. In *Mol Ther* 21 (1), pp. 109–118. DOI: 10.1038/mt.2012.186.

Münch, Robert C.; Muth, Anke; Muik, Alexander; Friedel, Thorsten; Schmatz, Julia; Dreier, Birgit et al. (2015): Off-target-free gene delivery by affinity-purified receptor-targeted viral vectors. In *Nat Commun* 6, p. 6246. DOI: 10.1038/ncomms7246.

Murphy, Samuel L.; Gaulton, Glen N. (2007): TR1.3 viral pathogenesis and syncytium formation are linked to Env-Gag cooperation. In *Journal of Virology* 81 (19), pp. 10777–10785. DOI: 10.1128/JVI.00816-07.

Navaratnarajah, Chanakha K.; Vongpunsawad, Sompong; Oezguen, Numan; Stehle, Thilo; Braun, Werner; Hashiguchi, Takao et al. (2008): Dynamic interaction of the measles virus hemagglutinin with its receptor signaling lymphocytic activation molecule (SLAM, CD150). In *J Biol Chem* 283 (17), pp. 11763–11771. DOI: 10.1074/jbc.M800896200.

Nonnenmacher, Mathieu; Weber, Thomas (2011): Adeno-associated virus 2 infection requires endocytosis through the CLIC/GEEC pathway. In *Cell Host Microbe* 10 (6), pp. 563–576. DOI: 10.1016/j.chom.2011.10.014.

Osuna, Christa E.; Lim, So-Yon; Kublin, Jessica L.; Apps, Richard; Chen, Elsa; Mota, Talia M. et al. (2018): Evidence that CD32a does not mark the HIV-1 latent reservoir. In *Nature* 561 (7723), E20-E28. DOI: 10.1038/s41586-018-0495-2.

Ou, Xiuyuan; Liu, Yan; Lei, Xiaobo; Li, Pei; Mi, Dan; Ren, Lili et al. (2020): Characterization of spike glycoprotein of SARS-CoV-2 on virus entry and its immune cross-reactivity with SARS-CoV. In *Nature communications* 11 (1), p. 1620. DOI: 10.1038/s41467-020-15562-9.

Papa, Guido; Mallery, Donna L.; Albecka, Anna; Welch, Lawrence; Cattin-Ortolá, Jérôme; Luptak, Jakub et al. (2020): Furin cleavage of SARS-CoV-2 Spike promotes but is not essential for infection and cell-cell fusion.

Pasternak, Alexander O.; Berkhout, Ben (2018): What do we measure when we measure cell-associated HIV RNA. In *Retrovirology* 15 (1), p. 13. DOI: 10.1186/s12977-018-0397-2.

Pasternak, Alexander O.; Berkhout, Ben (2023): HIV persistence: silence or resistance? In *Curr Opin Virol* 59, p. 101301. DOI: 10.1016/j.coviro.2023.101301.

Patel, Kashyap R.; Roberts, Jacob T.; Barb, Adam W. (2019): Multiple Variables at the Leukocyte Cell Surface Impact Fc γ Receptor-Dependent Mechanisms. In *Frontiers in immunology* 10, p. 223. DOI: 10.3389/fimmu.2019.00223.

Pedro, Kyle D.; Henderson, Andrew J.; Agosto, Luis M. (2019): Mechanisms of HIV-1 cell-to-cell transmission and the establishment of the latent reservoir. In *Virus Res* 265, pp. 115–121. DOI: 10.1016/j.virusres.2019.03.014.

Pekar, Jonathan E.; Magee, Andrew; Parker, Edyth; Moshiri, Niema; Izhikevich, Katherine; Havens, Jennifer L. et al. (2022): The molecular epidemiology of multiple zoonotic origins of SARS-CoV-2. In *Science (New York, N.Y.)* 377 (6609), pp. 960–966. DOI: 10.1126/science.abp8337.

Pillay, S.; Meyer, N. L.; Puschnik, A. S.; Davulcu, O.; Diep, J.; Ishikawa, Y. et al. (2016): An essential receptor for adeno-associated virus infection. In *Nature* 530 (7588), pp. 108–112. DOI: 10.1038/nature16465.

Polack, Fernando P.; Thomas, Stephen J.; Kitchin, Nicholas; Absalon, Judith; Gurtman, Alejandra; Lockhart, Stephen et al. (2020): Safety and Efficacy of the BNT162b2 mRNA Covid-19 Vaccine. In *N. Engl. J. Med* 383 (27), pp. 2603–2615. DOI: 10.1056/NEJMoa2034577.

Pupo, Amaury; Fernández, Audry; Low, Siew Hui; François, Achille; Suárez-Amarán, Lester; Samulski, Richard Jude (2022): AAV vectors: The Rubik's cube of human gene therapy. In *Mol. Ther.* 30 (12), pp. 3515–3541. DOI: 10.1016/j.ymthe.2022.09.015.

Rajah, Maaran Michael; Bernier, Annie; Buchrieser, Julian; Schwartz, Olivier (2022): The Mechanism and Consequences of SARS-CoV-2 Spike-Mediated Fusion and Syncytia Formation. In *Journal of molecular biology* 434 (6), p. 167280. DOI: 10.1016/j.jmb.2021.167280.

Ran, F. Ann; Le Cong; Yan, Winston X.; Scott, David A.; Gootenberg, Jonathan S.; Kriz, Andrea J. et al. (2015): *In vivo* genome editing using Staphylococcus aureus Cas9. In *Nature* 520 (7546), pp. 186–191. DOI: 10.1038/nature14299.

Reul, Johanna; Frisch, Janina; Engeland, Christine E.; Thalheimer, Frederic B.; Hartmann, Jessica; Ungerechts, Guy; Buchholz, Christian J. (2019): Tumor-Specific Delivery of Immune Checkpoint Inhibitors by Engineered AAV Vectors. In *Front. Oncol.* 9, p. 1432. DOI: 10.3389/fonc.2019.00052.

Riechert, Vanessa; Hein, Sascha; Visser, Mayken; Zimmermann, Mathias; Wesche, Jan; Adams, Philipp A. et al. (2023): FcγRIIA-specific DARPins as novel tools in blood cell analysis and platelet aggregation. In *J Biol Chem* 299 (6), p. 104743. DOI: 10.1016/j.jbc.2023.104743.

Riyad, Jalish M.; Weber, Thomas (2021): Intracellular trafficking of adeno-associated virus (AAV) vectors: challenges and future directions. In *Gene Ther* 28 (12), pp. 683–696. DOI: 10.1038/s41434-021-00243-z.

Roller, Devin G.; Dollery, Stephen J.; Doyle, James L.; Nicola, Anthony V. (2008): Structure-function analysis of herpes simplex virus glycoprotein B with fusion-from-without activity. In *Virology* 382 (2), pp. 207–216. DOI: 10.1016/j.virol.2008.09.015.

Rose, J. A.; Hoggan, M. D.; Shatkin, A. J. (1966): Nucleic acid from an adeno-associated virus: chemical and physical studies. In *Proc. Natl. Acad. Sci. U. S. A.* 56 (1), pp. 86–92. DOI: 10.1073/pnas.56.1.86.

Rothenberger, Sylvia; Hurdiss, Daniel L.; Walser, Marcel; Malvezzi, Francesca; Mayor, Jennifer; Ryter, Sarah et al. (2022): The trispecific DARPin ensovibep inhibits diverse SARS-CoV-2 variants. In *Nat. Biotechnol.* 40 (12), pp. 1845–1854. DOI: 10.1038/s41587-022-01382-3.

Samulski, R. Jude; Muzyczka, Nicholas (2014): AAV-Mediated Gene Therapy for Research and Therapeutic Purposes. In *Annual Review of Virology* 1 (1), pp. 427–451. DOI: 10.1146/annurev-virology-031413-085355.

Schoeman, Dewald; Fielding, Burtram C. (2019): Coronavirus envelope protein: current knowledge. In *Virol J* 16 (1), p. 69. DOI: 10.1186/s12985-019-1182-0.

Schubert, Ingo; Saul, Domenica; Nowecki, Stefanie; Mackensen, Andreas; Fey, Georg H.; Oduncu, Fuat S. (2014): A dual-targeting triplebody mediates preferential redirected lysis of antigen double-positive over single-positive leukemic cells. In *mAbs* 6 (1), pp. 286–296. DOI: 10.4161/mabs.26768.

Shang, Jian; Ye, Gang; Shi, Ke; Wan, Yushun; Luo, Chuming; Aihara, Hideki et al. (2020): Structural basis of receptor recognition by SARS-CoV-2. In *Nature* 581 (7807), pp. 221–224. DOI: 10.1038/s41586-020-2179-y.

Shen, Weiran; Liu, Shengjiang; Ou, Li (2022): rAAV immunogenicity, toxicity, and durability in 255 clinical trials: A meta-analysis. In *Front Immunol* 13, p. 1001263. DOI: 10.3389/fimmu.2022.1001263.

Shieh, Perry B.; Kuntz, Nancy L.; Dowling, James J.; Müller-Felber, Wolfgang; Bönnemann, Carsten G.; Seferian, Andreea M. et al. (2023): Safety and efficacy of gene replacement therapy for X-linked myotubular myopathy (ASPIRO): a multinational, open-label, dose-escalation trial. In *Lancet Neurol.* 22 (12), pp. 1125–1139. DOI: 10.1016/S1474-4422(23)00313-7.

Shitaoka, Kiyomi; Higashiura, Akifumi; Kawano, Yohei; Yamamoto, Akima; Mizoguchi, Yoko; Hashiguchi, Takao et al. (2023): Structural basis of spike RBM-specific human antibodies counteracting broad SARS-CoV-2 variants. In *Commun. Biol.* 6 (1), p. 395. DOI: 10.1038/s42003-023-04782-6.

Siliciano, Janet D.; Kajdas, Joleen; Finzi, Diana; Quinn, Thomas C.; Chadwick, Karen; Margolick, Joseph B. et al. (2003): Long-term follow-up studies confirm the stability of the latent reservoir for HIV-1 in resting CD4+ T cells. In *Nat. Med.* 9 (6), pp. 727–728. DOI: 10.1038/nm880.

Strecker, M. I.; Wlotzka, K.; Strassheimer, F.; Roller, B.; Ludmirski, G.; König, S. et al. (2022): AAV-mediated gene transfer of a checkpoint inhibitor in combination with HER2-targeted CAR-NK cells as experimental therapy for glioblastoma. In *Oncoimmunology* 11 (1), p. 2127508. DOI: 10.1080/2162402x.2022.2127508.

Sun, Weiwei; Gao, Ce; Hartana, Ciputra Adijaya; Osborn, Matthew R.; Einkauf, Kevin B.; Lian, Xiaodong et al. (2023): Phenotypic signatures of immune selection in HIV-1 reservoir cells. In *Nature* 614 (7947), pp. 309–317. DOI: 10.1038/s41586-022-05538-8.

Surosky, R. T.; Urabe, M.; Godwin, S. G.; McQuiston, S. A.; Kurtzman, G. J.; Ozawa, K.; Natsoulis, G. (1997): Adeno-associated virus Rep proteins target DNA sequences to a unique locus in the human genome. In *Journal of Virology* 71 (10), pp. 7951–7959. DOI: 10.1128/JVI.71.10.7951-7959.1997.

Tamaskovic, Rastislav; Simon, Manuel; Stefan, Nikolas; Schwill, Martin; Plückthun, Andreas (2012): Designed ankyrin repeat proteins (DARPins) from research to therapy. In *Meth. Enzymol* 503, pp. 101–134. DOI: 10.1016/B978-0-12-396962-0.00005-7.

Tapia-Galisteo, Antonio; Compte, Marta; Álvarez-Vallina, Luis; Sanz, Laura (2023): When three is not a crowd: trispecific antibodies for enhanced cancer immunotherapy. In *Theranostics* 13 (3), pp. 1028–1041. DOI: 10.7150/thno.81494.

Theuerkauf, Samuel A.; Herrera-Carrillo, Elena; John, Fabian; Zinser, Luca J.; Molina, Mariano A.; Riechert, Vanessa et al. (2023): AAV vectors displaying bispecific DARPins enable dual-control targeted gene delivery. In *Biomaterials* 303, p. 122399. DOI: 10.1016/j.biomaterials.2023.122399.

Theuerkauf, Samuel A.; Michels, Alexander; Riechert, Vanessa; Maier, Thorsten J.; Flory, Egbert; Cichutek, Klaus; Buchholz, Christian J. (2021): Quantitative Assays Reveal Cell Fusion at Minimal Levels of SARS-CoV-2 Spike Protein and Fusion-from-Without. In *iScience*, p. 102170. DOI: 10.1016/j.isci.2021.102170.

Vásquez, Joshua J.; Aguilar-Rodriguez, Brandon L.; Rodriguez, Leonardo; Hogan, Louise E.; Somsouk, Ma; McCune, Joseph M. et al. (2019): CD32-RNA Co-localizes with HIV-RNA in

CD3+ Cells Found within Gut Tissues from Viremic and ART-Suppressed Individuals. In *Pathog. Immun.* 4 (1), pp. 147–160. DOI: 10.20411/pai.v4i1.271.

Vormittag, Philipp; Gunn, Rebecca; Ghorashian, Sara; Veraitch, Farlan S. (2018): A guide to manufacturing CAR T cell therapies. In *Curr Opin Biotechnol* 53, pp. 164–181. DOI: 10.1016/j.copbio.2018.01.025.

Walls, Alexandra C.; Park, Young-Jun; Tortorici, M. Alejandra; Wall, Abigail; McGuire, Andrew T.; Veesler, David (2020): Structure, Function, and Antigenicity of the SARS-CoV-2 Spike Glycoprotein. In *Cell* 181 (2), 281-292.e6. DOI: 10.1016/j.cell.2020.02.058.

Wang, Dan; Tai, Phillip W. L.; Gao, Guangping (2019): Adeno-associated virus vector as a platform for gene therapy delivery. In *Nat. Rev. Drug. Discov.* 18 (5), pp. 358–378. DOI: 10.1038/s41573-019-0012-9.

Wang, Gang; Zhao, Na; Berkhout, Ben; Das, Atze T. (2016): CRISPR-Cas9 Can Inhibit HIV-1 Replication but NHEJ Repair Facilitates Virus Escape. In *Molecular therapy : the journal of the American Society of Gene Therapy* 24 (3), pp. 522–526. DOI: 10.1038/mt.2016.24.

Warrington, Kenneth H.; Gorbatyuk, Oleg S.; Harrison, Jeffrey K.; Opie, Shaun R.; Zolotukhin, Sergei; Muzyczka, Nicholas (2004): Adeno-associated virus type 2 VP2 capsid protein is nonessential and can tolerate large peptide insertions at its N terminus. In *J. Virol.* 78 (12), pp. 6595–6609. DOI: 10.1128/JVI.78.12.6595-6609.2004.

Watanabe, Yasunori; Allen, Joel D.; Wrapp, Daniel; McLellan, Jason S.; Crispin, Max (2020): Site-specific glycan analysis of the SARS-CoV-2 spike. In *Science (New York, N.Y.)* 369 (6501), pp. 330–333. DOI: 10.1126/science.abb9983.

Weed, Darin J.; Nicola, Anthony V. (2017): Herpes simplex virus Membrane Fusion. In *Advances in anatomy, embryology, and cell biology* 223, pp. 29–47. DOI: 10.1007/978-3-319-53168-7_2.

Whitney, James B.; Hill, Alison L.; Sanisetty, Srisowmya; Penaloza-MacMaster, Pablo; Liu, Jinyan; Shetty, Mayuri et al. (2014): Rapid seeding of the viral reservoir prior to SIV viraemia in rhesus monkeys. In *Nature* 512 (7512), pp. 74–77. DOI: 10.1038/nature13594.

Wilen, Craig B.; Tilton, John C.; Doms, Robert W. (2012): HIV: cell binding and entry. In *Cold Spring Harb. Perspect. Med.* 2 (8). DOI: 10.1101/cshperspect.a006866.

World Health Organization (2023): HIV and AIDS. Available online at https://www.who.int/news-room/fact-sheets/detail/hiv-aids, checked on 2/4/2024.

Wörner, Tobias P.; Bennett, Antonette; Habka, Sana; Snijder, Joost; Friese, Olga; Powers, Thomas et al. (2021): Adeno-associated virus capsid assembly is divergent and stochastic. In *Nat Commun* 12 (1), p. 1642. DOI: 10.1038/s41467-021-21935-5.

Wu, Leyun; Zhou, Liping; Mo, Mengxia; Liu, Tingting; Wu, Chengkun; Gong, Chunye et al. (2022): SARS-CoV-2 Omicron RBD shows weaker binding affinity than the currently dominant Delta variant to human ACE2. In *Sig. Transduct. Target. Ther.* 7 (1), p. 8. DOI: 10.1038/s41392-021-00863-2.

Wu, Vincent H.; Nordin, Jayme M. L.; Nguyen, Son; Joy, Jaimy; Mampe, Felicity; Del Rio Estrada, Perla M. et al. (2023): Profound phenotypic and epigenetic heterogeneity of the HIV-1-infected CD4+ T cell reservoir. In *Nat. Immunol.* 24 (2), pp. 359–370. DOI: 10.1038/s41590-022-01371-3.

Wünschmann, S.; Stapleton, J. T. (2000): Fluorescence-based quantitative methods for detecting human immunodeficiency virus type 1-induced syncytia. In *J. Clin. Microbiol.* 38 (8), pp. 3055–3060. DOI: 10.1128/jcm.38.8.3055-3060.2000.

Xia, Shuai; Lan, Qiaoshuai; Su, Shan; Wang, Xinling; Xu, Wei; Liu, Zezhong et al. (2020a): The role of furin cleavage site in SARS-CoV-2 spike protein-mediated membrane fusion in the presence or absence of trypsin. In *Sig. Transduct. Target. Ther.* 5 (1), p. 92. DOI: 10.1038/s41392-020-0184-0.

Xia, Shuai; Liu, Meiqin; Wang, Chao; Xu, Wei; Lan, Qiaoshuai; Feng, Siliang et al. (2020b): Inhibition of SARS-CoV-2 (previously 2019-nCoV) infection by a highly potent pan-coronavirus fusion inhibitor targeting its spike protein that harbors a high capacity to mediate membrane fusion. In *Cell Res.* 30 (4), pp. 343–355. DOI: 10.1038/s41422-020-0305-x.

Xia, Shuai; Wang, Lijue; Jiao, Fanke; Yu, Xueying; Xu, Wei; Huang, Ziqi et al. (2023): SARS-CoV-2 Omicron subvariants exhibit distinct fusogenicity, but similar sensitivity, to pan-CoV fusion inhibitors. In *Emerg. Microbes Infect.* 12 (1), p. 2178241. DOI: 10.1080/22221751.2023.2178241.

Yin, Chaoran; Zhang, Ting; Qu, Xiying; Zhang, Yonggang; Putatunda, Raj; Xiao, Xiao et al. (2017): *In Vivo* Excision of HIV-1 Provirus by saCas9 and Multiplex Single-Guide RNAs in Animal Models. In *Mol. Ther.* 25 (5), pp. 1168–1186. DOI: 10.1016/j.ymthe.2017.03.012.

Zeng, Cong; Evans, John P.; Pearson, Rebecca; Qu, Panke; Zheng, Yi-Min; Robinson, Richard T. et al. (2020): Neutralizing antibody against SARS-CoV-2 spike in COVID-19 patients, health care workers and convalescent plasma donors. In *JCI insight*. DOI: 10.1172/jci.insight.143213.

Zhang, Fuming; Aguilera, Javier; Beaudet, Julie M.; Xie, Qing; Lerch, Thomas F.; Davulcu, Omar et al. (2013): Characterization of interactions between heparin/glycosaminoglycan and adeno-associated virus. In *Biochemistry* 52 (36), pp. 6275–6285. DOI: 10.1021/bi4008676.

Zhang, Qi; Tang, Weichun; Stancanelli, Eduardo; Jung, Eunkyung; Syed, Zulfeqhar; Pagadala, Vijayakanth et al. (2023): Host heparan sulfate promotes ACE2 super-cluster assembly and enhances SARS-CoV-2-associated syncytium formation. In *Nat Commun* 14 (1), p. 5777. DOI: 10.1038/s41467-023-41453-w.

Zhang, Ran; Cao, Lin; Cui, Mengtian; Sun, Zixian; Hu, Mingxu; Zhang, Rouxuan et al. (2019): Adeno-associated virus 2 bound to its cellular receptor AAVR. In *Nature microbiology*. DOI: 10.1038/s41564-018-0356-7.

Zhang, Zhengrong; Zheng, You; Niu, Zubiao; Zhang, Bo; Wang, Chenxi; Yao, Xiaohong et al. (2021): SARS-CoV-2 spike protein dictates syncytium-mediated lymphocyte elimination. In *Cell death and differentiation* 28 (9), pp. 2765–2777. DOI: 10.1038/s41418-021-00782-3.

Zhu, Yuanmei; Yu, Danwei; Yan, Hongxia; Chong, Huihui; He, Yuxian (2020): Design of Potent Membrane Fusion Inhibitors against SARS-CoV-2, an Emerging Coronavirus with High Fusogenic Activity. In *J. Virol.* 94 (14). DOI: 10.1128/JVI.00635-20.

Zufferey, R.; Nagy, D.; Mandel, R. J.; Naldini, L.; Trono, D. (1997): Multiply attenuated lentiviral vector achieves efficient gene delivery *in vivo*. In *Nat Biotechnol* 15 (9), pp. 871–875. DOI: 10.1038/nbt0997-871.

8 Abbreviations

°C	Degree Celsius
µg	Microgram
µM	Micromolar
F11	CD32a-specific DARPin
55.2	CD4-specific DARPin
Å	Angstrom
AAP	Assembly-activating protein
AAV	Adeno-associated vectors
ACE2	Angiotensin-converting enzyme 2
AIDS	Acquired immunodeficiency syndrome
ANOVA	Analysis of variance
ART	Anti-retroviral therapy
ATCC	American Type Culture Collection
BSL	Biosafety level
CAR	Chimeric antigen receptor
cART	Combination antiretroviral therapy
CI	Confidence interval
CMV	cytomegalovirus
CRISPR	Clustered regular interspaced short palindromic repeats
Cryo-EM	Cryo-electron microscopy
Cryo-ET	Cryo-electron tomography
CTD1	C-terminal domain 1
CTD2	C-terminal domain 2
DARPin	Designed ankyrin repeat proteins
DART-AAV	Designed ankyrin repeat protein targeted-AAV
DMEM	Dulbecco’s modified eagle’s medium high glucose
DMSO	Dimethyl sulfoxid
DNA	Deoxyribonucleic acid
DSMZ	German Collection of Microorganisms and Cell Cultures
E	Envelope protein
E. coli	*Escherichia coli*
EDTA	Ethylenediaminetetraacetic acid
EF1α	Human elongation factor-1 alpha
ER	Endoplasmic reticulum
EU	European union
Fc	Fragment crystallizable

FCS	Fetal calve serum
FDA	Food and Drug Administration
FFWO	Fusion-from-without
g	Gravitational constant
GAPDH	Glycolytic glyceraldehyde-3-phosphate dehydrogenase
gB	HSV glycoprotein B
GC	Genome copies
gD	HSV glycoprotein D
GFP	Green fluorescence protein
GLIC/GEEC	Clathrin-mediated endocytosis, micropinocytosis and clathrin-independent carriers and GPI-enriched endocytic compartment
gRNA	Guide RNA
h	Hours
HAART	Highly active antiretroviral therapies
HIV	Human immunodeficiency virus
HR1	Heptad repeat domain 1
HR2	Heptad repeat domain 2
HRP	Horseradish peroxidase
HS	Heparan sulfate
HSPG	Heparan sulfate proteoglycan
HSV	Herpes simplex virus
i.v.	Intravenous(ly)
IL-15	Interleukin-15
IL-7	Interleukin-7
ITR	Inverted terminal repeat
kb	Kilobases
kDa	Kilo Daltons
LB	Luria-Bertani
LDL	Low density lipoprotein
LV	Lentiviral vectors
M	Membrane protein
MAAP	Membrane associated accessory protein
Major SA	Major splice acceptor site
MEM	Minimal essential medium eagle
MERS	Middle East Respiratory Syndrome virus
MFI	Mean fluorescence intensity
min	Minutes

Minor SA	Minor splice acceptor site
ml	Milliliter
mM	Milimolar
MOI	Multiplicity of infection
mRNA	Messenger RNA
MTM	X-linked myotubular myopathy
N	Nucleocapsid protein
ng	Nanogram
NiV	Nipah virus
NiV-GΔ34	Nipah virus g protein truncated by 34 amino acids C-terminally
nM	Nanomolar
NSG	NOD.Cg-Prkdc^{scid} Il2rg^{tm1Wjl}
NTD	N-terminal domain
ORF	Open reading frames
PBMC	Peripheral blood mononuclear cells
PBS	Phosphate-buffered saline
PCR	Polymerase chain reaction
PDB	Protein Data Bank
PEI	Polyethylenimine
PFA	Paraformaldehyde
PLA	Phospholipase
qPCR	Quantitative PCR
RBD	Receptor-binding domain
RLU	Relative light units
RNA	Ribonucleic acid
rpm	Rounds per minute
RPMI	Roswell park memorial institute
RT	Room temperature
S	SARS-CoV-2 spike protein
S2’	Second proteolytic cleavage site
SARS	Severe acute respiratory syndrome virus
SARS-CoV-2	Severe acute respiratory syndrome coronavirus type 2
sc	Self-complementary
scATACseq	Single-cell assay for transposase accessible chromatin-sequencing
SD	Splice donor site
SDS	Sodium dodecyl sulfate
SDS-PAGE	Sodium dodecyl sulfate-polyacrylamide gel electrophoresis

SFFV	Spleen focus forming virus
SIV	Simian immunodeficiency virus
spCas9	Cas9 derived from *Streptococcus pyogenes*
ss	Single-stranded
STD	Standard deviation
TMPRSS2	Transmembrane serine protease 2
TU	Transducing units
U	Units
VLP	Virus-like particles
VOA	Viral outgrowth-assay
VSV	Vesicular Stomatitis virus
VSVG	G protein of Vesicular Stomatitis virus

9 List of figures and tables

9.1 List of figures

9.2 List of tables

11 List of publications

Peer-reviewed first author publications

Theuerkauf, Samuel A.; Herrera-Carrillo, Elena; John, Fabian; Zinser, Luca J.; Molina, Mariano A.; Riechert, Vanessa et al. (2023): AAV vectors displaying bispecific DARPins enable dual-control targeted gene delivery. In *Biomaterials* 303, p. 122399. DOI: 10.1016/j.biomaterials.2023.122399-

Theuerkauf, Samuel A.*; Michels, Alexander*; Riechert, Vanessa; Maier, Thorsten J.; Flory, Egbert; Cichutek, Klaus; Buchholz, Christian J. (2021): Quantitative Assays Reveal Cell Fusion at Minimal Levels of SARS-CoV-2 Spike Protein and Fusion-from-Without. In *iScience*, p. 102170. DOI: 10.1016/j.isci.2021.102170

*equal contribution

Peer-reviewed co-author publication

Riechert, Vanessa; Hein, Sascha; Visser, Mayken; Zimmermann, Mathias; Wesche, Jan; Adams, Philipp A. et al. (2023): FcγRIIA-specific DARPins as novel tools in blood cell analysis and platelet aggregation. In *J Biol Chem* 299 (6), p. 104743. DOI: 10.1016/j.jbc.2023.104743

Oral presentation

30th Annual Meeting of the Society for Virology, digital conference (2021): Fusion activity of SARS-CoV-2 spike protein

Retreat on Biomedical Research of the Paul-Ehrlich-Institut, Ronneburg, Germany (2023): AAV vectors displaying bispecific DARPins enable dual-control targeted gene delivery

Retreat on Biomedical Research of the Paul-Ehrlich-Institut, digital conference (2022): CD32a-targeted viral vectors for HIV gene therapy

Poster presentation

Retreat on Biomedical Research of the Paul-Ehrlich-Institut, Ronneburg, Germany (2020): T cell specific vectors for HIV gene therapy

4th International Conference on Lymphocyte Engineering, Munich, Germany (2023): FcγRIIA-specific DARPins displayed on viral vectors for HIV gene therapy

PEGS Boston: The Essential Protein Engineering & Cell Therapy Summit, Boston, United States (2023): FcγRIIa-specific DARPins as novel tools in blood cell analysis and platelet clotting

11.1 Award

Paper of the Quarter Award Q4 2023, Deutsche Gesellschaft für Gentherapie
Awarded for the publication (Theuerkauf et al. 2023)

13 Declaration of collaboration

Except where stated otherwise by reference or acknowledgment, the work presented was generated by myself under the supervision of my advisors during my doctoral studies. All contributions from colleagues are explicitly referenced in the thesis. The material listed below was obtained in the context of collaborative research:

The data from figures shown in the result section of Part A: Fusion activity of the SARS-CoV-2 spike protein, which are modified from the publication (Theuerkauf et al. 2021), were collected and evaluated collaboratively with Alexander Michels (Paul-Ehrlich-Institut) as stated in the publication.

Alexander Michels designed, evaluated experiments and visualized the results.
I performed, designed, evaluated experiments and adapted visualization.

Figure 26: Western blot to show S expression level on effector cells compared to cells infected with authentic SARS-CoV-2.

Collaboration partner: Bevan Sawatsky, Paul-Ehrlich-Institut
Contribution: SARS-CoV-2 infection and preparation of cell lysates
My contribution: Prepared cell lysates of transfected 293T cells expressing S, Western blot analysis and data visualization

Figure 29 B: VP1-DARPin fusion proteins are efficiently incorporated into the capsid and do not affect the capsid morphology.

Collaboration partner: Petr Chlanda, University of Heidelberg
Contribution: Cryo-electron tomography analysis of AAV vectors
My contribution: Produced and characterized AAV stocks, visualization of the results

Figure 29 C: VP1-DARPin fusion proteins are efficiently incorporated into the capsid and do not affect the capsid morphology.

Collaboration partner: Fabian John, Paul-Ehrlich-Institut
Contribution: Measurement of the thermal stability of AAV vectors
My contribution: Produced and characterized AAV stocks, evaluation and visualization of the results

Figure 30 A: Targeted AAV stocks have a high full/empty ratio and similar genomic titer.

Collaboration partner: Fabian John, Paul-Ehrlich-Institut
Contribution: Staining of AAV vectors for electron-microscopy and

acquisition of images
My contribution: Produced and characterized AAV stocks, evaluation and visualization of the results

Figure 43: Transduction of primary cells.
Collaboration partner: Burak Demircan, Paul-Ehrlich-Institut
Contribution: Titration of AAVs on activated PBMC and measurement at the day of analysis
My contribution: Produced and characterized AAV stocks, evaluation and visualization of the results

Figure 45: spCas9 delivered by F11-AAV and F11-55.2-AAV protects against HIV infection.
Collaboration partner: Elena Herrera-Carrillo, Mariano Molina (University of Amsterdam)
Contribution: Infection and transduction of SupT1 cells with HIV and AAVs, respectively. Measurement of p24 levels in cells and cell culture supernatants.
My contribution: Produced and characterized AAV stocks, evaluation and visualization of the results

Whenever a figure, table or text is identical to a previous publication, it is stated explicitly in the thesis that copyright permission and/or co-author agreement has been obtained.

The following parts of the thesis have been previously published:
Some figures and tables shown in the result and discussion sections are either modified from (Theuerkauf et al. 2021) or (Theuerkauf et al. 2023). Each figure legend indicates the publication reference.

Frankfurt am Main, den 08.02.2024 S.Theuerkauf

14 Declaration of an oath

DECLARATION

I herewith declare that I have not previously participated in any doctoral examination procedure in a mathematics or natural science discipline.

Frankfurt am Main, 08.02.2024 (Date) ……S.Theuerkauf…… (Signature)

Author's Declaration

I herewith declare that I have produced my doctoral dissertation on the topic of

Molecular concepts for pandemic viruses: Membrane fusion assays and targeting of reservoir cells

independently and using only the tools indicated therein. In particular, all references borrowed from external sources are clearly acknowledged and identified.
I confirm that I have respected the principles of good scientific practice and have not made use of the services of any commercial agency in respect of my doctorate.

Frankfurt am Main, 08.02.2024 (Date) ……S.Theuerkauf…… (Signature)